STUDIES OF THE SURFACE REACTIVITY OF METAL OXYHYDROXIDES AND SULFIDES WITH RELEVANCE TO ENVIRONMENTAL CHEMISTRY

A Dissertation
Submitted to
the Temple University Graduate Board

In Partial Fulfillment
of the Requirements for the Degree of
DOCTOR OF PHILOSOPHY

---

by
Andro-Marc Pierre-Louis
December, 2014

Examining Committee Members:

Professor Daniel R. Strongin, Advisory Chair, Department of Chemistry
Professor Eric Borguet, Department of Chemistry
Professor Frank C. Spano, Department of Chemistry
Professor James Kubicki, External Member, Pennsylvania State University

ABSTRACT

Andro-Marc Pierre-Louis

Doctor of Philosophy

Temple University, 2014

Doctoral Advisory Committee Chair: Professor Daniel R. Strongin, Ph.D.

With the benefits of an ever increasing advance of industrialization around the globe come formidable environmental problems. Three environmental problems that have relevance to the research described in this thesis are the 1) buildup of atmospheric CO_2 gas through the burning of fossil fuels, 2) eutrophication of aquatic systems, and 3) the acidification of environments from acid mine drainage (AMD) resulting from coal-mining activities. In particular research is presented in this thesis that investigated the surface chemistry of CO_2 and phosphate (PO_4^{3-}) on a suite of environmentally relevant iron oxyhydroxide materials and the chemistry of phospholipid molecules on environmentally relevant iron sulfide surfaces to suppress AMD. To develop a microscopic understanding of the surface chemistry of the different systems, an array of experimental and computational techniques were used in the research. Techniques included X-ray photoelectron spectroscopy, atomic adsorption, X-ray diffraction, scanning transmission microscopy with electron dispersive X-ray spectroscopy (STEM/EDS), ion chromatography (IC), and attenuated total reflectance Fourier transform Infrared (ATR-FTIR). Results from the latter technique were interpreted with the aid of density function theory (DFT) calculations.

Iron oxyhydroxides, which consisted of ferrihydrite (FeOOH), goethite (α-FeOOH), ferrimagnetic ferrihydrite (FerriFh), and aluminum-doped iron oxyhydroxide (content from 0-100 mol%) were synthesized and studied before and after exposure to gaseous CO_2, CO_3^{2-}, and PO_4^{3-} species. FeOOH and mixed Al/Fe oxyhydroxide surfaces showed high affinities for the formation of carbonate and bicarbonate species upon exposure to gaseous CO_2. Within the Al/Fe oxyhydroxide circumstance, a low Al level of incorporation in the iron oxyhydroxide structure caused a slight increase in surface area and increase in the amount of oxyanion (e.g., CO_3^{2-} or PO_4^{3-}) adsorption up to an Al level of 30 mol%. Significant changes were observed in the binding geometry of the adsorbed complexes on the Al/Fe mineral compared to single phase α-FeOOH, AlOOH, and FeOOH surfaces. ATR-FTIR results combined with vibrational frequency (DFT) calculations suggested the formation of multiple phosphate surface complexes via a variety of configurations such as inner-sphere/outer-sphere bidentate, monodentate depending on the solution pH and the Al mol% substituted into the Fe-oxyhydroxide.

Studies investigated the adsorption of CO_2 on FerriFh and compared those results to CO_2 on ferrihydrite. The CO_2 pressures used in these particular studies ranged from 1 to 57.8 bars. It is found that citrate bound species, resulting from the synthesis conditions used to make FerriFh, blocked surface sites for the formation of carbonate and bicarbonate species on the magnetic FerriFh and ferrihydrite oxyhydroxide minerals upon $CO_{2(gas)}$ exposure. A bicarbonate or bent-CO_2 like species (~1220 cm^{-1}) formed at lower CO_2 pressures (≤ 3.5 bars) but was absent at the higher pressures.

Additional studies investigated the adsorption of various phospholipid molecules on pyrite, and iron sulfide with FeS_2 stoichiometry. These studies were focused on suppressing the oxidative decomposition of pyrite to sulfuric acid, the root cause of AMD. Batch and column studies were employed to investigate the ability of phospholipids to reduce AMD over an extended period of time (up to 3 years). In studies that used actual coal mining refuse, which contained significant amount of pyrite, it was shown that the rate of acid production from pyrite decomposition could be reduced by as much as 70% due to the presence of surface bound phospholipid. Assembly of the phospholipid into a bilayer motif on the sulfide surface was hypothesized to form a hydrophobic barrier that kept dissolved O_2 and bacteria from facilitating the oxidation of FeS_2. Column experiments showed that when water at pH 7 was flowed over the coal mining waste, the effluent had a pH close to 3. In contrast when water at pH 7 was flowed over the pyrite containing waste, which was pretreated with lipid, the effluent had a pH closer to 7, and the total amount of Fe (Fe^{2+}/Fe^{3+}) and SO_4^{2-} in the effluent waters was also reduced relative to the untreated pyrite containing waste circumstance. These studies showed that the application of phospholipid to pyrite containing coal mining waste could potentially be an environmentally friendly remediation technique.

DEDICATION

I have dedicated this dissertation to my loved parents, Pierre Pierre-Louis and Marie Aurelia Pierre-Louis, who have inspired me to pursue my education and dream bigger than the expectations that any others have in me. My parents will continue to inspire me forever. Without the qualities that they have instilled in me, and their belief in my abilities, I would not be here today. My entire extended family has also been instrumental in my success; especially Candice Johnson Pierre-Louis, and I am entirely grateful for their support, love, and encouragement.

ACKNOWLEDGMENTS

I would like to express my sincere gratitude to my Advisor, Dr. Daniel R. Strongin, for his mentorship, expertise, patience, support, and guidance. Dr. Strongin has inspired me with his hard work, collaboration, and dedication to research. I relied heavily on his encouragement and cherish his support during the most difficult times that I endured during my graduate studies, particularly with the passing of my mother and father, Aurelia Marie and Pierre Pierre-Louis, in addition to my first-born son Elijah-Marc Pierre-Louis. I wish one day to serve and carry the legacy of the wonderful mentorship I received from Dr. Strongin.

I am also grateful to my Committee Members: Dr. Eric Borguet, Dr. Frank Spano, and Dr. James Kubicki for their sincere comments, discussion, enthusiastic suggestions, support, and encouragement. Dr. Spano and Dr. Borguet have been diligent in their support and interest in my growth, and to them I express my sincere gratitude. I also thank all my undergraduate professors especially Dr. David Dalton, Dr. Susan Jansen-Varnum, and Dr. Jayakumar Gilbert for their thoughtful discussion, support, and encouragement. I have also been fortunate to work with very knowledgeable collaborators, who have been recognized as co-authors on various manuscripts. From the Stony Brook University in NY, with our colleagues from the collaborative research in chemistry (CRC), I want to thank Dr. Brian Philips, Dr. Wei Li, and Dr. Jongsik Kim. Dr. Dane Morgan and Dr. Nathan Pinney from the University of Wisconsin-Madison have also been helpful during several CRC video conferences over the past years. From the

Pennsylvania State University, I want to thank Dr. James Kubicki whom I have also looked up for serving as the outside committee member and for his guidance in quantum computational calculations (DFT).

I deeply thank, cherish and love my wife, Candice Johnson-Pierre-Louis for her encouragement in many more ways than words could express.

I also would like to thank my lab group members, past and present especially Dr. Juan Hao, Dr. Riley Murphy, Dr. Alex Gordon, Dr. Doug Hausner, Dr. Narayan Bhandari, Dr. Soujanya Singireddy, Kristin Lammers, Amber Riendeau, Elizabeth Cerkez, Samantha Shumlas, Leandre VanBurren, Joseph Craig Dalessandro, Akila Chathuranga Thenuwara, and Matthew Zuchero for their thoughtful lab presentation and fun lunch times. I also thank my colleagues and friends Johnny Perez, Paul Flanigan, Nejea I. Davis, Paul Gaspari, Kerisha Bowen, Goutham Kodali, Gopal Sirasani and Manasa Mamunooru, Jelena Drazenovic, Sandeep Kovadetti, Sudipto Mushi, Madi Narayanan, Mohit Patel, Rao P. Chinnam, Salome Bhagan, Jieutonne Acher, Tim Bohinski, Shalaka Dewan, Sepideh Afsarimamagahni, Devika Sil, Conrad Pfeiffer, Justin Griggs, Rene Oats, Wagh Bharat, Ian Glassford, Kimberly Jacoby, Xu Bolei, Raymond Pauszek, Brandon Presley, Santosh Karki, and Justin Kaplan for their collaboration, friendship, sports event, and nice discussion. The past and current undergraduate students Sopheavy Siek, Eric Bryant and Biran Fall, I also enjoyed working with you all.

I will always be thankful to my sisters and brothers: Marilene, Claudette, Malina, Jean-Ricot, Kesnel, Jacquis, Mackender, and Wigler for their love, support, and encouragements. Special thanks to my cousin Marjory and Magarette Cajoux, Cathelene,

and Lourdes Marie Vital for their friendship and support. I would also like to thank Dr. Georges H. Myer, James Ladd, and Steve Peterson from the Earth and Environmental Science Department for their helpful discussion in mineralogy analysis (SEM). I would also acknowledge Dr. Jacqueline Tanaka from the Biology Department and Dr. Zebulon V. Kendrick from the graduate office for their leadership and support. Dr. Linda Powell, Dr. Steeve Cox, and Mrs. Kenee Veniece from the Louis Stokes Alliances for Minority Participation (LSAMP), at the Community College of Philadelphia and Drexel University Office, I sincerely thank you for the partial financial support during the first two years for the Bridge to the Doctorate Program.

Mrs. Bobbi Johnson, Mrs. Regina Shapiro, Mrs. Jeanette Ford, Mrs. Sharon Kass (Main Office), Mr. Mark Krammerer (PC support), Mrs. Yelene Cherkashina and Mr. Chris Wise (Chemical supply), Mr. David Placket (Glass blowing), Mr. Donald Deigh-Kai, Dr. Hongwen Zhou (TEM), Mr. Matthew McCormick and Mr. Edward Kaczanowicz both from the machining facility, and all other Temple staff members not mentioned; I thank you all.

This research was made possible by support from the National Science Foundation (NSF) Collaborative Research in Chemistry grant (CRC/CHE-0714121), and a Bridge to Doctorate Fellowship.

Chapter 1 is a reprint from a published article in the Journal of Colloid and Interface Science (A-M Pierre-Louis et al., 2013), with the expressed written copyright permission of the publisher.

Chapter 5 includes a reprint of the ART-FTIR section from published articles in Langmuir (Kubicki et al., 2012) and Geochimica et Cosmochimica Acta (Wei et al., 2013). The co-authors listed on this published work are recognizable for their collaboration. All are reproduced with the expressed written copyright permission of the publishers.

TABLE OF CONTENTS

LIST OF FIGURES

LIST OF TABLES

CHAPTER 1

INTRODUCTION

1.1 Overview

Much of this dissertation focuses on understanding the surface reactivity of Fe-, Al-oxyhydroxide, and binary Al/Fe mineral systems towards adsorbed $CO_{2(gas)}$, carbonate, and phosphate complexes. The adsorption of these species can alter the surface charge on the metal oxyhydroxide minerals and perhaps affect their surface reactivity. Several advanced surface-sensitive characterization techniques were utilized to probe the structural and compositional changes that occur upon Al substitution into the Fe-oxyhydroxide minerals. The combination of a variety of surface science techniques such as XRD, XPS, TEM, and ATR-FTIR combined with quantum computational modeling provides a powerful tool to investigate the reactivity of iron oxyhydroxides such as, ferrihydrite, Al/Fe-oxyhydroxide, ferrimagnetic ferrihydrite, goethite, and alumina towards the adsorption of gaseous CO_2, carbonate and phosphate anions. In addition, the surface activity of pyrite (FeS_2) from acid mining waste rocks is explored in search of the development of an important technological remediation strategy using environmentally friendly phospholipid bilayer molecules. In particular, the role and effectiveness of adsorbed phospholipid bilayers to suppress iron sulfide oxidation from generated coal mining waste samples are investigated.

The findings in this dissertation are important for the prevention and/or control of atmospheric and aqueous pollutants. In addition, a remediation strategy for acid mine

drainage (AMD) waste; a significant environmental problem, is proposed. Finally, the organization of this thesis is outlined in the introduction.

1.2 Iron Oxyhydroxide Minerals

Iron exists in a variety of naturally occurring minerals in the form of oxides, oxyhydroxides, sulfides, and/or heterogeneous complex hydroxide species. Fe-oxyhydroxide minerals are encountered almost everywhere in natural systems and biological processes. Fe-oxyhydroxide particles surface areas vary between 100-700 m^2g^{-1}; range from the nano to micro-regime sizes; control an extraordinary amount of environmental chemistry; and their surface reactivity is often affected by varying levels of surface hydration (Strongin, Grey et al. 2010). Iron oxyhydroxides can also be found in alternative places such as, on the inside of steel water pipes/tanks, as feroxyhyte rust (δ-FeOOH) and in highly pressurized environments such as ocean floors.

Iron oxyhydroxides can be synthesized through dissolution, precipitation, bacterially driven redox reactions of aqueous species, weathering in processes such as acid mine drainage (AMD), and through biologically relevant processes, such as the formation of the inorganic ferric (i.e., ferrihydrite) pigment core within the ferritin protein (Taylor and McKenzie 1980; Ford, Harrison et al. 1984; Zhao, Huggins et al. 1994; Carta, Casula et al. 2009; Michel, Hosein et al. 2010). They are commonly found as a mixture of siderogel (colloid/limonite) with varying composition within the structure of goethite, lepidocrocite, quartz, and clay minerals.

A ubiquitous iron oxyhydroxide mineral, and one central to this thesis research is ferrihydrite (e.g., "2-line" vs. "6-line" structures). The structure of this material has been controversial over the last few decades. Prior work has suggested that it is isostructural to the akdalaite ($Al_2O_3.5H_2O$ and/or $Al_{10}O_{14}.(HO)_2$) crystal structure (Michel, Ehm et al. 2007; Manceau 2011). Ferrihydrite has been the topic of many prior studies in the context of surface reactivity, because of its relative stability with hydration, small particles size, high porosity and large surface area. Recently, the ferrihydrite structure has been proposed as a polyhedral representation of hexagonal unit cells contained in a cubane-like moiety and has been referred to as the Michel model (Figure 1.1) (Michel, Parise et al. 2007). Ferrihydrite ($5Fe_2O_3.9H_2O$) is a precursor to other stable minerals that include magnetite (Fe_3O_4), goethite (α-FeOOH), lepidocrocite (γ-FeOOH), akaganeite (β-FeOOH), and hematite (α-Fe_2O_3), and these minerals are also common to many soils. Given the high surface area and poor crystalline amorphous structures, the metastable nanophase ferrihydrite mineral can undergo phase transformations through dehydroxylation and hydrothermal aging (≤ 175°C) in the presence of adsorbed citrate and phosphate anions into more stable iron oxyhydroxide forms, such as the ordered crystalline ferrimagnetic ferrihydrite ($Fe_{10}O_{14}(OH)_2.H_2O$) mineral (Taylor and McKenzie 1980; Ford, Harrison et al. 1984; Zhao, Huggins et al. 1994; Carta, Casula et al. 2009; Michel, Hosein et al. 2010). Without the presence of these ligands, the most stable hematite (α-Fe_2O_3) iron oxide phase forms upon aging of ferrihydrite.

Goethite (α-FeOOH) surface is another important iron oxyhydroxide mineral and it has been widely studied. α-FeOOH is isostructural with diaspore (i.e., hexagonal closed pack as in α-AlOOH). In natural environments, goethite aggregates

occur in rocks, soils, and ochre deposits. Goethite can be transformed through dehydroxylation or loss of hydroxyl (OH) to the crystalline hematite form (Schwertmann 2000). Synthesized goethite, of well-ordered polycrystalline structural habits, can vary from nanometer sized (~237 nm, with measured surface area ~139 m^2g^{-1} , acicular-like shape) up to about a micrometer (~900 nm, size regime with SA ~68 m^2g^{-1}, fairly regular needle-like shape) (Kubicki, Paul et al. 2012). Thus, the iron oxyhydroxide mineral phases including their size dependent properties (< 1,500 nm), stability, phase transformation, and reactivity are ripe for study, because of their potential application in photoxidation, catalytic reactions, and also for their interaction with pollutants in the environment.

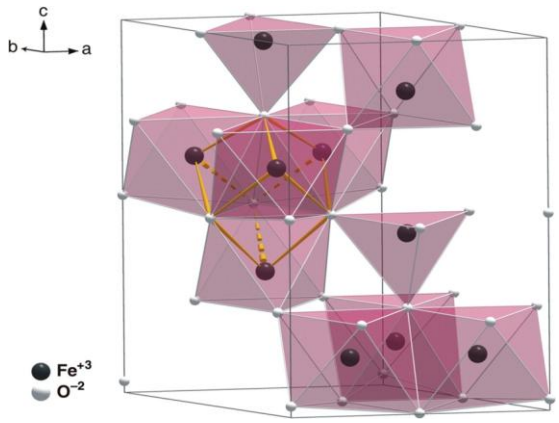

Figure 1.1. Crystal structure of ferrihydrite (P63mc) shown in the polyhedral representation of the hexagonal unit cell. Black atoms are iron Fe^{3+}, white atoms are O^{-2} oxygen, and hydrogen atoms are not shown (Reprinted with permission from the Science Journal). (Michel, Parise et al., 2007)

1.3 Binary Al/Fe Oxyhydroxide Minerals

Al-oxyhydroxide crystalline phases commonly appear in the environment as akdalaite ($5Al_2O_3 \cdot H_2O$), tohdite ($4Al_2O_3 \cdot H_2O$), boehmite (γ-AlOOH), diaspore (α-AlOOH), corundum (α-Al_2O_3), bayerite (β-$Al(OH)_3$), and gibbsite (α-$Al(OH)_3$). Alumina minerals are the main important constituents of the aluminum ore and bauxite mining. In the environment, iron oxyhydroxides that include ferrihydrite and goethite often contain Al. The octahedral Fe^{3+} ion within iron oxyhydroxides is often readily substituted, not only by Al, but by other metal cations such as Si and Mn (Anderson and Benjamin 1990). However, Al substitution is particularly favorable due to its ubiquity, mobility, and its abundance with Fe, during mineral dissolution/co-precipitation and weathering (Cornell et al., 1996). It has been postulated that metal cation incorporation may cause changes in the Fe-oxyhydroxide structural surface sites and properties depending on the valence number and/or charges of the substituted atomic element (e.g., Al^{3+}). In addition, results from these studies reported that the crystal size/unit cell parameters, aspect ratio, magnetic properties, and the rate of acid and reductive dissolution are altered with increasing Al substitution into Fe-oxyhydroxide (Cismasu, Michel et al. 2011; Cismasu, Michel et al. 2012).

Al/Fe oxyhydroxides have attracted great interest in recent research as sorbents due to increases in surface area, surface site-defects, fixed-stoichiometries, high stabilities and reactivities. This even makes these materials potential candidates for use as structural materials; as for example in high temperature applications. There have been investigations, whether or not the substitution of the Al^{3+} into the iron oxyhydroxide

structure leads to an isostructural mineral during the alternating reduction-oxidation cycles which is often promoted by the dissolution of Fe containing minerals and the re-precipitation of Al/Fe oxyhydroxides (Bazilevskaya, Archibald et al. 2011). Accordingly, as low as 2 mol% Al substitution in ferrihydrite is found to prevent its transformation into goethite via precipitation and crystallization reactions. The Al-substitution stabilizes the ferrihydrite structure by reducing the dissolution rate of the mineral and the resulting dissolution-repreciptation reactions that would be required to covert to goethite under environmentally relevant conditions (Bazilevskaya, Archibald et al. 2011). In addition, binary Al/Fe oxyhydroxides are often found to be difficult to characterize because of their variable composition, surface area, particle size, and crystallinity depending on the synthesis methods (Taylor and McKenzie 1980; Masue, Loeppert et al. 2007; Harvey and Rhue 2008). In this regard, Al/Fe oxyhydroxide systems are mainly investigated in this work for their surface reactivity towards adsorbed gaseous atmospheric pollutants (e.g., CO_2) and oxyanions such as CO_3^{2-} and PO_4^{3-}. The study of the mixed Al/Fe oxyhydroxide discussed in this these offers a better understanding of how the structural/electronic properties, the chemical reactivity, and adsorption properties of Al/Fe oxyhydroxide differs from the individual Al- and Fe-oxyhydroxide materials.

1.4 Reactivity Studies at the Mineral Surfaces

Ferrihydrite, mixed Al/Fe oxyhydroxide, magnetite, and goethite are ubiquitous in soils, and in aquatic and marine environments where they can adsorb many organic (e.g., humic and fulvic acids) and inorganic (e.g., Se and Cr) pollutants, as well as play a role

in controlling the bioavailability of toxic heavy metals (e.g., As, Pb, and Tl) and radionuclides (e.g.,U and La) (Hochella et al., 2005, Vengosh et al., 2013). Results from prior studies showed that goethite particles with different crystalline habits (e.g., nanorod suspensions are less stable compared to microrod) resulted in distinct differences of adsorbed CO_3^{2-} and PO_4^{3-} species on the surface of goethite crystal structures (Kubicki, Paul et al. 2012; Rubasinghege, Kyei et al. 2012).

While many studies use iron oxyhydroxide surfaces for reactivity and adsorption studies, mixed Al/iron oxyhydroxide mineral surfaces may be even more relevant materials to study due to their concomitant abundance in natural environments. Past studies investigated the adsorption of arsenate/arsenite and PO_4^{3-} surface complexes on the Al/Fe oxyhydroxide surfaces and the results indicated that concentration of adsorbed species are increased with an increasing Al substitution up to 30 mol% compared to the end-member iron and Fe- and Al-oxyhydroxide phases.

As mentioned, reactivity studies of Al/Fe oxyhydroxide systems have received little attention due to the complexity of the heterogeneous mineral system in synthesis and characterization methods. However, sorption (e.g., adsorption) phenomena on the Al/Fe oxyhydroxide surfaces can be investigated by using modern microscopic and spectroscopic techniques to decipher and understanding the chemical processes that occur in soils and aquatic environmental systems. Under various conditions such as temperature, pH, ionic strength, and loading; the surface charge potential and sorption behaviors of Al/Fe oxyhydroxide can be significantly affected. Thus, the protonation state of adsorbed oxyanions such as CO_3^{2-} and PO_4^{3-} surface complexes can be impacted as function of pH, molarity, and the symmetry of the surface complexes that adsorb on

the Al/Fe oxyhydroxide. Table 1.1 shows the different metal oxyhydroxides utilized in this study.

Table1. 1. Different characteristic of metal oxyhydroxide surfaces used in this study

Metal-oxyhydroxides	(m^2/g)	Crystallinity	Proposed Formula/Symbol	Size (nm)
Ferrihydrite	336	Poorly amorphous	$Fe_{8.2}O_{8.5}(OH)_{7.4}$+3H$_2$O	2
Al/Fe 5 mol%	326	Amorphous	_	< 2
Al/Fe 10 mol%	347	Amorphous	_	< 2
Al/Fe 30 mol%	387	Amor. to crystalline	_	< 5
Alumina	120	Poly-crystalline	AlO(OH)	> 100
Goethite	68	Poly-crystalline	α-FeOOH	> 1000
Ferrimagnetic ferrihydrite	161	Amor. to crystalline	FerriFh	10

1.5 Adsorption of Carbon Dioxide (CO_2) on Mineral Surfaces

Surface reactivity studies of Al- and Fe-oxyhydroxide particles with CO_2 and carbonate complexes (e.g., HCO_3^-/ CO_3^{2-}) are of significant interest due to their presence and interaction with suspended aerosols in the atmosphere and their bioavailability in subsurface environments (Villalobos 2000). The large surface areas of cloud aerosol particles can provide sites for heterogeneous chemistry reactions and interaction with $CO_{2(gas)}$ and other greenhouse gases. It has been reported that the concentration of gaseous CO_2 has increased from 280 parts per million (ppm) in 1800 to ~400 ppm in

2013. This represents an approximate 30% increase of CO_2 concentrations in the atmospheric. According to the Earth System Research Laboratory Global Monitoring Division, booming industrial development significantly contributed to the increases (Chadwick, Jones et al. 1986). There is significant evidence of global warming, several researchers have taken tremendous efforts to understand the extent and mechanism through which greenhouse gases (e.g., H_2O vapor, Cl_2, NO_x, CH_4, SO_2, O_3, CFC, and CO_2) become retained by aerosol suspended particles and the subsurface of geological materials. Accordingly, Fe-carbonate minerals are historically recognized as a carbon storage source in the pedosphere for geologically significant timeframes (~1000 years) (Bachu, Bonijoly et al. 2007; Izgec, Demiral et al. 2008). The reaction of gaseous CO_2 with aerosol particles and surface hydroxyl groups on FeOOH and AlOOH often forms reversibly bound and/or stable carbonate species (Baltrusaitis, Schuttlefield et al. 2007; Baltrusaitis, Schuttlefield et al. 2011). In this regard, the capture of CO_2 from anthropogenic sources (i.e., carbon produced from the combustion of wood, oil, coal, and natural gas) on the adsorption sites of FeOOH, AlOOH, and Al/Fe oxyhydroxide is well an interesting scientific issue to address. Research, however, is needed to understand the different chemical reactions occurring at their surfaces and research presented in this thesis will help fill in this knowledge gap. Studies showed that $CO_{2(gas)}$ remains trapped in a carbonated form deep into subsurface soils typically as stable siderite ($FeCO_3$), calcite/limestone ($CaCO_3$), and ankerite ($Ca(Fe,Mg,Mn)CO_3)_2$) for long geological time periods (Oelkers and Schott 2005; Murphy, Lammers et al. 2010; Murphy, Lammers et al. 2011; Oganov, Hemley et al. 2013).

1.6 Adsorption of Aqueous CO_3^{2-} on Metal Surfaces

Iron oxyhydroxide minerals have been widely involved in the adsorption of aqueous CO_3^{2-} over relatively wide pH ranges (6-9) and have been studied under closed and open systems. ATR-FTIR probing combined with quantum chemical calculations have been one of the primary tools used to assign the type of vibrational modes of adsorbed carbonate to particular adsorption complex geometries that include mononuclear monodentate, binuclear bidentate, and outer-sphere complexes (Wijnja and Schulthess 2001). The following reaction mechanism occurs upon $CO_{2\ (gas)}$ adsorption on dry iron oxyhydroxide surfaces:

In the absence of co-adsorbed water vapor:

$$Fe_2OH + CO_{2(gas)} \rightleftarrows Fe_2O_2COH \quad (4)$$

In the presence of co-adsorbed water vapor; the following unbalanced reaction occurred

$$FeOH + CO_{2(gas)} \rightleftarrows FeOCO_2 + 3H_2O \quad (5)$$

The transformation of ferrihydrite to siderite can also occur in the presence of supercritical $scCO_2$ and aqueous sulfide with the following proposed reaction mechanism (Murphy, Lammers et al. 2010):

$$5Fe_2O_3.9H_2O\ (aq) + 5S^{-2}_{(aq)} + 10CO_{2(aq)} \rightleftarrows 5S^0 + 10FeCO_3 + 10OH^- + 4H_2O \quad (6)$$

The reaction mechanism (6) is noteworthy because in the absence of $scCO_2$ and the presence of high concentration of aqueous carbonates, suspended ferrihydrite nanoparticles are readily transformed to hematite under hydro thermodynamic (~100 °C)

conditions (Jambor and Dutrizac 1998). Thus, molecular CO_2 is often strongly adsorbed in both aqueous and gaseous phases forming CO_3^{2-} on moist surfaces and both CO_3^{2-} and HCO_3^- on the dry iron, alumina, and mixed Al/Fe oxyhydroxide substrates. However, dissolved $CO_{2(gas)}$ in solution can act as an carbonate anion competitor for phosphate, sulfate, and arsenate species in aqueous media and soils (Villalobos 2000; Arai, Sparks et al. 2004; Hiemstra, Rahnemaie et al. 2004; Rahnemaie, Hiemstra et al. 2007). Here, we extended our study to investigate the formation of adsorbed carbonate species on a variety of Al/Fe oxyhydroxide surfaces and compared these species to those adsorbed on individual Al- and Fe-oxyhydroxide phases.

1.7 Adsorption of Aqueous Phosphate Complexes on Metal Surfaces

Phosphate is an essential nutrient for plants and is typically in limited amounts in most soils. Inorganic and organic phosphates are very important in biogeochemistry and biochemistry, and the biogeochemical cycling of phosphate is of great interest for many reasons. Inorganic phosphate minerals are very abundant in natural environments and may exist as, apatite ($Ca_5(PO_4)_3(F,Cl,OH)$), hydroxyapatite ($Ca_5(PO_4)_3OH$), augelite ($Al_2(OH)_3PO_4$), berlinite ($AlPO_4$) and childrinite ($Fe/Al(PO_4)OH_2.H_2O$). Inorganic phosphate salts are the main sources to obtain phosphorus compounds for use in agricultural fertilizer, corrosion inhibition, orthopedic dental etchant, dispersant agent, flux, preservative as foods additive, household detergents, and industrial etchants. Dissolution and transport of phosphate minerals from rocks also contribute to the major aqueous phosphate species found in natural environments, the oceans and soils. However,

Al and Fe oxyhydroxides dissolution by organic ligands (e.g., oxalate, humic and fulvic acid) account for the majority of phosphate available to plants by phytoremediation (Cornell R. M. 2003; Rhoton and Bigham 2005). Indeed, the excess amounts of phosphate in porous sub-soils can be reduced by adding moderate amount of materials containing high content of Al and iron oxide/oxyhydroxide minerals.

Phosphate ion can carry a +5 formal charge which is primarily found in the most stable orthorphosphate (e.g., H_3PO_4) species, but could have oxidation states from +5 to -3. Accordingly, the phosphate surface complexation models can be used for the interpretation of arsenate speciation or binding configuration at the mineral surfaces. The following acid dissociation reaction mechanisms for the triprotic orthophosphoric acid often occur in solution under equilibrium conditions:

$$H_3PO_{4(s)} + H_2O_{(l)} \rightleftarrows H_3O^+_{(aq)} + H_2PO^-_{4\,(aq)} \quad (pK_{a1} \sim 2.12) \qquad (7)$$

$$H_2PO^-_{4\,(aq)} + H_2O_{(l)} \rightleftarrows H_3O^+_{(aq)} + HPO^{2-}_{4\,(aq)} \quad (pK_{a1} \sim 7.21) \qquad (8)$$

$$HPO^{2-}_{4\,(aq)} + H_2O_{(l)} \rightleftarrows H_3O^+_{(aq)} + PO^{3-}_{4\,(aq)} \quad (pK_{a1} \sim 12.63) \qquad (9)$$

Similar to carbonate, phosphate adsorption mainly increases with increasing contact time, loading, and the uptake on the mineral surfaces is highest at the lower pH (3-5) range which often resulted in more protonation of the surface species (Figure 1.2). While the Al- and Fe-oxyhydroxide materials offer large reactive surface areas for phosphate adsorption up to 4.2 $\mu molm^{-2}$ of maximum phosphate loading; for example, synthetic goethite and Al/Fe rich minerals in natural sub-soils have shown to adsorb (Torrent, Schwertmann et al. 1992; Khare, Hesterberg et al. 2004; Gimsing and Borggaard 2007).

Here, we investigated and evaluated the different proton interactions of adsorbed phosphate species on various metal Al/Fe-oxyhydroxides with the aim of finding out whether the inner-sphere complexes are formed as the bidentate binuclear (BB), monodentate mononuclear (MM), or whether there are formation of multiple phosphate surface complexes at the Al/Fe interfaces. In addition to earlier works, which usually showed a single specific type of surface complexes formation on the mineral surface, our correlation studies suggested a good agreement between the experimental ATR/FTIR and the DFT calculated vibrational frequencies, indicating that multiple phosphate complexes can be present on the Al/iron oxyhydroxide surfaces (Tejedor Tejedor and Anderson 1990; Arai and Sparks 2001; Kwon and Kubicki 2004; Daou, Begin-Colin et al. 2007; Elzinga and Sparks 2007; Harvey and Rhue 2008; Choi, Drese et al. 2009; Kubicki, Paul et al. 2012; Li, Pierre-Louis et al. 2013).

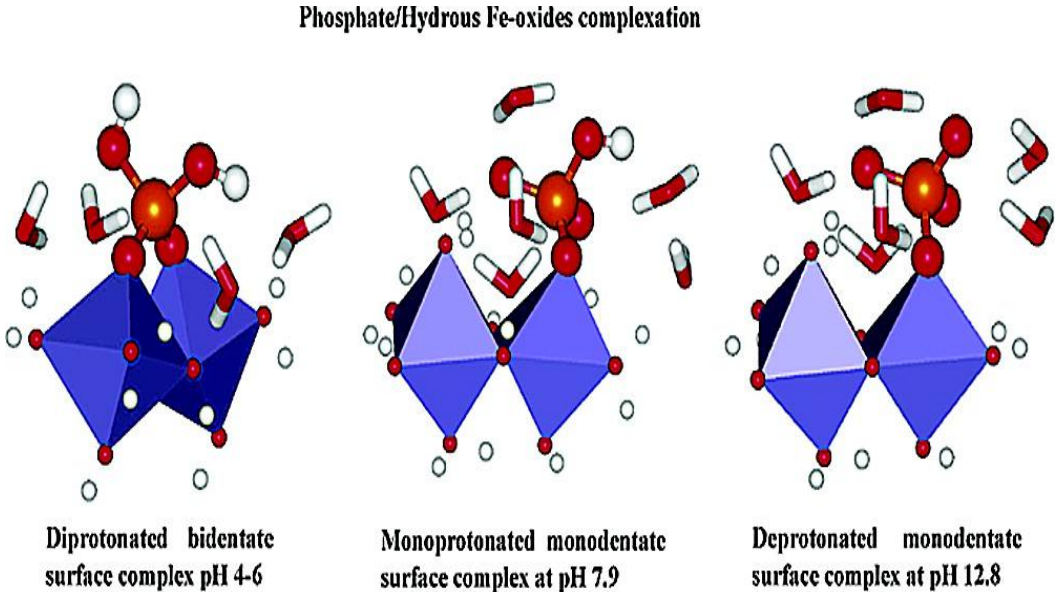

Figure 1.2. Different adsorbed phosphate surface complexation models onto iron oxyhydroxides (Reproduced with permission from the American Chemical Society publishing article (Kwon and Kubicki 2004))

1.8 Metal Sulfide Minerals

The iron sulfide, pyrite, is the most abundant metal sulfide in the Earth's crust. The mineral is often mistaken for gold and commonly named "fools gold" because of its shiny golden appearance. In the context of environmental chemistry, the oxidative decomposition of pyrite, is a significant contributor to the devastating environmental problems, acid mine drainage (AMD). This problem is acute to coal-mining regions, since pyrite is a major constituent (at least 2-20%) of coal mining overburden/waste rock (OWR) which can generate acidic effluent, sulfate, and releases various oxidized heavy metals such as arsenic in solution upon weathering by H_2O, microbes, and O_2 oxidation. The reaction of OWR to form sulfuric acid affects streams and rivers in areas where there

are abandoned industrial coal mining sites (e.g., in Northwestern China, Morocco, Pennsylvania and Massachusetts area, South Africa, etc…). An example, close to home, is the problem of AMD in Pennsylvania where thousands of kilometers of waterways are affected by AMD chemistry. A particularly well-known example of AMD includes the Iron Mountain mine, which previously affected the drinking water-supply quality system around the Sacramento River in which the AMD processes lead to pollution of rivers and streams from mining activities as described by the USGS/USEPA. The result is AMD water run-off containing high toxic levels of sulfate, ferrous iron, and traceable heavy metal elements (e.g., U, Mo, Pb, Cr, Hg, Cu, and As, to name a few), with high acidity ($pH < 4.5$). Another significant component of AMD chemistry occurring during coal mining OWR decomposition is specific different types of iron-oxidizing and sulfate-reducing bacteria which can contribute to further oxidation/reduction of metal sulfide FeS_2 minerals in anoxic. The remediation of such afflicted areas is expensive; just in Pennsylvania alone the clean-up cost of the problem to this point in time is over 5 billion dollars.

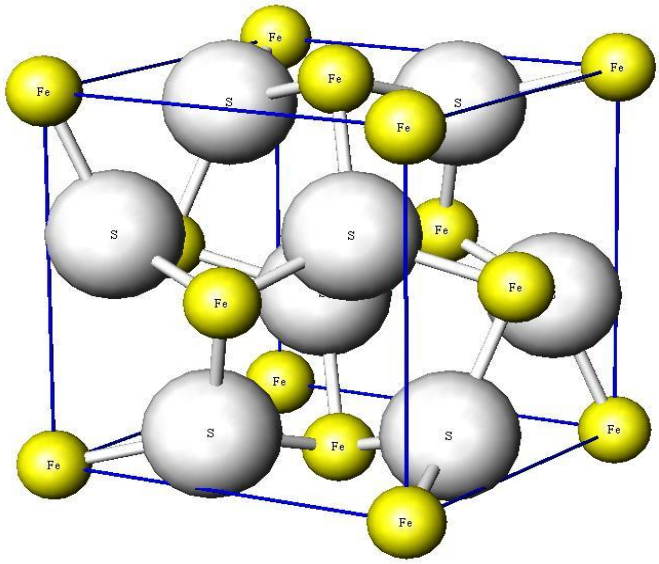

Figure 1.2. Crystal structure of pyrite (FeS_2). Space group is Pa3, and the Pearson symbol is cP12. At the center of the unit cell, white atoms with S-S linkages and yellow Fe atoms at the corners sharing Fe-S bonds are shown.

1.8.1 Phospholipids Suppression of Pyrite Oxidation in AMD Remediation

Previous studies have suggested numerous possible abatement strategies for AMD including the use of phosphate, silica, ascorbic and humic acids, municipal wastewater and activated sludge, manure and wood ash for the micro-encapsulation of the FeS_2 mineral (Evangelou, Seta et al. 1998; Elsetinow, Schoonen et al. 2001). It is found that phosphate and silica coatings provided a barrier to prevent pyrite oxidation, which are not sustained at pH < 4 due to ability of Fe^{3+} to attack the surface of pyrite sites (Elsetinow, Schoonen et al. 2001). Methods geared to the neutralization of AMD (e.g., $CaCO_3$, CaO, $Ca(OH)_2$ and silicate) often fall short and require high maintenance due to their lack of prolonged stability and robustness against pyrite oxidation. This maintenance cost, in turn may increase treatment costs.

Prior studies carried out in our laboratory have shown that phospholipid bilayers adsorbed on pyrite suppresses AMD-like chemistry (Elsetinow, Guevremont et al. 2000; Elsetinow, Schoonen et al. 2001; Elsetinow, Borda et al. 2003; Hao, Murphy et al. 2009). Research focused on understanding the mechanism by which phospholipid can suppress the oxidation rate of FeS_2-containing coal mining OWR is an important aspect of work presented in this thesis. The results showed that the application of these lipids to pyrite-containing OWR suppressed the release amount of SO_4^{2-}, Fe, and acidity pH from collected effluent (Elsetinow, Borda et al. 2003; Hao, Cleveland et al. 2006; Hao, Murphy et al. 2009; Zhang, Jia et al. 2012).

1.9 Organization of Thesis

The research detailed in this thesis is a combined study of the surface reactivity of Fe and Al oxyhydroxide nanoparticles and sulfide minerals (FeS_2); the latter having relevance to AMD environmental chemistry and remediation. Chapter 2 gives detailed descriptions of the various experimental techniques used to probe the surface reactivity of the minerals, that include X-ray photoelectron spectroscopy (XPS), atomic absorption (AA), scanning transmission electron microscopy with electron dispersive X-ray spectroscopy (STEM/EDS), X-ray diffraction (XRD), and attenuated total reflectance Fourier transform infrared spectroscopy (ATR-FTIR) combined with density functional theory (DFT) calculations. In chapter 3, the synthesis and characterization of mixed Al/Fe oxyhydroxides are described and the reactivity of the materials toward gaseous carbon dioxide (CO_{2gas}) and the formation of carbonate and bicarbonate as a function of increasing Al content were investigated. In chapter 4, the reactivity of the synthesized ferrimagnetic ferrihydrite (FerriFh, ~10-12 nm diameter) phase toward gaseous CO_2 adsorption was investigated and compared to its precursor 2-line ferrihydrite (2 nm diameter) under various pressure (0.35 to 58.6 bar) conditions. Chapter 5 investigates the reactivity of mixed Al/Fe oxyhydroxide toward aqueous PO_4^{3-} and CO_3^{2-} species are compared to single phase ferrihydrite, FerriFh, and goethite mineral surfaces. The formation of different protonated PO_4^{3-} complexes such as bidentate binuclear or monodentate complexes is emphasized and investigated as a function of pH, loading, and ionic strength. Chapter 6 shift attention to metal sulfide substrates and investigates the ability of phospholipid bilayers to form a barrier to prevent oxidizing species such as

dissolved O_2 and Fe(III), and microbial species from oxidizing pyrite-containing OWR to form acid. The effectiveness of the phospholipid remediation strategy to abatement AMD-chemistry resulting from the oxidation of FeS_2 was demonstrated for more than a year using flow-through column experiments. Chapter 7 provides a summary of these research findings, draws conclusions, and proposes further recommendations.

CHAPTER 2

EXPERIMENTAL TECHNIQUES

2.1 Overview

We now introduce an overview of the experimental techniques used in this work. Characterization of single phase and mixed metal Al/Fe oxyhydroxide nanoparticles is fairly difficult as both natural environmental and laboratory synthesized samples show different crystallinity, nucleation/aggregation between particles, and wide range of particles sizes. Furthermore, the differences in synthesis methods of metal oxyhydroxide nanomaterials often suggested slightly different products formation and may affect the structural properties and composition of Al- and/or Fe-oxyhydroxide size dependent particles. A wide array of analytical techniques such as X-ray photoelectron spectroscopy (XPS), scanning transmission electron microscopy coupled with energy dispersive X-ray analysis (STEM/EDAX), scanning electron microscopy (SEM), X-ray diffraction (XRD), attenuated total reflectance Infrared spectroscopy (ATR-FTIR), and density functional theory (DFT) calculations are essentially used for the characterization of laboratory synthesized iron, alumina, and mixed Al/Fe oxyhydroxide materials. The application of these analytical techniques helped us with the understanding of adsorbate/surface interactions and facilitated the interpretation of our experimental results. A brief detailed description of some of the experimental techniques used in this work is now presented.

2.2 Materials

2.2.1 X-ray Photoelectron Spectroscopy (XPS)

Photoelectron spectroscopy probes the band structure of solid material by irradiating the specimen surface with low mono-energetic X-rays beam (e.g., Al Kα at ~1486.6 eV or Mg Kα line at ~1253.6 eV) which excited either a valence or inner core level electrons in an atom upon the adsorption of electromagnetic radiation (photons). This process is also known as electron spectroscopy for chemical analysis (ESCA) and is mainly an application of Einstein's photoelectric effect. The kinetic of ejected photoelectrons (E_k) is directly related to the X-rays irradiating energy source (hν) the binding energy (E_b) of electron in the solid material, and W_f is the work function of the detector (see Equation 13). Photoelectrons are ejected typically in the range 10-1000 eV of energy which equate to electron mean free paths < 10 nm (D. Briggs 1992). XPS is a non-destructive surface sensitive and quantitative spectroscopic technique used to characterize the near surface region (7-10 nm) of our synthesized mixed Al/Fe nanoparticles from Chapter 3. As seen in Figure 2.1, electron energy or a concentric hemispherical analyzer (0-1.5 kV) collects and determines the binding energy of photoelectron ejected as a function of their kinetic energy using a photoelectron multiplier or channeltron detector. XPS analysis takes place under ultra-high vacuum (UHV) < 10^{-8} mbar pressure to prevent surface contamination. A typical XPS spectra plot the counts of photoelectron peak intensity as a function of binding energy. These generated XPS spectra can provide valuable information about elemental identification/composition, surface layers of thin film structures, catalysis, adhesion, corrosion, polymer surface modification, semiconductor and dielectric material, the

density of electronic state or mainly the chemical oxidation state analysis of the probed element, and thin film (1-8 nm) coatings used in a number of industrial applications. One major disadvantage of XPS is the low spatial resolution of the technique which often requires the analyzed area to be in the order of few square mm. Information relating to the bulk samples analysis is limited; however, the bulk of a sample can be explored by carrying out depth profiles where a beam of argon ions is utilized to etch away the surface between XPS analysis. Our XPS data measurements were carried out using a PHI 5100 spectrometer equipped with a rotating anode X-rays source (operated up to 7.5 kW). Our XPS spectra were collected using a monochromatized Al Kα (1486.6 eV; line width ~0.85 eV) radiation.

$$E_k = E_b - h\nu - W_f \qquad (13)$$

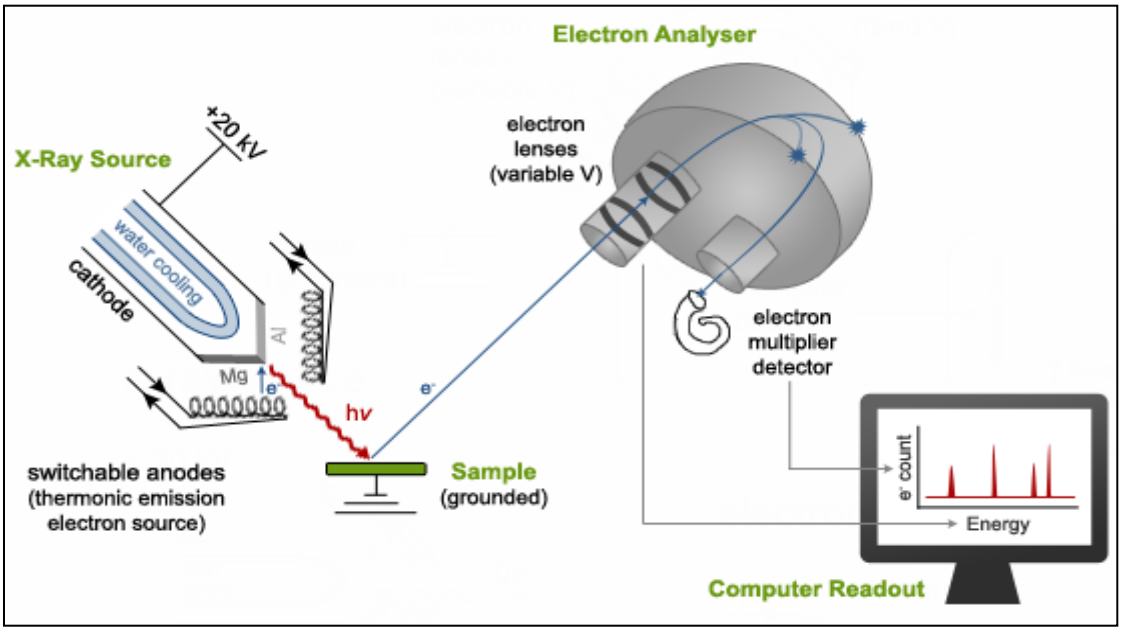

Figure 2.1. Diagram of an X-ray photoelectron spectrometer (XPS). (Courtesy of Dr. J. Hugh Horton, Queen's University)

2.2.2 X-ray Diffraction (XRD)

XRD is a conventional non-destructive tool for the characterization of mineral structures and phases. The XRD technique can be used to measure the average d-spacings between rows or layers of atoms, find the crystal structure of unknown materials, measure the size, shape, and internal stress of a small crystalline region, and determine the orientation of a single crystal or grain. XRD detection limits are within 3% in a two phase mixture, but can be around 0.1% with synchrotron radiation (no limitations for its spatial resolution). Most commonly known minerals XRD patterns and crystal structures have already been determined, published, and/or stored from the online mineral database or from the Joint Committee on Powder Diffraction Standards (JCPDS). The Braggs were awarded the Noble Prize in Physics in 1915 for their works characterizing NaCl, KCl, CaF_2, $CaCO_3$, ZnS, and (C) diamond single crystal structures. Their work gives rise to the vast application of the XRD technique which results from the interaction of electromagnetic waves (X-ray) scattering on a regular array of atoms within a crystal. Bragg's Law is mainly used to explain the constructive interference patterns of X-ray scattered by crystals. An important aspect of this technique is that diffraction patterns only occur when Bragg's law ($n\lambda = 2d\sin\theta$) is satisfied condition for constructive interference and can then be used to examine the structure of all states of matter (e.g., electrons, ions, protons, and neutrons) with any beam source (e.g., λ_{Cu} ~0.145 nm, λ_{Mo} ~0.071 nm, λ_{Fe} ~0.194, λ_{Co} ~0.179, λ_{Cr} ~ 0.229, and λ_{Ag} ~0.056) having a wavelength similar to the distance between the atomic layers or molecular structures of interest.

Extensive list for characteristic X-ray lines can be found in the International Tables for crystallography (Paufler 2007). Figure 2.2 depicted typical X-rays beam interference with a crystalline material to generate an XRD pattern with d represents the d-spacing or inter-atomic distance value, θ the angle of incident, n is any integer, and λ (0.1-10 nm) is the wavelength of the incident beam. Note the direction of incoming wavelength X-rays beam compared to the diffracted outgoing X-rays beam.

Different lattice planes have different d-spacings, and the Bragg angle θ must change as d-spacing changes (e.g., as d-spacing increase θ decreases) to satisfy the Bragg's law. In X-ray powder, the diffraction peaks occur at 2θ° positions which are directly proportional to the wavelength of incoming incident x-rays beam. Therefore it sometimes advantageous to use a longer X-rays wavelengths source which allows better observation and separation of low-angle peaks that could not be observable using shorter wavelength X-rays. The specific directions of diffracted beam appear as spots on the diffraction patterns and are described as XRD reflection lines or Miller indexes (hkl) of the crystal structure. Miller indexes are the reciprocals of fractional intercepts with the plane which makes the crystallographic axes. There are seven crystallographic systems which can vary from cubic, tetragonal, hexagonal, rhombohedral, orthorhombic, and monocyclic and triclinic. These crystal classes depend on the axis system (a, b, c) and the angle (α, β, γ) of variation form within a crystal unit cell. The unit cell is constituted of either a single atom or atoms in a periodic arrangement. However, the effects of sample thickness should be taken in consideration for specimen preparation because it can affect the adsorption and the intensity of transmitted X-rays as they leave the crystal material to form the diffraction patterns. Small amount of our synthesized sample in powder form

materials were finely ground and loaded into boron rich silica capillary glass tube (e.g., wall thickness ~ 0.01 mm and I.D. ~ 0.1 or 0.7 mm) resulting in minimum signal background. For the XRD materials analysis discussed in Chapter 3, a Scintag Powder Diffractometer instrument (Stony Brook University) with Cu Kα radiation source and equipped with a monochrometer to eliminate Fe fluorescence was used. While in Chapter 4-6, an Apex Duo: Bruker Instrument Service (Temple University) with the Mo Kα X-ray source at nearly constant irradiation volume in the 2θ range of 5-50 degrees, and a step size of 0.02° for 0.40 seconds per step was utilized. The Mo Kα is used to minimize the large background signal that could have been generated by Fe fluorescence under Cu Kα radiation for our iron oxyhydroxide and sulfide particles analyzed. Resulting XRD diffraction pattern were reported in the EVA evaluation software for the crystalline phases identification after filtering out the Kβ/Kα2 lines and baseline subtraction. Both instruments were equipped with a CCD area camera detector.

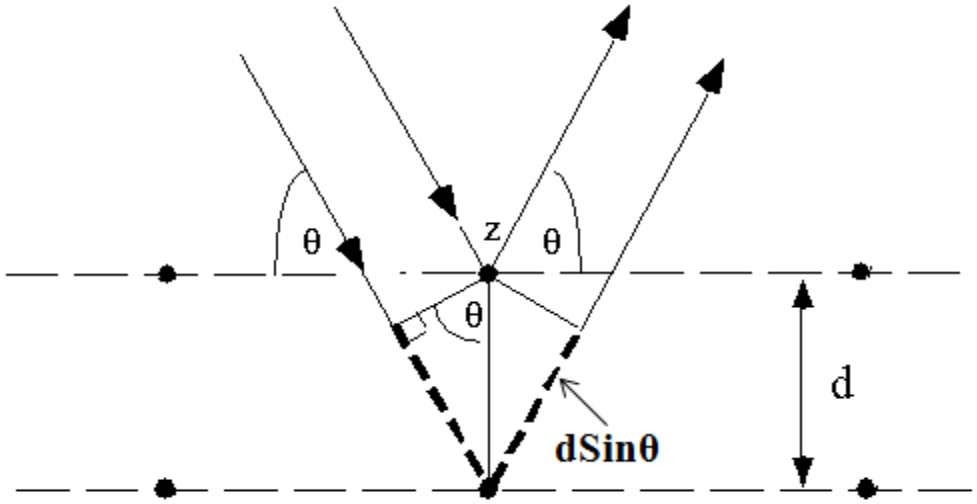

Figure 2.2. Typical X-rays beam interference with a crystalline material to generate an XRD pattern with d represents the d-spacing value of inter-atomic distance, θ the angle of incident, and n is any integer.

2.2.3 Scanning Transmission Electron Microscopy (STEM) with Energy Dispersive X-ray Analysis (EDAX)

TEM is one of the most powerful techniques for nanophase materials analysis and characterization having the ability to operate within a wide range of different imaging modes. TEM can provide atomistic information or on the sub-nanometer scale, elemental composition and electronic structure at high resolution. The resolution ($\lambda/2$) of a wave based microscope is limited by the minimal focal spot size formed by the wavelength (λ) of the light source. Optical microscopy is limited to about 200 nm for the violet light, and the largest advantage of TEM is due to its spatial resolution (e.g., for a 100 kV gives a λ ~ 0.004 nm) which has a magnification capability of roughly one million as compared to 1000 times for the best light optical microscope. For example, a beam of 120 kV accelerate electrons would have an approximate focus spot size of 5 pm resolution. Advanced TEM system could be equipped with energy electron sources having acceleration voltages up to 300 kV. TEM uses magnetic field lenses to focus the high electron beams transmitted through on an ultra-thin sample surface projected onto a phosphorescent imaging device. Diagrams of the TEM micrograph illustrate the electron beams pathways through several magnetic focusing lenses before reaching and projecting the specimen morphology are illustrated in Figure 2.3. Similar to XRD technique, TEM can provide selected area electron diffraction crystallographic patterns by generating information about the arrangement of atoms, imaging of atomic scale defects, and the degree of crystalline order from the specimen materials. The morphology of the specimen sample is often recorded on a film or by a charge-couple device (CCD) camera.

The interaction of electrons adsorption and differential scattering by different parts on the sample give rise to the contrast effects which associate lighter density areas from the specimen surface with lighter contrast imaging. While specimen sample with thicker areas density appear darker from the collected TEM imaging. Collected TEM images are thought to be a two dimensional projection down the optical axis. STEM couple with EDAX capability offers some state-of-the sensitive and high resolution in the sub-Å regime for the characterization of difficult to analyze synthesized nanomaterials such amorphous or polycrystalline mixed composition metal oxyhydroxide minerals. Nanoparticles suspension preparation onto carbon grids should be done with care to minimize the effect of particles aggregation within the submicron regime or less in order to collect efficient imaging morphology. In addition, the sample must be kept under high vacuum in the TEM column to avoid contaminations and instability of the beam electrons source. Two different TEM instruments were used for the analysis of the synthesized iron oxyhydroxide and sulfide particles. Transmission electron micrographs and selected area electron diffraction (SAED) were collected using a FEI Tecnai 12T TEM instrument, equipped with a 120 kV TEM microscope energy source with a Gatan DualVision 300W side-entry digital CCD camera, and it was located at the Microanalysis and Imaging Research Training Center at West Chester University. A JEOL JEM-1400 electron microscope equipped with EDS was also used to carry out Al/Fe and Fe/S particles size distribution and morphology, and elemental profiling and mapping of the synthesized nanoparticles. The JEOL JEM-1400 used a high brightness LaB_6 electron source (120 KeV) and was equipped with a Gatan large-area camera for imaging located at Temple University, Chemistry Department. Transmission electron microscopes have developed

new versatile research areas to examine a much bigger variety of specimens in the medical, biological, and physical science communities for nanoparticles and cell structures imaging.

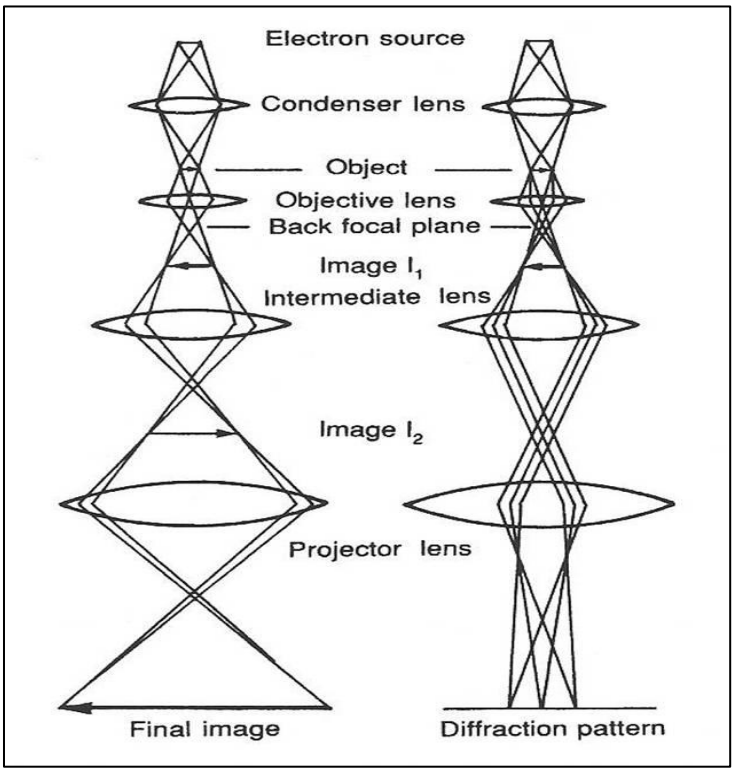

Figure 2.3. Transmission electron microscopes (TEM) for bright-field and dark-field imaging. (Reproduce with the permission of Cambridge University Press, McLaren 1991)

2.2.4 Scanning Electron Microscopy Energy Dispersive X-ray Analysis (SEM/EDAX)

SEM is a powerful tool which can provide three dimensional images, particles size distribution and topography, and elemental profiling and mapping of specimen materials. In SEM imaging, the electron beam generated by a high resolution Schottky field emission gun is focused through electromagnetic lens and scanning coils to raster across the sample surface. SEM can also be equipped with the energy dispersive spectroscopy (EDS take-off angle is ~35°) detector which is mainly used to generate high energy beam bombardment on the specimen surface causing by the excitation of core level electrons. SEM has a large depth of penetration profile at varied working distance (10-65 mm) which has allowed the imaging of thicker specimens to be in focus at one time, and the ability of SEM to image not only bulk samples but a wide variety of materials structure and composition make it versatile. The accelerating voltage (20-30 KeV), magnification (6-10^6 x) as well as the specimen current (up to 200 nA) from the electron probe micro analyzer (EPMA) can also be varied to gather quantitative elemental abundance and specific information about the characteristic line energy for each element from the sample surface. Upon the interaction of the electron incident beam with the sample surface, the characteristic X-rays energy are ejected in all direction which can be captured with a wide range of detectors; for example with a silicon drift detector or an Everhardt Thornley SED (secondary electron detector) can be utilized; and then converted into an image using an IR/Raman camera for viewing the sample surface in the chamber. The intensity of X-ray fluorescence spectra is produced as a function of energy

by the EDS detector which can measure the quantitative elemental composition of the specimen sample.

The secondary electron (SE_1) mode of SEM detection gives topographical imaging information about the specimen surface as a function of the angle between the sample surface and the incident beam. The primary backscattered electrons (BSE) provide atomic number and topographical information while the Auger electrons (AE) can generate surface sensitive compositional information. A tilted (of ~20-40° geometry) surface will ordinary emit the largest number of SE_1. Analogous to TEM, SEM imaging collected from the specimen samples with high density areas, adsorb, and scatter more electrons giving raise to imaging topography with contrast and high brightness effects. SEM does not have the same electron and resolution advantages as TEM does. While TEM strictly requires the use of high vacuum (< 6 $x10^{-4}$ Pa) technology to avoid sample and instrument contamination, SEM specimens can be recorded as well as in low vacuum (< 10 to 130 Pa) and in wet environmental extended vacuum mode (ESEM < 10-4000 Pa) conditions. SEM can achieve a resolution better than 1 nm. Whereas TEM is limited by the λ (nm) of electrons and the quality of its lenses, the resolution of SEM is limited by the relatively large interaction volume of the specimen and the spot size of electron beam. Characterization of traditional metals specimens, fractures and fine polished specimen, geological minerals, and non-conductive soft materials of polymers, pharmaceuticals, gels, filters, biological and plant tissues can be collected with high imaging resolution and accurate semi-quantitative elemental composition. Figure 2.4 shows a simplified diagram plan of a microscopy similar to the advance FEI Quanta 450FEG instrument. Previous SEM equipment model required that non-conductive and/or hydrated samples to

either be coated with a thin-layer of electrically conductive carbon, copper wire, Ag, Pt, or gold sputtering coater to enable charge-free imaging analysis.

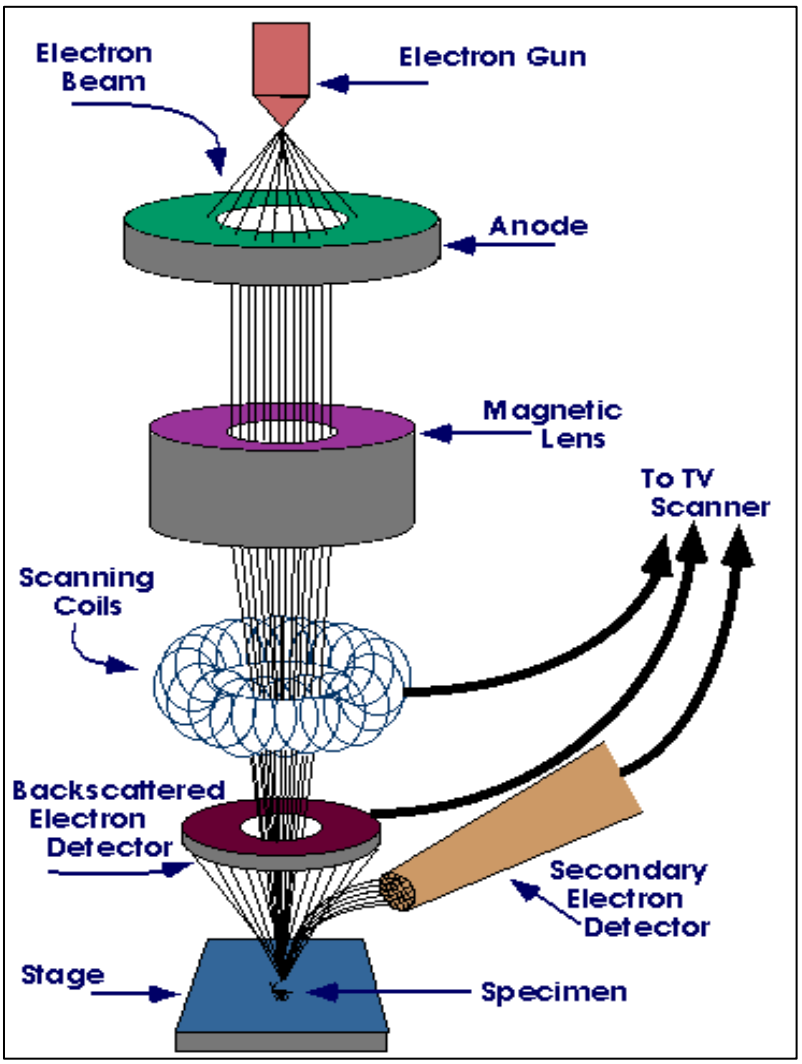

Figure 2.4. Illustrated diagram of the scanning electron microscopy (SEM). (Reproduced with the permission of Iowa State University)

2.2.5 Attenuated Total Reflection Infrared Spectroscopy (ATR-FTIR)

Fourier transformed infrared (FTIR) spectroscopy is generally used for the qualitative and quantitative analysis of sample's chemical composition (bulk or microscopic amounts) with little or no sample preparation. FTIR spectroscopy is best at the symmetric vibrations of polar groups. ATR-FTIR is a versatile, quick, and non-destructive tool used for a variety of samples characterization to confirm the identity of solid phase materials such as metal oxide, oxyhydroxide, and sulfide nanoparticles as well as polymeric resins, gels, pastes, powders, thermoplastic parts, and inorganic fillers. The ATR technique is also used for the analysis of gaseous and liquid (e.g., acids, bases, and oxidizing agents) phase materials or to distinguish the main polar functional groups or provide symmetric vibrational frequencies for the elucidation of molecular structure from various unknown mixed materials. IR spectroscopy is based on the transitions between molecular vibrational energy levels upon the absorption of mid-IR radiation. The interaction between light and matter is a resonance condition involving the electric dipole mediated transition with the molecular vibrational energy levels. In contrast, Raman spectroscopy is a two-photon inelastic light-scattering process in which the interaction between light and matter is off-resonance condition relating to the Raman polarizability of the molecule. The application of Raman spectroscopy is best used at symmetric vibrations of non-polar groups.

In ATR spectroscopy, the incident infrared radiation (IR) beam is totally internally reflected at the boundary between an optically dense medium (e.i., refractive index, n_1) and extends into an optically less dense medium (e.i., refractive index, n_2) with

an angle of incidence (θ) required to be greater than the critical angle (θc) which gives rise to the observation of a purely ATR spectral result. An evanescent wave is created within < 10 μm of the less dense optical medium which decays exponentially with distance from the surface boundary. Some of the energy of the evanescence wave is absorbed by the sample, and the reflected IR laser beam is returned to the detector. ATR technique requires excellent sample contact with the crystal element. Most mid-IR analyses are performed using either a highly sensitive with excellent linearity and easy to use deuterated triglycine sulfate (DTGS) or mercury cadmium telluride (MCT-A/MTC-B) detector. The MTC-A detector has a narrow band at ~ 650 cm^{-1} cut off holding the highest sensitivity while the MTC-B detector has a wide band at ~ 400 cm^{-1} cut off which can be used for slightly lower throughput and high-speed measurements of samples over a wide range of temperatures. However, both MTC-B and MTC-A detectors offer from 4 to 10 times higher sensitivity than the DTGS detector and are ideal for low throughput analysis when sampling speed is important while providing a significantly increase in the IR response or high spectral resolution (1-8 cm^{-1}) measurements for small amounts of energy reaching the detector.

It is also worth to note that if the critical angle is not met in ATR techniques, a combined ATR and reflectance results could be observed whenever the angle of incidence of the IR beam and the refractive index of the crystal are too low and if the refractive index of the sample is too high. Figure 2.5 shows a graphical representation of the ATR phenomenon for a single diamond crystal ATR (having a 2.5 refractive index and highest crystal hardness at ~1500 $Kgmm^{-2}$). ATR element also comes with multi-bounce horizontal systems (e.g., Ge, Si, ZnSe, AMTIR, and CdTe, etc…), with each

bounce is the evanescent wave penetrating and offering a greater contact with the sample which provides a better IR spectral resolution for weak absorbers or dilute solutions. Germanium (Ge) crystal has typically the highest index of refraction (~4.0) and covers a wide range of solutions pH (1-14) with the crystal hardness estimated at ~550 $Kgmm^{-2}$. Careful consideration should be made about the choice of ATR infrared crystals and properties (e.g., hardness and inertness, hygroscopic, brittleness or softness, withstands thermal and mechanical shock, high pressure and caution with solvents which attack material under certain pH conditions) when planning FTIR experiments. Importantly, the depth of penetration (d_p) is the distance required to decrease the electrical field amplitude to e^{-1} (37%) of its value and which depends on the path length (λ), the refractive index (n_1) of the sample surface, the refractive index (n_2) of the crystal, and the incident angle (θ) (Peter J. Larkin 2011). The sampling depth of ATR method is wavelength dependent, varied between 2-15 μm, increases with decreasing wavenumbers, and is given by Equation 14:

$$dp = \frac{\lambda}{2\pi(n_1^2 Sin^2\theta - n_2^2)^{1/2}} \qquad (14)$$

ATR intensities are lowered at higher wavenumbers compared to transmission spectra, and its sensitivity is limited by 3-4 orders of magnitude less than classical transmission spectra. The ATR technique is mostly used in this work and all the spectra acquisition were performed using the Nicolet 6700 FTIR or a Thermo Nicolet Magna-IR 560 spectrometer, equipped with a smart orbit ATR-FTIR accessory, and with either a

deuterated triglycine sulfate (DTGS) or a liquid nitrogen-cooled mercury cadmium telluride (MCTA) detector from Thermo Electron Corporation.

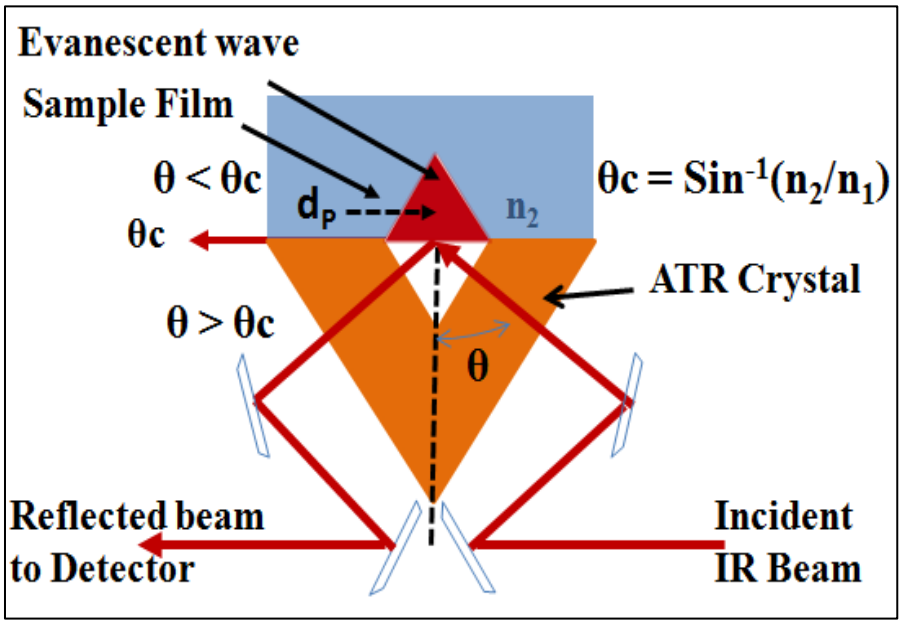

Figure 2.5. Graphical representation of a single beam attenuated total reflection (ATR) phenomenon.

2.2.6 Density Functional Theory (DFT)

DFT is the most dominant and successful methods to compute the electronic structure of matters and periodic systems. In recent years, DFT has been widely use by quantum chemists for simulation of surface adsorption complexes, and its applicability ranges from the simulation of energy surfaces in atoms to molecules, solids, nuclei, and classical fluids mechanic. In addition, DFT computations are widely used to predict a great variety of molecular complexes and properties, molecular dynamics, ionization and atomization energies, relativistic electrons, reaction pathways, thermodynamic properties and excited states, magnetic properties, and vibrational frequencies. At the center of the DFT is how to calculate the energy surfaces of a molecule by solving the Schrödinger equation (15). This involves the computation of the electron density that is one the main important properties in DFT in which the external potential or just the Halmiltonian (H) operator is determined. The variational principal named after the second Hohenberg-Kohn (H-K) theorem states that the functional delivers the lowest ground state energy (E_0) of the system, if and only if the input density is the true ground state density. We recall that the average total energy established by a particular functional [Ψ] of the wavefunction is the expectation value of the Hamiltonian, and can be writing as:

$$E[\Psi] = \int \Psi^* \hat{H}\Psi d\mathbf{r} \equiv \langle\Psi|\hat{H}|\Psi\rangle \;\; ; \;\; E[\Psi] \geq E_0 \qquad (15)$$

Other useful methods are the couple-cluster (e.g., CCSD requires both single and double substitution using Hartree-Fock approximation, and CCSD(T) includes triple non-iteratively excitations), local density approximation (e.g., LDA includes approximations

for the exchange correlation hole), and generalized gradient approximation (e.g., CGA which depends on both density and its gradient in addition to exchange correlation hole analytical properties). Nevertheless, hybrid density functional theory offers the ability to compute exact properties of the universal functional, and DFT can provide highly accurate and unbiased computational approximation to a wide range of materials complexes using modern software packages such as Gaussian. Molecular example of model clusters can be viewed in Chapter 5 as illustrated in Figure 5.19. DFT computations are quite difficult and computationally expensive. In most cases the B3LYP (Lee, Yang et al. 1988; Becke 1992) exchange and correlation functional combined with a variety of basis sets (e.g., 6-31G(d) and 6-31G(d)*) are of sufficient accuracy to predict the chemical properties (reaction rate, stability, binding geometries within a precision of ±1-5% for calculated bond lengths, and IR vibrational frequency within ±5-10% accuracy) of a system and interpreting the formation of adsorbed species (e.g., $CO_{2(gas)}$, phosphate) on mineral surface sites. The B3LYP/6-311+G(d, p) hybrid DFT exchange correlation functionals (Becke 1997) were reliable to simulate experimental binding energies, geometries, and vibrational frequencies of adsorbed carbonate and phosphates complexes on the various iron, Al, and mixed Al/Fe oxyhydroxide mineral surfaces.

CHAPTER 3
ADSORPTION OF CARBON DIOXIDE ON AL/FE OXYHYDROXIDE

Abstract

In this chapter nanoparticles structural reactivity of mixed Al/Fe iron oxyhydroxide (0-100 mol%) toward gaseous CO_2 were investigated with X-ray photoelectron spectroscopy (XPS), atomic absorption (AA), scanning transmission electron microscopy with electron dispersive X-ray spectroscopy (STEM/EDS), X-ray diffraction (XRD), and attenuated total reflectance Fourier transform Infrared Spectroscopy (ATR-FTIR) combined with density functional theory (DFT) calculations. Results showed that Al/Fe oxyhydroxide particles containing more than 20 mol% Al consisted at least in part of Fe-oxyhydroxide with incorporated Al and a discrete AlOOH phase. Results from ATR-FTIR experiments and DFT calculations suggested that the bicarbonate complex formed by passing CO_2 over the particles was accommodated on at least three distinct binding sites. At the lowest Al concentrations bicarbonate was bound to individual sites with primarily Fe or Al character. At the highest concentrations of Al (>20 mol %) bicarbonate bound to discrete AlOOH phases became apparent. Results also suggested that the amount of CO_2 adsorption for a given particle mass increased as the Al concentration was increased from 0 to 30%. This increase was likely due in large part to differences in the morphology of the particle aggregates that formed in the dry state, which would be expected to affect the amount of surface that was available to adsorb CO_2. This increase in adsorption capacity for CO_2 on Al/Fe-oxyhydroxide could be useful in CO_2 sequestration applications.

3.1 Introduction

Minerals that include Al^{3+} and Fe^{3+} bearing oxides and (oxy)hydroxides play important roles in geochemical processes that control the fate of environmentally relevant contaminants (Anderson and Benjamin 1990; Schwertmann, Friedl et al. 2000; Bazilevskaya, Archibald et al. 2011; Cismasu, Michel et al. 2011; Cismasu, Michel et al. 2012). One specific mineral that falls within this broad mineral category is ferrihydrite, an intrinsically nano-dimensioned phase that is involved in the geochemical cycling of iron and the mobility of heavy metals and metalloids (Filip, Zboril et al. 2007; Cismasu, Michel et al. 2011).

Ferrihydrite in general forms poorly crystalline nanoparticles and can be produced through a variety of mechanisms, including precipitation, redox, and weathering processes. The material can contribute with other minerals to CO_2 removal, adsorption, capture, and storage (Palandri and Kharaka 2005; Murphy, Lammers et al. 2011). Ferrihydrite is a metastable mineral that can act as a precursor to the more stable iron oxides such as goethite, hematite, and magnetite (Jentzsch 2006; Michel, Barron et al. 2010). It is also the inorganic core of the protein ferritin that acts as an iron reservoir in living organisms (Ford, Harrison et al. 1984; Michel, Hosein et al. 2010). Ferrihydrite, the least crystalline structure of hydrous ferric oxides, has been conventionally described as $5Fe_2O_3.9H_2O$, but recent research has suggested the stoichiometry of the material to be closer to $Fe_{8.2}O_{8.5}(OH)_{7.4}+3H_2O$ (Michel, Ehm et al. 2007; Michel, Barron et al. 2010; Michel, Hosein et al. 2010).

In natural environmental settings, ferrihydrite often contains traces of metals such as Al (Jambor and Dutrizac 1998; Schwertmann, Friedl et al. 2000; Bazilevskaya, Archibald et al. 2011). This realization has led to numerous studies focused on the structure of the Al/Fe oxyhydroxide system and the reactivity of the binary material with environmentally relevant aqueous species such as arsenate/arsenite and phosphate (Harvey and Rhue 2008; Liu and Hesterberg 2011; Basu, Gupta et al. 2012). In general, the preparation of the Al/Fe oxyhydroxide has used a synthetic protocol that relies on the hydrolysis of Fe(III) with increasing pH in the presence of aqueous Al(III). In the absence of the Al, this protocol would typically result in 2-line ferrihydrite (~2-3 nm diameter). Studies have shown that within the range of ~10-30 mol % Al the Al/Fe iron oxyhydroxide particles can be described as Fe-oxyhydroxide particles that contain incorporated Al(III) and small non-crystalline Al-hydroxide domains (Jambor and Dutrizac 1998; Cismasu, Michel et al. 2012). Studies have shown that within this concentration range of Al the reactivity of the Al/Fe oxyhydroxide surface toward species such as arsenite/arsenate and phosphate is a strong function of the Al/Fe mole % ratio that has an influence on such properties as the surface charge (Masue, Loeppert et al. 2007; Harvey and Rhue 2008; Liu and Hesterberg 2011). As the Al content is increased, prior work has shown that discrete crystalline AlOOH domains (gibbsite and bayerite) form (Schulze and Schwertmann 1984). Aqueous studies have generally shown that in this range of high Al-content the adsorption capacity of the particles toward arsenite/arsenate is reduced due to the lower affinity of AlOOH phases for arsenic oxyanions, whereas the capacity to adsorb phosphate is increased presumably due to the affinity of this species for Al containing phases (Harvey and Rhue 2008; Liu and

Hesterberg 2011; Basu, Gupta et al. 2012). The structural characterization in these prior studies, however, does not allow one to ascertain whether the ferrihydrite structure is maintained in the predominately Fe-oxyhydroxide domains. Using a more crystalline form of ferrihydrite (so called 6-line variety, 6 nm diameter), prior research has suggested that the structure of this form of ferrihydrite is maintained at low Al concentrations (~2.1 mol%) (Chadwick, Jones et al. 1986; Schwertmann 1991; Jentzsch 2006; Cismasu, Michel et al. 2012).

In this contribution, we investigate the effect of Al substitution on the reactivity of ferrihydrite toward gaseous CO_2 in addition to the structural changes that occur as Al is incorporated into the Fe-oxyhydroxide. Prior research showed that the exposure of ferrihydrite to CO_2 resulted in adsorbed carbonate and bicarbonate species (Hausner, Bhandari et al. 2009). The motivation for the present study of the Al-containing Fe-oxyhydroxide is two-fold. First, as mentioned ferrihydrite is expected to contain Al in natural settings and an understanding of the interaction of mineral phases with CO_2 whether in the aqueous or gas phase has significant environmental relevance. Second, previous studies have shown that the initial rate of CO_2 adsorption is faster on nano-dimensioned iron oxides than on aluminum oxide surfaces (Baltrusaitis, Schuttlefield et al. 2011), and from a fundamental standpoint it is of interest to determine how the presence of both metals in the same material affects the CO_2 surface chemistry. The prior studies mentioned above have shown that Al/Fe oxyhydroxide particles often exhibit a surface reactivity that cannot be explained as the simple sum of the reactivities associated with the individual Al and Fe hydroxide components. We emphasize that while the Al-free iron oxyhydroxide used in this study is 2-line ferrihydrite, it may not be accurate to

call the material ferrihydrite after Al incorporation. We, therefore, only refer to the Al-free material in this research contribution as ferrihydrite and when Al is added it is referred to as Al/Fe oxyhydroxide. Also, prior studies have characterized Al/Fe oxyhydroxides with techniques similar to those that are used in this study. Nevertheless, we feel it is important to present our results in this area, because the details of the Al/Fe oxyhydroxides particles vary from study to study. This variation is emphasized by differences in surface areas (Anderson and Benjamin 1990) and the dependence of crystallographic structure (by X-ray diffraction) with Al-content between studies (Borch, Masue et al. 2007; Liu and Hesterberg 2011). Differences in preparation likely cause these differences, but it also brings forward the need for us to present our own structural characterization results for the Al/Fe oxyhydroxides particles used in this study to support our reactivity results.

In the present study, ferrihydrite and Al/Fe oxyhydroxide were characterized by Brunauer-Emmet Teller (BET) analysis, X-ray photoelectron spectroscopy (XPS), and X-ray diffraction (XRD). Both transmission electron microscopy (TEM) and scanning transmission electron microscopy with energy dispersive spectroscopy (STEM/EDS) were used to determine the morphological and elemental composition of the oxyhydroxides. Attenuated total reflection infrared spectroscopy (ATR-FTIR) was used to identify the surface complexes that formed on ferrihydrite and Al/Fe oxyhydroxide in a CO_2 environment as a function of Al content. Interpretation of the ATR-FTIR data was aided by utilizing density functional theory (DFT) calculations. In general the experimental results showed that Al/Fe oxyhydroxide particles containing more than 20 mol% Al consisted at least in part of iron oxyhydroxide with incorporated Al and a

discrete AlOOH phase. Results from the ATR-FTIR experiments and DFT calculations for CO_2 adsorption suggested that at this Al concentration, a bicarbonate complex formed on individual sites with primarily Al or Fe character, and on the discrete AlOOH phase.

3.2 Experimental Methods

3.2.1 Synthesis

Ferrihydrite was synthesized using a modified method adapted from Cornell and Schwertmann (Schwertmann 1991). Briefly, 0.1 M of anhydrous ferric chloride ($FeCl_3$) was dissolved in distilled water followed by rapid neutralization with 1.0 M sodium hydroxide (NaOH). The pH was maintained in the 7-8 range for at least 30 minutes, and a red-brown precipitate was observed. The suspension was dialyzed for 10 days in deionized water. Subsequently, the sample was centrifuged, air dried, and stored in polyethylene bottles. Al/Fe iron oxyhydroxide was prepared such that the total metal cation (introduced into solution as $FeCl_3$ and $AlCl_3$) concentration was 0.1 M, but the relative ratio of the iron and aluminum cations were controlled to obtain Al/Fe oxyhydroxides containing 0, 5, 10, 20, 30, 70 and 100 mol% Al.

3.2.2 Characterization of Samples

The specific surface area (SSA) of the different samples was determined by the BET technique, using N_2 as the adsorption gas. Samples were de-gassed (i.e., desorbing residual superficial water) at 60 ˚C for 600 minutes prior to any BET measurement.

AA, using a MCC-TOX-100 analyzer (Galbraith Laboratories), and EDAX were used to determine the bulk concentrations of aluminum and iron in the different Al/Fe

oxyhydroxides. To complement the bulk determinations by AA and EDS, XPS was used to analyze the near surface region of the particles. XPS measurements were carried out on ferrihydrite and Al/Fe iron oxyhydroxide using a PHI 5100 spectrometer with a rotating anode X-ray source that operated at power levels up to 7.5 kW. Samples were prepared by pressing the ferrihydrite or Al/Fe oxyhydroxide powder onto carbon conductive tape. Spectra were collected using monochromatized Al K_{α} (1486.6 eV; line width ~ 0.85 eV) radiation. A high resolution energy analyzer (300 mm mean radius hemispherical electrostatic analyzer) and a multi-channel microchannel plate-CCD camera detector combination were used for electron analysis. The binding energy scale was referenced to the C 1s core level feature associated with adventitious carbon at 284.8.0 eV. Experimental data was analyzed with CasaXPS software (version 2.3.15). Gaussian (70%) and Lorentzian (30%) profiles were used to define each elemental component. XPS MultiQuant software was used to estimate the relative composition of the Al constituents in the Al/Fe oxyhydroxide samples (a homogeneous model was used) (Mohai 2004).

Samples for TEM analysis were sonicated in high purity distilled water (18.5 MΩ) for ~10 minutes. A drop of the dispersed particles was then placed onto an amorphous holey-carbon film supported by a copper-mesh TEM grid. Samples were dried in air at room temperature (for ~30 min). The various Al/Fe iron oxyhydroxide materials were analyzed by two different TEM instruments. Transmission electron micrographs and selected area electron diffraction (SAED) were collected using a FEI Tecnai 12T TEM instrument, equipped with a 120 kV TEM microscope energy source with a Gatan DualVision 300W side-entry digital charge coupled device (CCD) camera.

A JEOL JEM-1400 electron microscope equipped with EDS was used to carry out Al/Fe elemental profiling and mapping of the oxyhydroxide nanoparticles. The JEOL JEM-1400 used a high brightness LaB_6 electron source (120 KeV) and was equipped with a Gatan large-area camera for imaging.

XRD was carried out using a Scintag Powder Diffractometer instrument (Cu Kα radiation) equipped with a general area detector diffraction system (GADDS). The samples were scanned at a wavelength, λ, of 1.54 nm and at nearly constant irradiation volumes in the 2θ range of 10-80^o (step size of 0.02° at 0.40 s per step).

A Nicolet 6700 spectrometer (Thermo Scientific) equipped with an ATR-FTIR accessory and a deuterated triglycine sulfate (DTGS) detector were used to collect vibrational spectra. Approximately 1 mg of ferrihydrite or Al/Fe oxyhydroxide was suspended in 1 ml of deionized water and sonicated for 3 minutes, and then one drop of the suspension was placed on a diamond ATR element, that was then enclosed by a home-built gas cell. Dry nitrogen was passed through the cell to dry the sample into a thin film of Al/Fe iron oxyhydroxide. Nitrogen and carbon dioxide used in this study were research grade (Air Gas) and both gasses were used without further purification. The flow rate of all gases was maintained with a rotameter at five standard cubic feet per minute (SCFM). A total of 100 co-added scans at a resolution of 4 cm^{-1} were collected for all the ATR-FTIR experiments. The vibrational spectra were reprocessed using the clean diamond ATR element as the reference. The Omnic 7.3 program was used for data acquisition and processing.

3.2.3 DFT Calculations

DFT-based calculations were carried out for both energy minimization and vibrational frequency optimization. Vibrational frequency calculations with the B3LYP (Lee, Yang et al. 1988; Becke 1992) exchange and correlation functionals with a 6-31G(d) basis set (Becke 1997) were used to determine the different adsorbed carbonate and bicarbonate molecular species formed on Fe_2, (Fe, Al), and Al_2-octahedral dimers. The Gaussian 03 E.01 program was used to perform all calculations (Jensen, Pettersson et al. 2005; Hausner, Bhandari et al. 2009). To obtain accurate vibrational frequencies for the stable bicarbonate modes, energy minimizations were performed in two steps: the first constraining one C---O interatomic distance between the CO_2 and the metal-hydroxide dimer and the second allowing all atoms to relax. This procedure was described in an earlier publication form our laboratory (Hausner, Bhandari et al. 2009; Kubicki, Paul et al. 2012). A scaling factor of 0.956 was used to obtain agreement between calculated DFT and experimental vibrational frequencies (Hausner, Bhandari et al. 2009). This particular scaling factor was shown in prior research to work well for Fe-organic complexes to account for the anharmonicity of the carbonate and bicarbonate vibrational modes (Bargar, Kubicki et al. 2005; Rahnemaie, Hiemstra et al. 2007). Either a single Fe^{3+}or Al^{3+}octahedron, or an octahedral dimer linked via Fe-(OH)-Fe / Al-(OH)-Fe / Al-(OH)-Al binding, which is common in metal oxides and mostly in ferrihydrite and alumina, were used to create the cluster models (Bargar, Kubicki et al. 2005; Bazilevskaya, Archibald et al. 2011). The small unit cells or models system certainly do not yield absolute representations of the ferrihydrite or Al/Fe oxyhydroxide sorption sites,

but we contend that the models are relatively useful as a first-order approximation for the molecular interaction between carbonate and bicarbonate on ferrihydrite or Al/Fe oxyhydroxide surfaces. In order to interpret the Al/Fe oxyhydroxide system, an Al atom was substituted for Fe inside the molecular cluster models before running the DFT calculations.

3.3 Results and Discussion

3.3.1 Composition of the Al/Fe Oxyhydroxide Particles

Table 3.1 displays a summary of results associated with the characterization of the ferrihydrite and Al/Fe oxyhydroxide particles used in this study that were obtained by BET-SSA, AA, EDS, and XPS. An inspection of Table 1 shows that the mol% of Al in the different Al/Fe oxyhydroxide particles based on AA measurements was significantly different than the XPS derived values for the Al content in the particles. A general trend was that XPS overestimated the amount of Al in the different particles. For example, the Al/Fe oxyhydroxide particles synthesized from a solution containing 10% Al^{3+} and 90% Fe^{3+} were determined to have an AA and XPS-derived Al content of ~10.5 mol% and ~15.1 mol%, respectively. The discrepancy between AA and XPS derived concentrations became even larger when the Al/Fe oxyhydroxide particles were synthesized from a solution containing 30% Al^{3+} and 70% Fe^{3+}. In this circumstance, AA yielded an Al content of 30.5%, while the XPS derived Al content was ~58.9 mol%. Interestingly, at the highest Al doping level studied (i.e. 70% Al) the AA and XPS results are closest at 67% and 62%, respectively.

Table 3.1. Surface area and Al content of various Al/Fe oxyhydroxide particles used in the study

Al percent in initial Solution	BET Surface Area (SA)	AA	XPS[a]	STEM/EDS
(mole%)	(m^2/g)	(mole%) Al	(mole%) Al	(mole%) Al
0	336 ± 3	0	0	0
5	326 ± 3	5.1	10.4 ± 5	4.9
10	347 ± 2	10.5	15.1 ± 5	10.8
30	387 ± 2	30.5	58.9 ± 5	30.2
70	221 ± 3	67.5	62.2 ± 5	70.1
100	120 ± 1	100	100	100

[a] values obtained assuming a homogeneous model for the distribution of Al and Fe in the Al/Fe oxyhydroxides.

The AA-derived (and EDS values) Al mol% levels were assumed to be more representative of the actual Al content of the Al/Fe oxyhydroxide particles, because this measurement should not have been influenced by the spatial distribution of the Al in the Al/Fe oxyhydroxide. In the case of XPS, variations of the photoelectron intensity associated with the Fe and Al as a function of depth from the surface will depend on the kinetic energy of the photoelectron. Our XPS derived concentrations were derived by using a model where Al was homogeneously distributed in the oxyhydroxide particles (Mohai 2004). We propose then that the consistently higher values for the XPS derived Al concentration in the 0-30 mol% Al/Fe oxyhydroxide samples was due to a non-homogeneous distribution of Al in the nanoparticles where Al was more concentrated in the surface region. This general conclusion of Al enrichment at the Al/Fe oxyhydroxide surface was arrived at in prior research (Anderson and Benjamin 1990). The relatively small increase (59 to 62%) in the XPS derived Al mol% when the relative Al concentration in solution to make the particles was increased from 30 to 70% suggested that the concentration of the Al in the outer surface region reached a saturation level when the particles were made up of 30 mol% Al (by AA or EDS). We point out that our Al mol% derived from XPS for the 70 mol% Al/Fe iron oxyhydroxide was lower than the AA and EDS values. Within the experimental error of the measurements we take all these values to be similar, although we are uncertain why a higher XPS derived Al mol% (relative to that measured by AA and EDS) was not experimentally observable at this higher Al concentration. Significant changes in the morphology of the particles at the higher Al concentrations, which becomes apparent from data presented below, could have been a contributing factor.

XPS results also suggested that an increasing amount of AlOOH phase formation on the Fe oxyhydroxide surface occurred as the Al content of the Al/Fe oxyhydroxide increased. The Al 2p peak associated with the 10 mol% Al/Fe oxyhydroxide particles (Figure 3.1a) exhibited a peak maximum at 73.5 ± 0.5 eV with a full-width-half maximum-height (FWHMH) of 1.70 eV. The Al 2p peak associated with the 30 mol% (Figure 3.1b) and 70 mol% (Figure 3.1c) Al/Fe oxyhydroxide samples exhibited a ~0.5 eV shift of the peak maximum to higher binding energy relative to the Al 2p position associated with the 10 mol% Al particles. We suspect that Al 2p energy position for the 10 mol% Al/Fe oxyhydroxide particles was largely associated with Al(III) incorporated in the Al/Fe oxyhydroxide particle structure and not as a discrete AlOOH phase. In contrast, the higher Al 2p binding energy associated with the particles with a higher Al mol% was largely due to the formation of discrete AlOOH precipitate on the Al/Fe oxyhydroxide particle. We add that the Al 2p peak position of ~73.9 eV characteristic of the 30 and 70 mol% Al/Fe oxyhydroxide particles agrees well with the Al 2p peak position experimentally determined in prior research for pure AlOOH phases (Kloprogge, Duong et al. 2006).

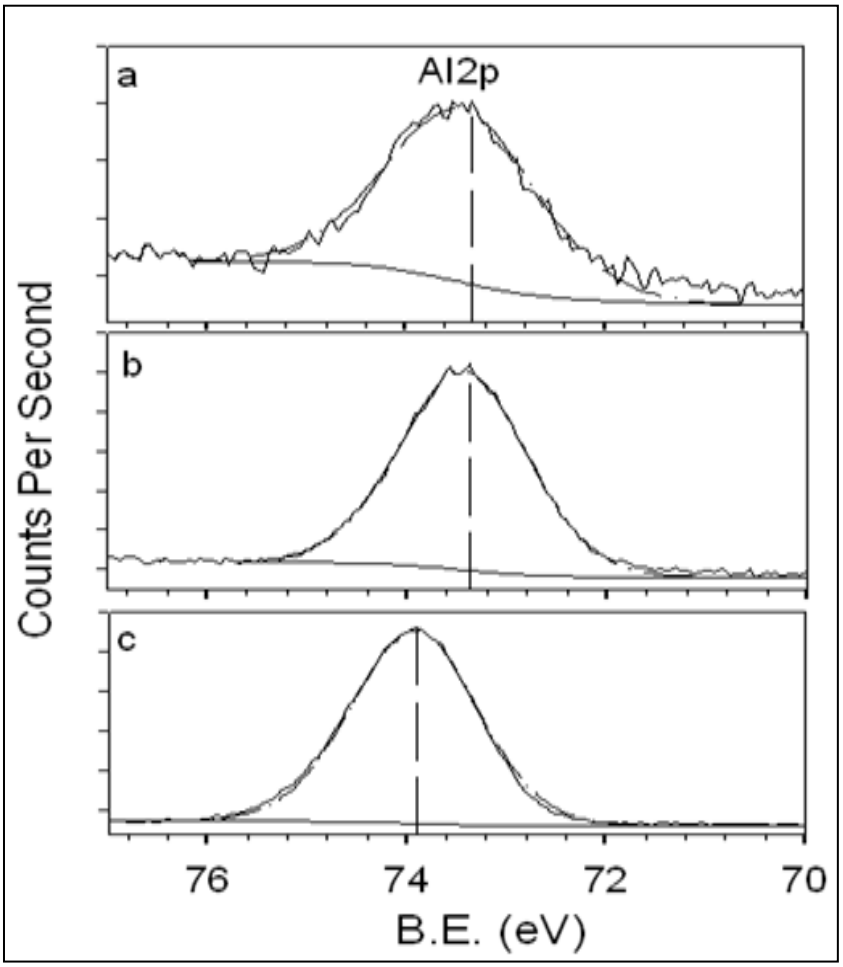

Figure 3.1. Al2p XPS associated with Al/Fe oxyhydroxides with (a) 10 mol% Al, (b) 30 mol% Al, and (c) 70 mol% Al. XPS data showed that the Al 2p binding energy feature broadens to higher energy when the Al mol% is increased from 10 to 30mol%. It is postulated that this broadening was due to the growth of AlOOH phases that coexist with Al that is substituted into the Fe oxyhydroxide material. The Al 2p binding energy associated with the Al mol% of 70% was primarily due to the preponderance of discrete AlOOH phases.

3.3.2 Structure of the Ferrihydrite and Al/Fe Oxyhydroxide

TEM and selected area electron diffraction (SAED) of ferrihydrite and Al/Fe oxyhydroxide particles having an Al mol% of 10, 30, and 100% are shown in Figure 3.2. Micrograph (a**)** of Figure 3.2 corresponds to ferrihydrite (i.e., 0 mol% Al) and examination of the image shows the expected morphological properties of this material, particularly a particle size of ~2 nm, and a SAED pattern showing two diffuse rings indicating a structure with poor crystallinity (Schwertmann 1991). Micrograph (b) is associated with 10 mol% Al/Fe oxyhydroxide and within the resolution of the TEM micrograph the morphology of the Al 10% Al/Fe oxyhydroxide was similar to the pristine ferrihydrite sample (see Figure 3.2a-b). While not shown, a similar morphology was observed with TEM for Al/Fe oxyhydroxide that had an Al content of 5 and 20 mol%. Based on Figure 3.2 (a) and (b) we can suggest that the particle size of the "ferrihydrite" was not greatly affected by Al addition up to ~20 mol%. The lack of significant changes in the particle morphology as viewed by TEM was also consistent with the BET measurements that showed that the surface area of the particles was similar within the 0-10 mol% Al range. TEM characterization of the 30 mol% Al/Fe oxyhydroxide (Figure 3.2c) exhibited differences with ferrihydrite and 10 mol% Al/Fe oxyhydroxide. Inspection of the 30 mol% Al/Fe oxyhydroxide particles with TEM showed the presence of ~2 nm particles, in addition to larger aggregate-like (~ 3-5 nm) ordered particles as illustrated in Figure 3.2c. We suspect that the larger particles were due to micro-aggregation of smaller size nanoparticles in the 30 mol% Al/Fe oxyhydroxides particles, since the surface area of these particles was higher than the

lower (or higher) Al mol% particles. The TEM/SAED image shown in the inset displays diffraction spots that we believe suggested that a crystalline phase associated with AlOOH likely existed as a separate phase in or on the Al/Fe oxyhydroxide particles and not as distinct Al oxyhydroxide particles. The TEM/SAED data for the 70 mol% Al/Fe oxyhydroxide and pure AlOOH showed changes in aggregate structure when compared with lower Al mol% Al/Fe oxyhydroxide particles (Figure 3.2d and Figure 3.2e).

The SAED data illustrated a higher order poly-crystalline morphology than that which was associated with the ≤ 30 mol% Al/Fe oxyhydroxides. Furthermore, the SAED patterns, which were calibrated against a gold standard, yielded d-spacings of 2.22, 1.62, and 1.46 Å that were associated with the (201), (222), and (142) reflection lines of the AlOOH phase, bayerite. The arrows present in the figure point toward triangular and pseudohexagonal micro-aggregates consistent with poly-crystalline bayerite (and gibbsite) formation (Gonzalez, Ballesteros et al. 2002). We will return to this point when XRD results are presented.

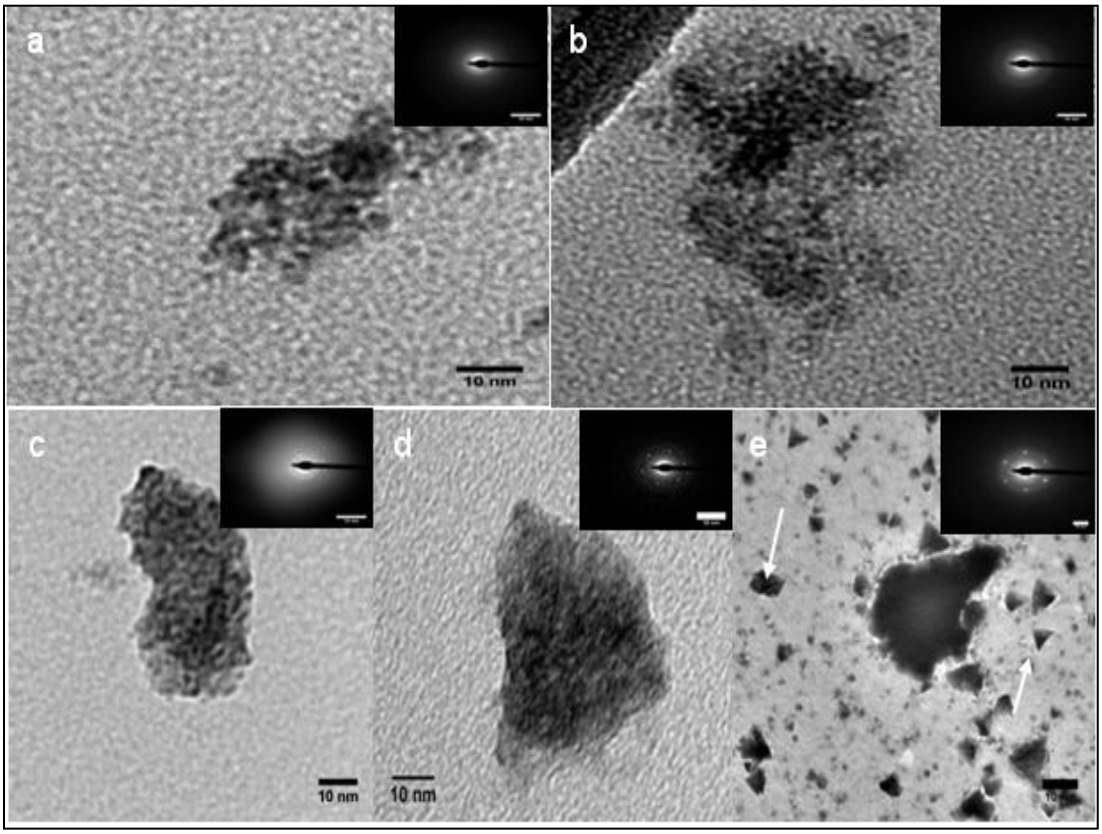

Figure 3.2. TEM micrographs of (a) "2-line" ferrihydrite and for Al/Fe oxyhydroxide with (b) 10 mol% Al, (c) 30 mol% Al, (d) 70 mol%, and (e) Al 100 mol.% (i.e., AlOOH). Insets to the TEM micrographs exhibit SAED data. At an Al mol% ≤ 10%, TEM showed the presence of 2 nm particles similar to the 2-line ferrihydrite morphology. At an Al mol% ≥ 30%, the presence of agglomerated particles with diameters close to 3-5 nm appeared with triangular and rectangular morphologies likely due to the formation of bayerite and gibbsite AlOOH phases. The presence of diffraction spots associated with the ≥ 30 mol% Al samples suggested that discrete AlOOH phases were present at these higher Al concentrations.

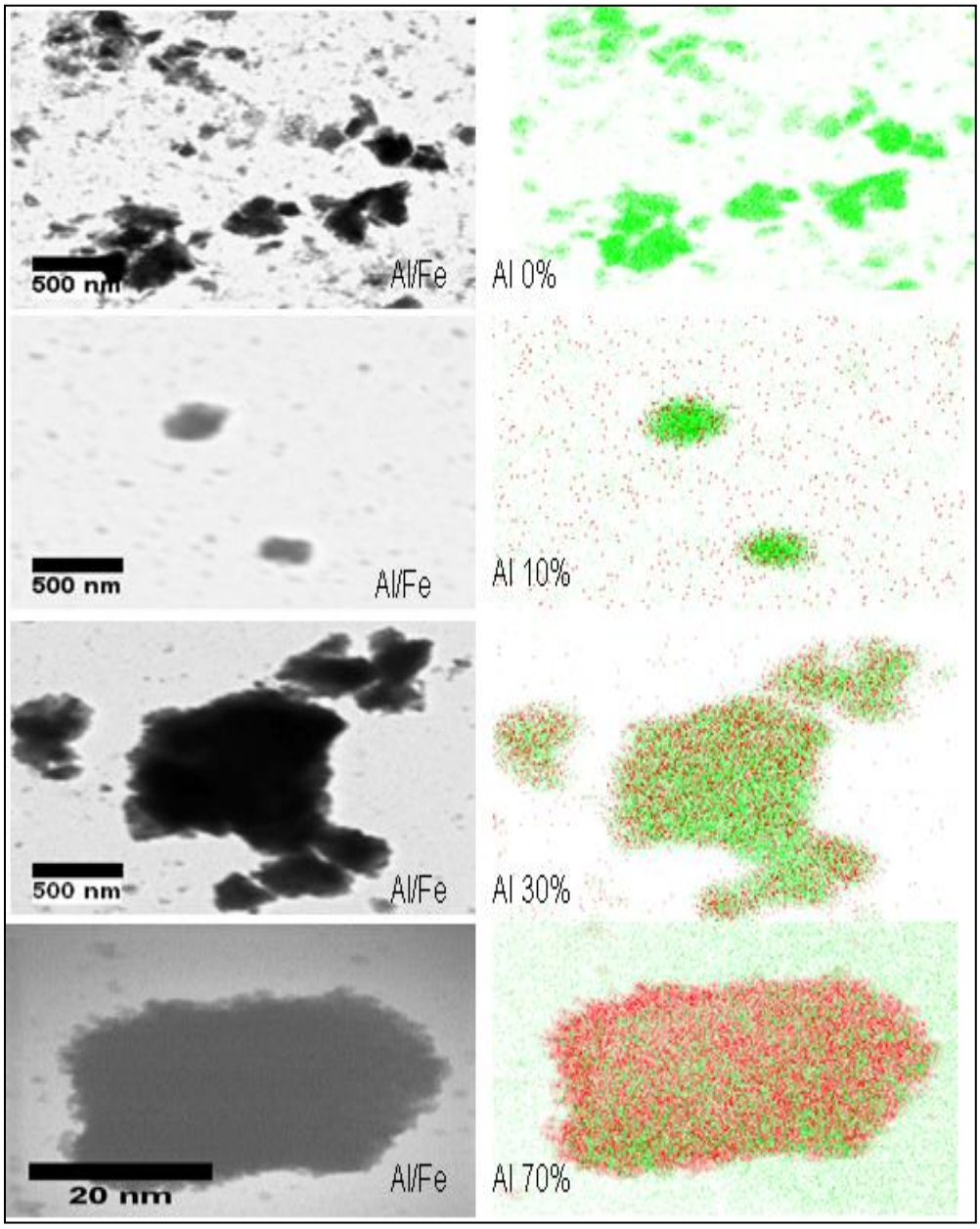

Figure 3.3. Selected STEM images, elemental dot maps, and EDS data for (Al 0%) "2-line" ferrihydrite and for Al/Fe oxyhydroxide with 10 mol% Al, 30 mol% Al, and 70 mol% Al. Light (green) and darker (red) dots correspond to the location of Fe and Al particles, respectively.

Figure 3.3 displays STEM/EDS data associated with ferrihydrite, 10 mol% Al/Fe oxyhydroxide, 30 mol% Al/Fe oxyhydroxide, and 70 mol% Al/Fe oxyhydroxide. While the spatial resolution of the elemental mapping was comparatively poor compared to data presented in Figure 3.2, the EDS data yielded information concerning the elemental makeup of the particles (analysis of data is in Table 3.1). Perhaps the most important aspect of these data was that within our spatial resolution, the 10 and 30 mol% Al/Fe oxyhydroxide particles appeared to consist of both Fe and Al. In short, we never observed images where particles solely consisted of either Al or Fe, suggesting that the Al was incorporated in the Al/Fe oxyhydroxide particles or existed as an AlOOH phase coprecipitated with the Al/Fe oxyhydroxides particle. The STEM/EDS derived morphology of the 70 mol% Al/Fe oxyhydroxides again showed the coexistence of Al and Fe, although in this circumstance the particles predominately consisted of AlOOH phases (darker color), perhaps coprecipitated with a minority Al/Fe iron oxyhydroxides phase.

To support some of the conclusions from electron microscopy, XRD was used to better investigate the evolution of ordered phases in the Al/Fe oxyhydroxides. XRD data are shown in Figure 3.4 for pristine ferrihydrite (diffractogram a) and for 5–70 mol% Al/Fe oxyhydroxides (diffractograms b-f). Also included in Figure 3.4 is a diffractogram (g) associated with a pure AlOOH precipitate that was synthesized in our laboratory from a solution that did not contain a source of Fe^{3+}, but contained the same amount of Al^{3+} that was used to obtain the 30 mol% Al/Fe oxyhydroxide.

It is useful to first compare the XRD diffractograms associated with pure ferrihydrite and the 5-30 mol% Al/Fe oxyhydroxide samples. Ferrihydrite exhibited two broad Bragg reflection features (2.6 and 1.5 Å), consistent with the relatively poor crystallinity of ferrihydrite (Childs 1992). An increase of the Al concentration to a level ≥ 10 mol% (diffractogram c) led to small, but noticeable changes in the respective XRD pattern. In particular, the diffractograms associated with 20 and 30 mol% Al (d-e) showed a decrease in intensity and broadening of the Bragg reflection lines relative to those associated with pristine ferrihydrite. The broadening may of been due to a small decrease in the lattice spacing of the ferrihydrite particles resulting from the substitution of the smaller Al^{3+}cation (ionic radius of 0.535Å) for the larger Fe^{3+}cation (r = 0.55Å). Such a substitution may of resulted in a contraction in the average size of the ferrihydrite structure which would be consistent with the peak shifts to higher 2θ values as the Al mol% of the Al/Fe oxyhydroxide increased (Bazilevskaya, Archibald et al. 2011). XPS, however, showed the formation of discrete AlOOH phases starting at Al ≥ 20 mol% and hence, we suspect that only a fraction of the Al could be substituting for Fe in the iron oxyhydroxides structure.

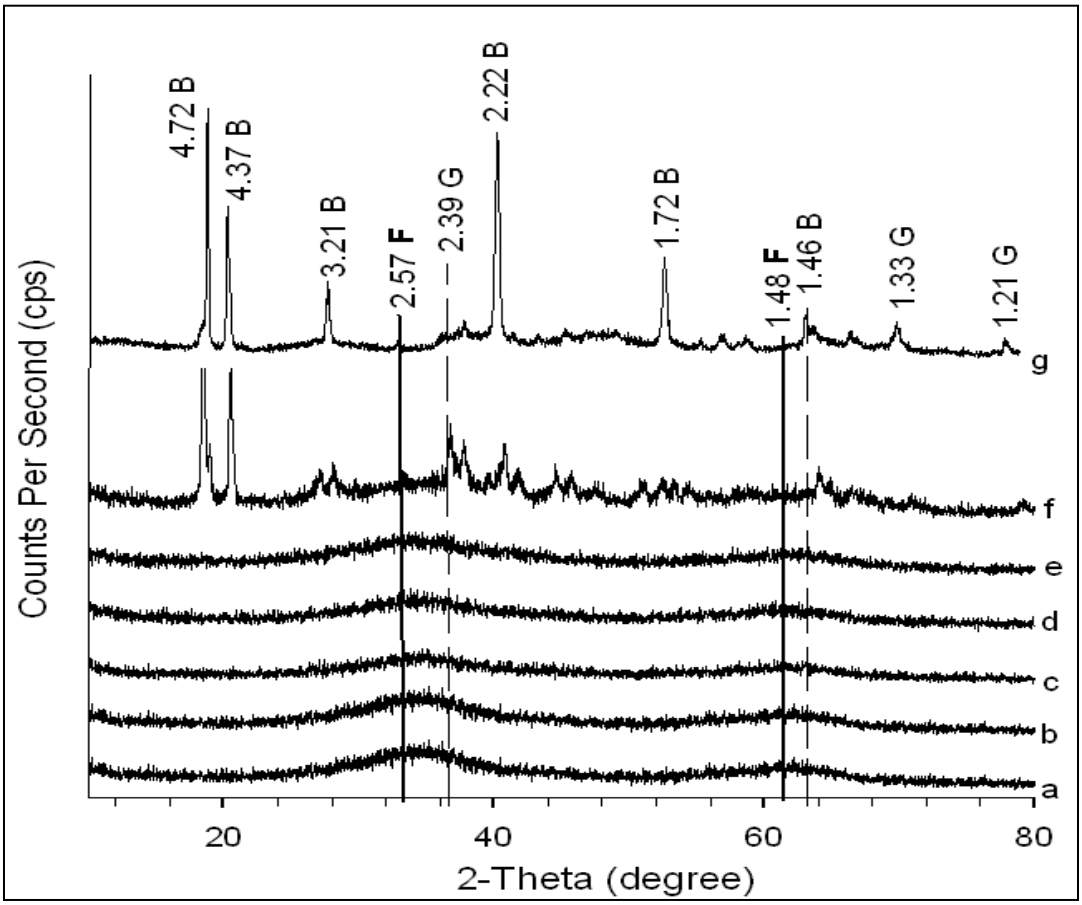

Figure 3.4. XRD diffractograms associated with (a) "2-line" ferrihydrite and for Al/Fe oxyhydroxide with (b) 5 mol% Al, (c) 10 mol% Al, (d) 20 mol% Al, (e) 30 mol% Al, (f) 70 mol% Al, and (g) AlOOH. The two main XRD lines are shown at ~ 2.57 Å and ~1.48 Å for "2-line" ferrihydrite and these lines were discernible for the 0-10 mol% Al/Fe oxyhydroxide samples. The XRD data for the 20-30 mol% Al samples were different than that associated with the samples having a lower concentration of Al in that they exhibited a decrease in intensity and a further broadening of Bragg reflection lines. The development of Bragg d-spacing reflection lines that were characteristic of poorly-crystalline bayerite/gibbsite phases occurred at an Al mol% ≥ 20%.

Furthermore, as mentioned earlier referring to an Al-substituted ferrihydrite on the basis of two relatively broad reflections is somewhat dubious without a more detailed structural characterization. An important experimental observation derived from the XRD is that the diffractograms associated with 30 mol% Al/Fe oxyhydroxide, 70 mol% Al/Fe oxyhydroxide, and pure AlOOH exhibit significant differences. The AlOOH solid exhibited sharp reflections with d-spacing of 4.72, 4.37, 3.21, 2.22, 1.72, and 1.45 Å that were consistent with the (β-$Al(OH)_3$) bayerite (B) phase although evidence of a small contribution from gibbsite (G) was present. Such phases have been suggested to form in the majority of prior studies of Al/Fe oxyhydroxides to varying degrees (Piszora and Wolska 1998; Jentzsch 2006; Masue, Loeppert et al. 2007; Bazilevskaya, Archibald et al. 2011). The 30 mol% Al/Fe oxyhydroxide did not exhibit the reflections associated with pure AlOOH to a significant degree while these diffraction lines were more apparent in the 70 mol% Al/Fe oxyhydroxide, which was most similar to the diffractograms associated with pure AlOOH. An important inference from this comparison is that this AlOOH phase cannot be easily identified in the 30 mol% Al/Fe oxyhydroxide particles, suggesting that the Fe^{3+} and Al^{3+} coprecipitated into composite Fe^{3+}/Al^{3+} particles and that individual FeOOH and AlOOH particles did not form. The XRD and TEM/SAED results presented above, however, did suggest that the 30 mol% Al/Fe oxyhydroxide particles included crystalline phases, likely due to AlOOH phases incorporated in or on the native iron oxyhydroxide particle. It is perhaps interesting that a prior study by Liu et al. (Liu and Hesterberg 2011) did not observe the evolution of AlOOH crystalline phases with increasing Al addition in the Al $\geq$ 20 mol% range, possibly due to differences in synthesis methods. Furthermore, the two broad reflections associated with ferrihydrite

were essentially lost at 20 mol% Al (diffractogram d). This comparison suggests that the details of the synthetic procedures in forming the Al/Fe oxyhydroxides particles likely have an effect on the resulting particle structure. Overall, however, the XRD data of the particles used in this study were similar within the 0-20 mol% Al range, perhaps suggesting that the best description of the particles in this range are Al-substituted ferrihydrite particles containing superficial AlOOH domains.

3.3.3 Attenuated Total Reflectance-Fourier Transform Infra-red (ATR-FTIR) of Ferrihydrite and Al/Fe Oxyhydroxide after Exposure to CO_2

Now that the Al/Fe oxyhydroxides particles have been characterized by a variety of techniques, their reactivity toward CO_2 was investigated. Figure 3.5 displays ATR-FTIR data for pure ferrihydrite, Al/Fe oxyhydroxide, and AlOOH before and after exposure to gaseous CO_2. The spectrum (thicker black line), which is associated with Al-free ferrihydrite prior to CO_2 exposure, exhibits vibrational modes in the 1800 to 1200 cm^{-1} region that we attribute to the presence of adsorbed carbonate. The 1630 cm^{-1} feature is due to the δ(OH) bending deformation mode of adsorbed and/or structural water, and the ~1475 cm^{-1} and ~1345 cm^{-1} features are assigned respectively to the $\nu_{2(O\text{-}C\text{-}O),\ Asym}$ and $\nu_{3(O\text{-}C\text{-}O),\ Sym}$ vibrational modes of adsorbed carbonate. This relatively small concentration of surface carbonate was intrinsic to the ferrihydrite used in this study, and was due to the reaction of the ferrihydrite with CO_2 in the ambient atmosphere (Hausner, Bhandari et al. 2009). The assignments are consistent with prior publications that have investigated carbonate adsorption on other iron oxides surfaces (Baltrusaitis and Grassian 2005; Baltrusaitis, Schuttlefield et al. 2007; Rahnemaie, Hiemstra et al. 2007). Also included is a spectrum associated with the pure AlOOH phase (dashed-line spectrum) that

exhibits the δ(OH) bending at 1640cm^{-1}, and weak carbonate derived modes at 1530 and 1445 cm^{-1}, possibly suggesting that the amount of carbonate intrinsic to pure AlOOH (dry conditions) was less than on ferrihydrite nanoparticles, consistent with a lower affinity of carbon dioxide for aluminum oxyhydroxide nanoparticles (relative to iron oxyhydroxides) (Baltrusaitis, Schuttlefield et al. 2011).

3.3.4 Bicarbonate on Ferrihydrite and Al/Fe Oxyhydroxide

Exposure of ferrihydrite to 1 bar of flowing $CO_{2(g)}$ resulted in the appearance of vibrational modes at 1619 ($\nu_{2(O\text{-}C\text{-}O),\ Asym}$), 1410 ($\nu_{3(O\text{-}C\text{-}O),\ Sym}$), and 1220 cm^{-1} ($\delta_{4(COH)}$) that were associated with adsorbed bicarbonate on ferrihydrite (Figure 3.5). This bicarbonate species on ferrihydrite adopted a monodentate binding configuration, based on prior comparisons between experimentally-determined and DFT-calculated vibrational frequencies (Villalobos 2000; Arai, Sparks et al. 2004; Hausner, Bhandari et al. 2009). It has been suggested in prior research that the transfer of a proton from surface hydroxyl groups to a CO_2 derived surface complex is involved in bicarbonate formation on ferrihydrite (Hausner, Bhandari et al. 2009). With increasing Al content, there were changes in the vibrational mode positions that lend insight into the binding of the bicarbonate species. Before these changes are discussed, we mention that the bicarbonate species coexisted with inner-sphere carbonate although the modes associated with the strongly bound carbonate species were largely obscured by the vibrational modes of the bicarbonate in the presence of the 1 bar $CO_{2(gas)}$ atmosphere. The carbonate modes, however, became apparent after the gaseous CO_2 in contact with the sample was replaced by a flow of dry nitrogen.

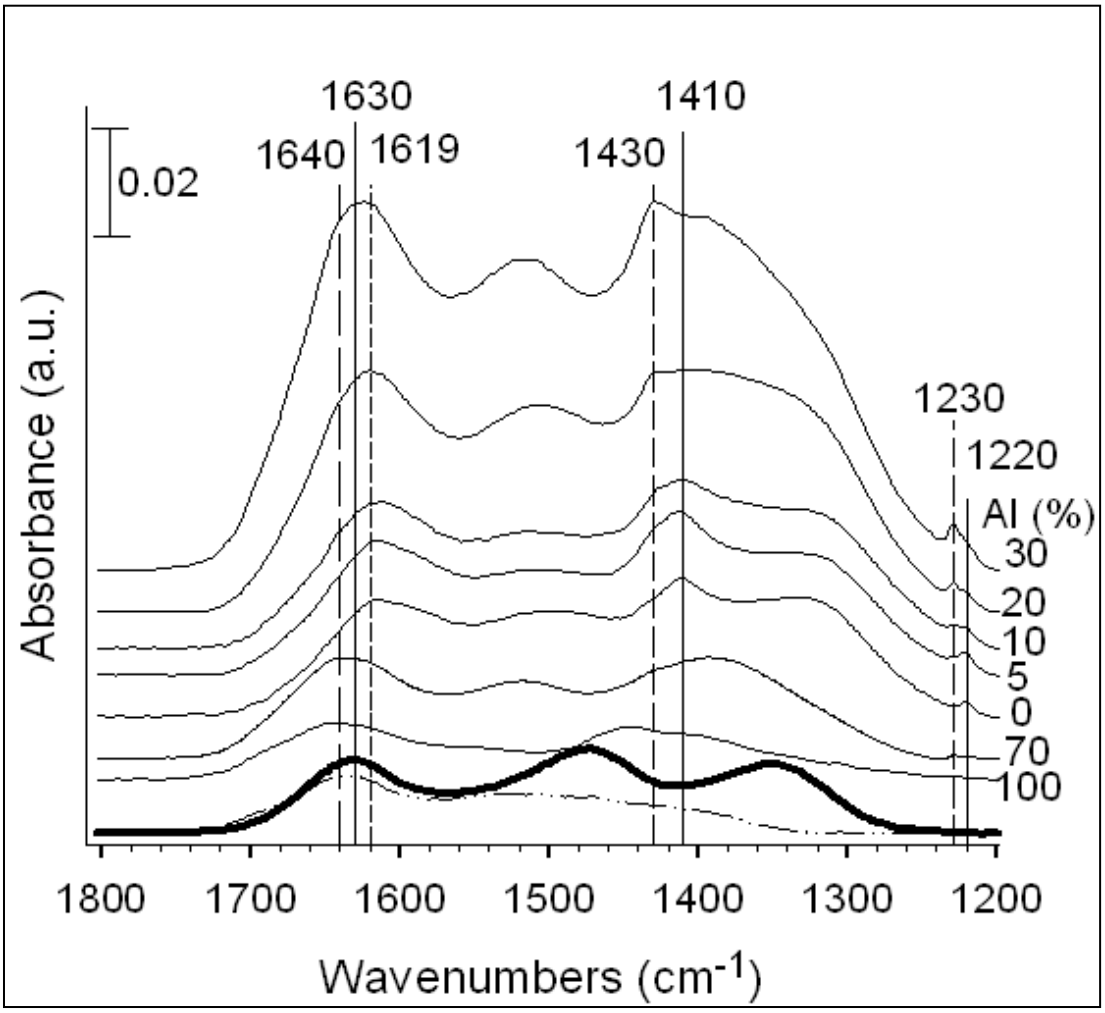

Figure 3.5. ATR-FTIR spectra for ferrihydrite, Al/Fe oxyhydroxides (at varying Al mol%), and AlOOH that was exposed to 1 bar of gaseous CO_2. The thick black line spectra and dotted line spectra are associated with Al-free ferrihydrite and AlOOH before exposure to $CO_{2(gas)}$, respectively.

Figure 3.6 illustrates these data, and based on prior research, we associated the vibrational modes in the ferrihydrite spectrum to carbonate that had a primarily bidentate binuclear binding geometry, but monodentate type complexes also likely existed (Palandri and Kharaka 2005; Michel, Ehm et al. 2007; Harvey and Rhue 2008; Liu and Hesterberg 2011). Due to the broadness of the vibrational modes it is difficult to discern any apparent trends in the positions of the vibrational modes as Al was incorporated into iron oxyhydroxide particles. The general similarity of the mode positions (~1340-1516 cm^{-1}) as the Al concentration was increased in the particles suggested that the binding geometry of carbonate was not significantly affected by the presence of Al. This suggestion is consistent with prior studies that have shown that the binding geometry of carbonate on small individual iron and aluminum oxide particles are similar (Busca and Lorenzelli 1982; Bargar, Kubicki et al. 2005; Hausner, Bhandari et al. 2009; Baltrusaitis, Schuttlefield et al. 2011).

Returning to a discussion of bicarbonate binding on ferrihydrite and Al/Fe oxyhydroxide, a particularly revealing part of the vibrational spectrum is contained within the 1210-1240 cm^{-1} range displayed in Figure 3.5. A magnified view of this region is shown in Figure 3.7, and we feel that a notable observation is that as the Al mol% was increased from 0 to 10%, spectral weight appeared at 1228 cm^{-1} and additional spectral weight at 1230 cm^{-1} became noticeable when the Al concentration reached 20 mol%. The three vibrational modes due to $\delta_4(HCO^-_3)$ stretching were still present at 70 mol% Al.

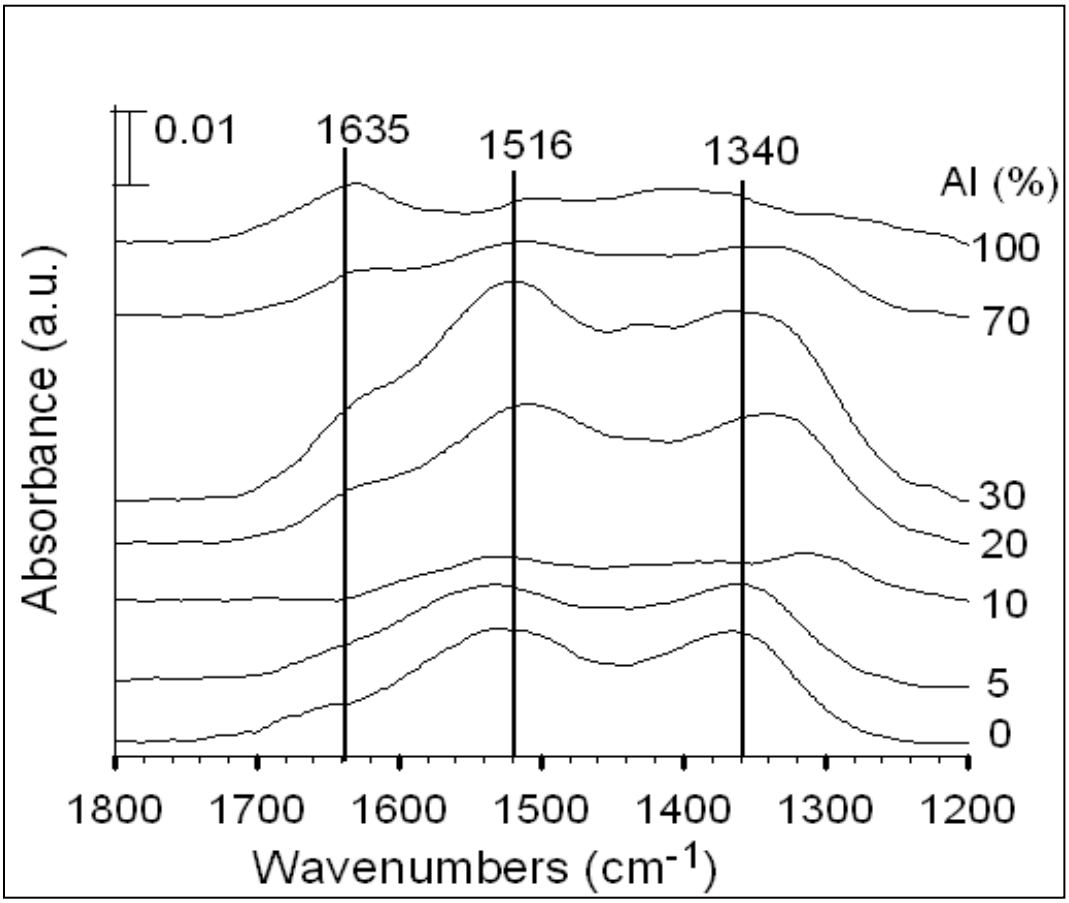

Figure 3.6. ATR-FTIR spectra are shown for the Al/Fe oxyhydroxide (0-100 Al mol%) after the oxyhydroxides were exposed to gaseous CO_2 and then to an inert nitrogen atmosphere. The vibrational modes were associated with binuclear carbonate inner-sphere binding complexes.

At 100 mol% Al (i.e., AlOOH) only the 1230 cm^{-1} mode remained, suggesting that the 1230 cm^{-1} mode associated with ≥ 20 mol % Al/Fe oxyhydroxide was due to bicarbonate binding on discrete AlOOH phases presumably contained at the surface of the sorbing particles. Above the 20 mol% Al incorporation, a significant number of reactive Fe sites appear to be eliminated causing a decrease in the intensity of the 1220 cm^{-1} mode and a shift in the spectral weight to 1230 cm^{-1}. This assertion is consistent with both the XRD and TEM results that showed the appearance of crystalline AlOOH in the particles at an Al concentration of 30 mol%.

The origin of the bicarbonate derived mode at 1228 cm^{-1} is proposed to be due to binding on the Al-component of Al/Fe oxyhydroxide. The rationale for this statement is that the 1228 cm^{-1} mode is associated with CO_2 adsorption on particles containing the lowest levels of Al (e.g., 10 mol%), where XRD, TEM, and XPS all showed no evidence of discrete AlOOH phase segregation. The assignment of the 1228 cm^{-1} mode to a primary interaction of $CO_{2(gas)}$ with the Al-component of Al/Fe oxyhydroxide was also is supported by computational results. In particular, we carried out DFT calculations to determine the vibrational modes of both carbonate and bicarbonate complexes on an Al-$(OH)_2$-Fe mixed cluster, Al-$(OH)_2$-Al cluster, and Fe-$(OH)_2$-Fe cluster (Figure 3.8a-d).

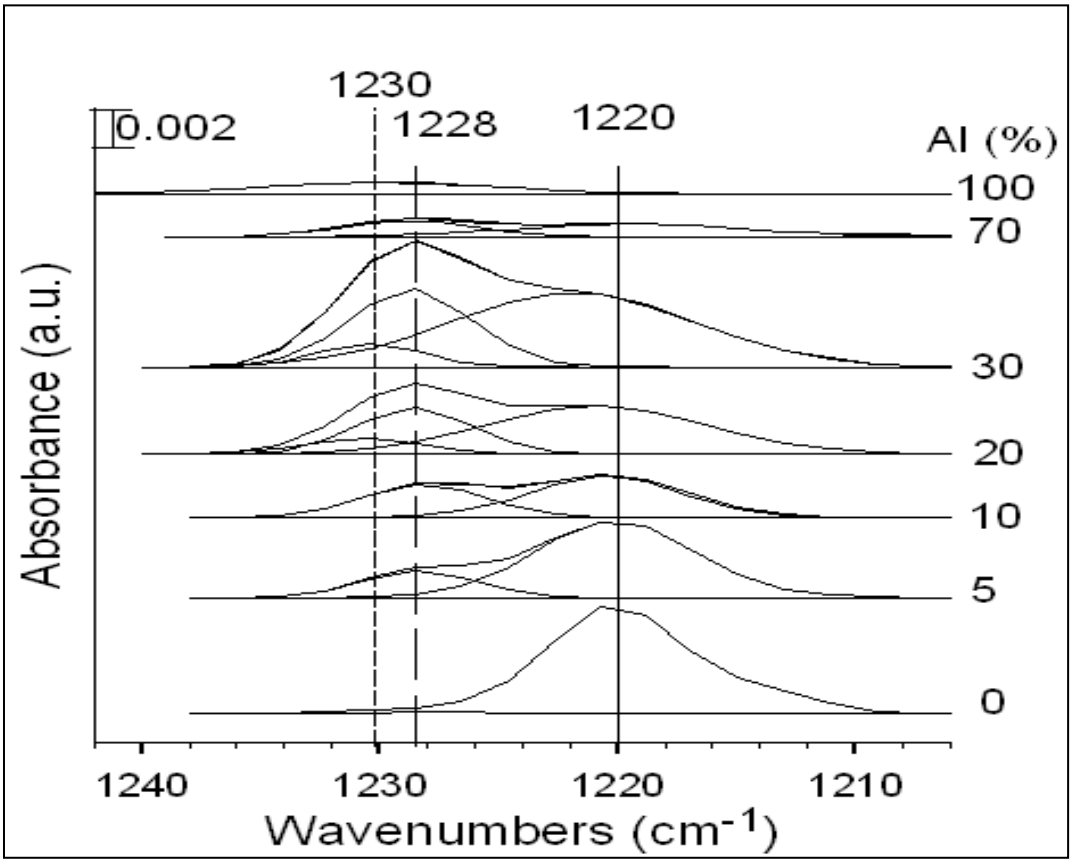

Figure 3.7. Fitted ATR-FTIR spectra in the 1240-1200 cm^{-1} region are shown for bicarbonate adsorbed on Al/Fe oxyhydroxides as a function of the Al mol%. The results suggested that the 1220 cm^{-1} feature was associated with bicarbonate binding on the Fe component of ferrihydrite and the Al/Fe oxyhydroxides. The 1228 cm^{-1} and 1230 cm^{-1} peaks were attributed to binding of bicarbonate on the Al component of the Al/Fe oxyhydroxides and discrete AlOOH phase, respectively. These assignments were supported by vibrational frequency DFT calculations.

Table 3.2 displays a summary of calculated vibrational frequencies for bicarbonate and carbonate species on the clusters. Of particular relevance to bicarbonate are the calculated DFT frequencies for the complexes shown in Figures 3.8a and 3.8b that represent a bent CO_2 species on a pure Fe and pure Al complex, respectively. The bent-CO_2 configuration was shown in a prior study to reproduce vibrational modes that were experimentally observed when ferrihydrite (Al-free) was exposed to 1 bar of CO_2 (Hausner, Bhandari et al. 2009). In particular, such a configuration (shown in Figure 3.8a) was associated with a calculated mode at 1228 cm^{-1} (δ_4, HCO^-_3) that was close in energy to an experimentally observed mode at 1220 cm^{-1} (δ_4, HCO^-_3) when ferrihydrite was maintained in a CO_2 atmosphere. In the current study a similar "bent-CO_2" configuration on an Al cluster (Figure 3.8b) was employed and the calculated $\delta_4(HCO^-_3)$ mode for this complex was 1238 cm^{-1}. Interestingly, bent-CO_2 bonded directly to the Fe or Al atomic site on the Al-Fe mixed cluster (see Figure 3.8c and Figure 3.8d) resulted in calculated vibrational frequencies at 1231 and 1235 cm^{-1}, respectively. This computational result suggests that bicarbonate bound on the Fe or Al site of a mixed Al/Fe oxyhydroxide cluster exhibits a $\delta_4(HCO^-_3)$ mode that is resolvable from the $\delta_4(HCO^-_3)$ mode associated with bicarbonate bound on a pure Fe (1227 cm^{-1}) or pure Al cluster (1238 cm^{-1}), respectively. We take from this result that the $\delta_4(HCO^-_3)$ mode associated with the Al-cluster appears ~10 cm^{-1} higher than when the bent CO_2 complex is associated with the Fe-cluster. Hence, this calculation is consistent with the experimentally observed mode at 1228 cm^{-1} being assigned to bicarbonate with mononuclear monodentate geometry on the Al site of a Al/Fe oxyhydroxide surface. We distinguish this species from the bicarbonate, which was bound on a distinct AlOOH

phase ($\delta_4(HCO^-_3)$ at 1230 cm^{-1}), that was associated with ≥ 20% Al/Fe oxyhydroxide and pure AlOOH that was exposed to CO_2. This latter assignment was consistent with a prior study that associated vibrational modes at ~1230 cm^{-1} resulting from the CO_2-exposure of γ-Al_2O_3 nanoparticles to bicarbonate (Baltrusaitis, Schuttlefield et al. 2007; Baltrusaitis, Schuttlefield et al. 2011).

The calculated frequencies for binuclear monodentate carbonate (ν_2C-O, Asym/Sym) at 1513/1333 cm^{-1} (cluster not shown), 1514/1440 cm^{-1} (see Figure 3.8e), and 1512/1384 cm^{-1} (Figure 3.8f) cluster models correlated with the experimentally determined vibrational modes that appeared at 1498/1333 cm^{-1} on Fe-oxyhydroxide, 1517/1363 cm^{-1} on Al/Fe-oxyhydroxide (e.g., 30 mol% Al; Figure 3.6), and 1515/1343 cm^{-1} on Al-oxyhydroxide, respectively. These modes were associated with adsorbed carbonate complexes formed from the reaction of gaseous phase CO_2 with adsorbed H_2O molecules resulting in solvated binuclear monodentate carbonate species. The results suggested that bicarbonate existed as mononuclear monodentate bound complexes (Figs. 3.8a-d) whereas carbonate adopted a binuclear monodentate configuration (Figs. 3.8e-f).

To better correlate the binding of bicarbonate with the Al and Fe component with the surface composition of the Al/Fe oxyhydroxide particles, the ratio of the integrated peak height of adsorbed bicarbonate between 1230/1228 (Al-binding) and 1220 cm^{-1} (Fe-binding) were calculated and plotted as a function of the mol% of Al in the Al/Fe oxyhydroxide (Figure 3.9). Inspection of the plot suggested that there was a monotonic increase in the peak ratio of adsorbed bicarbonate on the Al component relative to the fraction that adsorbed on Fe, as the Al increased from 0 to 10 mol%. We attributed this

increase to the increasing presence of Al in the surface of the Al/Fe oxyhydroxide particles. TEM, XPS and XRD all suggested that at least up to 10 mol% of Al; this metal was relatively homogeneously dispersed on the particle surface. As the Al mol% is increased from 10 to 30% there was an increasing amount of bicarbonate binding on discrete AlOOH phases. An increase of the Al mol% to 70% had little effect on the population of bicarbonate on Al and Fe binding sites relative to bicarbonate on 30 mol% Al/ferrihydrite. This result was consistent with XPS results that showed that the Al content in the near surface region of the particles was similar for the 30 and 70 mol % Al particles; albeit at the higher concentration, AlOOH phases dominated the composition of the particles.

There was also a significant difference in the vibrational mode intensity in the 1200-1240 cm^{-1} region (Figure 3.7) associated with bicarbonate/carbonate adsorption on the 30 and 70 mol% Al/Fe oxyhydroxide particles. In particular the integrated peak area in this region was 5.5 times greater for the spectrum associated with bicarbonate on the 30 mol% Al/Fe oxyhydroxide. A significant portion of this decrease was likely due to a reduction in the surface area of the particles that accompanied the increase in Al content from 30 to 70 mol%. For example, the BET derived surface areas associated with the 30 and 70 mol% Al particles were 387 and 221 m^2/g, respectively. The surface area difference was likely due to the increasing diameters of the particles as the Al concentration was raised above 30 mol % where precipitated AlOOH phases started to become an important structural component of the particles.

Table 3.2. Selected DFT calculated vibrational frequencies (cm^{-1}) mode assignments at the B3LYP hybrid DFT level of theory with a 6-31G(d) basis set for the gaseous CO_2 binding coordination on various (Fe, Al)-oxyhydroxide structural complexes.

Calculated Species	$\nu_{2C\text{-}O,\ Asym}$	$\nu_{3C\text{-}O,\ Sym}$
Carbonate binuclear monodentate		
$Fe_2(OH)_4(OH_2)_4\ CO_2^{-3} + 6H_2O$	1513	1333
$Al_2(OH)_4(OH_2)_4\ CO_2^{-3} + 6H_2O$	1601 (C=O)	
	1508	1440
Al-Fe $(OH)_4(OH_2)_4\ CO_2^{-3} + 6H_2O$	1611 (C=O)	
	1512	1384
Bicarbonate mononuclear monodentate "Bent $CO_{2(adsorbed)}$"		
$Fe_2(OH)_5(OH_2)_4\ HCO_3^- + 4H_2O$	1565	1227
$Al_2(OH)_5(OH_2)_4\ HCO_3^- + 4H_2O$	1557	1238
$Al\text{-}Fe(OH)_5(OH_2)HCO_3^- + 4H_2O$		
CO_2 bound to Fe atom	1561	1231
$Al\text{-}Fe(OH)_5(OH_2)HCO_3^- + 4H_2O$		
CO_2bound to Al atom	1565	1235

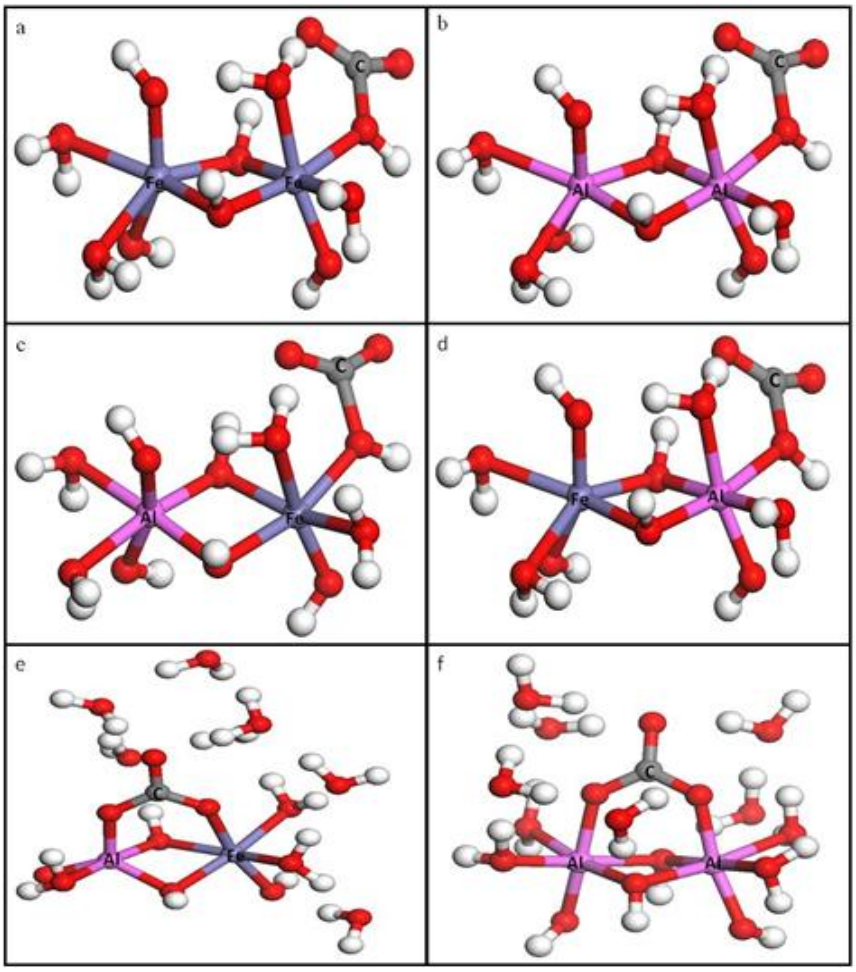

Figure 3.8. Optimized density functional theory (DFT) calculations of bicarbonate model surface species: (a) Fe_2 mononuclear monodentate, (b) Al_2 mononuclear monodentate, (c) (Fe, Al) mononuclear monodentate, and (d) (Al, Fe) mononuclear monodentate. Panel 3.8e and 3.8f are bridged solvated binuclear monodentate carbonate cluster models ($10H_2O$). Geometries were optimized at the B3LYP/6-31G(d) level using Gaussian 03 E.01 program. The results from DFT calculations were compared and agreed well with the experimental IR frequencies. The graphics are created with Materials Studio 6.0 (Accelrys Inc., San Diego CA) with color code visualization: red (O), white (H), blue (Fe), pink (Al), and grey (C).

Furthermore, surface area differences likely have a contribution from differences in the extent to which the particles with different Al concentrations aggregate in the dry state. At the lower concentrations of Al our results suggested that there is an increase in the effective surface area relative to the ferrihydrite and AlOOH samples. This result is consistent with prior research that also experimentally determined the surface area for a Al-Fe coprecipitated oxide material to be greater than the surface area of either individual component oxide alone (Anderson and Benjamin 1990). It was speculated in this earlier research that the presence of Al led to a decreased amount of aggregation. Normalization of our experimentally determined integrated infrared absorbencies by surface area showed that the sum of the carbonate and bicarbonate concentration on the 30 Al mol% particles was ~2 times greater than on the 70% particles (see Figure 3.5 and Figure 3.9). A decrease in the adsorption capacity of the particles as discrete AlOOH domains dominated (> 30 % Al) was expected, because prior research showed that the surface area normalized adsorption capacity of iron oxide was greater than that of an aluminum oxide phase (Violante, Krishnamurti et al. 1998; Violante, Barberis et al. 2003; Sujana and Anand 2010; Basu, Gupta et al. 2012).

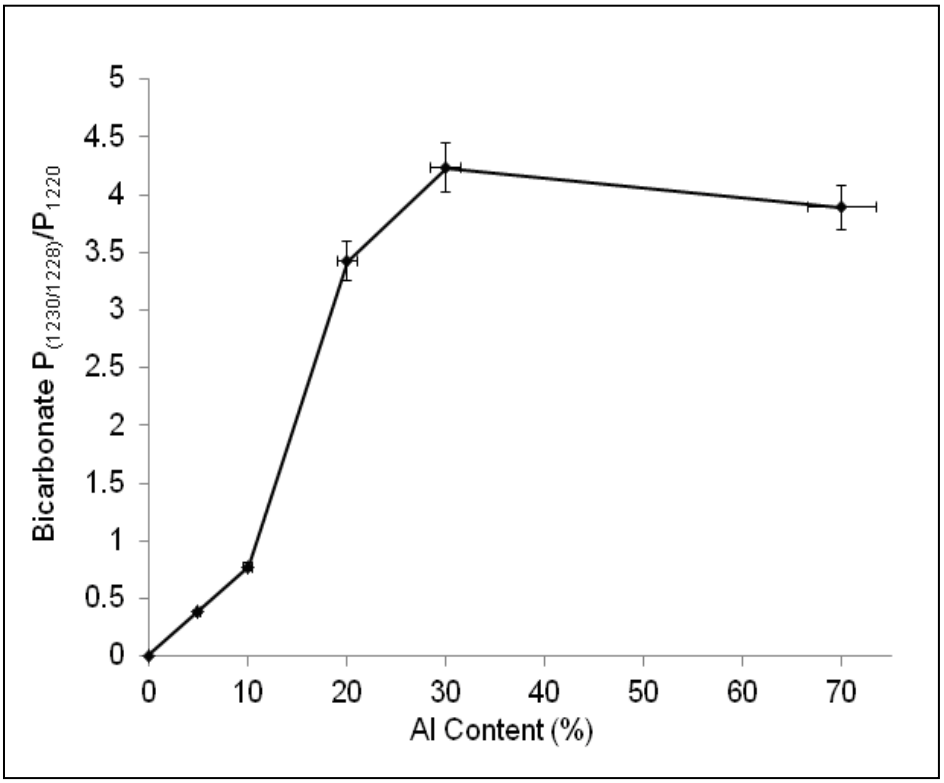

Figure 3.9. The ratio of the integrated peak height (1228/1230 to 1220 cm^{-1}) associated with adsorbed bicarbonate is plotted as a function of the Al mol% in the Al/Fe oxyhydroxides (IR spectra shown in Figure 3.7). Inspection of the plot suggested that there was a monotonic increase in the peak ratio as the mol% of Al increased from 0 to 10 mole%. As the Al mole% increased from 10 to 30% there was an increasing amount of bicarbonate binding on discrete AlOOH phases. An increase of the Al mol% to 70% had a relatively small effect on the population of bicarbonate on Al and Fe binding sites relative to bicarbonate on the 30 mol% Al/Fe oxyhydroxide. The error bars represent the standard deviation calculated from at least two separate measurements made under the same experimental conditions.

A similar analysis (using surface areas in Table 3.1) for the 0-20 Al mol% samples showed that the associated surface area normalized peak areas were all within 10% of each other suggesting that the presence of Al in this range did not have a drastic effect on the active site density for carbonate/bicarbonate adsorption (Figure 3.5 and 3.6). A significant and reproducible increase in the surface normalized peak area was experimentally observed when the 30 mol% Al/Fe oxyhydroxides sample was compared to the samples in the 0-20 mol% range. Specifically, the peak area associated with the carbonate/bicarbonate vibrational modes of the 30 mol% sample was ~1.5 greater than the samples with lower Al content.

While a reduced amount of particle aggregation for 30 mol% Al/Fe oxyhydroxides in the dry state was likely a primary reason for the increased amount of carbonate adsorption, it is also possible that smaller particles may of have been associated with this specific sample. A smaller particle could introduce a more structurally defective surface and a higher reactive site density. A correspondence between decreasing nanoparticles size and increasing defect density has been suggested in prior research (Liu and Osseo-Asare 2000; Schwertmann, Friedl et al. 2000). Perhaps more important is that the presence of Al in the iron oxyhydroxide increased the amount of $CO_{2(gas)}$ adsorption relative to ferrihydrite due to an increase in the amount of surface sites (on a per mass basis) exposed to the reactant gas. Hence, in the context of a substrate for CO_2 sequestration, for example, the addition Al to the iron oxyhydroxide appears to be beneficial.

3.4 Summary

The structure and reactivity of the iron oxyhydroxide, ferrihydrite and Al/Fe oxyhydroxides toward gaseous CO_2 were investigated. At low mol% levels of Al (<30 mol%), the metal incorporated into the FeOOH without the formation of discrete AlOOH phases. At higher levels of Al, discrete AlOOH phases appeared, as evidenced by XRD, XPS, and TEM. ATR-FTIR results showed that the binding geometry of carbonate and bicarbonate, which formed in the presence of gaseous CO_2, was not markedly affected as the amount of Al varied in the Al/Fe oxyhydroxide particles. The vibrational spectroscopy results did suggest, however, that the amount of $CO_{2(gas)}$ adsorbing on the Al/Fe oxyhydroxides particles showed a dependence on the amount of Al. In particular, the experimental results suggested that the amount of $CO_{2(gas)}$ that adsorbed on the Al/Fe oxyhydroxide particles increased as the Al content of the particle was increased from 0 (pure ferrihydrite) to 30 mol% Al. There was a decrease in the amount of $CO_{2(gas)}$ adsorption at higher Al concentrations where discrete AlOOH phases became a significant property of the Al/Fe oxyhydroxide particles. The increase in the CO_2 adsorption as the Al mol% increased from 0 to 30% may be a result of changes in how the particles aggregated in the dry state rather than an increasing number of active sites for CO_2 adsorption.

Acknowledgments

This work was supported by a National Science Foundation (NSF) Collaborative Research in chemistry grant. In addition to NSF support (grant No. CHE-0714121 and No. CHE-0923077), D.R.S. appreciates partial funding for this research from the Department of Energy, Basic Energy Sciences (DEFG-029ER14644). The assistance of Hongwen Zhou in obtaining the TEM images is acknowledged. We thank Alfred Miller and Frederick C. Monson, for their help with XPS and TEM experiments at Lehigh and West Chester University, respectively. The author also thanks the Bridge to Doctorate program and the Louis Stokes Alliances for Minority Participation (LSAMP/NSF) for financial assistance. Work done at Argonne and use of the Advanced Photon Source was supported by the U.S. Department of Energy, Office of Science, Office of Basic Energy Science, under contract No. DE-AC02-06CH11357. Computational support was provided by the Research Computation and Cyberinfrastructure group at The Pennsylvania State University.

References

Anderson, P. R. and M. M. Benjamin (1990). "Surface and Bulk Characteristics of Binary Oxide Suspensions." Environmental Science & Technology **24**(5): 692-698.

Arai, Y., D. L. Sparks, et al. (2004). "Effects of Dissolved Carbonate on Arsenate Adsorption and Surface Speciation at the Hematite-Water Interface." Environmental Science and Technology **38**(3): 817-824.

Baltrusaitis, J. and V. H. Grassian (2005). "Surface reactions of carbon dioxide at the adsorbed water-iron oxide interface." Journal of Physical Chemistry B **109**: 12227-12230.

Baltrusaitis, J., J. Schuttlefield, et al. (2007). "FTIR spectroscopy combined with quantum chemical calculations to investigate adsorbed nitrate on aluminium oxide surfaces in the presence and absence of co-adsorbed water." Physical Chemistry Chemical Physics **9**(36): 4970-4980.

Baltrusaitis, J., J. Schuttlefield, et al. (2011). "Carbon dioxide adsorption on oxide nanoparticle surfaces." Chemical Engineering Journal **170**(2-3): 471-481.

Bargar, J. R., J. D. Kubicki, et al. (2005). "ATR-FTIR spectroscopic characterization of coexisting carbonate surface complexes on hematite." Geochimica Et Cosmochimica Acta **69**(6): 1527-1542.

Basu, T., K. Gupta, et al. (2012). "Performances of As(V) adsorption of calcined (250 degrees C) synthetic iron(III)-aluminum(III) mixed oxide in the presence of some groundwater occurring ions." Chemical Engineering Journal **183**: 303-314.

Bazilevskaya, E., D. D. Archibald, et al. (2011). "Aluminum coprecipitates with Fe (hydr)oxides: Does isomorphous substitution of Al(3+) for Fe(3+) in goethite occur?" Geochimica Et Cosmochimica Acta **75**(16): 4667-4683.

Becke, A. D. (1992). "Density-Functional Thermochemistry .1. the Effect of the Exchange-Only Gradient Correction." Journal of Chemical Physics **96**(3): 2155-2160.

Becke, A. D. (1997). "Density-functional thermochemistry .5. Systematic optimization of exchange-correlation functionals." Journal of Chemical Physics **107**(20): 8554-8560.

Borch, T., Y. Masue, et al. (2007). "Phosphate imposed limitations on biological reduction and alteration of ferrihydrite." Environmental Science & Technology **41**(1): 166-172.

Busca, G. and V. Lorenzelli (1982). "Infrared Spectroscopic Identification of Species Arising from Reactive Adsorption of Carbon Oxides on Metal-Oxide Surfaces." Materials Chemistry **7**(1): 89-126.

Chadwick, J., D. H. Jones, et al. (1986). "A Mossbauer Study of Ferrihydrite and Aluminum Substituted Ferrihydrites." J. Magn. Magn. Mater. **61**(1-2): 88-100.

Childs, C. W. (1992). "Ferrihydrite - a Review of Structure, Properties and Occurrence in Relation to Soils." J.Plant Nutr. Soil Sc. **155**(5-6): 441-448.

Cismasu, A. C., F. M. Michel, et al. (2012). "Properties of impurity-bearing ferrihydrite I. Effects of Al content and precipitation rate on the structure of 2-line ferrihydrite." Geochim. Cosmochim. Acta **92**: 275-291.

Cismasu, A. C., F. M. Michel, et al. (2011). "Composition and structural aspects of naturally occurring ferrihydrite." CR Geoscience **343**(2-3): 210-218.

Filip, J., R. Zboril, et al. (2007). "Environmental applications of chemically pure natural ferrihydrite." Environmental Science & Technology **41**(12): 4367-4374.

Ford, G. C., P. M. Harrison, et al. (1984). "Ferritin - Design and Formation of an Iron-Storage Molecule." Philosophical Transactions of the Royal Society of London Series B-Biological Sciences **304**(1121): 551-&.

Gonzalez, E., M. C. Ballesteros, et al. (2002). "Reductive dissolution kinetics of Al-substituted goethites." Clays and Clay Minerals **50**(4): 470-477.

Harvey, O. R. and R. D. Rhue (2008). "Kinetics and energetics of phosphate sorption in a multi-component Al(III)-Fe(III) hydr(oxide) sorbent system." Journal of Colloid and Interface Science **322**(2): 384-393.

Hausner, D. B., N. Bhandari, et al. (2009). "Ferrihydrite reactivity toward carbon dioxide." Journal of Colloid and Interface Science **337**(2): 492-500.

Jambor, J. L. and J. E. Dutrizac (1998). "Occurrence and Constitution of Natural and Synthetic Ferrihydrite, a Widespread Iron Oxyhydroxide." Chemical Reviews (Washington, D. C.) **98**(7): 2549-2585.

Jensen, M. B., L. G. M. Pettersson, et al. (2005). "CO2 sorption on MgO and CaO surfaces. A comparative quantum chemical cluster study." Journal of Physical Chemistry B **109**(35): 16774-16781.

Jentzsch, T. L. (2006). "Influence of aluminum doping on ferrihydrite nanoparticle reactivity (vol 110, pg 11746, 2006)." Journal of Physical Chemistry B **110**(37): 18729-18729.

Kloprogge, J. T., L. V. Duong, et al. (2006). "XPS study of the major minerals in bauxite: Gibbsite, bayerite and (pseudo-)boehmite." Journal of Colloid and Interface Science **296**(2): 572-576.

Kubicki, J. D., K. W. Paul, et al. (2012). "ATR-FTIR and Density Functional Theory Study of the Structures, Energetics, and Vibrational Spectra of Phosphate Adsorbed onto Goethite." Langmuir **28**(41): 14573-14587.

Lammers, K., R. Murphy, et al. (2011). "CO2 Sequestration through Mineral Carbonation of Iron Oxyhydroxides." Environ. Sci. Technol. **45**(24): 10422-10428.

Lee, C. T., W. T. Yang, et al. (1988). "Development of the Colle-Salvetti Correlation-Energy Formula into a Functional of the Electron-Density." Physical Review B **37**(2): 785-789.

Liu, Q. Y. and K. Osseo-Asare (2000). "Synthesis of monodisperse Al-substituted hematite particles from highly condensed metal hydroxide gels." Journal of Colloid and Interface Science **231**(2): 401-403.

Liu, Y.-T. and D. Hesterberg (2011). "Phosphate Bonding on Noncrystalline Al/Fe-Hydroxide Coprecipitates." Environmental Science & Technology **45**(15): 6283-6289.

Masue, Y., R. H. Loeppert, et al. (2007). "Arsenate and arsenite adsorption and desorption behavior on coprecipitated aluminum : iron hydroxides." Environmental Science & Technology **41**(3): 837-842.

Michel, F. M., V. Barron, et al. (2010). "Ordered ferrimagnetic form of ferrihydrite reveals links among structure, composition, and magnetism." Proc. Natl. Acad. Sci. U.S.A. **107**(7): 2787-2792.

Michel, F. M., L. Ehm, et al. (2007). "Similarities in 2- and 6-line ferrihydrite based on pair distribution function analysis of x-ray total scattering." Chemistry of Materials **19**(6): 1489-1496.

Michel, F. M., H.-A. Hosein, et al. (2010). "Reactivity of ferritin and the structure of ferritin-derived ferrihydrite." Biochim. Biophys. Acta, Gen. Subj. **1800**(8): 871-885.

Michel, F. M., H. A. Hosein, et al. (2010). "Reactivity of ferritin and the structure of ferritin-derived ferrihydrite." Biochimica Et Biophysica Acta-General Subjects **1800**(8): 871-885.

Mohai, M. (2004). "XPS MultiQuant: multimodel XPS quantification software." Surface and Interface Analysis **36**(8): 828-832.

Palandri, J. L. and Y. K. Kharaka (2005). "Ferric iron-bearing sediments as a mineral trap for CO_2 sequestration: Iron reduction using sulfur-bearing waste gas." Chem. Geol. **217**(3-4): 351-364.

Piszora, P. and E. Wolska (1998). X-ray powder diffraction study on the solubility limits in the goethite-diaspore solid solutions. Epdic 5, Pts 1 and 2. R. Delhez and E. J. Mittemeijer. **278-2:** 584-588.

Rahnemaie, R., T. Hiemstra, et al. (2007). "Carbonate adsorption on goethite in competition with phosphate." Journal of Colloid and Interface Science **315**(2): 415-425.

Schulze, D. G. and U. Schwertmann (1984). " The influence of aluminum on iron-oxides.10. Properties of Al-substituted goethites." Clay Minerals **19**(4): 521-539.

Schwertmann, U. (1991). Iron Oxides in the Laboratory: Preparation and Characterization. Weinheim. New York . Chichester, Willey-VCH.

Schwertmann, U. (1991). "Solubility and Dissolution of Iron-Oxides." Plant and Soil **130**(1-2): 1-25.

Schwertmann, U., J. Friedl, et al. (2000). "The effect of Al on Fe oxides. XIX. Formation of Al-substituted hematite from ferrihydrite at 25 degrees C and pH 4 to 7." Clays and Clay Minerals **48**(2): 159-172.

Schwertmann, U., J. Friedl, et al. (2000). "The effect of clay minerals on the formation of goethite and hematite from ferrihydrite after 16 years' ageing at 25 DegC and pH 4-7." Clay Minerals **35**(4): 613-623.

Sujana, M. G. and S. Anand (2010). "Iron and aluminium based mixed hydroxides: A novel sorbent for fluoride removal from aqueous solutions." Applied Surface Science **256**(23): 6956-6962.

Villalobos, J. O. L. a. M. (2000). "Carbonate adsorption on goethite under closed and open CO_2 conditions " Geochemica et Cosmochimica Acta **64**(22): 3787-3802.

Violante, A., E. Barberis, et al. (2003). "Factors affecting the formation, nature, and properties of iron precipitation products at the soil-root interface." Journal of Plant Nutrition **26**(10 & 11): 1889-1908.

Violante, A., G. S. R. Krishnamurti, et al. (1998). "Formation and stability of hydroxy aluminum iron montmorillonite complexes: Influence of ferrous iron." Soil Science Society of America Journal **62**(5): 1448-1454.

CHAPTER 4
FERRIMAGNETIC FERRIHYDRITE REACTIVITY TOWARD ADSORPTION OF CARBON DIOXIDE

Abstract

This chapter investigates the reactivity of synthesized ferrimagnetic ferrihydrite (FerriFh) toward gaseous CO_2 adsorption. X-ray diffraction (XRD), scanning transmission electron microscopy (STEM), and attenuated total reflectance Fourier transform Infrared spectroscopy (ATR-FTIR) were used to probe the FerriFh surface reactivity under various CO_{2gas} pressure conditions. The results showed that remaining adsorbed citrate species, used during the synthesis of the material, on the FerriFh nanoparticles blocked binding sites for adsorbed carbonate and bicarbonate formation. Only after the removal of residual citrate did ATR-FTIR results reveal the formation of adsorbed carbonate and bicarbonate modes on FerriFh surface under low CO_2 pressure conditions (0.35 to 3.5 bars). Bicarbonate species that formed at lower pressure ($\leq$ 3.5 bars) disappeared with an increase in CO_2 pressure up to 58.6 bars. The result is due to an increase in condense liquid state (e.g., above 5.17 bar and 298.13 Kelvin) which favored the reaction of $CO_{2(gas)}$ with surface OH^{2+} sites instead of O-H group contributing to the loss of bicarbonate (1220 cm^{-1}) on the mineral surfaces under high pressure conditions. FerriFh exhibited a similar surface reactivity to its precursor ferrihydrite, toward adsorbed carbonate and bicarbonate complexes. The binding configurations of the adsorbate on both surfaces are affected at elevated pressure.

4.1 Introduction

Previous studies have investigated the structural, compositional, and magnetic changes which occurred upon hydrothermal aging of "2 line" ferrihydrite in the presence of various organic ligands (Barron, Torrent et al. 2003; Silva, Amaral et al. 2006; Zhang, Ellery et al. 2007). These studies showed that ferrihydrite, when subjected to hydrothermal conditions, resulted in the formation of hematite (α-Fe_2O_3). However, in the presence of organic ligands and within the optimum concentration, pH, and temperature range (e.g., phosphate, tartrate, fulvic acid, and citrate); the formation of the hematite or goethite phases occurred less rapidly, and an intermediate ferrimagnetic ferrihydrite (FerriFh) phase forms (R. M. Cornell 2003; Cabello, Morales et al. 2009; Barron, Torrent et al. 2012). This growth of FerriFh seems to occur through adsorption of organic anions (e.g., oxalate, phosphate, and citrate) on ferrihydrite, via aggregation, to inhibit or retard the rate of crystallization to goethite or hematite products. The common product obtained was previously referred to as a maghemite-like phase (γ-Fe_2O_3) or "hydromaghemite" and was observed through the use of external field Fe Mössbauer spectroscopy, XRD, and FTIR data (Jambor and Dutrizac 1998). But recent critical review has reported that the hydromaghemite and FerriFh structures are indeed similar (Barron, Torrent et al. 2012). It has been demonstrated that the presence of tetrahedral coordinated iron Fe(III)(^{IV}Fe) in the magnetically enhanced intermediate product occurred slowly during the hydrothermal transformation of ferrihydrite into hematite at a temperature ranging from 125-200 ºC over a period of 0.2 to 180 days at a molar of P/Fe ratio of 0-6% and citrate/Fe ratio of 3% (Barron, Torrent et al. 2003; Violante, Barberis et al. 2003).

Ferrihydrite (~2-6 nm) mineral is ubiquitous in the environment and has been extensively studied because of their availability in ground water, air, soils, and acid mine drainage sites (Schwertmann 1991; Bishop and Murad 2002). Hydrated iron oxides of ferrihydrite (e.g. ~6-nanometer dimension) have been also found in the iron core storage of protein ferritin ((holding ~4000 iron atoms) with magnetic properties called "magnetoferritin" and have been used in biomedical imaging templates and separation procedures (Ford, Harrison et al. 1984; Meldrum, Heywood et al. 1992; Geremias, Laus et al. 2008; Gorham, St Pierre et al. 2008; Cismasu, Michel et al. 2011). However, ferrimagnetic (FerriFh) is commonly formed under hydrothermal settings or tropical environments from aqueous media, and has received limited research in the context of its surface reactivity. The magnetic enhancement of many paleosols has prior been attributed to the presence of magnetite (Fe_3O_4) and hydromaghemite/maghemite (γ-Fe_2O_3) in Earth and Martian soils (Barrn and Torrent 2002; Barron, Torrent et al. 2003; Bertelsen, Goetz et al. 2004). The presence of extracellular magnetic bacteria has also been suggested to contribute to the magnetic properties of some magnetofossils showing signs of iron dissolution and corrosion (Fassbinder, Stanjekt et al. 1990). However, FerriFh has been laboratory synthesized and maintaining a ferromagnetic behavior at room temperature. Contrary to its precursor ferrihydrite which is not considered to contribute to large magnetic enhancement in soils, FerriFh nanoparticles may have contributed to ferromagnetic properties in aerobic soils (Bertelsen, Goetz et al. 2004; Cismasu, Michel et al. 2011). Although the structure of ferrihydrite is still a subject of debate; it has been conventionally described as either $Fe_5O_3(OH)_9$, $5Fe_2O_3.9H_2O$, and/or Fe(O)OH

stoichiometry that is recently proposed to be closer to the $Fe_{8.2}O_{8.5}(OH)_{7.4}+3H_2O$ structure (Schwertmann 1991; Zhang, Ellery et al. 2007; Parise, Harrington et al. 2010).

Michel et al., have confirmed that the ordered FerriFh magnetism differs significantly from that of the magnetite and maghemite ferrimagnets (Zhang, Ellery et al. 2007). According to their calculated results, the coercivity (antiferromagnetism) and high magnetism (ferrimagnetism) of the FerriFh structure at 5 K was found much higher (~52.5 mT) than previously measured values for the proposed maghemite/hydromaghemite structures (Zhang, Ellery et al. 2007). The formation of the intermediate FerriFh phase was found to be dependent on the temperature and the concentration of the ligands (Liu, Moran et al.). The average particles size diameter measured was ranged within 3-10 nm depending on the iron, inorganic and organic hybrid matrices concentration (Silva, Amaral et al. 2005; Geremias, Laus et al. 2008). An optimum citrate/Fe concentration ratio of 3% was found to favor the formation of the ordered ferrimagnetic phase at temperatures ~175 °C and within 8 hr aging (Zhang, Ellery et al. 2007). In addition, detailed structural information from thermogravimetric analysis experiment (TGA), which measured the total Fe and hydration loss, revealed a new structural composition for the disordered FerriFh similar to $Fe_{8.2}O_{8.5}(OH)_{7.4}+3H_2O$, with relatively distinct and identifiable diffraction lines compared to previously proposed ordered ferrihydrite ($Fe_{10}O_{14}(OH)_2$ + ~H_2O) stoichiometry (Jambor and Dutrizac 1998; Zhang, Ellery et al. 2007; Michel, Hosein et al. 2010). Furthermore, the intermediate magnetic Fe-oxyhydroxide phase has shown an increase in particle size (~4-12 nm) and fewer defects, more structural relaxation and electron spin ordering, and pronounced ferrimagnetism compared to its ferrihydrite precursor (Schwertmann, Friedl et al. 1999;

Zhang, Ellery et al. 2007; Cabello, Morales et al. 2009). Despite all the prior studies conducted on the properties of magnetite and ferromagnetic (oxy)hydroxide which are widely used in various industrial applications (Bachu, Bonijoly et al. 2007); however, there are not as many reactivity studies completed on the surface of the intermediate FerriFh product.

Ferrimagnetic iron oxyhydroxides may have the ability to remove toxic aerosol particulates and play a significant role in geological CO_2 storage. Environmental contaminants such as nitrous oxide, methane, chlorofluorocarbon (CFCs), sulfur dioxide, and carbon dioxide constitute the primary greenhouse gases in the atmosphere and can affect the climate of Earth in various ways. However, exploiting the reactivity of magnetic iron oxyhydroxide surfaces (e.g., ferrihydrite and FerriFh) have been of significant scientific interest for the adsorption of these gases. In a recent study, Murphy and Lammers et al., investigated the reactivity of different iron oxyhydroxide polymorphs of lepidocrocite (γ-FeOOH), goethite (α-FeOOH), akaganeite (β-FeOOH), and Fh for the CO_2 sequestration through mineral carbonation (e.g., siderite-$FeCO_3$ formation) in the presence of aqueous sulfide and supercritical CO_2 fluid (Murphy, Lammers et al. 2010). From these studies, siderite ($FeCO_3$) was the main mineral carbonation formed in the presence of supercritical CO_2 fluid. In a separate study, hydrotalcite doped with alumina (boehmite) or iron compounds have also been investigated for the adsorption of carbon dioxide, and it was found that at 20 °C the amount of adsorbed CO_2 was between 2.0 and 2.5 mmol/g with the hydrotalcite/alumina samples showing the largest capacity for CO_2 absorption (Aschenbrenner, McGuire et al. 2011). In a recent study, Al/Fe oxyhydroxide nanoparticles have shown to exhibit an increasing reactivity toward CO_2 adsorption as Al

is incorporated into ferrihydrite up to 30 mol% Al (Pierre-Louis, Hausner et al. 2013). Results from these studies also highlighted the benefits of iron oxides and oxyhydroxides having large surface areas and high reactive sites toward achieving mass scale sequestration of CO_2 (Ismail, Cadenhead et al. 1997; Baltrusaitis, Schuttlefield et al. 2007; Hausner, Bhandari et al. 2009). The effective large surface area of these materials is likely to be a crucial factor for enhancing the chemical reaction at the iron oxyhydroxide mineral interfaces. While the subsequent formation of carboxylate, carbonate, and bicarbonate on the iron oxyhydroxide mineral surfaces have been thoroughly investigated under low $CO_{2(gas)}$ pressure environments (Houghton 1996; Izgec, Demiral et al. 2008; Hausner, Bhandari et al. 2009; Baltrusaitis, Schuttlefield et al. 2011); limited studies have been carried out under relatively high pressure and dry conditions.

In this chapter we present results from an investigation of the compositional and structural changes of ferrihydrite to FerriFh. Then, we used infra-red spectroscopy to probe the adsorption of CO_2 on FerriFh and compared the adsorption to CO_2 on ferrihydrite. Our ATR-FTIR results suggested that the presence of residual sorbed citrate blocked the adsorption of CO_2 on FerriFh. FTIR spectra revealed that only after the removal of citrate did adsorbed carbonate and bicarbonate form on FerriFh surface under dry and low pressure conditions ($\leq$ 3.5 bar). Adsorbed bicarbonate was weakly bound and disappeared with increasing pressure ($\geq$ 3.5 bar) up to 58.6 bar. The disappearance of this species could be due to an increase in co-adsorbed CO_2 vapor (~57.2 bar; due to an increase in relative humidity) preventing the reaction of CO_2 with surface hydroxyl (OH)

group on the iron oxyhydroxide surfaces. Studies also showed that a bent-CO_2 species appeared at pressures below 100 psi on FerriFh and Fh.

4.2 Experimental Methods

4.2.1 Materials Synthesis

We synthesized "2-line"ferrihydrite using a modified method adapted from Cornell and Schwertmann (Schwertmann 1991; Hausner, Bhandari et al. 2009; Murphy, Lammers et al. 2010). The synthesis details for the intermediate ferrimagnetic (FerriFh) phase can be found in prior publications. In short, we followed Michel et al. synthesis method (Zhang, Ellery et al. 2007). Ferrimagnetic ferrihydrite was synthesized using 0.1 M of anhydrous ferric chloride ($FeCl_3$) dissolved in deionized (DI) water (18 MΩ) followed by the addition of 3% molar ratio sodium citrate ($N_3C_6H_5O_7.2H_2O$) with respect to iron. A 1.0 M sodium hydroxide (NaOH) solution was used to maintain the pH at ~7.5 for 30 min. Then, the suspension was placed into a Teflon liner (100 mL) tightly capped inside a temperature controller Parr reactor cell fixed at 175 ˚C for 8 hr. After 8 hr aging, the aqueous suspension resulted in the formation of a red-brown intermediate ferrimagnetic ferrihydrite (FerriFh) precipitates. However, a separate ferrihydrite suspension that was placed in the Parr reactor cell, under similar hydrothermal conditions in the absence of organic citrate ligand, resulted in iron oxide nanoparticles (e.g., hematite) with a reddish color. All synthesized samples were subsequently washed in dialysis bags with deionized water to remove the counter ions (Cl^-, OH^-, and Na^+). Once the electric conductivity of the equilibrium solution was less than 0.01 dSm^{-1}; the suspended particles were centrifuged, air dried, and stored as a solid in polyethylene

bottles. The air dried samples were crushed in a ceramic mortar with a pestle to produce iron nano-powders and then characterized using BET, XRD, TEM, and FTIR within few days of preparation.

4.2.2 Characterization of Samples

XRD characterization of the ferrimagnetic ferrihydrite product in the presence and after the removal of citrate was collected and compared to its precursor ferrihydrite phase. Iron oxyhydroxide nanoparticles in powder form were packed into small 0.7 mm capillary XRD sample holder glass tubes. All XRD analyses were performed using an Apex Duo:Bruker Instrument Service equipped with a CCD diffraction system. Samples were scanned at the wavelength $\lambda = 0.71073$Å using the molybdenum (Mo) Kα X-ray source at nearly constant irradiation volume in the 2θ range of 5-50 degrees, and a step size of 0.02° for 0.40 seconds per step. Copper (Cu Kα) source radiation was not used to avoid interference from the Fe fluorescence which would have caused the attenuation of the X-ray diffraction patterns of the iron oxyhydroxide particle.

Transmission electron microscopy (TEM) images were obtained using a JEOL JEM-1400 instrument, equipped with a Gatan DualVision digital charge-coupled device (CCD) camera and high brightness LaB_6 electron source. The field emission gun in Schottky mode as an electron source was used at 120 kV to operate the TEM instrument. Samples were prepared for TEM analysis by first sonicating (~0.1 mg) suspension of finely Fe oxyhydroxide nanoparticles in DI water (1 ml) for approximately 10 minutes. Then, a drop of the ultrasonically dispersed particles was placed onto an amorphous holey-carbon film supported by a copper-mesh TEM grid. All samples were left to dry on the

supported grid in air at room temperature (~30 min) and then under low vacuum (15 min) chamber to remove sorbed impurities. FerriFh samples (~0.5 mg) were then placed on microscope slides and irradiated with UV light (~2 mW/cm^2) from a medium-mercury (Hg) pressure vapor lamp (Quartz) under low oxygen environment that generated ozone which was equipped with a temperature controlled (PSD-UVT) from NOVASCAN. The UV/O_3 system was used to clean residual citrate sorbed on the FerriFh surface as a function of various temperature and times of exposure (see Fig. 4.4). The UV light was emitted at two wavelengths (λ) around 185 nm and 254 nm which photochemically produced ozone and radicals. The 185 nm is absorbed by oxygen and many organic molecules to produce O_3 byproducts while the 254 nm is not absorbed by O_2 and does not lead to O_3 generation. However, the 254 nm radiation is absorbed by most organic molecules and contributed to O_3 destruction under the UV chamber system. This process is substantially important to remove physisorbed citrate which would otherwise hinder the adsorption of $CO_{2(gas)}$ on the FerriFh vacancy sites.

A Thermo Nicolet Magna-IR 560 spectrometer, equipped with a smart orbit attenuated total reflectance Fourier transform infra-red (ATR-FTIR) accessory and a liquid nitrogen-cooled mercury cadmium telluride (MCTA) detector, was used to probe the vibrational spectra of the interaction of the adsorbate onto the iron oxyhydroxide minerals. ATR-FTIR spectroscopy was employed to investigate the adsorption of citrate bound species on FerriFh and Ferrihydrite nanoparticles. After UV/O_3 removal of residual citrate sorbed on the FerriFh surfaces, FTIR vibrational spectroscopy was used to obtain vibrational carbonate and bicarbonate modes on the FerriFh nanoparticles upon the adsorption of gaseous CO_2. High pressure stainless steel vacuum from High Pressure

equipment (HiP) combined with the ATR-FTIR accessory were used for the reaction studies of CO_2 at elevated pressure. Approximately 1 mg of Ferrihydrite or FerriFh oxyhydroxide nanoparticles was suspended into 1 ml conical vial and sonicated for 10 min. Then, ~0.1 ml droplet of the suspension (ferrihydrite or FerriFh) was placed on the diamond ATR element to form thin-films, and dried under Ar or N_2 stream that was enclosed in a home-built gas cell attached on the ATR diamond element. Upon drying, CO_2 stream was flowed on the thin-film using a high pressure gauge monitored from 0.35 to 58.6 bar. In a separate control experiment, aqueous citrate (~10 mM) adsorbed on clean Ferrihydrite nanoparticles was then exposed to CO_{2gas} to study the competitive effect of citrate and carbonate species under similar pressure conditions as to compare to citrate bound FerriFh surfaces. Supernatant from the sorbed citrate/Ferrihydrite mineral slurry was decanted and washed with three aliquots of deionized water before collected the FTIR spectra of adsorbed citrate on the ferrihydrite particles. A total of 500 co-added scans at a resolution of 4 cm^{-1} were collected between 4000-400 cm^{-1}. The vibrational spectra were reprocessed using the diamond (background) as the reference with an automated ATR correction to obtain the final spectra of the adsorbed species. Gaseous CO_2 phase adsorption spectra were also subtracted from all the reported adsorbed spectra under the same pressure condition. CO_2 (100% Vol.), high purity argon, and nitrogen gas tanks were purchased from Air Gas. FTIR spectra analysis and processing were completed with the Omnic 7.3 software.

4.3 Results and Discussion

4.3.1 Composition of ferrihydrite and FerriFh

Identification of mineral phases was obtained using X-ray powder diffraction (XRD), Figure 4.1. XRD patterns of ferrihydrite are shown in Figure 4.1a. The two main broad Bragg reflection lines with d-spacing values are found at ~0.25 nm and ~0.15 nm corresponding to the disordered crystalline "2 line" ferrihydrite. The broadening of the XRD patterns are characteristic of crystalline amorphous nanoparticles and are similar to those previously reported in the literature (Schwertmann, Friedl et al. 1999; Zhang, Ellery et al. 2007; Parise, Harrington et al. 2010; Strongin, Grey et al. 2010). Ferrihydrite XRD patterns were confirmed by comparing to its XRD patterns found in the Joint Committee on Powder Diffraction Standards (JCPDS) database.

XRD patterns of FerriFh after aging (8 hr/175 ^{0}C) in the presence of 3% molar ratio of citrate/Fe are shown in Figure 4.1b. The FerriFh XRD patterns (Fig. 4.1b) are exemplified by the sharpening of the two Bragg diffraction peaks (0.25 nm and 0.15 nm) and with d-spacing values at ~0.641, 0.373, 0.328, 0.169, 0.131, and 0.105 nm. The FerriFh XRD diffractograms are different than those associated with the pristine ferrihydrite showing additional ordered crystalline reflection lines as indicated by the development of a new structural phase. FerriFh particles that were exposed to UV-O_3 cleaning for the removal of surface bound citrate displayed similar XRD patterns (not shown) compared to the as-prepared sample which indicated that the FerriFh did not undergo further structural changes under the UV treatment. However, the XRD patterns of the FerriFh product differ significantly not only from its precursor ferrihydrite, but also

from the hematite crystal structure as illustrated in Figure 4.1c. (Zhao, Huggins et al. 1994; Janney, Cowley et al. 2000; Zhang, Ellery et al. 2007; Barron, Torrent et al. 2012).

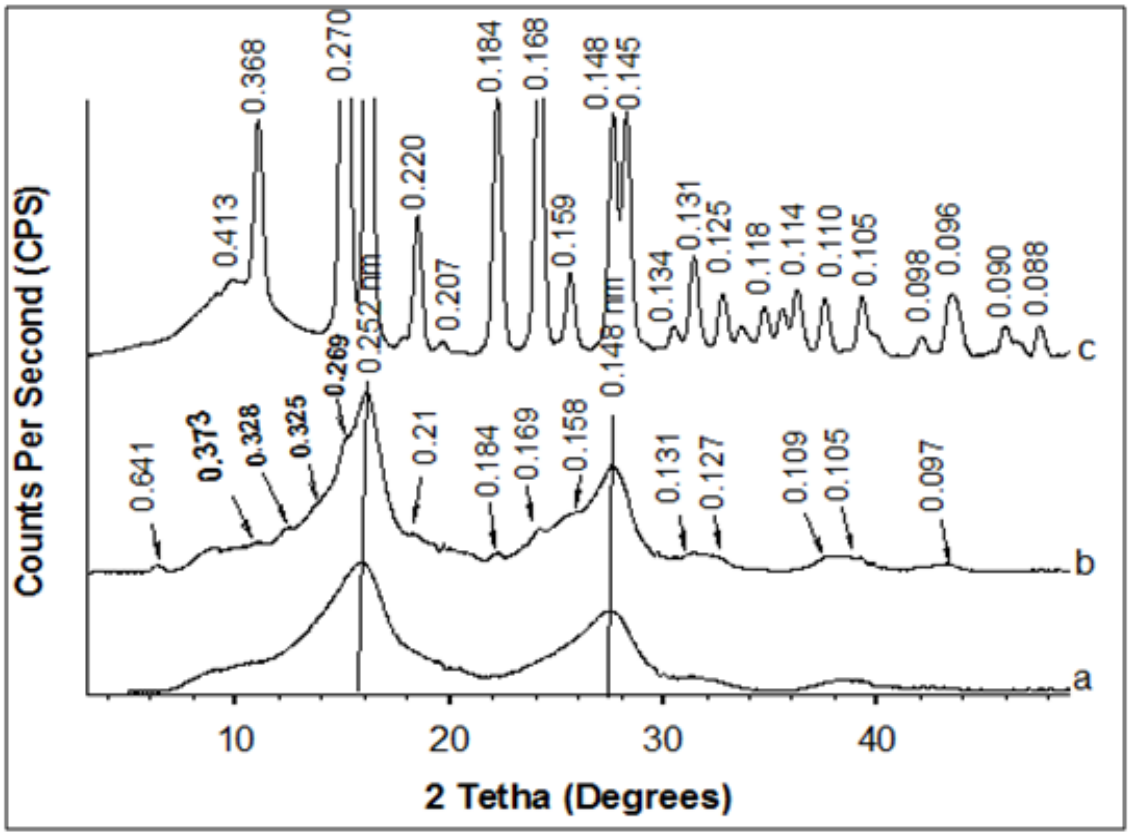

Figure 4.1. XRD patterns of (a) "2-Line" Ferrihydrite, (b) FerriFh, (c) hematite synthesized nanoparticles. Additional XRD reflection lines development are shown (arrows) for the ordered FerriFh crystalline phase compared to its Ferrihydrite amorphous precursor and hematite crystal structure.

Diffractograms (Fig. 4.1c) of crystalline hematite phase display strong sharp reflection lines (with d-spacing values at ~0.368, 0.270, 0.220, 0.148, 0.168, 0.148, and 0.145 nm) that differ from those shown in the intermediate FerriFh phase. The hematite XRD reflection lines are similar to those previously reported (Jambor and Dutrizac 1998; Vu, Shaw et al. 2008).

A ferrihydrite suspension placed under hydrothermal conditions in the absence of organic citrate has been shown to favor a phase transformation to hematite than goethite at around neutral pH. Our results are consistent with these prior studies (Cudennec and Lecerf 2006). Transformation to goethite crystal phases is expected to occur under alkaline (pH 9-12) conditions (Violante, Barberis et al. 2003; Cudennec and Lecerf 2006). Riley et al., have also found that in the absence of aqueous sulfide and supercritical CO_2 ferrihydrite directly transformed to hematite at temperature around 100 °C (Murphy, Lammers et al. 2010). Other studies have also investigated the influence of organic acid (e.g., citric, meso-tartaric, L-tartaric, lactic, maleic, and oxalic) on the crystallization and transformation of ferrihydrite to more stable hematite and goethite iron oxyhydroxide forms (Cornell and Schwertmann, 1979). Organic acids differ in their size, shape, molecular structure, and in the number of carboxyl and hydroxyl groups. They are available for bonding on the Fe oxyhydroxide surface and in our case retard the transformation rate of ferrihydrite to hematite and goethite structures (Torrent and BarrÃ³n 2000; R. M. Cornell 2003; Torrent, Liu et al. 2007). In short, XRD patterns obtained for the hematite product show similar sharp and intense Bragg reflection lines previously reported on in the literature (Campbell 1999; Barron, Torrent et al. 2003).

Figure 4.2 displays scanning transmission electron microscopy (STEM) images of ferrihydrite and FerriFh. TEM imaging of ferrihydrite (Figure 4.2a) shows ~2 nm diameter particles, characteristic of amorphous "2-line" ferrihydrite. The insert, which shows selected area electron diffraction (SAED) patterns, illustrates two diffuse rings indicating a poorly crystalline disordered ferrihydrite nanophase (Fig. 4.2a). FerriFh images show an increase in particle size between 5-10 nm which could be due to nucleation/agglomeration of smaller sized particles (Michel et al., 2010). The SAED patterns for the ordered FerriFh display polycrystalline showed diffraction spots in addition to two amorphous rings commonly found in ferrihydrite..

In Table 4.1, FerriFh d-spacing calibrated values are reported from the TEM/SAED experiments along with values for hematite. The formation of nanophase FerriFh showed a higher degree of crystallinity. FerriFh also exhibited a decrease in SSA (~161 ± 3 m^2/g) from the BET measurements relative to ferrihydrite (~332 ± 2 m^2/g), which correlated well with the observed value from the literature (~156 m^2/g) (Zhang, Ellery et al. 2007). TEM imaging of FerriFh containing adsorbed citrate and after treatment with UV/O_3 was similar to that of untreated FerriFh.

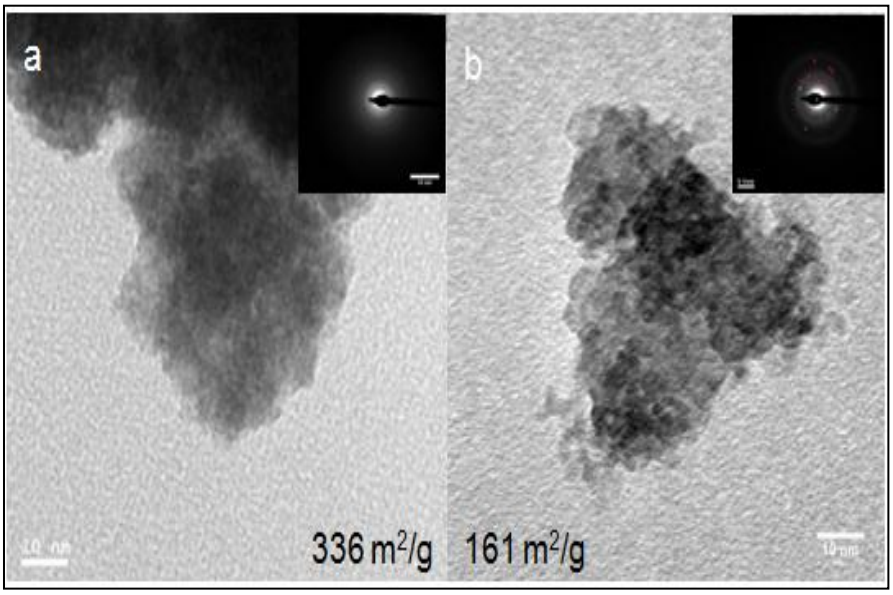

Figure 4.2. TEM/SEAD micrographs of (a) "2-line" ferrihydrite nanoparticle (~2 nm) compared to (b) FerriFh. FerriFh nanoparticles showed an increase in agglomerated particles between 4-11 nm sizes. Inserts to the TEM micrographs display SAED data for the ordered FerriFh crystalline phase shown small diffraction spots compared to its amorphous (two rings) ferrihydrite counterpart.

Table 4.1. Ferrimagnetic ferrihydrite (FerriFh) d-spacing values obtained from TEM/SAED compared to XRD results and hematite XRD crystalline phase.

Ferrifh		Hematite
TEM-SAED	XRD	XRD
(nm)	(nm)	(nm)
0.22	0.64	0.37
0.18	0.25	0.27
0.13	0.18; 0.17; 0.16	0.25
0.11	0.15; 0.13, 0.11	0.22
0.096	0.097	0.18; 0.088

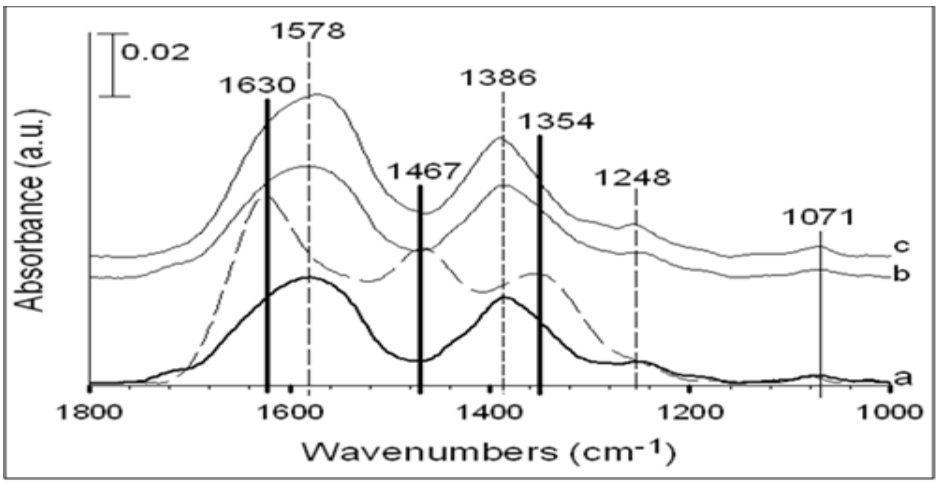

Figure 4.3. ATR-FTIR spectra are shown for the synthesized (a) FerriFh and ferrihydrite (dashed-lines) nanoparticles dried under N_2 stream. Spectrum (b) is collected for FerriFh particle exposed to ~0.1 bar gaseous CO_2, and spectrum (c) when pressurized to ~3.5 bar $CO_{2(gas)}$ under dry conditions.

Prior studies suggested that the conversion of ferrihydrite to FerriFh in the presence of citrate is due to a dissolution-crystallization reaction which may be initiated by the dissolution of Fe oxyhydroxide particles. The nucleation/precipitation to medium size crystalline FerriFh could be formed on the surface (Barron, Torrent et al. 2003; R. M. Cornell 2003; Cao, Wu et al. 2008). Accordingly, this indicates that a 3% molar ratio of citrate relative to Fe is presumably high enough to inhibit rapid nucleation to hematite crystals and plays a significant role in inhibiting the conversion of ferrihydrite to more stable iron oxide phases (e.g., goethite or/and hematite) under hydrothermal conditions. This assertion is supported by our TEM and XRD results.

4.3.2 ATR-FTIR of CO_2 Adsorption on Ferrimagnetic Ferrihydrite with Citrate

Figure 4.3 exhbits vibrational spectra for "2-line" ferrihydrite (dashed-line) and FerriFh (thick-line) that were dried under a N_2 flow. The "2-line" ferrihydrite (dashed-line) data shows a band at ~1630 cm^{-1} which is attributed to the $\delta_{(OH)}$ bending structural water mode, and the 1465 cm^{-1} and 1345 cm^{-1} modes are associated with the asymmetrical ($\nu_{2(O\text{-}C\text{-}O),\ Asym}$) and symmetrical ($\nu_{3(O\text{-}C\text{-}O),\ Sym}$) vibrational modes of adsorbed carbonate, respectively. These carbonate modes are often observed due to dissolved aqueous carbonate adsorption that adsorbs on the Fh during preparation. The FerriFh (thick-line) spectra, contrary to ferrihydrite, showed two strong broad modes at 1578 ($\nu_{2(O\text{-}C\text{-}O),\ Asym}$) and 1386 ($\nu_{3(O\text{-}C\text{-}O),\ Sym}$) cm^{-1} with a shoulder at 1248 ($\nu_{(O\text{-}C\text{-}O\text{-}H),\ Skel}$) cm^{-1} which are assigned to adsorbed citrate vibrations on the surface. An additional small shoulder is observed at ~1730 cm^{-1}, due to carboxylate (CO-O) and/or carbonyl (CO-H) modes. The mode at 1071 cm^{-1} in the lower region appeared on both Fh ferrihydrite and

FerriFh, and is assigned to the carbonate $\delta_{(C-O)}$ bending mode. Spectrum 3b and 3c exhibit vibrational modes for FerriFh, which has adsorbed citrate, that was exposed to ~0.1 and ~3.5 bar of gaseous CO_2, respectively. These spectra do not show the presence of carbonate/bicarbonate modes, due to adsorbed citrate species blocking FerriFh surface sites.

4.3.3 $CO_{2(gas)}$ Adsorption onto FerriFh Surfaces after Citrate Removal

Figure 4.4 illustrates the vibrational spectra for FerriFh that was treated with UV/O_3 to remove adsorbed citrate. A reference spectrum for ferrihydrite (dashed-line spectra) is also shown (Figure 4.4a). Spectra for FerriFh (thick-lines) are shown that were treated with UV/O_3 at 100 ºC (Fig 4.4b), 80 (Fig. 4.4c), and 40 ºC (Fig. 4.4d) for ~4 hr. Upon removal of residual citrate species with the UV/O_3 treatment, adsorbed carbonate modes appeared at 1467 and 1354 cm^{-1}.

The IR data shown in Figure 4.4b exhibited vibrational modes for adsorbed carbonate at ~1480 ($\nu_{2(O-C-O),\ Asym}$) and 1356 ($\nu_{3(O-C-O),\ Sym}$) cm^{-1}, but an intensity loss in the water peak around 1630 cm^{-1} δ(O-H) bending mode was also observed. The decrease in the intensity of the peak at 1630 cm^{-1} could be an indication of structural adsorbed water (H_2O) loss from FerriFh due to the elevated temperature associated with the pretreatment. According to Michel et al., the removal of loosely bound or surface-adsorbed water (< 125 °C) and the dehydroxylation of more strongly bound structural water (>125 °C) were observed for Ferrihydrite by TGA. Their results also reported, after 8 hr of hydrothermal aging, water losses of ~2% and ~8% were observed when ferrihydrite was heated to 125 °C and 1000 °C, respectively (Zhang, Ellery et al. 2007).

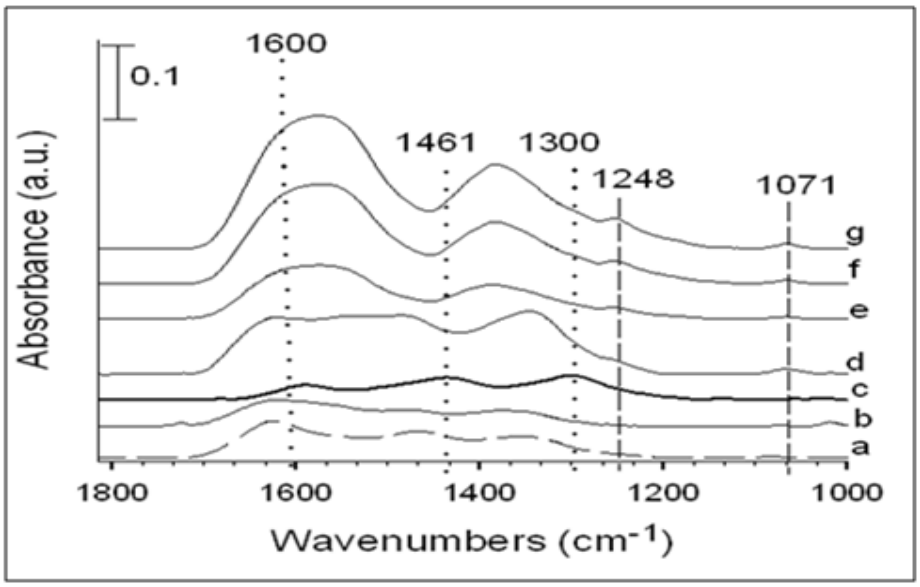

Figure 4.4. ATR-FTIR spectra (a) ferrihydrite (dashed-lines) compared to FerriFh surface after exposure to UV/O_3 treatment at temperatures of 100 ºC (Fig 4,4b), 80 (Fig. 4.4c), and 40 ºC (Fig. 4.4d) for ~4 hr. The vibrational spectra show shifts upon desorption of citrate bound species and conversion to adsorbed carbonate modes formation at ~1461 and ~1354 cm^{-1} on the FerriFh surface. However, the FerriFh material treated under UV/O_3 cleaning at 100 ºC for 1 hr (Fig. 4.4e) and at 80 ºC from 1 hr (Fig. 4.4g) to 2 hr (Fig. 4.4f) did not show any significant removal of citrate modes.

Other studies have also investigated the transformation of ferrihydrite to hematite using both thermogravimetric (TG) and differential scanning calorimetric (DSC) analysis, and their findings showed no disruption of the ferrihydrite structure at temperatures below 300 ºC which corresponds to a H_2O-weight loss of 25.6% (Xu, Hausner et al. 2011). These results suggest that the increased temperature used in the UV/O_3 cleaning process probably did not cause any further structural or phase transformation of FerriFh to other stable iron oxyhydroxide phases. UV/O_3 treatment, the 254 nm line used is the primary wavelength of the lamp, and it has been shown that hot electrons generated by the UV excitation of metal surfaces are responsible for the direct desorption of hydrocarbon or O_2^- creation (Ye, Wynn et al. 2001). Spectrum 4.4c shows the removal of physisorbed citrate modes from FerriFh. Adsorbed carbonate modes appeared in place of the citrate modes at ~1600 ($\delta_{(O\text{-}H)}$), 1461 ($\nu_{2(O\text{-}C\text{-}O),\ Asym}$), and 1300 ($\nu_{3(O\text{-}C\text{-}O),\ Sym}$) cm^{-1}. IR spectra shown in Figure 4.4d illustrate the carbonate symmetrical mode at 1354 cm^{-1}, but citrate-modes appeared in the same region as the carbonate modes (1520/1467 cm^{-1}). Hence, citrate was not completely removed from the FerriFh.

The decomposition of physisorbed citrate was found to be optimum in the 60-100 ºC temperature range (~5 hrs exposure to UV-O_3). IR data for FerriFh treated at this temperature showed carbonate modes ($\nu_{2(O\text{-}C\text{-}O),Asym}$ (~1473 cm^{-1}) and $\nu_{3(O\text{-}C\text{-}O),Sym}$ (~1348 cm^{-1})) (Fig. 4.4b-c). The energy positions of the IR modes for adsorbed carbonate on clean FerriFh were at similar peak positions to carbonate on ferrihydrite. The results also suggested that sorbed citrate bound on either FerriFh or ferrihydrite blocked the adsorption of $CO_{2(gas)}$. In addition, FerriFh material treated with UV/O_3 cleaning at 100 ºC for 1 hour (Fig. 4.4e) and 80 ºC for 1 hr (Fig. 4.4g) or 2 hr (Fig. 4.4f) did not show the

removal of adsorbed citrate species, indicated by the strong peak intensity at ~1587, 1386, and 1248 cm^{-1}.

Figure 4.5 shows the ATR-FTIR spectra recorded after clean ferrihydrite (thick-line) surfaces were exposed to 10 mM aqueous citrate solution, rinsed with deionized water, dried under argon, followed by $CO_{2(gas)}$ exposure. In addition, the overlay top spectra were obtained as a function of increasing pressure from 6.9, 20.7, 41.4, and 58.6 bar, respectively. These infrared spectra were collected as control experiments for the competitive adsorption of citrate and carbonates on the mineral surfaces under high pressure CO_2 exposure. The broad band at ~3232 cm^{-1} is due to stretching vibrational ($\delta_{(O-H)}$) modes of water on the ferrihydrite.

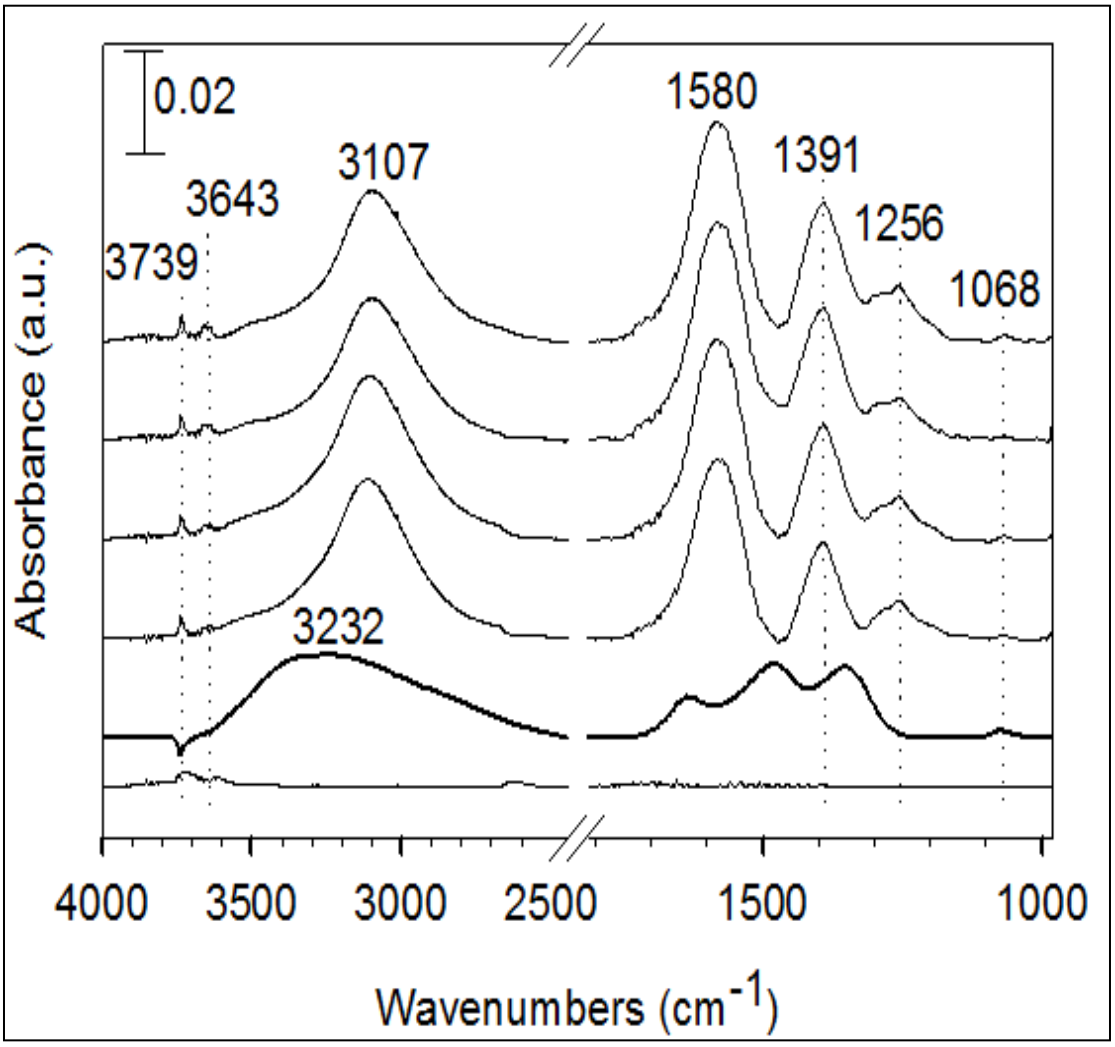

Figure 4.5. ART-FTIR of clean ferrihydrite (thick-line) and then exposed to 30 mM citrate dried under argon stream. The remaining (bottom-to-top) spectra were recorded as a function of increasing pressure of $CO_{2(gas)}$ at 6.9, 20.7, 41.4, and 58.6 bars. The thin-line (bottom) spectrum is of gaseous CO_2 adsorption (58.6 bars) subtracted from the adsorbate/mineral spectra.

Ferrihydrite spectra in the absence of citrate are shown in Figure 4.6. Ferrihydrite spectra exposed to $CO_{2(gas)}$ were also collected as a function of increasing pressure from 0.4, 0.7, 3.5, 6.9, 20.7, 41.4, and 58.6 bars, respectively, from bottom to top. Exposure of ferrihydrite to $CO_{2(gas)}$ at 0.1 to 3.5 bar, results in the appearance of modes at ~1619 ($\nu_{2(O-C-O),\ Asym}$), 1410 ($\nu_{3(O-C-O),\ Sym}$), and at 1220 cm^{-1} ($\delta_{4(CO-H)}$) that are assigned to monodentate adsorbed bicarbonate. Additional modes at around ~1556, 1532, 1327 cm^{-1} are shown on ferrihydrite, and the 1075 cm^{-1} peak shifts to a lower frequency at ~1035 cm^{-1} which is associated with the bidentate form of carbonate, which form at $CO_{2(gas)}$ pressures above 3.5 bars.

In addition to the growth of bicarbonate modes in the lower frequency regions, $\nu_{(OH)}$ stretching bands appear at ~3730, 3700, and 3596 cm^{-1} when adsorbed bicarbonate species form on FerriFh at $CO_{2(gas)}$ pressures $\geq$ 3.5 bars. These modes increase with increasing CO_2 pressure. The band at ~3331 cm^{-1} is assigned to structural hydroxyl (OH) groups hydrogen-bonded with CO_2 on the Fe oxyhydroxide. As the pressure increased from 6.9 to 58.6 bars, an increase in the IR peak intensities at ~1619, 1410, and 1327 cm^{-1} occurred, but the adsorbed bicarbonate mode (~1220 cm^{-1}) that was previously observed ($\leq$ 3.5 bars) became attenuated. However, bidentate adsorbed carbonate modes were shown to coexist with monodentate adsorbed bicarbonate contributions on ferrihydrite and Al-doped Fe-oxyhydroxide (Baltrusaitis, Schuttlefield et al. 2007; Hausner, Bhandari et al. 2009; Baltrusaitis, Schuttlefield et al. 2011; Pierre-Louis, Hausner et al. 2013). The thin-line spectra (Fig. 4.6) were obtained as the CO_2 pressure over the iron oxyhydroxide was step-wise decreased. The weakly bound bicarbonate 1220 cm^{-1} mode reappeared as the pressure was decreased to the 3.5-0.35 bars range.

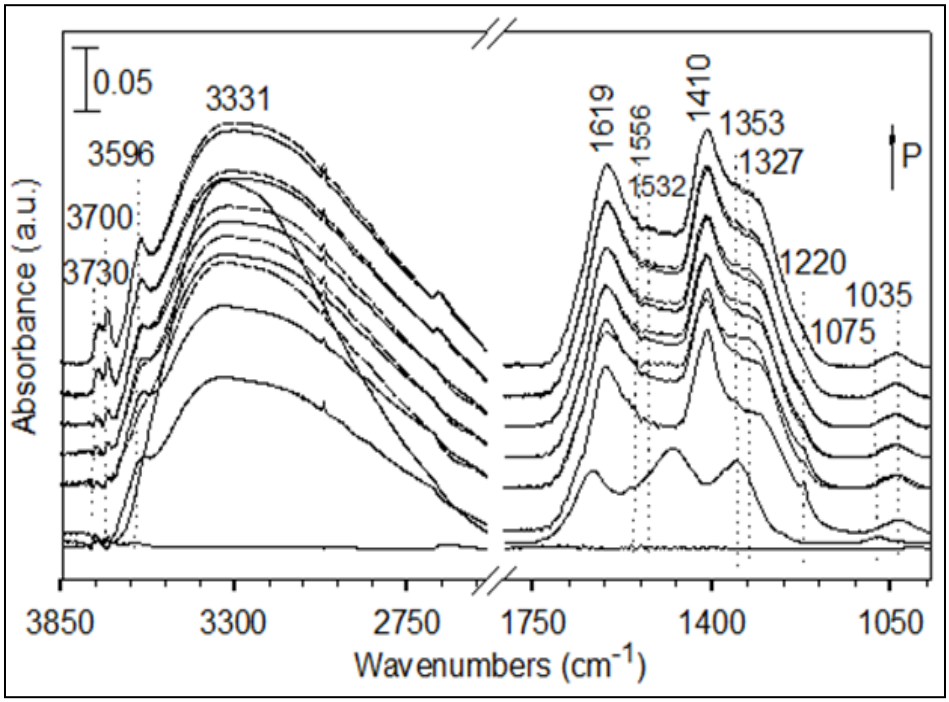

Figure 4.6. ATR-FTIR of CO_2 adsorption on ferrihydrite nanoparticle at increasing pressure of 0.4, 0.7, 3.5, 6.9, 20.7, 41.4, and 58.6 bars, respectively. The thin-line (bottom) spectra are shown reversibly at decreasing identical pressure. CO_2 gas-phase adsorption are subtracted from the adsorbed spectra (bottom spectrum). The results show the disappearance of the weakly bound CO_2 bent bicarbonate like species at 1220 cm^{-1} ($\delta_{4(COH)}$) mode on the mineral surface at increasing pressure (> 3.5 bars).

ATR-FTIR spectra shown in Figure 4.7 are associated with citrate-free FerriFh that was exposed to CO_2 pressures ranging from 0.4 to 58.6 bars. The bottom spectra exhibits modes due to adsorbed carbonate at ~1492 cm^{-1} ($\nu_{2(O\text{-}C\text{-}O),\ Asym}$) and ~1350 ($\nu_{3(O\text{-}C\text{-}O),\ Sym}$) cm^{-1}. Note that these carbonate modes are only associated with FerriFh when citrate bound species were removed with the UV/O_3 treatment. The vibrational modes shown at ~3737, 3701, and 3609 cm^{-1} are assigned to $\nu_{(OH)}$ when adsorbed bicarbonate species form on FerriFh in the presence of $CO_{2(gas)}$ (they become most intense at pressures near 3.5 bars). The band at ~3350 cm^{-1} is assigned to hydrogen bonding of CO_2 with hydroxyl (OH) groups from structural water on the Fe oxyhydroxide surface. The results correlate well with prior studies that have shown the loss of hydroxyl (OH) groups due to the reaction of these groups with CO_2 and the resulting formation of monodentate adsorbed bicarbonate products (Hausner, Bhandari et al. 2009),(Baltrusaitis and Grassian 2010; Baltrusaitis, Schuttlefield et al. 2011). A further inspection of the data shows similar mode positions at ~1612, 1408, 1221 cm^{-1} as the $CO_{2(gas)}$ pressure increased and suggested that monodentate adsorbed bicarbonate species on FerriFh adopt identical binding configurations as those observed on ferrihydrite. These adsorbed bicarbonate modes were not significantly affected at low pressures ($\leq$ 3.5 bars). However, the disappearance of the vibrational mode at ~1221 cm^{-1} occurred between successive collected spectra at increasing pressures up to 58.6 bars, and the trend is similar to what was observed in the ferrihydrite circumstance.

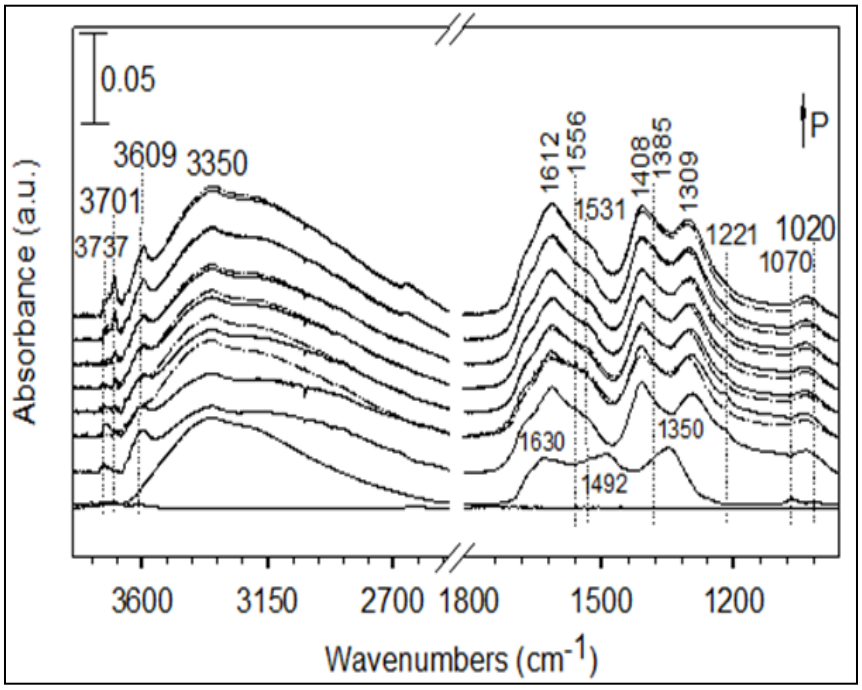

Figure 4.7. ATR-FTIR of CO_2 adsorption on citrate-free FerriFh particles at reversible pressure of 0.4, 0.7, 3.5, 6.9, 20.7, 41.4, and 58.6 bars, respectively. The dashed-thin-line (bottom) spectra are collected reversibly at identical decreasing pressure. Gas-phase CO_2 adsorption are subtracted from the adsorbed spectra (bottom spectrum).

The subsequent decrease and disappearance in the 1221 cm^{-1} mode associated with the CO_2 bent-like species occurred concomitantly with an increase in mode intensity at ~1612 and 1410 cm^{-1}. The additional shoulders shown at ~1531 and 1309 cm^{-1} are assigned to remaining adsorbed carbonate species on the surface.

We note that adsorbed bicarbonate species usually co-exist with strong inner-sphere adsorbed carbonate complexes on iron oxyhydroxide surfaces in CO_2 environments. The results further indicated that the binding geometry of carbonate and bicarbonate species on ferrihydrite and citrate-free FerriFh are quite similar, but could be significantly affected and/or hindered by the adsorption of other oxyanion species such as citrate. These findings are of significant interest due to the structural and compositional changes that can occur as ferrihydrite transforms to FerriFh under hydrothermal conditions. The reactivity of FerriFh toward CO_2 exhibited high affinity for adsorbed carbonates, bicarbonate, and carboxylate formation depending on the relative humidity, adsorbed anions (e.g., citrate) present, and various pressure conditions. Similarly, the type of functional (OH/OH_2^+) groups involved in proton donating interactions are important for the formation of specific or multiple adsorbed carbonate and bicarbonate complexes at the surfaces studied here.

Figure 4.8a displays ATR-FTIR spectra for FerriFh (thin-line) and ferrihydrite (thick-line) after the 30 min evacuation of a CO_2 stream that was flowing over the surfaces in the pressurized cell. ATR spectra of Figure 4.8b were collected after complete removal of $CO_{2(gas)}$ and kept under Ar atmosphere.

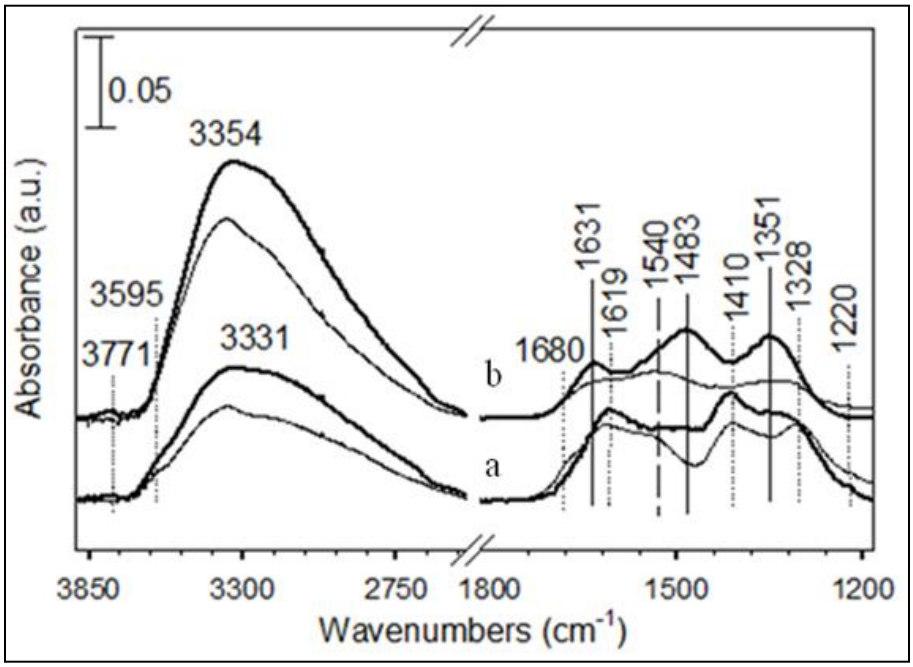

Figure 4.8. ATR-FTIR spectra overlay of CO_2 adsorption on (a) citrate-free FerriFh (thin-line) compared to ferrihydrite (thick-line) surfaces collected after 30 min evacuation of the $CO_{2(gas)}$ cell. Spectra (b) are collected under Ar stream. IR spectra of CO_2 gas-phase are subtracted from the adsorbed spectra.

After the 30 min evacuation under low $CO_{2(gas)}$ (< 0.35 bar) environment, it can be seen that spectra 8a exhibits modes associated with adsorbed bicarbonate (~3595, 1619, 140, and 1220 cm^{-1}) on both FerriFh and ferrihydrite. Further inspection of spectra 4.8b shows vibrational modes at ~1483/1351 ($\nu_{2(O\text{-}C\text{-}O),\ Asym}$/ $\nu_{3(O\text{-}C\text{-}O),\ Sym}$) cm^{-1} on ferrihydrite, but these modes appear at ~1540/1328 cm^{-1} for FerriFh. These modes are mainly associated with bidentate inner-sphere adsorbed carbonate.

Table 4.3 reports the vibrational modes of adsorbed carbonate and bicarbonate in the presence and absence of adsorbed citrate upon exposure to $CO_{2(gas)}$ flow. Prior studies have assigned these modes to binuclear bidentate complexes of solvated carbonate on iron oxyhydroxide due to the presence of co-adsorbed water (i.e., under hydrated condition). Our ATR-FTIR results agree well with the prior studies that have investigated carbon dioxide adsorption on various iron oxides and oxyhydroxides (Baltrusaitis and Grassian 2005; Bargar, Kubicki et al. 2005; Baltrusaitis, Schuttlefield et al. 2011).

Table 4.2. ATR-FTIR of adsorbed carbonate and bicarbonate mode assignments on ferrihydrite and ferrimagnetic nanoparticles in the presence and absence of citrate.

Vibrational mode assignments	Ferrihydrite (Fh) Without citrate (cm^{-1})	Ferrihydrite (Fh) With Citrate (cm^{-1})
$\nu_2(C\text{-}O)_{Asym}$	1467 (Outer-S)* / 1473 (Inner-S)*	1580
$\nu_3(C\text{-}O)_{Sym}$	1354 (Outer-S) / 1345 (Inner-S)	1391, 1256
$\delta(C\text{-}O)_{Tot.\ bending}$	1075	1068
	Ferrimagnetic Fh (ferrifh)	Ferrimagnetic Fh (ferrifh)
$\nu(C{=}O)_{Asym}$	1667 (Outer-S) / 1680 (Inner-S)	1730
$\nu_2(C\text{-}O)_{Asym}$	1492 (Outer-S) / 1540 (Inner-S)	1578
$\nu_3(C\text{-}O)_{Sym}$	1350 (Outer-S) / 1328 (Inner-S)	1386, 1248
$\delta(C\text{-}O)_{Tot.\ bending}$	1071	1070
Vibrational Frequencies of $CO_{2(gas)}$ at increasing pressure conditions (5-850 psi) without citrate		
	Fh	Ferrifh
$\nu_1(OH)$	3596	3690
$\nu_2(C\text{-}O)_{Asym}$	1619	1612
$\nu_3(C\text{-}O)_{Sym}$	1410/1327	1408/1309
$\delta(HCO_3^-)$, Bent CO_2	1220 (≤ 50 psi)	1221 (≤ 50 psi)
$\delta(C\text{-}O)_{Tot.\ bending}$	1035	1020

*Outer-Sphere and Inner-Sphere

This work further on providing a fundamental understanding on the interactions of $CO_{2(gas)}$ on the FerriFh compared to its precursor ferrihydrite. One of the important aspects of the study is dedicated to the reactivity of FerriFh with CO_2 at the molecular spectroscopic level investigation to decipher the different carbonate and bicarbonate complexes formed on the reactive surface hydroxyl (with either OH vs. OH_2^+) groups under various environments. The study demonstrated that organic molecules (having short carbon length from 0.6 to 1.0 nm) such as citrate adsorbed on metal oxyhydroxide surfaces (e.g., ferrihydrite) formed relatively immobile complexes by facilitating the formation of ordered crystalline FerriFh product and inhibited ferrihydrite transformation to crystalline hematite under aging conditions (~175 ºC and 8 hrs). BET-SSA results showed a significant decrease in measured specific surface area of the ordered crystalline FerriFh that is due to an increase in aggregated size particles. These results evidenced that the physical changes that occurred within the intermediate FerriFh gave rise to different chemically adsorbed carbonate, bicarbonate, and carboxylate species at the FerriFH surface. Results obtained from the present study are important and play particular roles in environmental soils and atmospheric systems involving the application of various ferrimagnetic metal oxyhydroxides. In addition, the reactivity of crystalline ferrimagnetic Fe-oxyhydroxide (e.g., FerriFh, magnetite, and/or maghemite) are of great interest in mineral carbonation and their surface can play key factors controlling the fate of CO_2 injected into deep geological formations in the Earth's subsurface under elevated pressure. Importantly, the results showed the surface structural differences of FerriFh and ferrihydrite affect carbonate speciation when reacted in the presence of sorbed citrate and condensed CO_2 bound species. Adsorbed citrate anion prevented both the formation of

carbonate and bicarbonate complexes while under only low CO_2 vapor pressure that adsorbed bicarbonate species are present. In addition, we speculate that the intermolecular proton transfer interactions by neighboring surface OH groups with $CO_{2(gas)}$ are mainly contributed to the formation of adsorbed bicarbonate. However, bicarbonate was not formed at elevated pressure due to CO_2 in its condensed phase reaction with specific OH_2^+ sites at the surface which further favored the formation of adsorbed carboxylate complexes (~1730 cm^{-1}) (Baltrusaitis and Grassian 2005).

As we mentioned, spectroscopic details information about the composition and reactivity of FerriFh is of great debate. The adsorption of gaseous CO_2 on ferrimagnetic iron oxyhydroxide adsorbents is important to assess other anions adsorption and reaction mechanism (Xu, Hausner et al. 2011). For example, magnetite (Fe_3O_4) mineral has previously studied for its surface reactivity and shown good CO_2 adsorption capacity (e.g. ~0.5 mol CO_2/amine) at elevated temperature (~120 °C). Prior results suggested that magnetite, Fe_3O_4, can be coalesced with polyaniline (PANI) organic framework, a process that is almost similar to "Amine scrubbing" of CO_2 capture used in the industry, to form nanocapsules based nanocomposite for the formation of carbonate, bicarbonate, and carboxylates on the surface (Tamilarasan and Ramaprabhu 2012). Here in the present study, we showed that CO_2 adsorption can thermodynamically be stable on the ferrimagnetic ferrihydrite surface and adsorbed different carbonate and bicarbonate complexes. Other studies suggested similar adsorbed carbonate and bicarbonate mechanism by direct CO_2 adsorption or ligand exchange with OH/OH_2^+ sites on goethite and hematite iron oxyhydroxide surfaces (Baltrusaitis, Schuttlefield et al. 2011).

However, the presence of adsorbed water humidity and/or CO_2 vapor condensation under high pressure on the Ferrimagnetic oxyhydroxide surface only contributed to the formation of inner-sphere adsorbed carbonate with additional carboxylate species presence. This assumption gives evidence to the disappearance of metastable bicarbonate (i.e., CO_2 bent-like species) mode at ~1220 cm^{-1}. I addition, the bicarbonate modes formation at ~1620, 1410 with additional shoulder peaks around 1730 cm^{-1} are assigned to the presence of adsorbed carbonic acid (H_2CO_3) and/or carboxylate species formation. The results are, however, consistent with prior studies that have shown only adsorbed carbonate species formed under high relative humidity (RH) while metastable bicarbonate complexes are preferred at < 10% RH on Fe-oxyhydroxides (Bargar, Kubicki et al. 2005; Hausner, Bhandari et al. 2009; Baltrusaitis, Schuttlefield et al. 2011; Pierre-Louis, Hausner et al. 2013). Hence, the results showed how the surface structural differences between FerriFh and its precursor ferrihydrite mineral affect their reactivity toward CO_2 adsorption in the formation of stable and metastable carbonation complexes. This study is relevant in the geological capture of CO_2 and perhaps in the understanding of mineral carbonation in contact with magnetic iron oxides.

4.5 Summary and Implications

The adsorption of CO_2 on the ferrimagnetic ferrihydrite surfaces compared to its precursor ferrihydrite was investigated. Organic citrate was found to play a major role in the transformation of ferrihydrite to the intermediate FerriFh under hydrothermal conditions. Citrate adsorbed on FerriFh and/or ferrihydrite inhibited the formation of carbonate and bicarbonate complexes on both mineral surfaces upon gaseous CO_2 under

dry conditions, as evidenced by ATR-FTIR. In particular, the citrate-free FerriFh surface showed an increase affinity for the adsorption of $CO_{2(gas)}$. Both citrate-free FerriFh and ferrihydrite have shown similar binding geometries toward adsorbed carbonate and bicarbonates complexes under various CO_2 pressure conditions. However, ATR-FTIR results suggest that carbonate species mostly formed a bidentate binuclear structure while bicarbonate preferred monodentate-like complexes with similar binding configurations as those adsorbed on ferrihydrite. The results also indicates that the metastable bicarbonate species are weakly bound on the Fe-oxyhydroxide surfaces, and these modes do not form under high CO_2 vapor pressure ($\geq$ 5.18 bar). Ferrimagnetic iron oxyhydroxides (FerriFh) may serve as geologic sinks for various oxyanions such as citrate, carbonate, carboxylate, carbonic acid, and bicarbonate complexes.

4.6 Acknowledgments

This work was supported by a National Science Foundation (NSF) Collaborative Research in chemistry grant. In addition to NSF support (Grant Nos. CHE-0714121 and CHE-0923077), D.R.S. appreciates partial funding for this research from the Department of Energy, Basic Energy Sciences (DEFG-029ER14644). Work done at Argonne and use of the Advanced Photon Source was supported by the US Department of Energy, Office of Science, Office of Basic Energy Science, under contract No. DE-AC02-06CH11357. Computational support was provided by the Research Computation and Cyberinfrastructure group at The Pennsylvania State University.

References

Aschenbrenner, O., P. McGuire, et al. (2011). "Adsorption of carbon dioxide on hydrotalcite-like compounds of different compositions." Chemical Engineering Research & Design **89**: 1711-1721.

Bachu, S., D. Bonijoly, et al. (2007). "CO2 storage capacity estimation: Methodology and gaps." International Journal of Greenhouse Gas Control **1**(4): 430-443.

Bae, J. S. and S. K. Bhatia (2006). "High-pressure adsorption of methane and carbon dioxide on coal." Energy & Fuels **20**(6): 2599-2607.

Baltrusaitis, J. and V. H. Grassian (2005). "Surface reactions of carbon dioxide at the adsorbed water-iron oxide interface." Journal of Physical Chemistry B **109**: 12227-12230.

Baltrusaitis, J. and V. H. Grassian (2010). "Carbonic Acid Formation from Reaction of Carbon Dioxide and Water Coordinated to Al(OH)(3): A Quantum Chemical Study." Journal of Physical Chemistry A **114**: 2350-2356.

Baltrusaitis, J., P. M. Jayaweera, et al. (2009). "XPS study of nitrogen dioxide adsorption on metal oxide particle surfaces under different environmental conditions." Physical Chemistry Chemical Physics **11**: 8295-8305.

Baltrusaitis, J., J. Schuttlefield, et al. (2007). "FTIR spectroscopy combined with quantum chemical calculations to investigate adsorbed nitrate on aluminium oxide surfaces in the presence and absence of co-adsorbed water." Physical Chemistry Chemical Physics **9**: 4970-4980.

Baltrusaitis, J., J. Schuttlefield, et al. (2007). "FTIR spectroscopy combined with quantum chemical calculations to investigate adsorbed nitrate on aluminium oxide surfaces in the presence and absence of co-adsorbed water." Physical Chemistry Chemical Physics **9**(36): 4970-4980.

Baltrusaitis, J., J. Schuttlefield, et al. (2011). "Carbon dioxide adsorption on oxide nanoparticle surfaces." Chemical Engineering Journal **170**: 471-481.

Baltrusaitis, J., J. D. Schuttlefield, et al. (2007). "Surface reactions of carbon dioxide at the adsorbed water-oxide interface." Journal of Physical Chemistry C **111**: 14870-14880.

Bargar, J. R., J. D. Kubicki, et al. (2004). "ATR-FTIR characterization of inner-sphere and outer-sphere carbonate surface complexes on hematite." Abstracts of Papers of the American Chemical Society **227**: 172-GEOC.

Bargar, J. R., J. D. Kubicki, et al. (2005). "ATR-FTIR spectroscopic characterization of coexisting carbonate surface complexes on hematite." Geochimica Et Cosmochimica Acta **69**: 1527-1542.

Barrn, V. and J. Torrent (2002). "Evidence for a simple pathway to maghemite in Earth and Mars soils." Geochimica et Cosmochimica Acta **66**(15): 2801-2806.

Barron, V., J. Torrent, et al. (2003). "Hydromaghemite, an intermediate in the hydrothermal transformation of 2-line ferrihydrite into hematite." American Mineralogist **88**: 1679-1688.

Barron, V., J. Torrent, et al. (2012). "Critical evaluation of the revised akdalaite model for ferrihydrite-Discussion." American Mineralogist **97**(1): 253-254.

Bertelsen, P., W. Goetz, et al. (2004). "Magnetic Properties Experiments on the Mars Exploration Rover Spirit at Gusev Crater." Science **305**(5685): 827-829.

Bishop, J. L. and E. Murad (2002). "Spectroscopic and geochemical analyses of ferrihydrite from springs in Iceland and applications to Mars." Geological Society, London, Special Publications **202**(1): 357-370.

Busca, G. and V. Lorenzelli (1982). "INFRARED SPECTROSCOPIC IDENTIFICATION OF SPECIES ARISING FROM REACTIVE ADSORPTION OF CARBON OXIDES ON METAL-OXIDE SURFACES." Materials Chemistry **7**: 89-126.

Cabello, E., M. P. Morales, et al. (2009). "MAGNETIC ENHANCEMENT DURING THE CRYSTALLIZATION OF FERRIHYDRITE AT 25 AND 50 degrees C." Clays and Clay Minerals **57**: 46-53.

Campbell, A. S., U. Schwertmann, et al. (1997). "Formation of cubic phases on heating ferrihydrite." Clay Minerals **32**(4): 615-622.

Cao, F. L., Y. F. Wu, et al. (2008). "Preparation and property of discoid aluminum-doped alpha-Fe2O3 particles." Acta Chimica Sinica **66**(12): 1405-1410.

Choi, S., J. H. Drese, et al. (2009). "Adsorbent Materials for Carbon Dioxide Capture from Large Anthropogenic Point Sources." ChemSusChem **2**(9): 796-854.

Cornell, R. M. and U. Schwertmann (1979). "Influence of Organic-Anions on the Crystallization of Ferrihydrite." Clays and Clay Minerals **27**(6): 402-410.

Cudennec, Y. and A. Lecerf (2006). "The transformation of ferrihydrite into goethite or hematite, revisited." Journal of Solid State Chemistry **179**(3): 716-722.

Fassbinder, J. W. E., H. Stanjekt, et al. (1990). "Occurrence of magnetic bacteria in soil." Nature **343**(6254): 161-163.

Ford, G. C., P. M. Harrison, et al. (1984). "Ferritin - Design and Formation of an Iron-Storage Molecule." Philosophical Transactions of the Royal Society of London Series B-Biological Sciences **304**(1121): 551-&.

Grenfell, J. L., J. W. Stock, et al. (2010). "Oxidation of CO on surface hematite in high CO2 atmospheres." Planetary and Space Science **58**(10): 1252-1257.

Hausner, D. B., N. Bhandari, et al. (2009). "Ferrihydrite reactivity toward carbon dioxide." Journal of Colloid and Interface Science **337**: 492-500.

Houghton, J. T., Meria Filho, L.G., Callander, B.A., Harris, N., Kattenberg, A., Maskell, K., (1996). "The Climate change." Cambridge University Press

Ismail, H. M., D. A. Cadenhead, et al. (1997). "Surface reactivity of iron oxide pigmentary powders toward atmospheric components: XPS, FESEM, and gravimetry of CO and CO2 adsorption." Journal of Colloid and Interface Science **194**: 482-488.

Izgec, O., B. Demiral, et al. (2008). "CO2 injection into saline carbonate aquifer formations I: laboratory investigation." Transport in Porous Media **72**(1): 1-24.

Jambor, J. L. and J. E. Dutrizac (1998). "Occurrence and Constitution of Natural and Synthetic Ferrihydrite, a Widespread Iron Oxyhydroxide." Chemical Reviews (Washington, D. C.) **98**(7): 2549-2585.

Janney, D. E., J. M. Cowley, et al. (2000). "Transmission electron microscopy of synthetic 2- and 6-line ferrihydrite." Clays Clay Miner. **48**(1): 111-119.

Kubicki, J. D., L. M. Schroeter, et al. (1999). "Attenuated total reflectance Fourier-transform infrared spectroscopy of carboxylic acids adsorbed onto mineral surfaces." Geochimica et Cosmochimica Acta **63**(18): 2709-2725.

Liu, Q. S., V. Barron, et al. (2008). "Magnetism of intermediate hydromaghemite in the transformation of 2-line ferrihydrite into hematite and its paleoenvironmental implications." Journal of Geophysical Research-Solid Earth **113**.

Maher, B. A. and R. M. Taylor (1988). "Formation of Ultrafine-Grained Magnetite in Soils." Nature **336**(6197): 368-370.

Meldrum, F. C., B. R. Heywood, et al. (1992). "Magnetoferritin - Invitro Synthesis of a Novel Magnetic Protein." Science **257**(5069): 522-523.

Michel, F. M., V. Barron, et al. (2007). "Ordered ferrimagnetic form of ferrihydrite reveals links among structure, composition, and magnetism." Proceedings of the National Academy of Sciences of the United States of America **107**(7): 2787-2792.

Michel, F. M., V. Barron, et al. (2010). "Ordered ferrimagnetic form of ferrihydrite reveals links among structure, composition, and magnetism." Proceedings of the National Academy of Sciences of the United States of America **107**: 2787-2792.

Michel, F. M., L. Ehm, et al. (2007). "The structure of ferrihydrite, a nanocrystalline material." Science **316**: 1726-1729.

Michel, F. M., H.-A. Hosein, et al. (2010). "Reactivity of ferritin and the structure of ferritin-derived ferrihydrite." Biochim. Biophys. Acta, Gen. Subj. **1800**(8): 871-885.

Murphy, R., K. Lammers, et al. (2010). "Ferrihydrite phase transformation in the presence of aqueous sulfide and supercritical CO2." Chem. Geol. **271**(1-2): 26-30.

Oganov, A. R., R. J. Hemley, et al. (2013). "Structure, Bonding, and Mineralogy of Carbon at Extreme Conditions." Reviews in Mineralogy and Geochemistry **75**(1): 47-77.

Parise, J. B., R. Harrington, et al. (2010). "Understanding the composition and structure of ferrihydrite." Geochimica Et Cosmochimica Acta **74**: A793-A793.

Pierre-Louis, A.-M., D. B. Hausner, et al. (2013). "Adsorption of carbon dioxide on Al/Fe oxyhydroxide." J Colloid Interface Sci.

Santoro, M., F. Gorelli, et al. (2011). "Silicon carbonate phase formed from carbon dioxide and silica under pressure." Proceedings of the National Academy of Sciences of the United States of America **108**(19): 7689-7692.

Schwertmann, U. (1991). Iron Oxides in the Laboratory: preparation and Characterization. Weinheim. New York . Chichester, Willey~VCH.

Schwertmann, U., J. Friedl, et al. (1999). "From Fe(III) ions to ferrihydrite and then to hematite." Journal of Colloid and Interface Science **209**(1): 215-223.

Silva, N. J. O., V. S. Amaral, et al. (2005). "Magnetic behavior of iron (III) oxyhydroxy nanoparticles in organic-inorganic hybrid matrices." J. Magn. Magn. Mater. **290-291**(Pt. 2): 962-965.

Silva, N. J. O., V. S. Amaral, et al. (2006). "Structural and magnetic studies in ferrihydrite nanoparticles formed within organic-inorganic hybrid matrices." Journal of Applied Physics **100**(5).

St Pierre, T. G., N. T. Gorham, et al. (2002). "Apparent magnetic energy-barrier distribution in horse-spleen ferritin: Evidence for multiple interacting magnetic entities per ferrihydrite nanoparticle." Physical Review B **65**(2).

Strongin, D. R., C. P. Grey, et al. (2010). "Surface science studies of environmentally relevant iron (oxy)hydroxides ranging from the nano to the macro-regime." Surface Science **604**(13-14): 1065-1069.

Tamilarasan, P. and S. Ramaprabhu (2012). "Polyaniline-magnetite nanocapsules based nanocomposite for carbon dioxide adsorption." International Journal of Greenhouse Gas Control **10**: 486-493.

Torrent, J. and V. BarrÃ³n (2000). "Key Role of Phosphorus in the Formation of the Iron Oxides in Mars Soils?" Icarus **145**(2): 645-647.

Torrent, J., Q. S. Liu, et al. (2007). "Magnetic enhancement and iron oxides in the upper luochuan Loess-paleosol sequence, Chinese Loess plateau." Soil Science Society of America Journal **71**: 1570-1578.

Violante, A., E. Barberis, et al. (2003). "Factors affecting the formation, nature, and properties of iron precipitation products at the soil-root interface." Journal of Plant Nutrition **26**(10-11): 1889-1908.

Vu, H. P., S. Shaw, et al. (2008). "Transformation of ferrihydrite to hematite: an in situ investigation on the kinetics and mechanisms." Mineralogical Magazine **72**: 217-220.

Waite, T. D. and F. M. M. Morel (1984). "Photoreductive Dissolution of Colloidal Iron-Oxide - Effect of Citrate." Journal of Colloid and Interface Science **102**(1): 121-137.

Wijnja, H. and C. P. Schulthess (2001). "Carbonate adsorption mechanism on goethite studied with ATR-FTIR, DRIFT, and proton coadsorption measurements." Soil Science Society of America Journal **65**: 324-330.

Xu, T. F., L. G. Zheng, et al. (2011). "Reactive transport modeling for CO2 geological sequestration." Journal of Petroleum Science and Engineering **78**: 765-777.

Xu, W., D. B. Hausner, et al. (2011). "Structural water in ferrihydrite and constraints this provides on possible structure models." American Mineralogist **96**(4): 513-520.

Ye, T., D. Wynn, et al. (2001). "Photoreactivity of Alkylsiloxane Self-Assembled Monolayers on Silicon Oxide Surfaces." Langmuir **17**(15): 4497-4500.

Zhao, J. M., F. E. Huggins, et al. (1994). "Ferrihydrite - Surface-Structure and Its Effects on Phase-Transformation." Clays and Clay Minerals **42**(6): 737-746.

Zukal, A., J. Mayerova, et al. (2010). "Adsorption of Carbon Dioxide on High-Silica Zeolites with Different Framework Topology." Topics in Catalysis **53**: 1361-1366.

CHAPTER 5
ADSORPTION OF PHOSPHATE AND CARBONATE TO BINARY FE- AND AL/FE OXYHYDROXIDE MINERALS: ATR-FTIR COMBINED WITH DENSITY FUNCTIONAL THEORY (DFT) STUDIES

Abstract

In this chapter research is presented that investigated the reactivity of Al/Fe-oxyhydroxides (0-100 mol%) individually adsorbed and coadsorbed phosphate (PO_4^{3-}) and carbonate (CO_3^{2-}). The morphology of the Al/Fe oxyhydroxide was characterized with transmission electron microscopy (TEM), X-ray diffraction (XRD), and pair distribution function analysis (PDF). The reactivity of the Al/Fe oxyhydroxide toward the oxyanions was investigated with, and attenuated total reflectance Fourier transform Infrared spectroscopy (ATR-FTIR) combined with density functional theory (DFT) calculations. Results from the ATR-FTIR experiments showed that the structure of PO_4^{3-} and CO_3^{2-} surface complexes on the oxyhydroxide surface was a strong function of not only the Al content of the Al/Fe oxyhydroxide surface, but also was dependent on the solution pH (range of 5-9) and ionic strength. Results from the ATR-FTIR/DFT studies suggested that PO_4^{3-} at low pH adsorbed as monodentate and bidentate binuclear protonated ($H_2PO_4^-$/HPO_4^{2-}) species, while at high pH adsorbed as non-protonated PO_4^{3-} complexes on the Al/Fe oxyhydroxide surfaces. The investigations also showed that the surface concentration (per unit surface area) of PO_4^{3-} on Al/Fe oxyhydroxide surfaces (5-30 mol%) was greater than on ferrihydrite, ferrimagnetic ferrihydrite (FerriFh), goethite, and AlO(OH).

5.1 Introduction

Both of the oxyanions PO_4^{3-} and CO_3^{2-} are ubiquitous in natural systems that include soils and lake sediments. These species have often been associated with the transport and bioavailability of amorphous/polycrystalline metal oxides/hydroxides such as: iron, aluminum, manganese, magnesium, calcium, and mixed Al/Fe oxyhydroxides. In addition, phosphate can also finds its way into ground and surface waters from animal wastes, laundry and cleaning detergents, industrial effluents and plants fertilizer runoff (> 0.1 mg/L level) (Arai and Sparks 2007). Accordingly, a molecular scale understanding of phosphate adsorption mechanism is of great significance. Many studies suggested that phosphate and carbonate can be released to solution upon the reductive dissolution of phosphate and carbonate containing iron oxide systems (Villalobos 2000). While carbonate minerals system play an important buffering role in regulating freshwater pH; phosphate can range from 20 to 80% of total phosphorous in soils and may be a limiting nutrient for plant growth and where excess fertilization leads to eutrophication (Arai and Sparks 2007). Phosphate also can impose limitations on the biological reduction and/or abiotic alteration of ferrihydrite and pyrite (FeS_2) minerals (Benali et al. 2002; Bocher et al. 2004; Borch et al. 2007; Elsetinow et al. 2001).

Prior research has shown that PO_4^{3-} adsorbs strongly on Al/Fe oxyhydroxide surfaces via electrostatic interactions or/and ligand exchange reactions between the oxyanions with the terminal surface (-OH) sites (Cismasu et al. 2012; Guan et al. 2005; Hong et al. 2011; Kwon and Kubicki 2004). It has been also suggested that the reactivity of Al/Fe oxyhydroxide nanostructures toward PO_4^{3-} is dependent of the Al/Fe mol% ratio

[22,] (Harvey and Rhue 2008). These findings indicate that the mineral surface charge properties can be strongly influenced as the sorption of oxyanions (AsO_4^{3-}, PO_4^{3-} , and CO_3^{2-} species) increase on the Fe- and/or Al-oxyhydroxide structure (Arai et al. 2004; Giles et al. 2011; Harvey and Rhue 2008; Hong et al. 2011; Hong et al. 2010). These studies also revealed that the mixed Al/Fe sorbents often exhibit different reactivity properties, kinetics, and higher phosphate sorption capacity than the single phase metal oxide/oxyhydroxide sorbents (Anderson and Benjamin 1990; Borch et al. 2007; Cismasu et al. 2012; Harvey and Rhue 2008).

Motivated by prior studies, we investigated the reactivity of low Al (0-30 mol%) substituted Fe-oxyhydroxide (i.e., ferrihydrite) toward single and co-adsorption of phosphate and carbonate species as a function of loading (5 μM to 1 mM) and pH (5 to 9) conditions. This study was the first to study the coadsorption of phosphate and carbonate on Al/Fe oxyhydroxide surfaces. This is an important issue to investigate, since many environments expose Al/Fe oxyhydroxides to waters that would contain both oxyanions, and it is likely that the two adsorbates would compete for sites on an adsorbing substrate.

Also of interest is the structure of adsorbed PO_4^{3-} and CO_3^{2-} on the Al/Fe oxyhydroxide surface. There exists a significant amount of prior work that has investigated the structure of PO_4^{3-}, and CO_3^{2-} complexes on individual Al and Fe oxyhydroxide surfaces (Cismasu et al. 2012; Kubicki et al. 2012a; Kwon and Kubicki 2004), but not on the mixed Al/Fe system that is environmental relevant. Here, we combine multiple analytical techniques that include XRD, PDF, ATR-FTIR, and DFT calculations to provide complementary information about the adsorption and structure of

PO_4^{3-}, and CO_3^{2-} complexes on Al/Fe oxyhydroxide. DFT calculations are used to help interpret the complicated IR vibration spectra associated with the adsorption of PO_4^{3-}, and CO_3^{2-} on the nano-dimensioned Al/Fe oxyhydroxide.

5.2 Experimental Methods

5.2.1 Synthesis and Solution Preparation

Various metal-oxyhydroxide (ferrihydrite, Al/Fe-oxyhydroxide, α-FeOOH, FerriFh, and AlOOH) mineral phases were prepared. We synthesized "2-line" ferrihydrite (Ferrihydriteyd) using a modified method adapted from prior research (Bhandari et al. 2010; Hausner et al. 2009; Schwertmann 1991). Shortly, ferrihydrite mineral was prepared using 0.1 M of anhydrous ferric chloride ($FeCl_3$) dissolved in deionized (DI) water (18 MΩ) at pH between 7-8 range by adding aliquots of sodium hydroxide (~1.0 M), and then a red-brown precipitate was observed. Similarly, the synthesis details for the Al/Fe oxyhydroxide nanoparticles can be found in prior publications (Borch et al. 2007; Cismasu et al. 2012; Kubicki et al. 2012b). Briefly, Al/Fe-oxyhydroxide colloidal particles were co-precipitated using a total mixture of 0.1 M $FeCl_3$ and $AlCl_3$ metal cations neutralized with 1 M NaOH. The relative Al/Fe cations ratio was maintained from 0, 5, 10, 30, 70, and 100 mol% Al during the synthesis of Al/Fe oxyhydroxide materials. The Al 0 and 100 mol% products are referred to the end-member of pure Ferrihydrite and AlOOH phases.

FerriFh mineral phase was prepared using similar prior published methods (Barron et al. 2003; Cismasu et al. 2011). Ferrimagnetic ferrihydrite, FerriFh, was

synthesized by using dissolved solution of 0.1 M anhydrous $FeCl_3$ in the presence of 3% molar ratio of sodium citrate ($N_3C_6H_5O_7.2H_2O$) relative to iron. Then, the iron oxyhydroxide/citrate precipitates suspension was neutralized with 1.0 M solution NaOH solution and red-brown Ferrihydrite/citrate precipitates were observed. The complete details about the synthesis of ferrimagnetic ferrihydrite can be revised in the prior chapter 4. Then, all synthesized products were washed in dialysis bags suspended into double-distilled water, with frequent water changes, to remove the counter ions (Cl^-, OH^-, and Na^+) until the electric conductivity of the equilibrium solution was < 0.01 dSm^{-1}. The rinsed colloidal nanoparticles suspensions were then centrifuged, air or freeze dried, and stored in powder form into polyethylene bottles.

Goethite samples of nano- and micron-sized dimension were synthesized by using a modified method adapted from Cornell and Schwertmann (Cornell R. M. 2003). Goethite micro-sized particles were synthesized using a similar procedure that was adopted by Kubicki et al. 2012 and elsewhere. Approximately 50 g of $Fe(NO_3)_3.9H_2O$ was added into 830 ml of DI water and titrated with a basic solution of 5 M NaOH until a pH ~12 was achieved. The α-FeOOH suspension was then aged in Pyrex bottle placed in an oven at 60 °C for 24 hours (Kubicki et al. 2012; Schwertmann 2000). The micro-sized goethite particles were also used to compare with the phosphate adsorption onto Al/Fe-oxyhydroxide minerals. To synthesize nano-goethite, a ferrihydrite precursor was first precipitated by adding 180 mL of 5 M NaOH to 100 mL $Fe(NO_3)_3 \cdot 9H_2O$ solution (0.1 M) at pH approximately 12.5. The resulting suspension was diluted to 2 liter with deionized water and held in a closed Pyrex bottle in a 70 ˚C oven for 60 hours. During the aging time, the red-brown ferrihydrite suspension was transformed into a yellow nano-sized

goethite precipitate. Micron-sized goethite was synthesized by first adding 50 g of $Fe(NO_3)_3 \cdot 9H_2O$ to 830 mL of double-distilled water. Sodium hydroxide (NaOH ~5 M) was added to the solution until a pH of ~12 was achieved. The resulting suspension was placed in a sealed Pyrex bottle and aged in an oven at a temperature of 60 ˚C for a period of 24 hours. Goethite from each synthetic protocol were dialyzed in de-ionized water (DI) for 5-10 days with frequent water changes to remove counter ions (Na^+, NO_3^-) from the suspensions. Goethite sample suspensions were subsequently centrifuged, air-dried, and individually stored in polyethylene bottles. The dried samples were crushed to produce finely divided goethite powders. All stock phosphate solutions were prepared from sodium dibasic anhydrous ($NaH_2PO_4.H_2O$) purchased from Sigma-Aldrich.

5.2.2 Characterization Techniques

Scanning Transmission electron microscopy (STEM) images of the synthesized particles were obtained using a JEOL JEM-1400 (120 KeV) instrument, equipped with energy dispersive spectroscopy (EDS), a Gatan charge-coupled device (CCD) large-area camera imaging, and a high brightness LaB_6 electron source. The EDS was used to semi-quantify the Al/Fe composition of the Al/Fe-oxyhydroxide materials. Droplets of the ultrasonically dispersed particles suspension was placed onto an amorphous coated or holey-carbon film supported by a copper-mesh TEM grid. All samples were dried for 30 min on the supported grid at room temperature and then inserted into a low vacuum (~15 min) chamber to further remove sorbed impurities.

X-ray powder diffraction patterns of synthesized Al/Fe-oxyhydroxide (Al substitution from 0-70 mol%) samples were revised and obtained using an Apex Duo Bruker

Instrument Service (MoKα radiation λ = 0.71073 nm) equipped with CCD diffraction system. Copper (Cu Kα) source radiation was not used to avoid interference from Fe fluorescence. Additional information on the Al/Fe samples XRD characterization could found in prior publications (Borch et al. 2007; Kubicki et al. 2012a; Kubicki et al. 2012b). Briefly, high energy X-ray scattering experiments coupled with pair distribution function (PDF) analysis were carried out for the Al substitution of 0, 5, and 30 mol% Al/Fe oxyhydroxide surfaces at the beam line 11-ID-C from the Advanced Photon Source (APS), Argonne National Laboratory using monochromatic radiation of energy 114.46 KeV (λ = 0.10786 Å). Dried powder form of Al/Fe nanomaterials were loaded into a polyimide (kapton) capillary. The diffracted beam was collected using a Perkin-Elmer amorphous silicon detector. Then, the conversion from 2D to 1D was carried out using the program Fit2D (Hammersley et al. 1996). PDF signals were generated by Fourier transform of the total structure function, S(Q) (Q_{max} = 30 $Å^{-1}$), corrected as outlined in prior publication using the program PDFgetX2 (Chupas et al. 2003; Hammersley et al. 1996; Qui 2004). The Fourier transform of the total structure function, S(Q) (Q_{max} = 30 $Å^{-1}$) for the dry samples yields the PDF analysis or G(r) which is a real space representation of the atomic ordering of the materials.

A Nicolet 6700 spectrometer (Thermo Scientific) equipped with a smart Orbit attenuated total reflectance Fourier transform infra-red (ATR-FTIR) accessory and a deteurated triglycine sulfate (DTGS) detector was used to probe the vibrational spectra. Droplets suspension of Fe-oxyhydroxide minerals and Al/Fe oxyhydroxide nanoparticles were placed on the diamond ATR element and were dried with a N_2 stream to form a thin-film. After drying, aliquots of ~10 ml reference water solution containing 10 mM

NaCl was then flowed, and IR spectra of the thin-film/H_2O samples at specific pH value (5, 7, or 9) were recorded. Then, a 100 μM phosphate/carbonate aqueous solution at a specific pH value (~ 5, 7, and 9) was flowed either separately or in competition on top of the washed nanoparticles thin-film using a syringe pump. In this case, adsorbate mineral surface interactions were carried out in-situ and monitored in a reaction cell covered by a home built T-shape glass cell under low stream of N_2 atmosphere on the IR diamond plate, at a steady flow rate of ~0.4 ml/min. All stock solutions of phosphate and carbonate were prepared from sodium dibasic anhydrous ($N_2H_2PO_4 \cdot H_2O$) and sodium hydrogen carbonate (Na_2HCO_3) purchased from Sigma-Aldrich.

5.2.3 Phosphate adsorption on goethite (α-FeOOH) structure

Goethite samples to be analyzed were placed on a diamond ATR element in the form of a suspension and were dried under a stream of N_2 to form a thin film. The film was covered and rinsed with deionized water (DI ~10 mL) containing 10 mM NaCl to maintain the background electrolyte and to eliminate loosely bound goethite particles. Depending on the experiment, the reference water solution was flowed across the goethite film at a specific pH value (4.22, 5.71, 7.51, or 7.96). Then, a 100 μM phosphate solution at the pH of interest (4.22, 5.71, 7.51, or 7.96) was pumped (via a syringe pump) through a reaction cell that enclosed the goethite nanoparticle thin film. The flow of solution was maintained at ~0.4 mL/min, respectively. In-situ ATR-FTIR spectra of adsorbed phosphate on goethite nanoparticles were reprocessed or either subtracted against the referenced spectra of DI H_2O that was syringe-pumped over the same goethite thin film sample at the same pH. Then, all reported spectra were manually

baseline-corrected in the 1200-800 cm^{-1} or the 1200-900 cm^{-1} regions due to the magnitude of the strong goethite modes contribution near 889 and 796 cm^{-1}.

Nanogoethite and microgoethite (each sample having a mass of 0.216 g) were individually added to 30 mL of a 100 μM phosphate solution contained of 10 mM NaCl. The phosphate/goethite suspension was sonicated for 3-5 minutes to disperse the particles in solution. The desired pH condition for a particular experiment was adjusted with an appropriate volume of NaOH and HCl solutions under vigorous stirring conditions. Phosphate/goethite suspensions were left to preequilibrate for 30 minutes at the specific pH of interest (i.e., 4.22, 5.71, 7.51, and 7.96) using a 718 STAT Titrino Metrohm (Brinkmann) pH meter. After equilibration, an aliquot of phosphate/goethite suspension was centrifuged, and the supernatant was decanted, isolating the goethite particles. Before drying, all phosphate/goethite samples were rinsed with three times with Di H_2O at the same pH and then dried on the diamond ATR under N_2 stream. In all cases, ATR-FTIR collections were done at 200 scans with a resolution of $4cm^{-1}$. All collected spectra were reprocessed against the ATR diamond and manually baseline-corrected in the phosphate region. The Omnic 7.3 software program was used for data acquisition, processing, and peak deconvolution procedures. Aqueous-phase IR spectra of sodium phosphate (Thermofisher analytical grade) at given pH values were collected by loading 2 drops of previously pH-adjusted 25 mM sodium phosphate solution on a diamond ATR element. In all of the FTIR experiments, data were collected as a single beam (resolution 4 cm^{-1}) of 100 co-added scans and the water spectrum was subtracted from each individual spectrum to get the final spectrum.

5.2.4 Phosphate adsorption onto Al/Fe oxyhydroxides

An approximate amount of 0.05 g of Al/Fe oxyhydroxide (0 to 30 mol%) dry materials powder were added separately into a total volume of ~ 200 ml with the initial 1 mM phosphate and 10 mM NaCl background electrolyte. Batch reactions were left to equilibrate for 30 min, and phosphate adsorption curves were then measured at various pH ranging from 3.55 to 11 using an autotitrator (Metrohm STAT 718) with diluted HCl (0.1 M) under vigorous stirring condition. Phosphate sorption isotherms on the Al/Fe surfaces (0-100 mol%) were also investigated in batch experiments (ex-situ) compared to single phase "2-line" ferrihydrite, α-FeOOH, and AlOOH minerals. Fixed amount of ~10 mg dry powder of mixed Al/Fe from 0 to 30 mol% and approximately 100 mg of α-FeOOH, FerriFh, and AlOOH oxyhydroxide powder minerals were added separately to a total volume of ~200 ml purged deionized water (i.e., DI H_2O with 10 mM NaCl) under slow stirring to form a slurry (for ~13 hours) of suspended particles. During the sorption isotherms, the nanoparticles suspensions were purged with a stream of N_2 gas bubbling, while adding phosphate at the desired concentration ranging from 0.005 mM, 0.05, 0.1, 0.4, 0.8, and 1.0 mM PO_4^{3-} at constant pH 5 for 30 minutes reaction times, to prevent contamination of carbonate ions from aqueous CO_2 dissolution. After each equilibration, the supernatant solutions (~1 ml syringe) were filtered using 0.22 μm Millipore Millex-GV membrane filters. The amount of phosphate adsorbed on the particles was calculated by taking the difference between the initial PO_4^{3-} amount added in solution and the solution phase equilibrium PO_4^{3-} concentration as measured by ion chromatography (IC). Then, the resulting adsorbed PO_4^{3-}/nanoparticles slurry was centrifuged down washed three times with DI H_2O to remove loosely bound outer-sphere complexes and analyzed

by ATR-FTIR (ex-situ) at the desired 100 μM adsorbed phosphate. Phosphate adsorption isotherms were done in duplicate, and all reported final data were normalized to the BET-SSA of the minerals. All ATR-FTIR spectra were recorded with an average of 200 co-added scans at 4 cm^{-1} resolution, and either reprocessed with an ATR correction or subtracted from the reference water spectrum (with 10 mM NaCl) or the clean mineral thin-film surface at the same pH. All spectra were normalized to the Al-O/Fe-O modes between the 700-600 cm^{-1} and manually baseline corrected in the 1700-1200 cm^{-1} or the 1300-780 cm^{-1} region. FTIR spectra analysis, processing, and peak fitting analysis were obtained with the Omnic 7.3 program.

5.2.5 Phosphate adsorption onto Alumina (α-Al_2O_3)

Corundum used in this study was purchased from Alfa Aesar as α-Al_2O_3 crystallites. No impurity phase was detected by either powder XRD, IR or ^{27}Al solid state NMR. The solid has a specific surface area (SSA) of 7.6 m^2g^{-1} as measured by the N_2-BET method. The point of zero charge (pH_{pzc}) is 8.1 based on the electrophoresis mobility (EM) method (Del Nero et al., 2010). The Nicolet 6700 FTIR spectrometer with a deuterated triglycine sulfate (DTGS) detector and equipped with a Smart Orbit ATR attachment with N_2 purge gas generator was used for data collection. Sample preparation for the ATR-FTIR experiments involved placing 50 mg of corundum into a 50 ml Nagel plastic vial that contained 40 ml of 1 mM phosphate (prepared by using $Na_2HPO_4 \cdot H_2O$, Sigma Aldrich) at the desired pH. After 15 min of mixing the sample was centrifuged to separate out the adsorbed phosphate/corundum suspension. The resulting phosphate/corundum slurry was then deposited on the ATR element. A total of two

hundred continuous scans at a resolution of 4 cm^{-1} were averaged to obtain the reported spectra. Since phosphate vibrational modes occur in the mid-infrared, data were collected in the 1200-960 cm^{-1} region. The spectra associated with unreacted corundum were subtracted from that of the corresponding reacted phosphate/corundum samples at the same pH to obtain the reported IR spectra results. All spectra were normalized with respect to the aluminum oxide modes (800-500 cm^{-1}) and baseline-corrected.

5.2.6 Density functional theory (DFT) computations

Density functional theory (DFT) molecular cluster calculations were performed for energy minimization and vibrational frequency optimization based on the minimized energy structures. Energy minimizations were carried out using the Gaussian 09 program with all the Fe/Al hydroxide dimers initially frozen, and then all atoms were allowed to relax. The B3LYP (Becke 1992; 1997) exchange and correlation functional with a 6-311+G(d, p) basis set was used to compute all the different adsorbed phosphate molecular complexes formed on the Fe_2, (Fe, Al), and Al_2-octahedral dimmers (see Figure 5.10) (Lee et al. 1988). Upon completion of the energy minimizations, DFT vibrational frequencies were scaled by a factor of 0.9614 to obtain accurate correlation compared to the experimental IR modes. This scaling factor was prior utilized on Fe-organic complexes to account for systematic errors such as neglect anharmonicity, basis set effects, and approximating electron correlation (Kubicki et al. 2012a; Scott and Radom 1996). Monodentate and bidentate phosphate complexes with different protonation states were modeled with (10 H_2O) and without explicit H_2O solvation molecules on either a single Fe^{3+} or Al^{3+}-octahedron dimer or Fe-$(OH)_2$-Fe, Al-$(OH)_2$-Al,

Al-$(OH)_2$-Fe binding cluster models, which are common in ferrihydrite and alumina metal oxyhydroxides. In addition, either one or two Na^+ atoms were added above the metals octahedra in the clusters to include the ionic solvation effect at the interface and which can have considerable effect on the vibrational frequencies of anionic species. Molecular/atomic animation correlating to the calculated vibrational frequencies and graphical molecular clusters visualization were analyzed through the Chemcraft program. DFT calculated frequencies for the cluster models were compared to the experimental modes resulting from the (i.e., in-situ and ex-situ) ATR-FTIR frequencies. The Fe/Al structural models are rather important as shown by previous results on molecular carbonate and phosphate iron- and Al-oxyhydroxide-water system (Kubicki et al. 2012a; Kubicki et al. 2012b; Kwon and Kubicki 2004).

5.3 Results and Discussion

5.3.1 Structure of Al/Fe-oxyhydroxide

Earlier research presented in Chapter 3 investigated the morphology and structure of Al/Fe oxyhydroxide with TEM and XRD. Here we use the pair distribution function (PDF) technique to complement the results derived from TEM and XRD. Figure 5.3a, b, and c show high resolution real-space PDF patterns for 0, 5, and 30 mol% Al/Fe oxyhydroxides, respectively. The PDF associated with Ferrihydriteyd (0% Al) is consistent with prior research (Cismasu et al. 2011; Harrington et al. 2011). Inspection of the PDF data in Figure 5 shows that the two most intense scattering features in the 1-5 Å range are consistent with prior PDF research of Al/Fe oxyhydroxide by Michel et al. and Cismasu et al. (Cismasu et al. 2012; Harrington et al. 2011). In addition, the PDF signal

for the ferrihydrite mineral attenuates by 2 nm (Fig. 5.3a) consistent with the expected particle diameter for ferrihydrite phase of 2 nm. Further analysis of the data shows that the attenuation of the PDF features associated with the 5 and 30 mol% Al/Fe oxyhydroxide occur at shorter distances (~18 to 15 Å, respectively) compared to ferrihydrite. This observation suggests that the average size of the Al/Fe oxyhydroxide is slight smaller than that of ferrihydrite. The positions of the scattering peak are similar for both of the Al/Fe oxyhydroxide data sets suggesting that an increase in the amount of Al substitution does not drastically change the structure of the Al/Fe oxyhydroxide (at least up to 30%). To resolve the differences between the PDF data associated with ferrihydrite and Al/Fe oxyhydroxide, we fit the PDF data with possible contributions from Al (oxy)hydroxide phases: gibbsite, bayerite, and boehmite. This fitting process did not yield any evidence for the existence of possible Al-bearing phases in the Al/Fe oxyhydroxide (supporting information; Figures 2-4; Appendix A) (Michel et al. 2006). This result, taken together with the XRD data shown in Chapter 3, suggests that at least up to Al concentration up to 30 mol%, the geometric structure of the Al/Fe oxyhydroxide is similar to ferrihydrite structure.

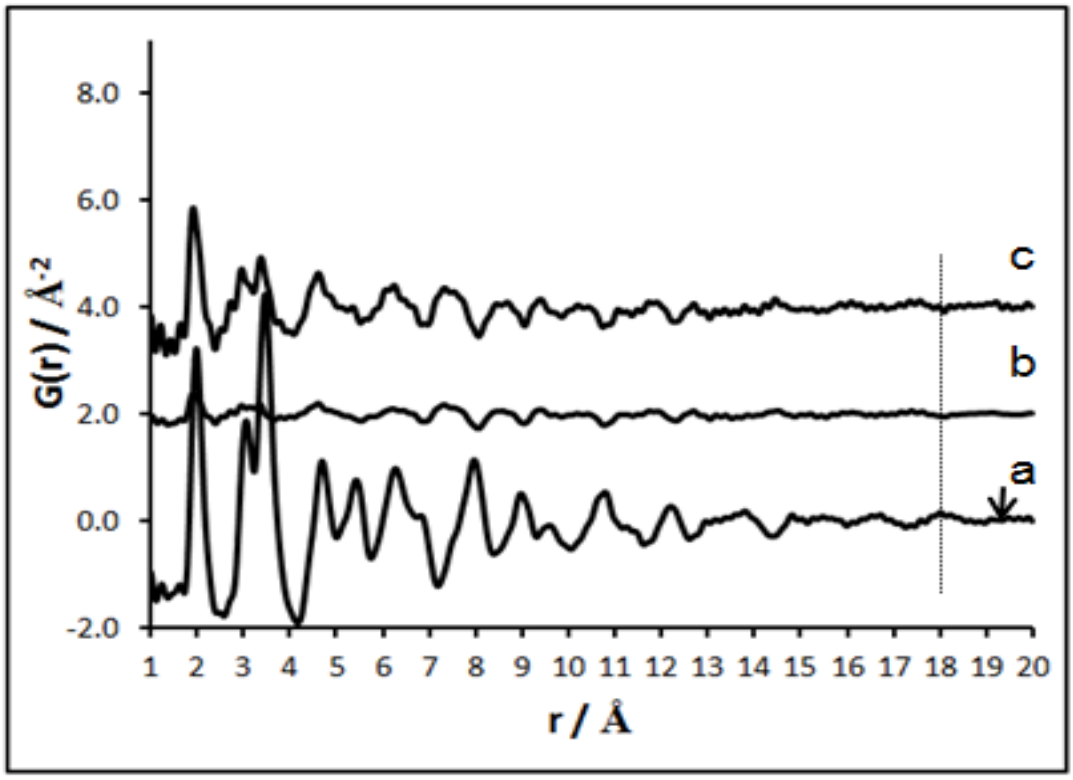

Figure 5.1. PDF signals for (a) "2-line" Ferrihydrite, (b) 5 mol%, and (c) Al 30 mol% substituted Al/Fe oxyhydroxide. The PDF data for Al 5 and 30 mol% showed a decrease in peak intensities, and the peak positions slightly shifted toward smaller radial distances (~18 to 14 Å) compared to ferrihydrite which show signal attenuation at ~20Å. The difference PDFs (Fig. 3b-c) are obtained by the subtraction of ferrihydrite PDF signals from those of Al 5 and 30 mol% Al/Fe oxyhydroxide materials.

5.3.2 ATR-FTIR of Adsorbed CO_3^{2-}, PO_4^{3-}, and CO_3^{2-}/PO_4^{3-} on Al/Fe Oxyhydroxide

Table 5.1 lists vibrational frequencies associated with adsorbed CO_3^{2-}, PO_4^{3-}, and coadsorbed CO_3^{2-}/PO_4^{3-} on ferrihydrite and 5-30 mol% Al/Fe oxyhydroxide. Figure 5.4 exhibits ATR-FTIR data for Al/Fe (0-30 mol%) oxyhydroxide that was exposed to 100 μM CO_3^{2-} at near neutral pH (the 1560 to 750 cm^{-1} region is shown). The IR features exhibited at ~1463 cm^{-1} $\nu_{2(O\text{-}C\text{-}O),\ Asym}$ and ~1348 cm^{-1} $\nu_{3(O\text{-}C\text{-}O),\ Sym}$ in Figure 5.4a are due to the asymmetrical and symmetrical stretching modes of adsorbed CO_3^{2-} on ferrihydrite. The vibrational modes shifts observed as well as the presence of the shoulder peak shown at ~1261 and 1274 cm^{-1} might be from the small contribution of bicarbonate species adsorbed on the Al/Fe surfaces due to CO-H bend stretching. These vibrational modes shifted to higher frequencies at around 1491, 1387 cm^{-1} as Al increased up to 30 mol% into Al/Fe-oxyhydroxide. In addition, the deconvoluted IR peak fittings shown at the lower region at ~1189, 1070, 1024, 963, 906, 858, and 820 cm^{-1} are contributions from the total adsorbed carbonate vibrational symmetry.

Table 5.1. In-situ ATR-FTIR vibrational frequencies upon adsorption of carbonate, phosphate, and co-adsorbed PO_4^{3-}/CO_3^{2-} at 0.1 mM onto Al/Fe oxyhydroxide nanoparticles at around pH 7.

Adsorbed CO_3^{2-}				Adsorbed PO_4^{3-}				Co-adsorbed PO_4^{3-}/CO_3^{2-}			
Fh	Al 5%	Al 10%	Al 30%	Fh	Al 5%	Al 10%	Al 30%	Fh	Al 5%	Al 10%	Al 30%
820	809	827	838	821	822	820	805	825	817	8005	805
858	839	845	855	885	885	879	841	887	889	862	842
906	890	887	885	939	945	851	888	935	955	934	903
963	952	965	960	990	993	951	946	988	1033	1006	1014
1024	1027	1050	1035	1030	1032	1019	1014	1037	1083	1024	1091
1070	1090	1095	1097	1067	1067	1071	1075	1075	1110	1075	
1189	1195	1194	1169	1105	1100	1110	1114	1109	1175	1170	1182
1265	1261	1274		1175	1179	1181	1189	1156	1203	1209	1237
1348	1355	1349	1387	1198	1201	1206	1216	1199	1261	1253	1260
1463	1477	1472	1491	1259	1262	1260		1263	1403	1368	1393
								1346	1490	1490	1494
								1478	1549	1560	

The peak position for these later modes did not change significantly, but greater amplification of peak area under the curves is detected as Al increase up to 30 mol% compared to pure Ferrihydrite mineral. The symmetry of absorbed carbonate IR mode splitting ($\Delta\nu_3$) difference is measured at ~122 cm^{-1} for Al 5% and Al 10%, ~104 for Al 30 mol% samples compared to 115 cm^{-1} found for the single Ferrihydrite oxyhydroxide phase. The degree of splitting, $\Delta\nu_3$, bands exhibits a significant decrease in absorbed carbonate binding geometry of approximately 7 to 11 cm^{-1} as Al increased from 5% to 30 mol% Al/Fe oxyhydroxide surfaces compared to Ferrihydrite nanophase. This could be interpreted as an effect of the Al substitution in the Al/Fe oxyhydroxide structure. Considerable reduction in the band splitting values may occur due to CO-H bonding formation in solution (e.g., HCO_3^-) and could be useful to differentiate the monodentate compared bidentate carbonate complexes formation at the Al/Fe mineral interfaces (Lefevre 2004). Thus, the IR band spectra of carbonate adsorption are assigned to inner-sphere absorbed carbonate species which are similarly observed in prior studies of carbonate complexes formation on α-FeOOH particles (Hiemstra et al. 2004; Villalobos 2000).

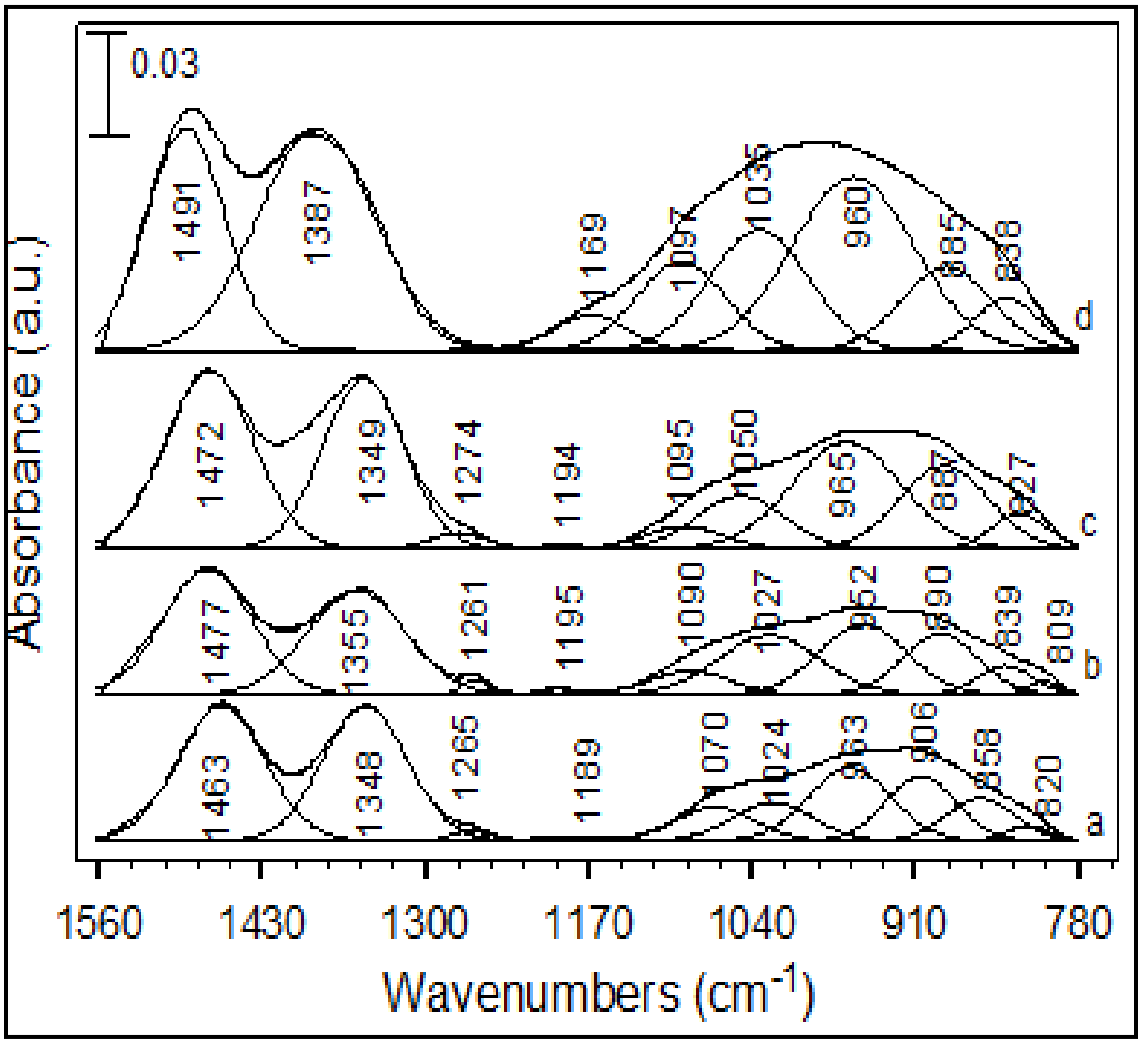

Figure 5.2. ATR-FTIR spectra of 100 μM adsorbed carbonate (In-situ)) vibrational modes peak fittings at pH 7 onto various mol% Al/Fe oxyhydroxide particles (a) Al 0% (i.e. ferrihydrite), (b) Al 5%, (c) Al 10%, and (d) Al 30% iron oxyhydroxide. The solution phase mineral spectra are subtracted from the adsorbed $CO_3^{2-}{}_{(aq)}$ on the thin-film nanoparticles taken at the same pH.

ATR-FTIR spectra of 5-30 mol% Al/Fe oxyhydroxide after exposure to 100 μM PO_4^{3-} at pH 7 are shown in Figure 5.5(a-d). Fitting of the data in the 1300 to 750 cm^{-1} range leads to vibrational features at ~1259, 1198, 1175, 1105, 1087, 1030, 990, 939, 885, and 821 cm^{-1} for PO_4^{3-} on ferrihydrite. Shifts in the ATR-FTIR peak positions (Figure 5.5b-d), relative to PO_4^{3-} on ferrihydrite, occured when PO_4^{3-} is adsorbed on 5, 10, and 30 mol% Al/Fe oxyhydroxide. Also, an intensity decrease in the modes shown at ~1262, 1201, and 1179 cm^{-1} occur when PO_4^{3-} is adsorbed on 5 mol% Al/Fe oxyhydroxide, relative to PO_4^{3-} on ferrihydrite, although the PO_4^{3-} bands appear at similar vibrational frequencies compared to the Al-free ferrihydrite. In contrast, PO_4^{3-} on 10 and 30 mol% Al/Fe oxyhydroxide show strong IR bands and peak shifts in the modes shown at ~1260, 1189, 1114, 1075, 1014, 946, and ~842 cm^{-1}, relative to the respective peaks for PO_4^{3-} on ferrihydrite. The data shows that the concentration of adsorbed PO_4^{3-} complexes is enhanced with increasingly Al-content, illustrated by the increasing peak area under the Gaussian curves as the Al content in the Al/Fe oxyhydroxide is increased to 30 mol%.

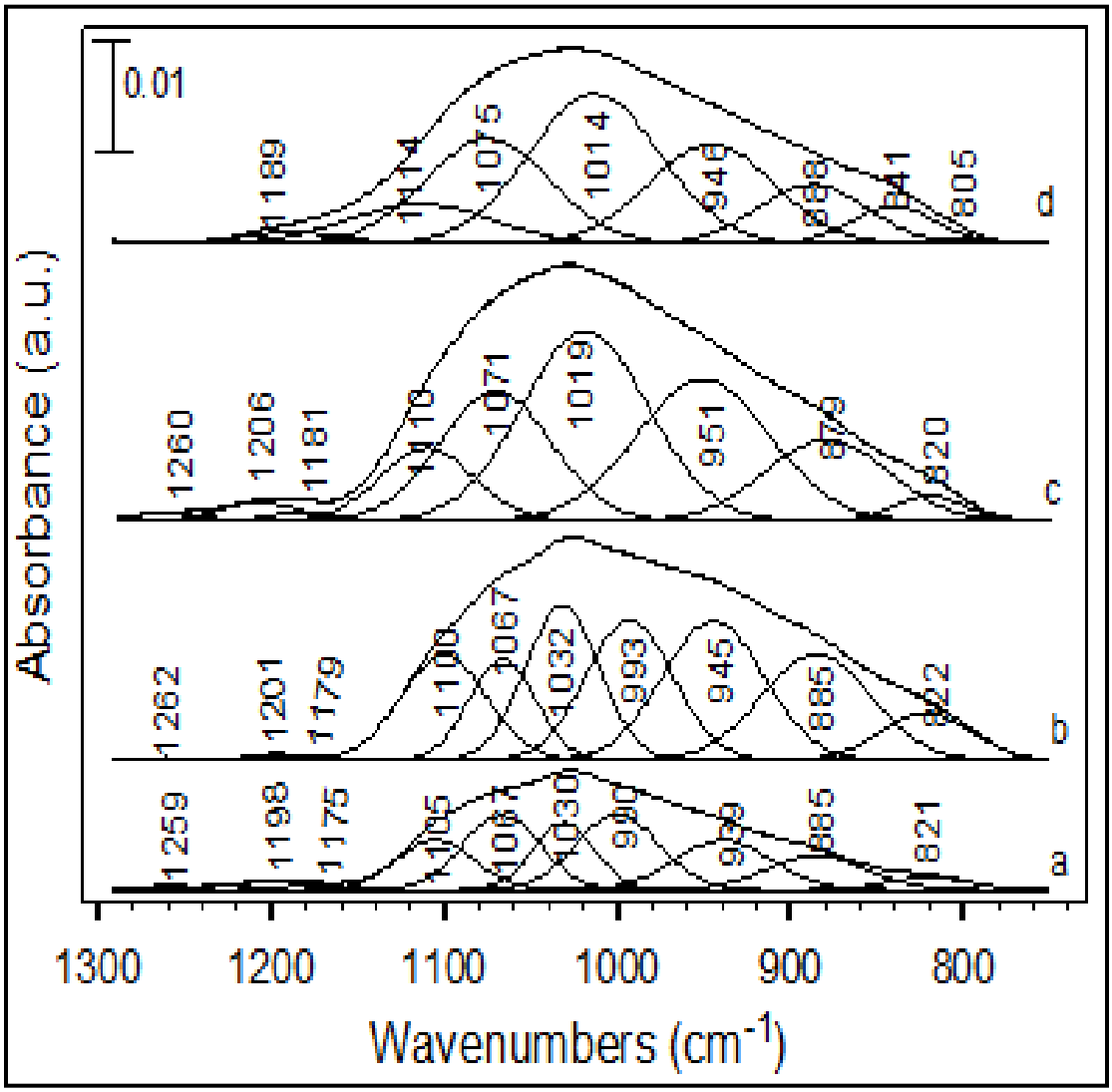

Figure 5.3. ATR-FTIR of 100 μM adsorbed phosphate (In-situ) as a function of increasing Al mol% (a) Al 0%, (b) Al 5%, (c) Al 10%, and (d) Al 30% substituted Al/Fe oxyhydroxide particles at constant pH 7. All spectra are reported after subtraction of the water solution phase from the adsorbed phosphate on the Al/Fe mineral surface taken at the same pH.

Figure 5.6 depicts ATIR-FTIR spectra associated with Al/Fe oxyhydroxide after exposure to a solution containing both CO_3^{2-} and PO_4^{3-} (100 μM) at pH 7. The vibrational modes at ~1478 and 1348 cm^{-1} are assigned to the $\nu_{2(O\text{-}C\text{-}O),\ Asym}$ and $\nu_{3(O\text{-}C\text{-}O),\ Sym}$ modes of adsorbed CO_3^{2-} (Fig. 5.2a). Exposure of 5 mol% Al/Fe oxyhydroxide to CO_3^{2-}/ PO_4^{3-} mixture resulted in the appearance of modes at ~1490 cm^{-1}, 1403, and a shoulder peak at ~1549 cm^{-1}, which we assign to the $\nu_{2(O\text{-}C\text{-}O),\ Asym}$ and $\nu_{3(O\text{-}C\text{-}O),\ Sym}$ of CO_3^{2-}. Fitted modes associated with adsorbed CO_3^{2-} exhibited vibrational shifts to ~1494 and 1393 cm^{-1} as the Al concentration increased to 30 mol%. The degree of $\Delta\nu_3$ on the different mineral surfaces are estimated at ~132, 87, 122, and 101 cm^{-1} as Al content increased (0-30 mol%) in the Al/Fe oxyhydroxide. In addition, the adsorbed CO_3^{2-} mode intensity was significantly reduced in the presence of adsorbed PO_4^{3-} which are strongly pronounced in the lower phosphate region between 1250 and 800 cm^{-1} as a function of Al content. However, the CO_3^{2-} modes correlate well to binuclear monodentate inner-sphere CO_3^{2-} complexes on the Al/Fe oxyhydroxide.

We mentioned that the vibrational modes appearing in the lower wavenumbers region (1250-750 cm^{-1}) are largely associated with adsorbed PO_4^{3-} and to a lesser degree to adsorbed CO_3^{2-} species on ferrihydrite and Al/Fe oxyhydroxide. Peak fitting of this region for PO_4^{3-}/CO_3^{2-} species on ferrihydrite led to features at ~1199, 1156, 1109, 1075, 1037, 988, 935, 887, and 825 cm^{-1}. For 5 mol% Al/Fe oxyhydroxide, peak fitting yields vibrational modes for coadsorbed PO_4^{3-}/CO_3^{2-} at ~1203, 1175, 1110, 1083, 1033, 955, 889, 817 cm^{-1}.

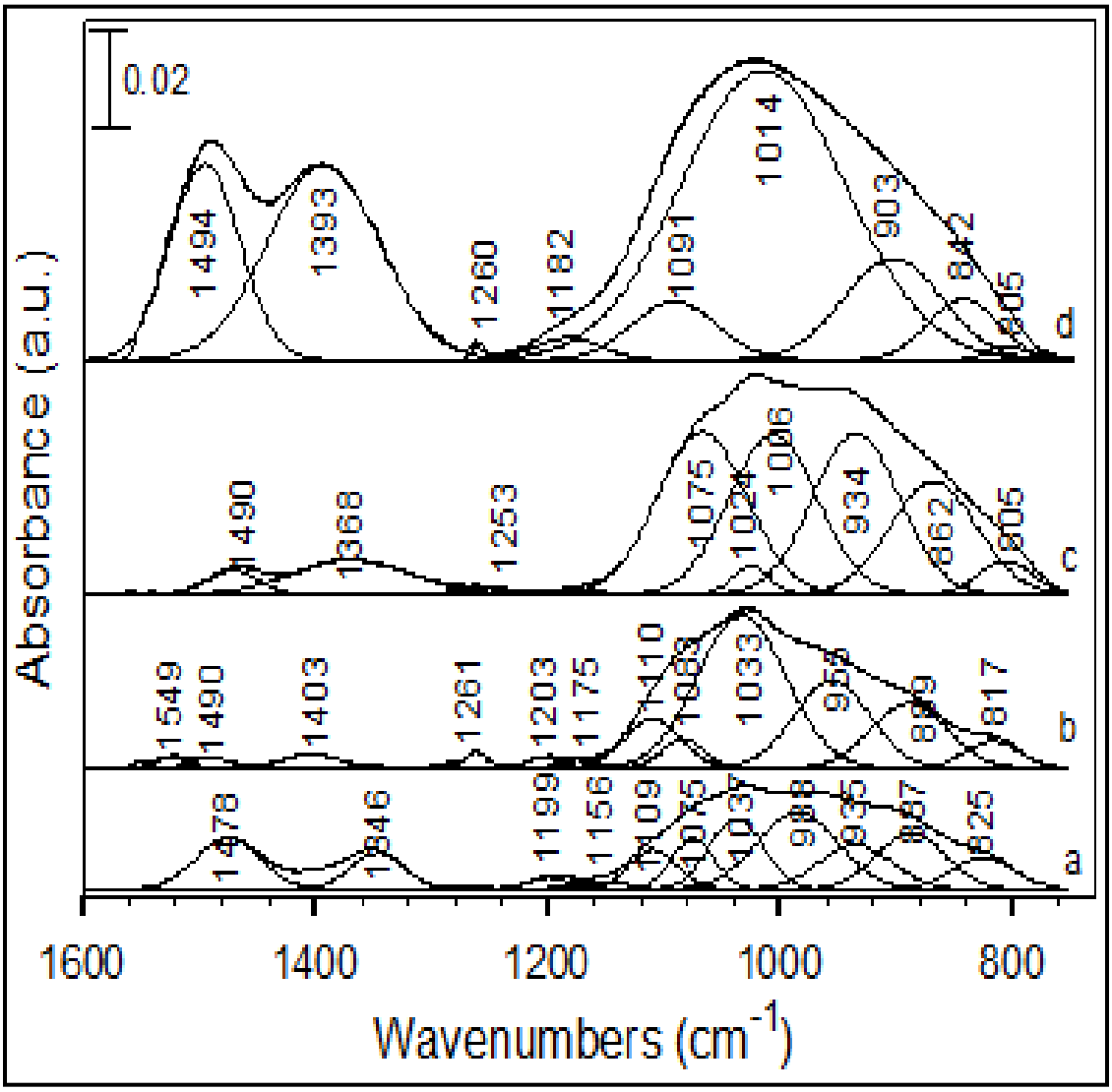

Figure 5.4. In-situ ATR-FTIR of co-adsorbed phosphate/carbonate (100 μM) as a function of increasing Al mol% (a) Al 0%, (b) Al 5%, (c) Al 10%, and (d) Al 30% Al/Fe oxyhydroxide particles at pH 7. The DI water solution phase mineral spectra are subtracted from the mixed PO_4^{3-}/CO_3^{2-} adsorption spectra at the same pH.

Additional modes associated with coadsorbed PO_4^{3-}/CO_3^{2-} appear at ~1253, 1075, 1024, 1006, 934, 862, 805 cm^{-1} for the 10 mol% Al/Fe oxyhydroxide. These modes further shift to ~1260, 1182, 1091, 1014, 903, 842, and 805 cm^{-1} when the Al concentration is raised to 30 mol% (Table 5.1). The shifts of the vibrational modes indicate that there are significant differences in the binding geometry of coadsorbed PO_4^{3-} and CO_3^{2-} on Al/Fe oxyhydroxide relative to the individually adsorbed species on Al/Fe oxyhydroxide. Also, the data shows that the amount of Al in the Al/Fe oxyhydroxide affects the binding of the two adsorbates. The results suggest that PO_4^{3-} and CO_3^{2-} competed for similar binding sites on the Al/Fe oxyhydroxide surfaces, and the PO_4^{3-} complexes appear to bind more strongly as the Al content is increased. This assertion is based on the considerable decrease in the CO_3^{2-} derived peak intensities (~1490/1368 cm^{-1}) and increase in the intensity of the PO_4^{3-} bands as the concentration of Al is increased in the Al/Fe oxyhydroxide. Overall, however, PO_4^{3-} and CO_3^{2-} adsorbed on Al/Fe oxyhydroxide exhibit more intense bands than when the same adsorbates are on ferrihydrite. Some of this increase may be due to the increased surface area of the 30 mol% Al/Fe oxyhydroxide relative to ferrihydrite, but we suspect that it is primarily due to the stronger binding affinity of PO_4^{3-} and CO_3^{2-} on Al/Fe oxyhydroxide surface sites.

Table 5.2. ATR-FTIR (ex-situ) after phosphate adsorption on various mixed Al/Fe oxyhydroxide particles compared to previously adsorbed phosphate modes on different iron oxyhydroxide phases as a function of pH**.**

pH		5.0		4.0	4.2-5.71			7.0		6.0	7.5	7.9			9.0		8	9	9.4
Fhyd	Al 5%	Al 10%	Al 30%	Tejedor	Persson	Fhyd	Al 5%	Al 10%	Al 30%	Tejedor	Arai	Persson	Fhyd	Al 5%	Al 10%	Al 30%	Tejedor	Arai	Persson
800	808	805	808			801	800	800	808				805	819	800	800			
852	847	851	869			855	852	844	856		887		848	865	846	841			840
865	876	888	872		876	896	908	922	925			900	877	893	881	879		890	876
933	933	936	944		939	931	956	966	976	996	952	939	952	956	963	949		940	940
1000	1000	1006	984	1002	1001			1004	1017	1025	1021	1001		1015	1009	986	1001		
1021	1021	1045	1025	1041		1022	1021	1041	1056	1045	1088	1049	1027	1038	1045	1027	1023	1025	
1077	1077	1076	1066	1098	1049	1083	1073	1074	1077	1097		1122	1073	1071	1105	1042	1045		1030
1148	1148	1113	1102	1120	1122	1152	1168	1126	1135				1094	1098	1123	1110	1088	1070	1100
1164	1164	1139	1159		1178			1192					1160	1163	1150	1132			
1210	1210	1194	1215			1207	1220		1217						1199				
1261	1261	1238	1261			1261	1260						1260	1259		1213			

5.3.3 PO_4^{3-} adsorption on Al/Fe oxyhydroxide compared to FeOOH and AlO(OH)

Figure 5.7a shows the results for the batch adsorption of PO_4^{3-} as a function of pH (3.55 - 11) on the (0-30 mol%) Al/Fe oxyhydroxides, at an ionic strength of 10 mM. The amount of adsorbed PO_4^{3-} decreased with increasing pH. In addition, the surface charge could be reversed by exchange of H^+ with OH^- with increasing pH and the resulting deprotonation of PO_4^{3-} surface and solution species likely results in a reduction of PO_4^{3-} adsorption due to electrostatic repulsion with the negatively charged surface. However, overall there is an increase in the amount of PO_4^{3-} that adsorbs as the Al mol% increases in the Al/Fe oxyhydroxide for most of the pH range studied (Figure 5.7a).

PO_4^{3-} absorption isotherms were also investigated at pH 5 and at PO_4^{3-} concentrations that ranged from 5 μM to 1 mM (~30 min equilibration) in the presence of 10 mM NaCl electrolyte. These studies used (0-100 mol%) Al/Fe oxyhydroxide, crystalline α-FeOOH, FerriFh, and $Al(OH)_3$ as substrates (Fig. 5.7b). We chose pH 5 based on prior isotherm results that indicated a higher PO_4^{3-} adsorption envelop at the lower pH range (Cismasu et al. 2012; Kukkadapu et al. 2001). PO_4^{3-} adsorption on the substrates occurred rapidly in the lower concentration range (0.005 to 0.3 mM) with the exception of FerriFh, which showed a slight continuous increase in the concentration of adsorbed PO_4^{3-} up to 0.7 mM. The surface loadings of adsorbed PO_4^{3-} in this lower concentration range was ~2.5 μmole/m^2 for ferrihydrite, ~ 5.2 μmole/m^2 for 5 mol% and 10 mol% Al/Fe oxyhydroxide, and ~7.5 μmole/m^2 on the 30 mol% Al/Fe oxyhydroxide surfaces. Adsorbed PO_4^{3-} showed an increase as the concentration of solution phase PO_4^{3-} was increased up to ~1 mM. Comparatively, adsorbed phosphate decreased on the surface of FerriFh (~1.73 μM/m^2), α-FeOOH (~1.3 μM/m^2), and AlOOH (~0.2 μmole/m^2)

relative to the Al/Fe oxyhydroxide surfaces under similar conditions. Our results for the adsorbed PO_4^{3-} on α-FeOOH, FerriFh, and AlOOH correlate well with prior trend in adsorbed PO_4^{3-} sorption isotherms studies(Arai and Sparks 2007; Chen et al. 2007).

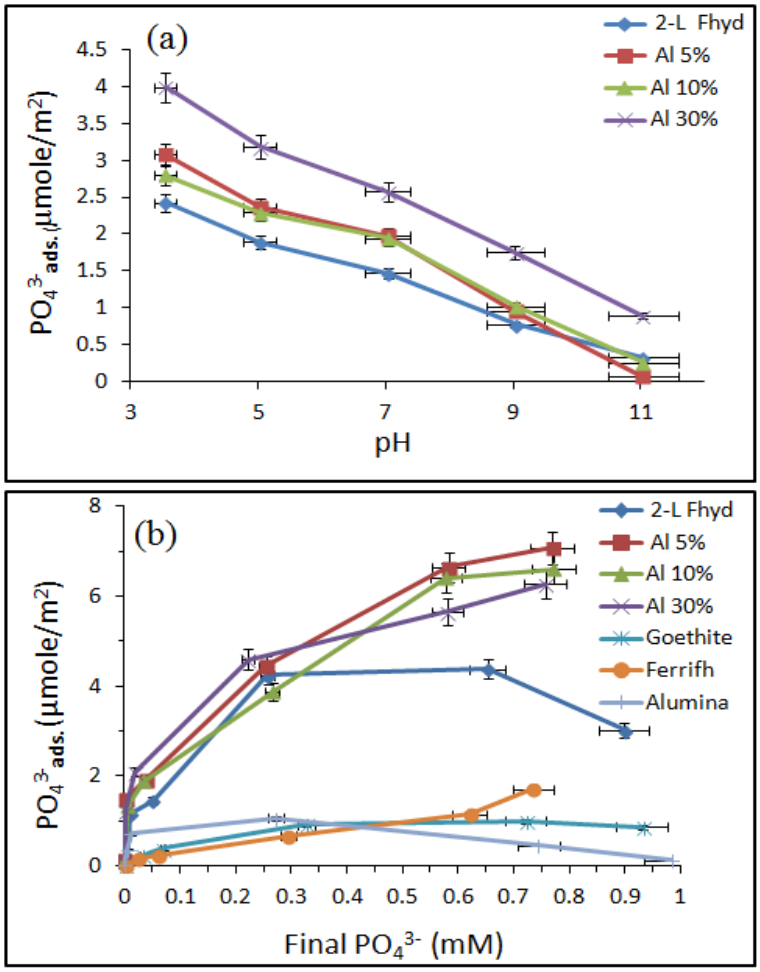

Figure 5.5. (a) Isotherms (ex-situ) of adsorbed phosphate (100 µM and 10 mM NaCl) on the Al/Fe (0-30 mol%) oxyhydroxides normalized surface area as a function of pH (3.55 to 11). (b) PO_4^{3-} adsorption envelops taken at various molarities from 0.005 to 1 mM in with ionic strength of 10 mM on Al/Fe oxyhydroxide (0-100 mol%) suspended particles compared to single crystalline α-FeOOH, ferrihydrite, and FerriFh phases at constant pH 5. The equilibrium amounts (~30 min) of adsorbed PO_4^{3-} are measured from the subtraction of the amount detected by IC from that was initially added in solution and plotted against the normalized amount of phosphate adsorbed per surface area. Error bars are added for duplicate measurements.

5.3.4 ATR-FTIR of PO_4^{3-} after Adsorption on the Al/Fe oxyhydroxide surfaces

To support some of the changes observed from the ex-situ PO_4^{3-} isotherm (associated with Fig. 5.7a), the ATR-FTIR of wet-paste spectra, depicted in Figure 5.8, were collected after phosphate reaction on the 0-30 mol% Al/Fe-oxyhydroxide surfaces in the pH 5-9 range. Note that spectra of the adsorbed/solid particles were taken immediately (washed three times with DI H_2O to remove loosely bound phosphate species) after the completion of the adsorption isotherm (~30 min) at pH 5, 7, 9, and 11. At pH 5, adsorbed PO_4^{3-} on ferrihydrite exhibited strong IR modes at ~1261, 1164, 1077, 1021, 933, 852, and ~800 cm^{-1}. There is almost no significant changes on the PO_4^{3-} vibrational modes at around 1261, 1210 and, 801 cm^{-1} after increasing the pH to 7, and then to 9. However, the intensity of the bands at 1152, 1083, 1022, 931, 896, 855 cm^{-1} significantly decreased after increasing the pH. The ATR spectra of adsorbed PO_4^{3-}, at pH 9, exhibited weak vibrational modes at ~1224, 1193, 1128, 1094, 1047 cm^{-1}, and a broadening of the peaks can be observed in the lower 980-848 cm^{-1} region (e.g., note the increase in the spectra scaling factor as pH increased to 9; see Fig. 5.8a). Similarly, adsorbed PO_4^{3-}vibrational modes on the 5 mol% Al/Fe oxyhydroxide were not significantly affected as the solution pH increased from 5 to 9 as shown in Figure 8b. Adsorbed PO_4^{3-} spectra for 5 mol% Al/Fe oxyhydroxide exhibited IR mode at pH 5 showed peaks at ~1184 cm^{-1}, 1104, 1075, 1035, 1006/998, 961, and 847 cm^{-1}. Moreover, the PO_4^{3-} mode intensity at around 933 cm^{-1} shifted on the 5 mol% Al/Fe oxyhydroxide compared to the vibrational mode associated with PO_4^{3-} on ferrihydrite. As the pH increased to 7, additional IR shoulder peaks appear at ~1122, 1049, 921, 908, 882, 852,

and 840 cm^{-1} (see the arrows sign). Small vibrational modes are also shown at ~1130, 1108, 1015 cm^{-1}, and these modes are broadening in the lower region centered at ~935 cm^{-1} on the surface of the 5 mol% Al/Fe oxyhydroxide at pH 9.

In contrast to the Al/Fe oxyhydroxide having an Al-content in the 0-5 mol% range, which showed similar adsorbed PO_4^{3-} binding configurations as a function of pH, the spectral features of adsorbed PO_4^{3-} on the 10 and 30 mol% Al/Fe-oxyhydroxide showed significant differences. The main PO_4^{3-} modes were observed at about 1113, 1076, 1045, and 851 cm^{-1} at pH 5 on the 10 mol% Al/Fe oxyhydroxide surface. At pH 7, the position of the major modes are shifted to 1110, 1041, 1004, 969, and 844 cm^{-1}. The intensity of these bands decreased at pH 9 and are shown at around 1123, 1045, 1009 with additional shoulder modes shown at ~1199, 963, 949, 918, and ~845 cm^{-1} on the 10 mol% Al/Fe oxyhydroxide. However, the ATR-FTIR spectra of adsorbed PO_4^{3-} on 30 mol% Al/Fe-oxyhydroxide shows broad convoluted modes (1180-800 cm^{-1} region) at pH 5 with additional spectral broadening at pH 9. Peak fittings revealed narrow bands centered near 1104, 1066, 1025, 984, 944, and 905 cm^{-1} at pH 5 as illustrated in Figure 5.8d. As the solution pH increased to 7, the vibrational modes shifted to 1135, 1077, 1056, 1017, 976 cm^{-1} with a slight shifts and an increase in the peak intensities at around 925, 883, and 856 cm^{-1}. In addition, modes associated with adsorbed PO_4^{3-} adsorbed on 30 mol% Al/Fe oxyhydroxide at pH 9 increased in intensity in the lower frequency region for almost all the frequencies shown: at ~1042, 1027, 986, 949, 914, 873, and 840 cm^{-1}.

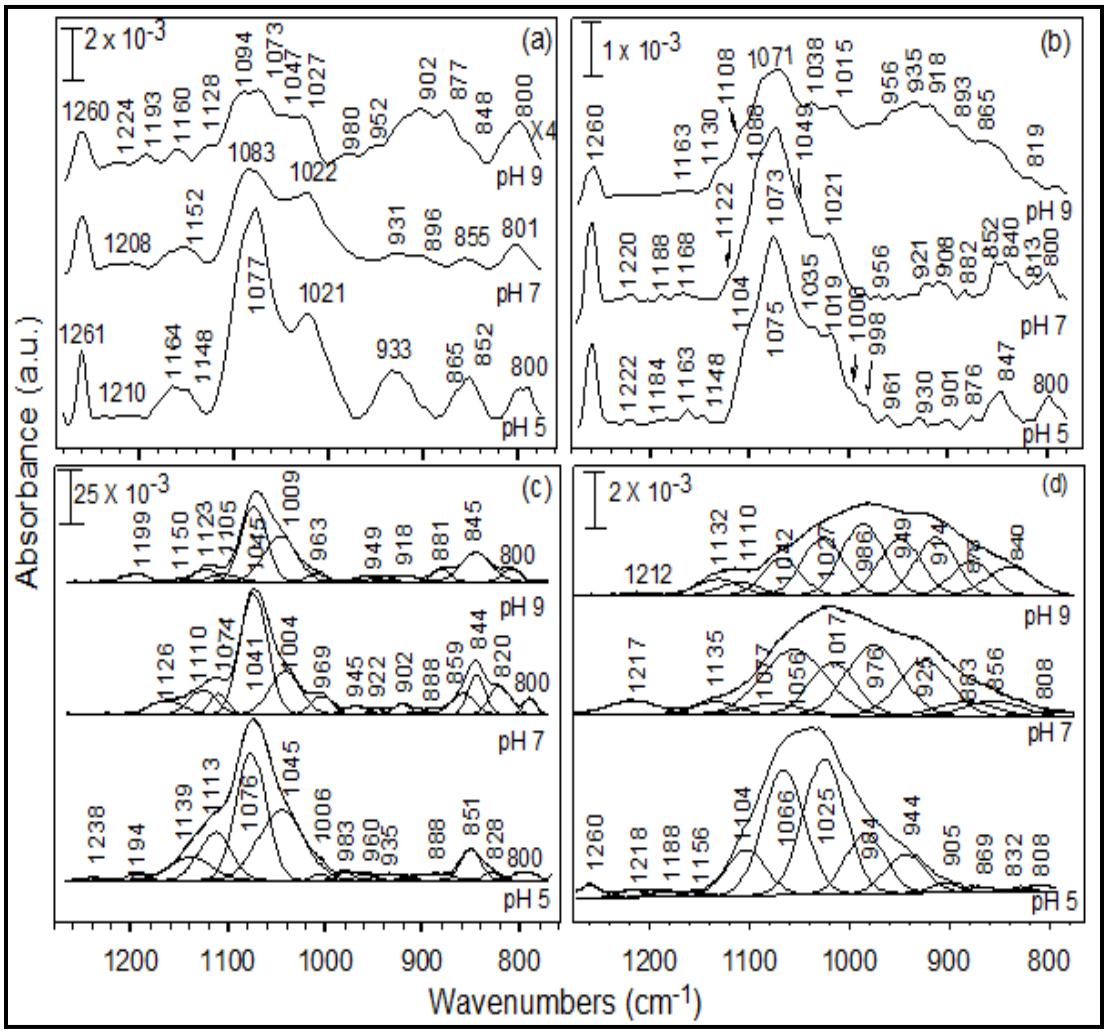

Figure 5.6. ATR-FTIR spectra of adsorbed phosphate (100 μM) after sorption isotherm of PO_4^{3-} adsorbed (Ex-situ) in aqueous solution onto (a) Al 0%, (b) Al 5%, (c) Al 10%, and (d) Al 30% Al/Fe oxyhydroxide particles at various pH 5-9. The supernatant solution phase spectra are subtracted from the adsorbed $PO_4^{3-}{}_{(aq.)}$ surface of the wet paste materials at the same pH.

Figure 5.9(a-d) exhibits the ATR-FTIR vibrational spectra of adsorbed phosphate (~100 μM PO_4^{3-}) taken after the isotherm experiments (i.e., associated Figure 5.7b) in the presence of 10 mM NaCl and pH 5 on the surface of single phase ferrihydrite as compared to other ferrimagnetic ferrihydrite, and goethite. Adsorption of phosphate is shown for the aluminum oxyhydroxide particles after equilibrium phosphate adsorption of 1 mM at pH 5 to increase the ATR-FTIR spectral quality (Fig. 5.9d). The fitted peaks in Figure 5.9a of adsorbed phosphate modes are related to those previously described in Figure 5.8a at pH 5 for the pure ferrihydrite surface. However, broad phosphate spectra features are shown on the surface of FerriFh nanoparticles with IR bands deconvolution shown at ~1254 cm^{-1}, 1137, 1110, 1080, 1053, 1026, 997, 968, 941, 907, 872, 853, and 832 cm^{-1} (Fig. 5.9b). The modes at ~1243 cm^{-1}, 1197, 1176, 1137, 1126, 1114 cm^{-1}, 1102, 1085, 1069, 1058, 1024, 1013, and 996 cm^{-1} appeared on the micro-goethite crystalline particles surface (Figure 5.9c) which were collected below the magnitude of the strong Fe-OOH mode contributions usually appear at ~889 and 796 cm^{-1}. Kubicki et al., 2012 observed similar vibrational bands position under their experimental conditions at pH 5.71 (Kubicki et al. 2012a). The increase in peak area observed in the 1250-950 cm-1 region for the AlOOH surfaces is due to a higher surface phosphate loading. However, the modes shown at ~1248, 1227, 1178, 1133, 1099, 1067, 1035, 1004 cm^{-1} are shifted and are characteristic of similar phosphate binding configurations on the AlOOH compared to FeOOH surfaces. The weak shoulder peaks exhibit at ~954, 914, 889, 869, 852, and 803 cm^{-1} form the lower frequency region may be slightly influenced by the Al-O stretching-bending coupling from the AlOOH structure. The results imply that the binding configuration and loading of adsorbed phosphate surface complexes increased as

an effect of an increase binding affinity for the high Al substitution in the Al/Fe-oxyhydroxides or the AlOOH surfaces.

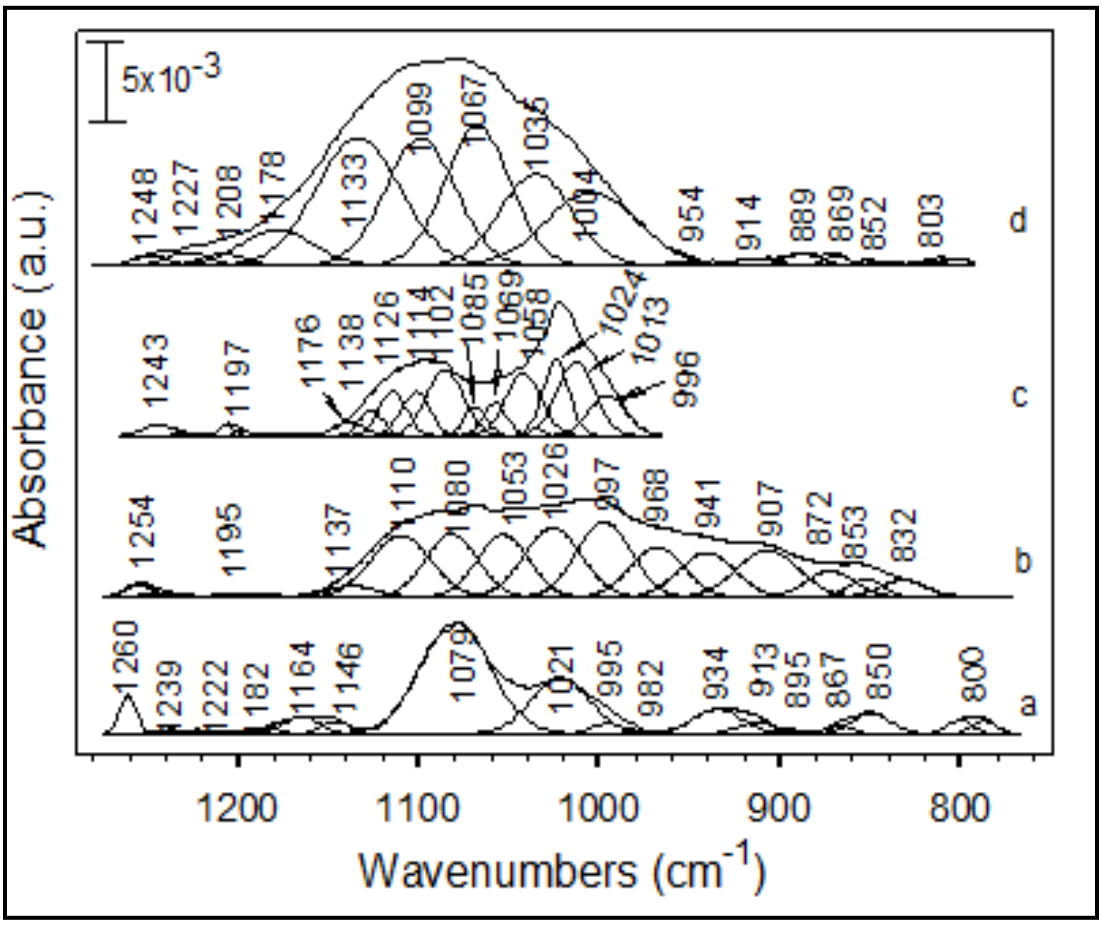

Figure 5.7. ATR-FTIR spectra (ex-situ) after sorption isotherm of PO_4^{3-} (100 μM) adsorbed onto suspended (a) ferrihydrite (b) ferrimagnetic ferrihydrite (FerriFh), (c) goethite, and (d) pure AlOOH particles surface at (1 mM PO_4^{3-}) pH 5. The solution phase spectra on a specific mineral are subtracted from the adsorbed $PO_4^{3-}{}_{(aq.)}$ surface of the wet paste particles at the same pH.

5.3.4 ATR−FTIR spectra of phosphate adsorbed onto different goethite structures

We mentioned that Section 5.3.4 and 5.3.5 are modified reprints from the publications in Langmuir by Kubicki et al., 2012 and Geochimica et Cosmochimica Acta by Wei Li et al., 2013, respectively. The data are reproduced with the expressed written copyright permission of the publishers. Figure 5.10 shows the XRD patterns for the micro-goethite as compared to the nano-goethite synthesized materials. The micro-goethite (Fig. 5.10a) shows more intense polycrystalline Bragg diffraction lines with some slight differences in the sharpness of the d-spacing values as compared to the nano-goethite phase (Fig. 5.10b). The XRD patterns are similar to those previously reported in the database of the International Center for Diffraction Data (ICDD). The most notable difference between the patterns is displayed between the 5 to 25 2θ° regions showing a slight shift in the diffraction lines from 15 to 13.5 2θ°. As a result of the synthesis methods, the degree of crystallinity is shown to be higher in the micro-goethite (67.6 ± 0.3 $m^2 g^{-1}$) than in the nano-goethite (139.1 ± 0.8 $m^2 g^{-1}$) XRD patterns as deduced from the XRD patterns.

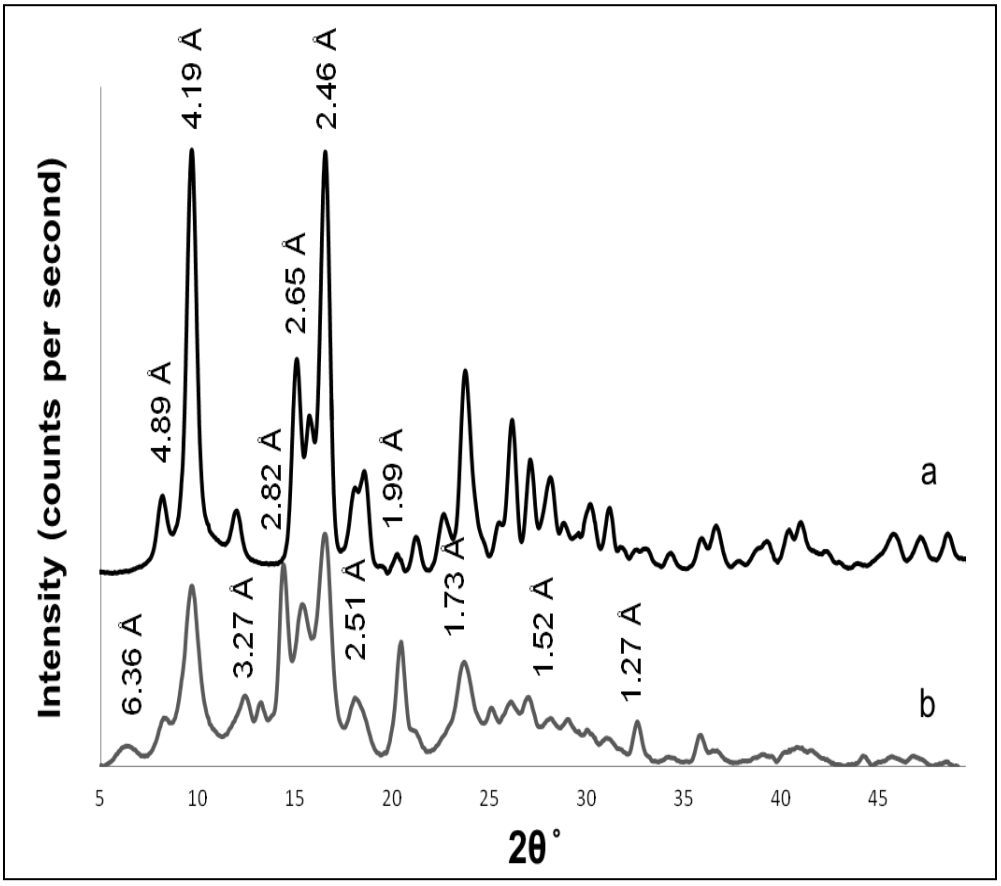

Figure 5.8. XRD patterns for (b) nano-goethite and (a) micro-goethite.

TEM was used to characterize the goethite of varying crystallinity that was observed from XRD analysis. Representative TEM images for the synthesized micro-goethite and nano-goethite are shown in Figure 5.11. The TEM images show acicular nanorods with lengths measured around 100-200 nm and widths of ca. 70 nm for nano-goethite (Fig. 5.11a-b), while more polycrystalline microrods goethite shows lengths between approximately 200 and 900 nm and ca. 50 nm width (Fig. 5.11c-d). The nano-goethite exhibited a rough, irregular, star like surface whereas the micro-goethite showed narrow, rectangular needle crystalline rods with well-ordered smooth edges. In addition, the nano-goethite structure formed star-like (aggregates) poorly-crystalline arrangements, which may contain small presence of amorphous nanoparticles lying on top of the crystalline nanorods geothite phases contributing to a broader and lower intensity in the Bragg diffraction reflection lines (see Fig. 5.10b). The TEM results for the micro-goethite show the morphology of microrods crystalline phases, which corresponds well to the slight shift in full width at half maximum height (FWHM) and an increase in the X-ray diffraction lines intensity contributing to an high degree of the goethite crystalline structure formed (see Fig. 5.10a).

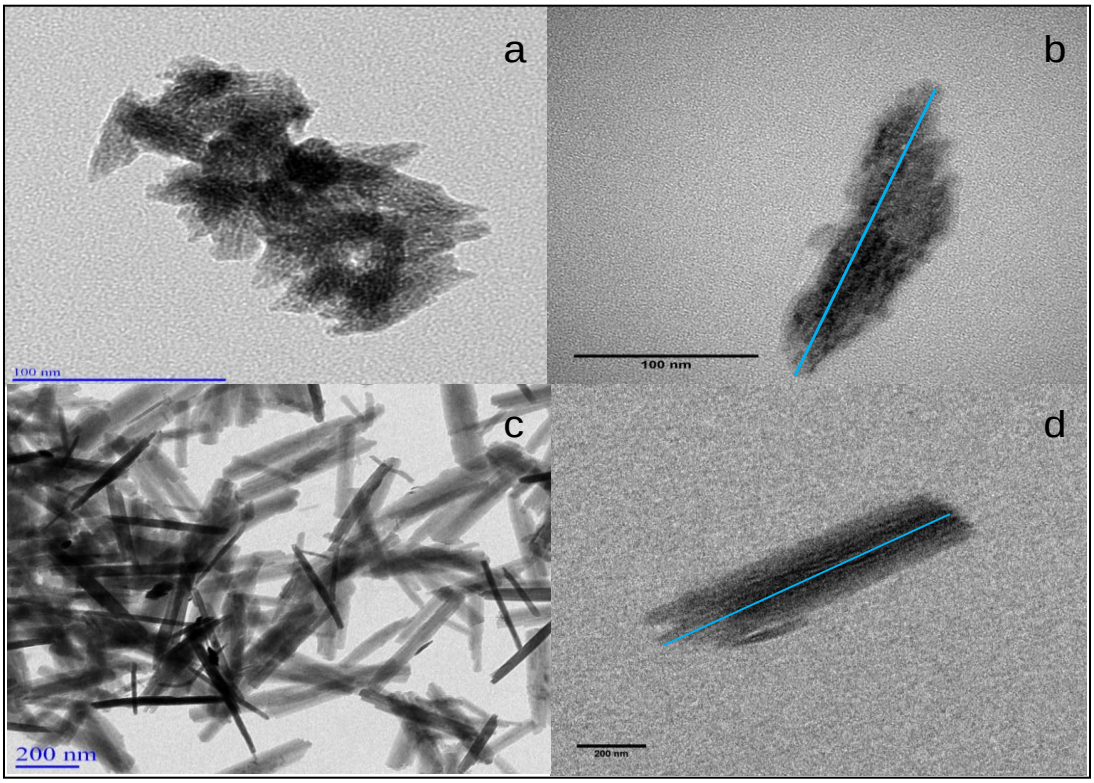

Figure 5.9. TEM images of (a) acicular crystalline and (b) nanorods of goethite with measured lengths of approximately 237 nm. TEM images of (c) needles and (d) single microrods of goethite with measured lengths of approximately 900 nm. Note the more irregular habits of the nano-goethite compared to the micro-goethite.

Nanogoethite. Figure 5.12 exhibits in situ ATR−FTIR results for the adsorbed phosphate on the nanogoethite phase for the 1200 to 800 cm^{-1} region. Note that surface loading decreases as the pH increases, necessitating greater amplification of the IR intensity in the spectra of the higher-pH samples. The ATR−FTIR of adsorbed phosphate vibrational modes on either goethite phase exhibit broad bands. The fitted pH 4.22 spectrum shows three main bands at 1084, 1044, and 1005 cm^{-1}. The pH 4.22 IR spectrum also indicates the presence of significant peaks at 1176, 1117, 957, 876, and 857 cm^{-1} (Figure 5.12a). For the pH 5.71 spectrum (Figure 5.12b), the peak deconvoluted modes appeared mainly at 1122, 1089, 1039, and 1004 cm^{-1} with additional spectral intensity at 962, 932, and 876 cm^{-1} illustrated in Figure 5.12b. As the pH increased to 7.51, the associated fitted spectrum exhibited adsorbed phosphate modes at 1128, 1083, 1038, and 1009 cm^{-1} and spectral shoulders at 966, 932, and 884 cm^{-1} (Figure 8c). At pH 7.96, the associated fitted spectrum shows modes at 1124, 1082, 1036, 1006, 966, 935, 887, and 865 cm^{-1} (Figure 5.12d).

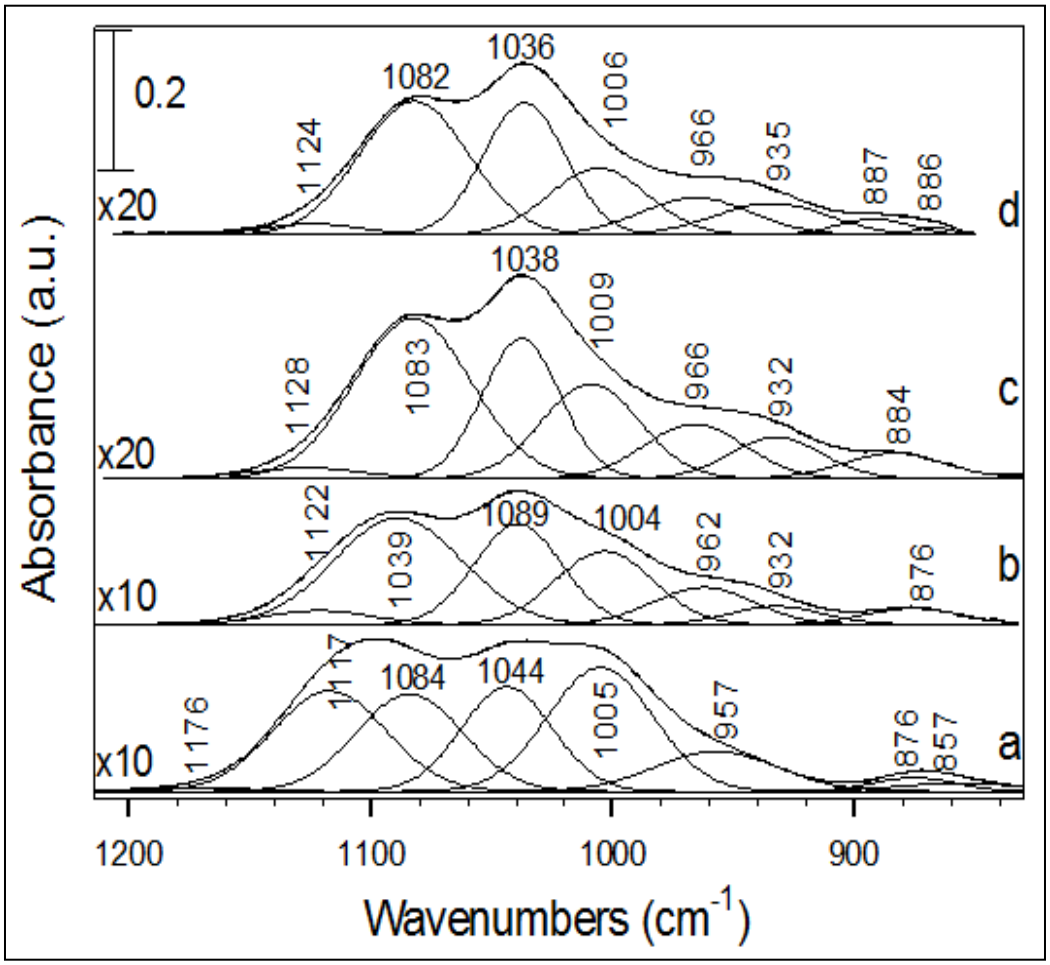

Figure 5.10. Fitted ATR-FTIR data for adsorbed phosphate (100 μM) on nano-goethite at pH (a) 4.22, (b) 5.71, (c) 7.51, and (d)7.96.

The IR bands experimentally observed in this study are similar to prior vibrational modes of adsorbed orthophosphate complexes on goethite ($FeHPO_4^+$) reported in a study by Tejedor−Tejedor and Anderson as shown in Table 5.3 (Tejedor Tejedor and Anderson 1990). Tejedor−Tejedor and Anderson assigned modes at approximately 1120 and 1001−1088 cm^{-1} to the $\nu_{(PO)}$ stretching modes of a monodentate protonated phosphate complex in the pH range of 3.6−6.0. Furthermore, the possible presence of a $FeH_2PO_4^{2+}$ complex at the lower end of the pH range had also been postulated in their study. In their study, the $\nu_{(PO)}$ stretching modes observed near 1089, 1044, and 945 cm^{-1} were assigned to either the nonprotonated bidentate $(FeO)_2PO_2$ or monoprotonated monodentate $(FeO)_2(OH)PO_2$ complexes at a higher pH of 9.2 (Luengo et al. 2006).

Microgoethite. Using a similar experimental procedure, we investigated the adsorption of phosphate at various pH values on microgoethite with ATR−FTIR. The resulting spectra are illustrated in Figure 5.13 in the range of 1200−900 cm^{-1}. The fitted spectrum associated with adsorbed phosphate on microgoethite at the lower pH of 4.22 exhibits vibrational modes at 1157, 1122, 1091, 1044, 1009, and 982 cm^{-1} (Figure 5.13a). An increase in the pH to 5.71 resulted in the appearance of modes at 1120, 1090, 1043, and 1012 and two weak modes at 954 and 941 cm^{-1} (Figure 5.13b). The fitted IR spectrum of adsorbed phosphate at a nearly neutral pH of 7.51 exhibited relatively strong vibrational bands at 1084 and 1043 cm^{-1} with a mode fitted at 1022 cm^{-1} and weak bands at 1124, 946, 923, and 903 cm^{-1} (Figure 5.13c). As the pH increased to 7.96, the associated deconvoluted spectrum exhibited modes at 1095, 1076, 1039, 1005, 971, and 938 cm^{-1} and relatively weak peaks at 1160, 1129, and 915 cm^{-1} (Figure 5.13d).

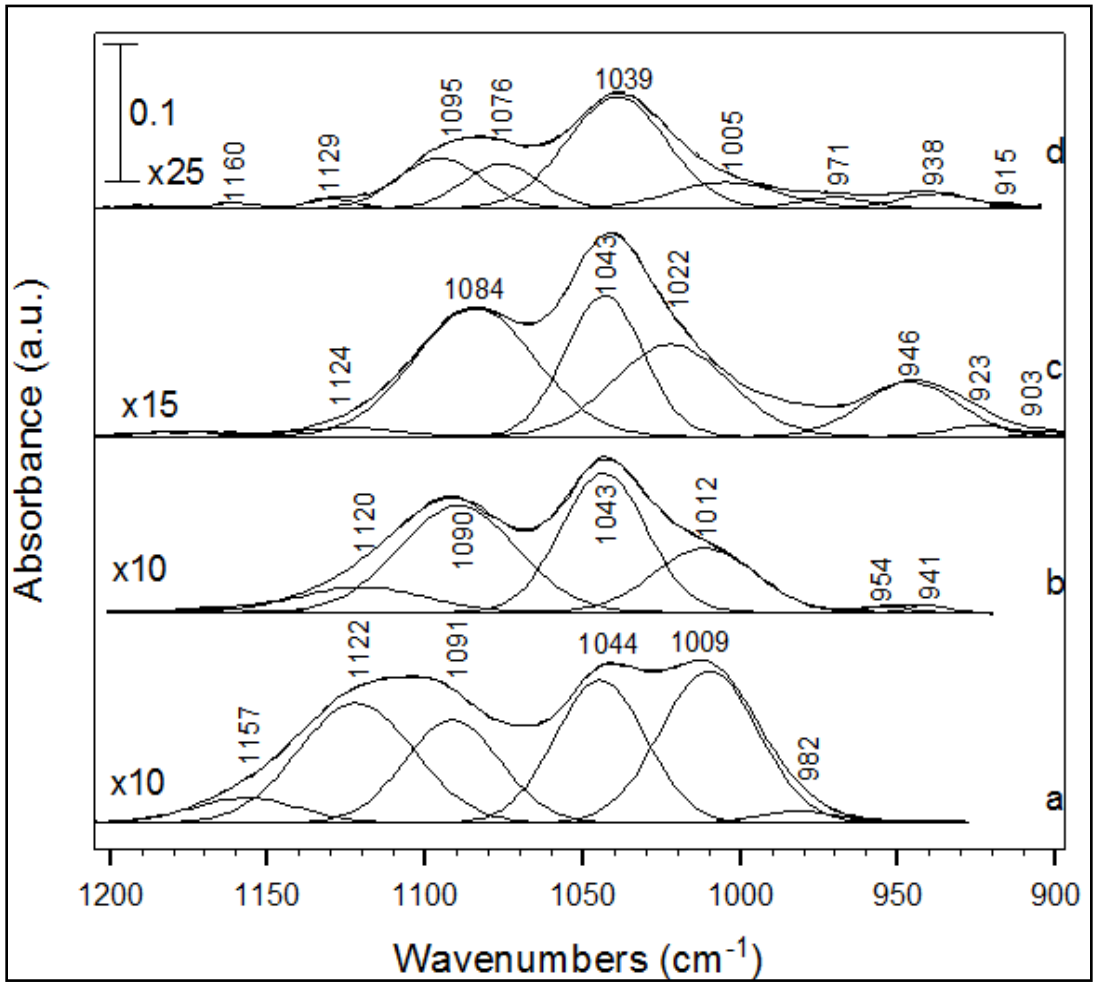

Figure 5.11. Fitted ATR-FTIR data for adsorbed phosphate (100 μM) on micro-goethite at pH (a) 4.22, (b) 5.71, (c) 7.51, and (d) 7.96.

Although the phosphate modes associated with nanogoethite and microgoethite show similar trends with pH, a direct comparison shows that there are differences in the positions of modes for the two systems. For example, at pH 4.22 phosphate exhibited modes at ~1117, 1084, and 957 cm^{-1} when adsorbed on nanogoethite, whereas on microgoethite these modes are observed at ~1157, 1091, and 982 cm^{-1} (Table 5.3). As the pH increased above 4.22 to 7.96, the differences in the location of the vibrational modes associated with phosphate adsorbed on nanogoethite and microgoethite persisted. These frequency variations between the two samples are probably due to differences in the crystalline goethite habits associated with nanogoethite and microgoethite. Prior studies, for example, have shown that the surfaces of high-specific-area (SA) goethite nanoparticles are mostly composed of (101) and (001) faces, whereas the surface of goethite with low SA contains an additional high degree of (010)/(210) faces (Pnma space group) with high surface density (Villalobos 2000). Hence, although we were not able to characterize the surfaces present on the samples used in this study, the vibrational shifts between adsorbed phosphate modes on nanogoethite and microgoethite at a given pH are at least in part due to differences in the crystal habit between the two samples.

Goethite Dried Samples. Figure 5.14 displays ATR−FTIR spectra of adsorbed phosphate on a micro-goethite surface after being dried with a stream of N_2. At pH 4.22, adsorbed phosphate exhibited strong modes at 1176, 1123, and 1003 cm^{-1} (Table 5.4 and Figure 5.14a). The positions of the adsorbed phosphate modes on the microgoethite surface were not greatly affected as the pH was increased from 4.22 to 7.96, as illustrated in Figure 5.14(a−d). However, the intensity of these phosphate modes decreased on the

surface as the pH increased most likely because of less adsorption of phosphate at the higher pH (Note the increasing scale factors in Figure 5.14.). To isolate the spectral features of adsorbed phosphate better, deconvolution of the spectra was carried out, and these analyses revealed modes near 1087, 1066, 1050, 1017, and 965 cm^{-1} as the pH was increased to 7.96. These changes with pH suggest different phosphate species coordinated as a function of pH.

Table 5.3. ATR−FTIR frequencies of adsorbed phosphate at 100 μM on different nanogoethite and microgoethite phase at various pH values.

For Phosphate under Wet Sample Conditions														
	4.0	4.22		4.2−5.7	5.71		6.0	7.5	7.51		7.9	7.96		8
pH	Tejedor[27]	(micro)	(nano)	Persson[23]	(micro)	(nano)	Tejedor[27]	Arai[24]	(micro)	(nano)	Persson[23]	(micro)	(nano)	Tejedor[27]
			857							823			886	
			876	876		876		887	903	884	900	915	887	
		939		939	941	932			923	932	939	938	935	
			957		954	962		952	946	966		952	966	
		982										971		
	1002	1009	1005	1001	1012	1004	996			1009	1001	1005	1006	1001
							1025	1021	1022					1023
	1041	1044	1044	1049	1043	1039	1045		1043		1049	1039	1036	1045
			1084						1084			1076	1082	
	1098	1091			1090	1089	1097	1088				1095		1088
	1120	1122	1117	1122	1120	1122			1124		1122		1124	
		1157	1176	1178	1164	1176			1177				1129	
		1195												

For a 0.1 mM Dried Phosphate Sample after Adsorption								
	4.22		5.71		7.51		7.96	
pH	(micro)	(nano)	(micro)	(nano)	(micro)	(nano)	(micro)	(nano)
			963			962	965	
	1003	997	1002	1005	994	1000	998	992
		1017			1017	1022	1017	1017
	1032	1044	1033	1030	1043			1041
	1059		1052		1058		1050	1057
			1068	1062	1077	1068	1066	1077
	1091	1087	1089	1083	1087	1088	1087	1087
				1100	1098	1099	1104	1098
	1107		1109	1113	1110	1109		1112
	1123	1119	1123	1128	1123	1122	1121	
	1138		1137		1135	1137	1136	1133
		1142		1143	1143			1144
	1155	1156	1151	1158	1155	1156	1155	1156
		1173	1172		1169			1170
	1176			1182	1179	1175	1176	1182
		1191			1192			1192
	1198		1202	1202	1204		1200	1203
	1224	1216			1221	1223	1225	1223
		1249	1235		1254	1245	1244	1250

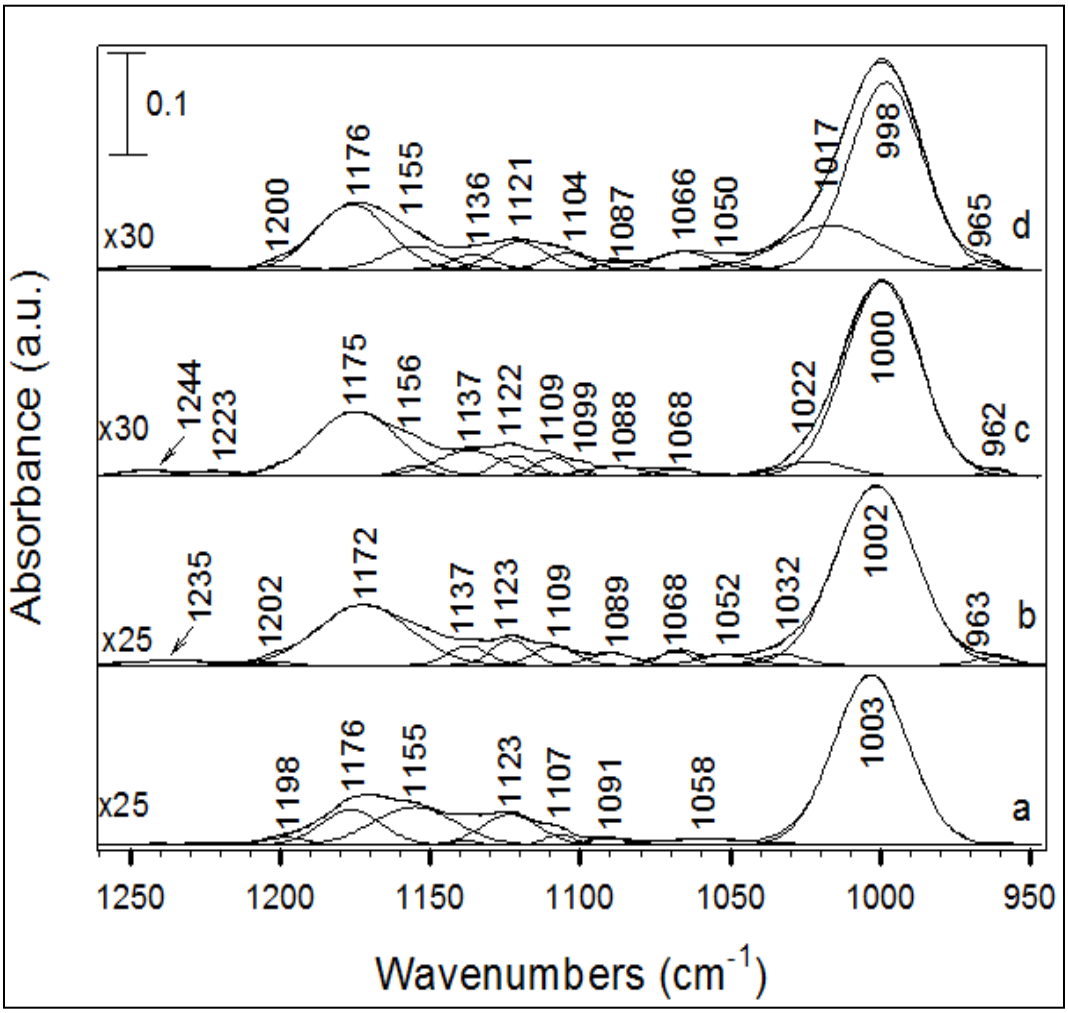

Figure 5.12. Fitted ATR−FTIR data for adsorbed phosphate (100 μM) on microgoethite at pH (a) 4.22, (b) 5.71, (c) 7.51, and (d) 7.96 after drying.

These other species also increase in concentration with increasing pH as shown in Figure 5.14(b−d). Tejedor−Tejedor and Anderson observed three set of bands under their experimental conditions (Tejedor Tejedor and Anderson 1990). Their mode positions shown at 1123, 1006, and 982 cm^{-1} were assigned to either $(FeO)_2(OH)PO$ monodentate protonated or to $(FeO)(OH)_2PO$ diprotonated bidentate complexes in the pH range of 3.6−6. The modes found at 1096 and 1044 cm^{-1} were assigned to the PO_2 group and were attributed to either nonprotonated bidentate or the monoprotonated monodentate complexes in the pH range of 6 to 8.4. Their 1025 and 1001/998 cm^{-1} band assignments were correlated to the monodentate deprotonated complex at a pH above 9.6. Although these bands have been assigned to give information on the protonation/depro-tonation of phosphate complexes on an identical crystalline goethite surface that could contain multiple surfaces, our ATR−FTIR results differ slightly and show that under a lower phosphate concentration the adsorption bands at any of the given experimental pH values are mostly indistinguishable from each other.

Adsorbed phosphate species on the nanogoethite sample after drying are shown in Figure 5.15. The modes illustrated at 1119 and 1017 cm^{-1} appeared at pH 4.22 (Figure 5.15a). As the pH increased from 4.22 to 7.96, the position of the adsorbed phosphate modes changed slightly as shown by the peak fittings of additional small shoulder vibrational modes. Overall, the main positions of the 1123 and 1017 cm^{-1} modes were present in all of the spectra under all pH conditions. Furthermore, the spectral results showed the development of modes near 1087, 1057, 1041, and 992 cm^{-1} with additional modes around 1250 and 1182 cm^{-1} as the pH increased to 7.96 as illustrated in Figure 5.15(b−d). The mode at 1250 cm^{-1} has been assigned to the $\nu_{(C-O)}$ stretching mode that is

due to an increase in adsorbed carbonate species above pH 7 resulting from the reaction of the sample with atmospheric CO_2, but this could also be due to a P−O−H bending mode.

Similar to the microgoethite surface, the nanogoethite surface exhibits no significant changes in phosphate vibrational band positions as the pH increases. However, the nanogoethite surfaces did exhibit some differences from the microgoethite surfaces, notably the asymmetrical adsorbed phosphate mode on the microgoethite crystalline surface at 1176 cm^{-1} at high pH, compared to the analogous mode at 1123 cm^{-1} associated with the nanogoethite surface. The symmetrical adsorbed phosphate mode centered at 1000 cm^{-1} on the microgoethite surface also showed a shift to 1017 cm^{-1}, which is approximately 17 cm^{-1} higher than the analogous phosphate mode associated with nanogoethite. These results suggest that the structures of the phosphate complexes are sensitive to the goethite crystallographic habit on which they adsorb. Differences in the microscopic structure of the two different goethite surfaces play a crucial role in the binding of the adsorbed phosphate species. Persson et al., 1996, found similar results in a prior phosphate/goethite study reported in Table 5.3 (Persson et al. 1996). At low pH (3 to 4), two main bands at 1178 and 1001 cm^{-1} dominated their phosphate/goethite vibrational data whereas at higher pH (10.8 to 12.8) the 1120 cm−1 band disappeared and two additional modes appeared at 1057 and 966 cm^{-1}. Their findings agree well with those of Tejedor−Tejedor and Anderson as a function of pH (Tejedor Tejedor and Anderson 1990).

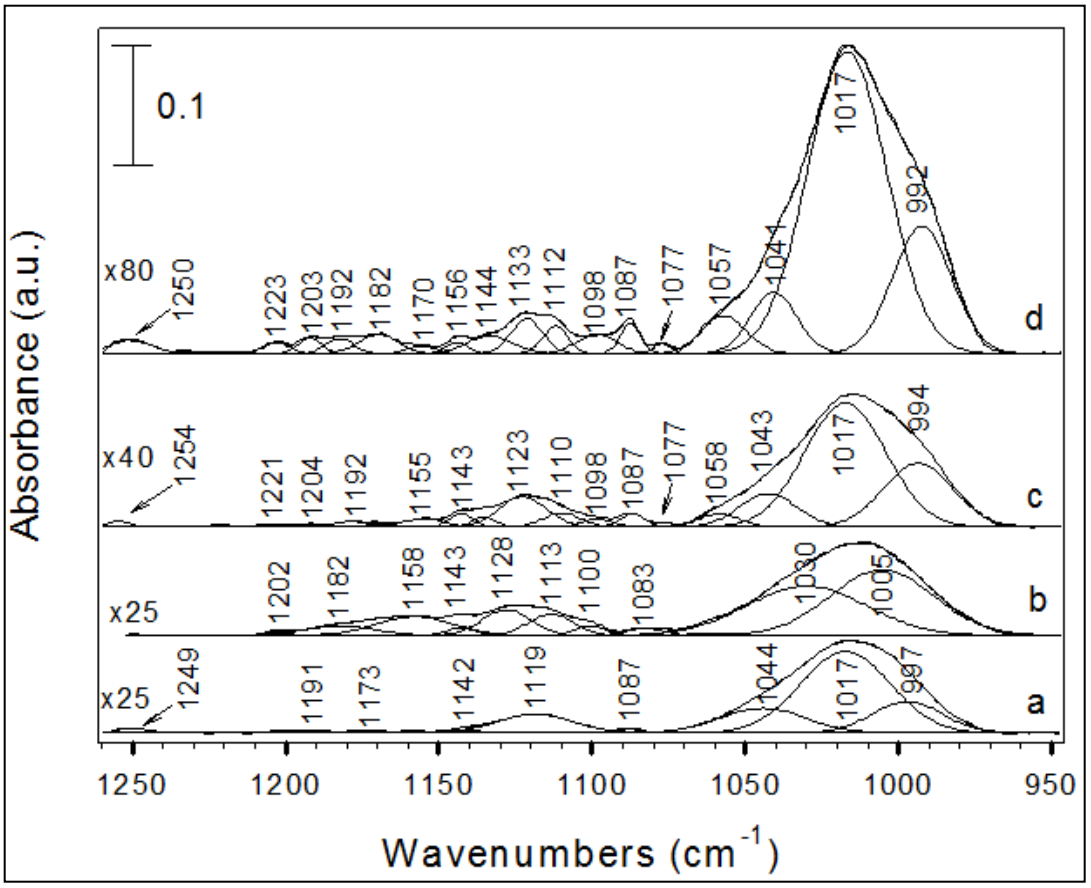

Figure 5. 13. Fitted ATR−FTIR data for adsorbed phosphate (100 μM) on nanogoethite at pH (a) 4.22, (b) 5.71, (c) 7.51, and (d) 7.96 after drying.

Although the cited prior works investigated phosphate adsorption complexes on goethite that could contain multiple surfaces, our study shows that adsorbed phosphate on two different goethite samples leads to a variety of surface complexes depending on the crystal habits of the mineral. The changes in our IR spectra (Figures 5.14 and 5.15) with pH for the adsorbed phosphate complexes on the microgoethite and nanogoethite surfaces suggest that several phosphate species coexist. Again, it should be pointed out that the IR vibrational shifts for phosphate on the different samples are likely to be more strongly related to the presence of different adsorbed phosphate surface complexes due to structural variations between the goethite. The potential differences between surfaces present on nanogoethite and microgoethite will be examined in the Discussion Section below in light of the calculated frequencies for each surface model.

5.3.5 Structure and ATR-FTIR of Phosphate Adsorbed onto Corundum (α-Al_2O_3)

The ATR-FTIR spectra of phosphate adsorbed on corundum prepared from pH 5 to pH 9 are shown in Figure 5.16. Spectrum (a) represents a clean corundum surface obtained from the subtraction of pH 9 from pH5 of the α-Al_2O_3/water spectra without phosphate in the region of 850-1400 cm^{-1}. Frequencies lower than 960 cm^{-1} are not considered due to overlap with the IR background of corundum and complicated stretching–bending coupling. All the spectra show poorly resolved broad features, consistent with prior published report (Del Nero et al. 2009). An apparent spectral drifting to the lower wavenumbers from pH 5 to pH 9 was observed. This pH effect is similar to the IR studies of phosphate adsorbed on hematite (Elzinga and Sparks 2007), which may arise from the different H-bonding network around phosphate at different pH

conditions, deprotonation of surface adsorbed phosphate, or different coordination of phosphate to surface Al. These FTIR spectra suggest a dominant inner-sphere complexation mechanism. Compared to the experimental IR spectra of aqueous phosphates, the IR feature centered at ~1100 cm^{-1} at pH 5 (Fig. 5.17e) differs significantly from those of aqueous $H_2PO_4^-$ (Fig. 5.17b), the predominant species in solution at pH 5, suggesting the dominance of inner-sphere P complexes on the corundum surface. Given that the broad feature covers all IR frequencies of aqueous $H_2PO_4^-$, it is possible to have some outer-sphere complexes or free $H_2PO_4^-$ on the corundum surface. Similar conclusions can be drawn from the comparison between the spectra for the adsorbed sample at pH 9 (Fig. 5.17f) and aqueous HPO_4^{2-} (Fig. 5.17b).

Unfortunately, more specific and detailed structural interpretation could not be obtained to distinguish between bidentate and monodentate complexes because of the poor resolution of the IR bands (Del Nero et al. 2009). In this case, it appears that analysis of phosphate bonding on aluminum (hydr)oxides is more difficult than characterizing the phosphate bonding structure on iron (hydr)oxides, in which well separated IR peaks could be observed. Compared to the IR studies of phosphate on goethite (Tejedor Tejedor and Anderson 1990) and/or hematite (Elzinga and Sparks 2007), the spectral region used in the present study was smaller, due to the strong Al–O (< 900 cm^{-1}) absorption band associated with corundum that overlaps the phosphate vibration band near 800 cm^{-1}.

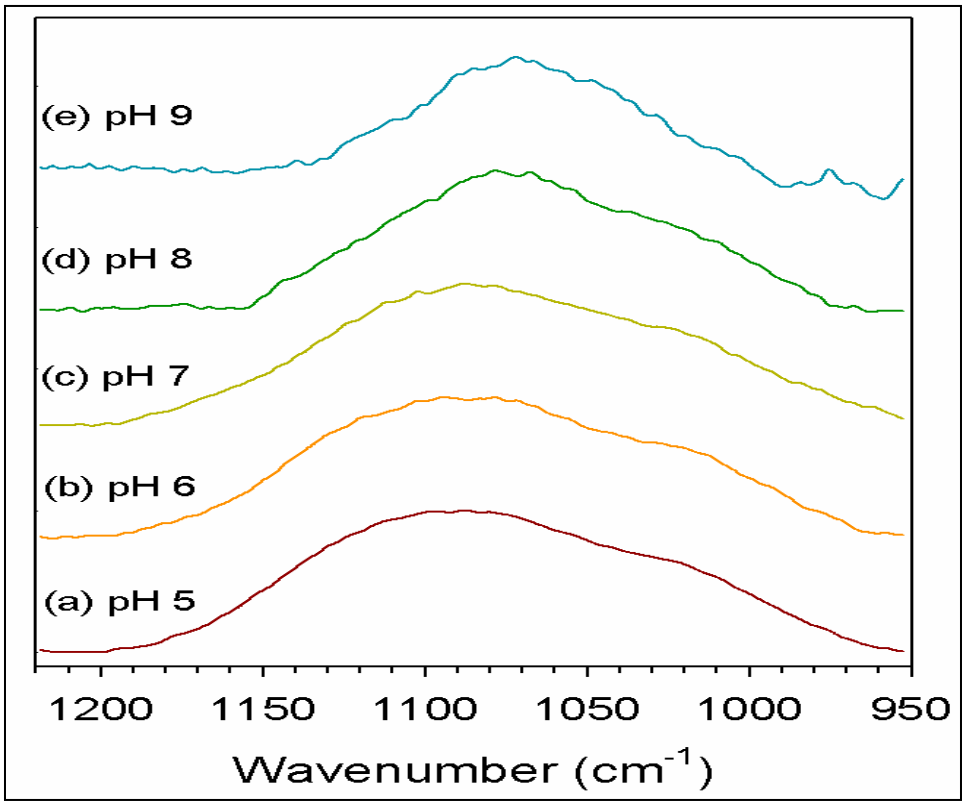

Figure 5.14. Phosphate stretching region of in situ ATR-FTIR baseline corrected difference spectra for adsorbed phosphate (1 mM) on corundum from pH 5 to pH 9.

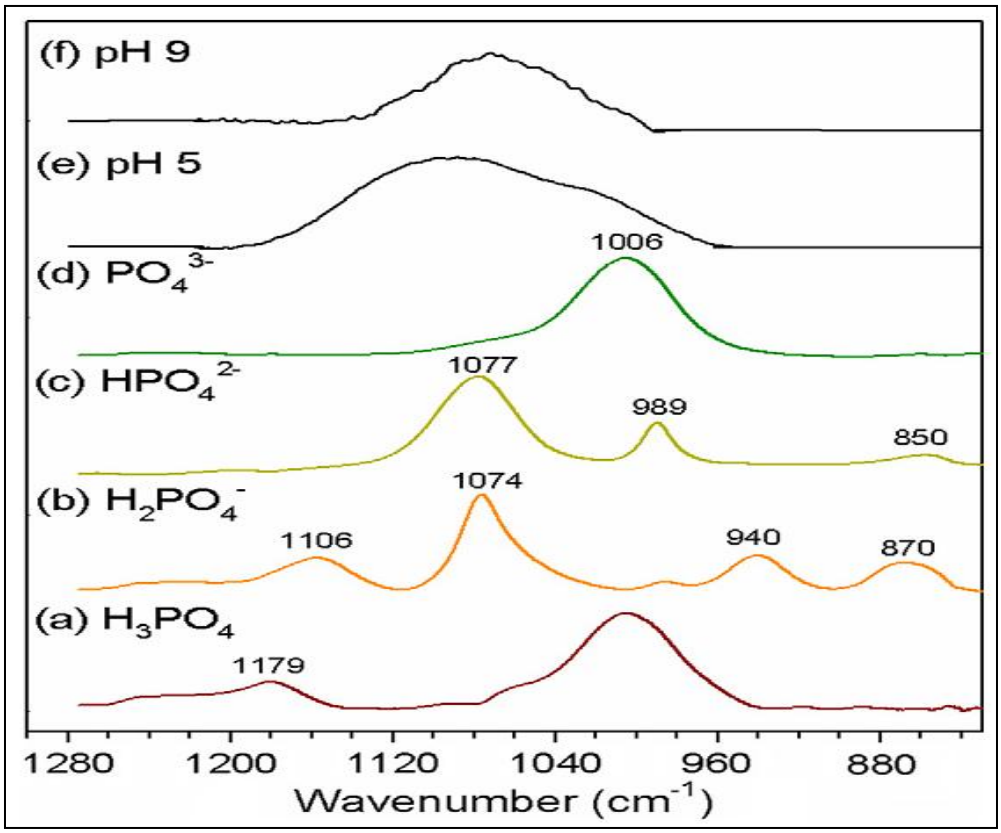

Figure 5.15. Phosphate stretching region of in situ ATR-FTIR baseline corrected difference spectra for phosphate absorbed on corundum at pH 5 and pH 9 and comparison of observed spectra with frequencies observed for aqueous phosphate species.

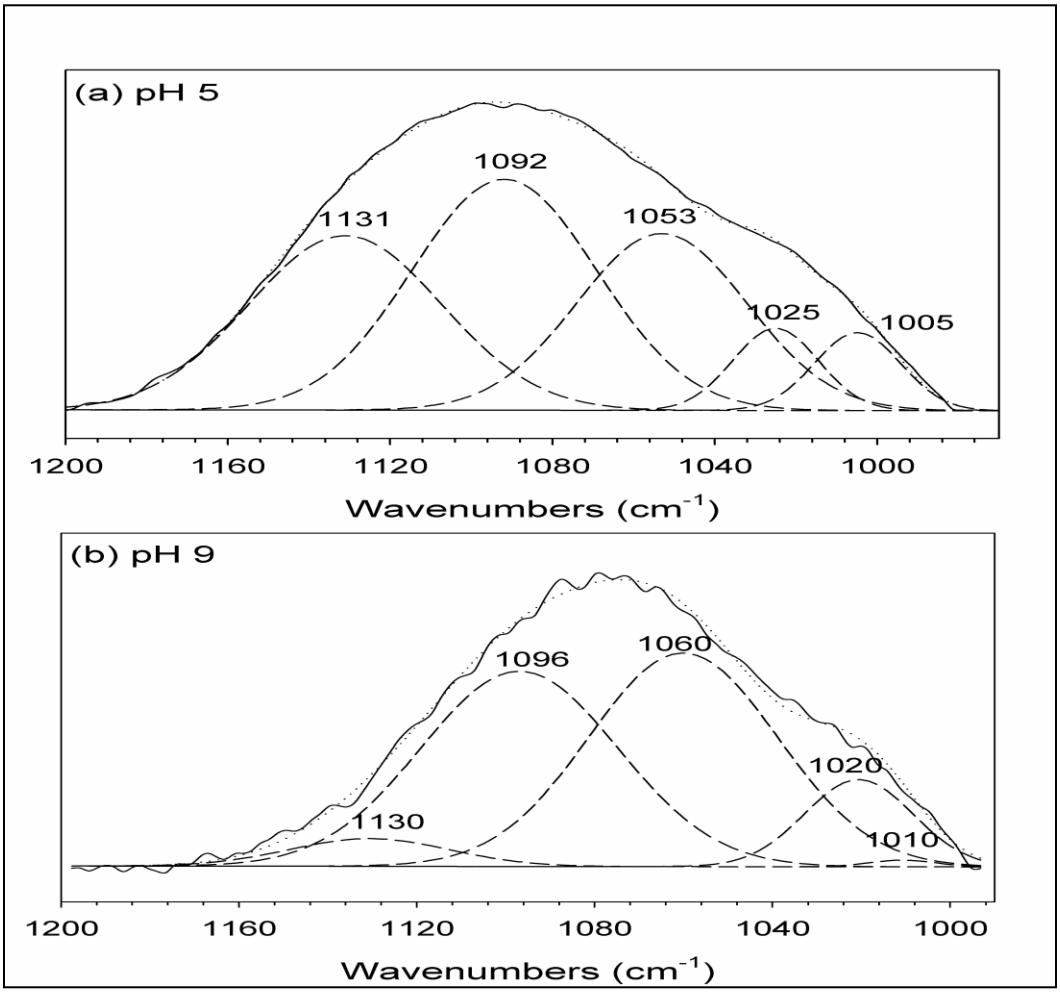

Figure 5.16. Deconvolution of the in situ ATR-FTIR spectra for adsorbed phosphate (1 mM) on corundum at pH 5 and pH 9.

5.6 DFT Vibrational Frequencies Computations

A summary of the calculated vibrational frequencies are shown in Table 5.4 for the PO_4^{3-} binding surface complexes on Fe_2, Al_2 dimers, and Al/Fe oxyhydroxide structures. Also provided in the table are vibrational frequencies for PO_4^{3-} on selected surfaces by Tejedor-Tejedor,(Tejedor Tejedor and Anderson 1990) Arai and Sparks,(Arai and Sparks 2001) Persson and co-workers (Kwon and Kubicki 2004), and to those resulted from our experiments (see Table 5.2). We performed the DFT vibrational frequency calculations by varying the number of protonations (H+) of phosphate species including ten explicit (10 H_2O) solvation molecules. Examples are the bidentate, $Me_2(OH)_4(OH_2)_4 \cdot (H_2O)_6$, and monodentate, $Me_2(OH)_4(OH_2)_5 \cdot (H_2O)_6$, hydroxide clusters (Me is equivalent to Fe, Al dimmers or (Fe, Al)) with diprotonated ($H_2PO_4^-$), monoprotonated ($NaHPO_4^{2-}$), or deprotonated ($Na_2PO_4^{3-}$) phosphate complexes as illustrated in Figure 5.19. Linear-correlation analysis (expected within a ±5% error based on the average scaling factor of the Scott and Random(Scott and Radom 1996) value of 0.9614) were carried out between the calculated and experimental vibrational frequencies to assign which type of adsorbed PO_4^{3-} complexes formed on Al/Fe oxyhydroxide under our various experimental conditions (see Appendix B). The observed frequencies values varied with the different molecular surfaces as Al was interchanged for Fe in the molecular clusters and upon variation of the PO_4^{3-} protonation species. Determining binding geometry models by using correlations between calculated vibrational frequencies with experimental modes is a difficult process. Many of the configurations determined to be reasonable were based on correlations derived from a graphical analysis that analyzed the slopes of plots of calculated versus experimentally observed mode

positions. Plots yielding slopes of ~0.91 to 1.32 and R^2 = 0.98 to 1.00 values were considered good correlations.

Table 5.4. Calculated vibrational frequencies of bidentate (BD) and monodentate (MD) phosphate surface complexes on Fe-Fe, Al-Al dimmers, or (Fe, Al) with phosphate bound to either Fe^{3+} or Al^{3+} atom from the structural models. The relative peak intensities are shown in parentheses.

Fe_2_dimers BD PO_4^{3-}			Al_2_dimers BD PO_4^{3-}			Al/Fe BD PO_4^{3-}		
BDH2	BDH1	BDH0	BDH2	BDH1	BDH0	BDH2	BDH1	BDH0
908 (200)	918 (250)	846 (273)	932 (353)	887 (131)	874 (189)	964 (195)	889 (106)	888 (191)
1027 (139)	969 (320)	869 (185)	946 (323)	969 (183)	885 (490)	970 (311)	977 (400)	897 (279)
1042 (376)	992 (144)	884 (164)	1054 (306)	987 (278)	930 (290)	1021 (102)	1006 (214)	948 (149)
1111 (197)	1012 (356)	932 (104)	1098 (194)	1034 (473)	949 (250)	1076 (524)	1019 (204)	961 (107)
1123 (425)	1048 (386)	1000 (681)	1132 (306)	1066 (378)	1044 (437)	1096 (489)	1063 (344)	1007 (600)
1309 (218)	1112 (120)	1092 (399)	1140 (287)	1120 (178)	1082 (465)	1262 (102)	1119 (202)	1064 (145)
	1243 (200)		1250 (173)	1262 (179)		1311 (108)	1284 (195)	1075 (458)

Fe_2_dimers MD PO_4^{3-}			Al_2_dimers MD PO_4^{3-}			Al/Fe MD PO_4^{3-} bound Al			Al/Fe MD PO_4^{3-} bound Fe		
MDH2	MDH1	MDH0	MDH2	MDH1	MDH0	MDH2	MDH1	MDH0	MDH2	MDH1	MDH0
920 (234)	889 (478)	891 (196)	841 (188)	910 (400)	955 (122)	888 (139)	909 (434)	974 (518)	933 (123)	888 (509)	863 (125)
929 (187)	944 (220)	909 (576)	899 (147)	950 (208)	964 (478)	942 (220)	948 (136)	981 (706)	951(299)	935 (139)	891(224)
945 (256)	976 (114)	976 (267)	935 (451)	990 (593)	973 (708)	988 (273)	980 (568)	1000 (585)	990 (452)	960 (387)	913 (714)
994 (265)	1094 (111)	993 (400)	1056 (294)	1005 (147)	985 (823)	1008 (261)	991 (136)	1023 (142)	1066 (169)	1024 (174)	972 (192)
1084 (115)	1115 (204)	1018 (604)	1073 (192)	1066 (321)	1024 (173)	1035 (388)	1092 (288)	1067 (256)	1122 (312)	1094 (109)	996 (436)
1094 (171)	1135 (202)	1078 (105)	1161 (420)	1120 (442)	1050 (171)	1062 (180)	1102 (116)	1124 (114)	1229 (120)	1123 (373)	1025 (584)
1326 (156)	1337 (169)		1348 (115)	1332 (176)		1122 (274)	1128 (424)		1236 (145)	1337 (172)	
						1251 (169)	1339 (167)				

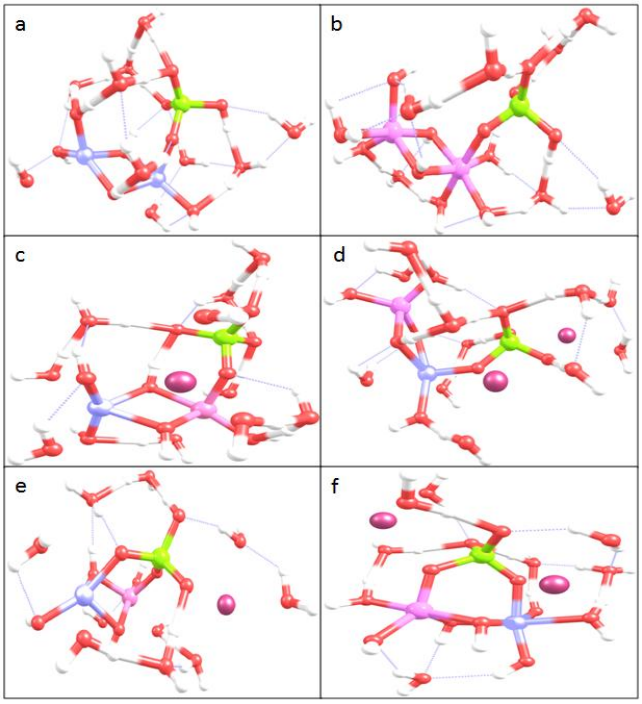

Figure 5.19. Optimized density functional theory (DFT) calculations of phosphate model surface complexes onto structures of predicted Al^{3+} substitution into iron oxyhydroxide (e.g., Ferrihydrite) clusters: (a) Fe_2 mononuclear monodentate and (b) Al_2 mononuclear monodentate monoprotonated, (c) (Al, Fe) mononuclear monodentate monoprotonated bound to an Al atom, and (d) (Fe, Al) mononuclear monodentate de-protonated bound to an Fe atom. Panel (e) and (f) are bidentate binuclear with $NaHPO_4^{2-}$ (mono-protonated) and $Na_2PO_4^{3-}$ (non-protonated), respectively on the (Fe, Al) cluster models ($10H_2O$). Geometries were optimized at the B3LYP/6-31+G(d, p) level using Gaussian 09 program. The graphics were created using Chemcraft software with color code visualization: red (O), white (H), light-blue (Fe), pink (Al), and phosphorous (P) atoms. (The reader is referred to the web version of this article for interpretation of the references to color in this figure).

The calculated vibrational frequencies were compared to the experimental IR modes collected at pH 7. The predicted stability of the bidentate ($H_2PO_4^-$) and monodentate ($NaHPO_4^{2-}$) protonated phosphate species are found to be well correlated to at least one of the observed IR spectra obtained from the different Al/Fe oxyhydroxide surfaces. These results indicated that both the bidentate ($H_2PO_4^-$) and monodentate ($NaHPO_4^{2-}$) protonated PO_4^{3-} surface complexes could coexist under acidic and neutral conditions. The calculated bidentate deprotonated phosphate ($Na_2PO_4^{3-}$) surface complexes are more consistent with the IR modes collected at pH 9. Our reported calculated frequencies are more closely related to those in prior published studies (Arai and Sparks 2001; Kwon and Kubicki 2004). In addition, based on a recent study reported by Kubicki and coworkers (Kubicki et al. 2012a), it is suggested that it is very difficult to make a simple one-to-one correlations for adsorbed PO_4^{3-} surface complexes, because the vibrational frequencies of PO_4^{3-} could have contribution from a variety of adsorbed complexes. However, we have shown that in our circumstance the only species present are the bidentate ($H_2PO_4^-$) and monodentate ($NaHPO_4^{2-}$) protonated PO_4^{3-} surface complexes in the pH range of 4-8. The bidentate deprotonated phosphate ($Na_2PO_4^{3-}$) surface complexes are closely related to the experimental results. Tejedor-Tejedor and Anderson reported the bridging bidentate phosphate surface complexes at the lower pH (3.5 - 6.5), and the formation of monodentate mononuclear at pH 6.5 to 8.0 for adsorbed PO_4^{3-} species on goethite mineral surfaces. It is important to note that on the basis of the correlation results between the calculated vibrational frequencies and the experimental modes, our study shows similar findings compared to prior published works {Arai, 2001 #5; Li, 2013 #152; Kubicki, 2012 #66; Persson, 1996 #88}. Most importantly, our ATR-

FTIR/DFT results showed that phosphate species adsorbed via inner-sphere/outer-sphere bidentate and monodentate bonding configurations, but the relative concentration of each was a function of pH and Al-content in the Al/Fe-oxyhydroxide.

5.7 Summary and Implications

Results from ATR-FTIR coupled with DFT calculations suggest that the adsorption of PO_4^{3-} on Ferrihydrite, goethite, alumina, and mixed Al/Fe-oxyhydroxides occurred through a variety of surface complexes such as monodentate, bidentate, and outer-sphere geometries. PO_4^{3-} surface complexes bonding to either Fe-O-Fe, Al-O-Al, or to either the Al- or Fe-component in the mixed Al-O-Fe cluster models gives rise to different vibrational frequencies which correlate well with the adsorbed phosphate IR experimental spectral modes. We identify similar inner-sphere bidentate PO_4^{3-} complexes on the Fe-, Al-, and/or Al/Fe-oxyhydroxide surfaces as compared to prior studies which have investigated the adsorption of PO_4^{3-} onto various metal oxyhydroxides. Our results are in good agreement with prior published works indicating the presence of multiple PO_4^{3-}binding configurations adsorbed on different surface sites, edges, and crystal habits of iron oxyhydroxide surface. The results showed that adsorbed PO_4^{3-} complexes are largely dependent on the mineral crystalline properties, particle aggregation, and/or surface sites in addition to the solution pH. The lower range of Al substitution (0-30 mol%) in the Al/Fe-oxyhydroxide precipitates have led to an increase in SSA which offers high adsorption capacity and reactivity compared to the end member mineral counterparts toward oxyanions of adsorbed PO_4^{3-} and CO_3^{2-}, and perhaps for the

adsorption of other metal(loid)/ionic species that could be relevant in a number of environmental and technological settings.

REFERENCES

Anderson P. R. and Benjamin M. M. 1990 Surface and Bulk Characteristics of Binary Oxide Suspensions. Environmental Science & Technology 24, 692-698.

Arai Y. and Sparks D. L. 2001 ATR-FTIR spectroscopic investigation on phosphate adsorption mechanisms at the ferrihydrite-water interface. Journal of Colloid and Interface Science 241, 317-326.

Arai Y. and Sparks D. L. 2007 Phosphate reaction dynamics in soils and soil components: A muiltiscale approach. *In* Advances in Agronomy, Vol 94. pp 135-179.

Arai Y., Sparks D. L. and Davis J. A. 2004 Effects of Dissolved Carbonate on Arsenate Adsorption and Surface Speciation at the Hematite-Water Interface. Environmental Science and Technology 38, 817-824.

Barron V., Torrent J. and de Grave E. 2003 Hydromaghemite, an intermediate in the hydrothermal transformation of 2-line ferrihydrite into hematite. American Mineralogist 88, 1679-1688.

Becke A. D. 1992 Density-Functional Thermochemistry .1. the Effect of the Exchange-Only Gradient Correction. Journal of Chemical Physics 96, 2155-2160.

Becke A. D. 1997 Density-functional thermochemistry .5. Systematic optimization of exchange-correlation functionals. Journal of Chemical Physics 107, 8554-8560.

Benali O., Abdelmoula M., Refait P. and Genin J. M. R. 2002 The behaviour of phosphate ions as corrosion inhibitor for Fe(II)-Fe(III) hydroxycarbonate green rust, 2002. pp 223-230.

Bhandari N., Hausner D. B., Kubicki J. D. and Strongin D. R. 2010 Photodissolution of Ferrihydrite in the Presence of Oxalic Acid: An In Situ ATR-FTIR/DFT Study. Langmuir 26, 16246-16253.

Bocher F., Gehin A., Ruby C., Ghanbaja J., Abdelmoula M. and Genin J. M. R. 2004 Coprecipitation of Fe(II-III) hydroxycarbonate green rust stabilised by phosphate adsorption. Solid State Sciences 6, 117-124.

Borch T., Masue Y., Kukkadapu R. K. and Fendorf S. 2007 Phosphate imposed limitations on biological reduction and alteration of ferrihydrite. Environmental Science & Technology 41, 166-172.

Chen Z. N. Xie H. F., Yang H., Wang Z. L. and Cheng R. S. 2007 Analysis of the composition of complicated binary mixture by quantitative sec. Acta Polymerica Sinica, 689-692.

Chupas P. J., Qiu X. Y., Hanson J. C., Lee P. L., Grey C. P. and Billinge S. J. L. 2003 Rapid-acquisition pair distribution function (RA-PDF) analysis. Journal of Applied Crystallography 36, 1342-1347.

Cismasu A. C., Michel F. M., Stebbins J. F., Levard C. and Brown G. E., Jr. 2012 Properties of impurity-bearing ferrihydrite I. Effects of Al content and precipitation rate on the structure of 2-line ferrihydrite. Geochim. Cosmochim. Acta 92, 275-291.

Cismasu A. C., Michel F. M., Tcaciuc A. P., Tyliszczak T. and Brown G. E. 2011 Composition and structural aspects of naturally occurring ferrihydrite. CR Geoscience 343, 210-218.

Cornell R. M. S. U. 2003 The Iron Oxides:Structure, Properties, Reactions, Occurences and Uses. Willey~VCH Verlag GmbH & Co, Weinheim. New York . Chichester. 658 pp p.

Elsetinow A. R., Schoonen M. A. A. and Strongin D. R. 2001 Aqueous geochemical and surface science investigation of the effect of phosphate on pyrite oxidation. Environmental Science & Technology 35, 2252-2257.

Elzinga E. J. and Sparks D. L. 2007 Phosphate adsorption onto hematite: An in situ ATR-FTIR investigation of the effects of pH and loading level on the mode of phosphate surface complexation. Journal of Colloid and Interface Science 308, 53-70.

Giles D. E., Mohapatra M., Issa T. B., Anand S. and Singh P. 2011 Iron and aluminium based adsorption strategies for removing arsenic from water. Journal of Environmental Management 92, 3011-3022.

Guan X. H., Liu Q., Chen G. H. and Shang C. 2005 Surface complexation of condensed phosphate to aluminum hydroxide: An ATR-FTIR spectroscopic investigation. Journal of Colloid and Interface Science 289, 319-327.

Hammersley A. P., Svensson S. O., Hanfland M., Fitch A. N. and Hausermann D. 1996 Two-dimensional detector software: From real detector to idealised image or two-theta scan. High Pressure Research 14, 235-248.

Harrington R., Hausner D. B., Xu W., Bhandari N., Michel F. M., Brown G. E., Strongin D. R. and Parise J. B. 2011 Neutron Pair Distribution Function Study of Two-Line Ferrihydrite. Environmental Science & Technology 45, 9883-9890.

Harvey O. R. and Rhue R. D. 2008 Kinetics and energetics of phosphate sorption in a multi-component Al(III)-Fe(III) hydr(oxide) sorbent system. Journal of Colloid and Interface Science 322, 384-393.

Hausner D. B., Bhandari N., Pierre-Louis A. M., Kubicki J. D. and Strongin D. R. 2009 Ferrihydrite reactivity toward carbon dioxide. Journal of Colloid and Interface Science 337, 492-500.

Hiemstra T., Rahnemaie R. and van Riemsdijk W. H. 2004 Surface complexation of carbonate on goethite: IR spectroscopy, structure and charge distribution. Journal of Colloid and Interface Science 278, 282-290.

Hong H-J., Yang J-S., Kim B-K. and Yang J-W. 2011 Arsenic Removal Behavior by Fe-Al Binary Oxide: Thermodynamic and Kinetic Study. Separation Science and Technology 46, 2531-2538.

Hong H. J., Farooq W., Yang J. S. and Yang J. W. 2010 Preparation and Evaluation of Fe-Al Binary Oxide for Arsenic Removal: Comparative Study with Single Metal Oxides. Separation Science and Technology 45, 1975-1981.

Kubicki J. D., Aryanpour M., Kabalan L. and Zhu Q. 2012 Quantum mechanical calculations on FeOH nanoparticles. Geoderma 189â€“190, 236-242.

Kubicki J. D., Paul K. W., Kabalan L., Zhu Q., Mrozik M. K., Aryanpour M., Pierre-Louis A-M. and Strongin D R 2012b ATR-FTIR and Density Functional Theory Study of the Structures, Energetics, and Vibrational Spectra of Phosphate Adsorbed onto Goethite. Langmuir 28, 14573-14587.

Kukkadapu R. K., Zachara J. M., Smith S. C., Fredrickson J. K. and Liu C. X. 2001 Dissimilatory bacterial reduction of Al-substituted goethite in subsurface sediments. Geochimica Et Cosmochimica Acta 65, 2913-2924.

Kwon K. D. and Kubicki J. D. 2004 Molecular orbital theory study on surface complex structures of phosphates to iron hydroxides: Calculation of vibrational frequencies and adsorption energies. Langmuir 20, 9249-9254.

Lee C. T., Yang W. T. and Parr R. G. 1988 Development of the Colle-Salvetti Correlation-Energy Formula into a Functional of the Electron-Density. Physical Review B 37, 785-789.

Lefevre G. 2004 In situ Fourier-transform infrared spectroscopy studies of inorganic ions adsorption on metal oxides and hydroxides. Advances in Colloid and Interface Science 107, 109-123.

Luengo C., Brigante M., Antelo J. and Avena M. 2006 Kinetics of phosphate adsorption on goethite: Comparing batch adsorption and ATR-IR measurements. Journal of Colloid and Interface Science 300, 511-518.

Michel F .M., Antao S M, Celestian A. J., Schoonen M. A., Parise J. B., Liu G., Strongin D. R., Lee P. L. and Chupas P. J. 2006 Size and structure of ferrihydrite from PDF analysis. Abstracts of Papers, 232nd ACS National Meeting, San Francisco, CA, United States, Sept. 10-14, 2006, GEOC-133.

Persson P., Nilsson N. and Sjoberg S. 1996 Structure and bonding of orthophosphate ions at the iron oxide aqueous interface. Journal of Colloid and Interface Science 177, 263-275.

Qui X. 2004 PDFgetX2: a GUI-driven program to obtain the pair distribution function from x-ray powder diffraction data. Journal of Applied Crystallography 37, 678.

Schwertmann U. 2000 Iron Oxides in the Laboratory: preparation and characterization. Willey~VCH, Weinheim. New York . Chichester.

Schwertmann U 1991 Solubility and Dissolution of Iron-Oxides. Plant and Soil 130, 1-25.

Scott A. P. and Radom L. 1996 Harmonic Vibrational Frequencies: An Evaluation of Hartree-Fock, Møller-Plesset, Quadratic Configuration Interaction, Density Functional Theory, and Semiempirical Scale Factors. The Journal of Physical Chemistry 100, 16502-16513.

Tejedor Tejedor M. I. and Anderson M. A. 1990 Protonation of Phosphate on the Surface of Goethite as Studied by Cir-Ftir and Electrophoretic Mobility. Langmuir 6, 602-611.

Villalobos J. O. L. M 2000 Carbonate adsorption on goethite under closed and open CO_2 conditions Geochemica et Cosmochimica Acta 64, 3787-3802.

CHAPTER 6
EFFECTS OF PHOSPHOLIPID ON METAL SULFIDE OXIDATION AND MICROBIAL COMMUNITIES UNDER SIMULATED ACID MINE DRAINAGE (AMD) CONDITIONS

Abstract

The effectiveness of the adsorption of phospholipid (i.e., phosphatidylcholine type) on pyrite-containing coal mining overburden/waste rock (OWR) as a means to suppress acid mine drainage (AMD) chemistry was investigated. Metagenomic analyses also were carried out to understand how the microbial community structure, which developed during the oxidation of OWR, was affected by the presence of phospholipid. Using columns packed with OWR (with and without lipid modification), the SO_4^{2-} released and soluble metals (e.g., Fe_{Tot}) were investigated. Exposure of lipid-free OWR to flowing pH 7 water resulted in an acidic effluent with a pH that ranged between 2 and 4.5 over a 3 yr period. The average concentration of iron ($[Fe]_{Tot}$) and sulfate ($[SO_4^{2-}]$) in the effluent was $\geq$ 20 and $\geq$ 30 mg/L, respectively. In contrast, in packed-column experiments where OWR was first treated with phospholipid, the effluent pH remained at ~6.5 and the average concentrations of $[Fe]_{Tot}$ and $[SO_4^{2-}]$ were $\leq$ 2 and l.6 mg/L, respectively. Metagenomic analyses carried out via polymerase chain reaction amplification of 16S rRNA genes showed that AMD-like microbial communities developed in the packed

columns that contained untreated OWR, although such AMD-like communities did not develop when the OWR was pretreated with phospholipid. Results suggested that the treatment of OWR with phospholipid could be a promising technology for the suppression of AMD-chemistry.

6.1 Introduction

Acid mine drainage (AMD) is a severe environmental problem afflicting streams and rivers in areas where there are both active and abandoned industrial mining sites (Herlihy, Kaufmann et al. 1993; Ostrofsky and Schworm 2011). A root cause of AMD is the exposure of mining tailings (i.e., overburden, waste rock, and tailings), which typically contains 1-20% pyrite (FeS_2) and less amounts of other metal sulfides (e.g., marcasite and pyrrhotite), to water, microbes, and air (Marchand and Plumb 2005; Akcil and Koldas 2006). Both the abiotic and biotic oxidation of the metal sulfide component, during and after the mining operation, leads to the oxidation of the sulfur component to sulfuric acid. A composite reaction for the oxidation of the sulfide under abiotic conditions can be written as:

$$FeS_2 + 7/2O_2 + H_2O \rightarrow Fe^{2+} + 2SO_4^{2-} + 2H^+ \quad (1)$$

Reaction (1), where dioxygen is the oxidizing agent, is relatively slow compared to the circumstance where ferric iron is the oxidizing agent. Certain types of microbes, common to AMD environments can vastly accelerate the production of acid via a so-call indirect mechanism. *Acidithiobacillus ferrooxidans*, for example, that are frequent at AMD sites,

can drastically increase the rate of ferric iron production described by the following reactions(Edwards, Schrenk et al. 1998; Gleisner, Herbert et al. 2006):

$$14Fe^{2+} + 7/2O_2 + 14H^+ \rightarrow 14Fe^{3+} + 7H_2O \quad (2)$$

$$FeS_2 + 8H_2O + 14Fe^{3+} \rightarrow 15Fe^{2+} + 2SO_4^{2-} + 16H^+ \quad (3)$$

where the rate of Fe^{2+} oxidation (Eq. (2)) is accelerated in the presence of iron oxidizing bacteria.(Singer and Stumm 1970) In essence, specific microbes can recycle ferrous iron product of Eq. (3) into ferric iron(Gleisner, Herbert et al. 2006); a reaction that would be exceedingly slow in the absence of microbial action at a pH near 4.

Due to the detrimental environmental ramifications of AMD, there have been significant past and current efforts to find a viable solution to the problem. Current remediation schemes often include the frequent use of alkaline reagents such as limestone ($CaCO_3$), hydrated lime ($Ca(OH)_2$), quick lime (CaO), caustic soda (NaOH) to neutralize AMD.(Hammarstrom, Sibrell et al. 2003) This type of remediation can be costly and personnel intensive due to the continuous application of neutralizing agents in impacted areas, and may require long term management of sites.

Prior works in our laboratory have investigated the use of phospholipid to suppress the oxidation of the pyrite under conditions that would be associated with AMD environments.(Elsetinow, Borda et al. 2003; Hao, Murphy et al. 2009; Zhang, Jia et al. 2012) In short, prior studies showed that specific phospholipids could be used to produce robust hydrophobic coatings on pyrite that significantly reduced the amount of iron and sulfur oxidation under abiotic and biotic environments. (Hao, Cleveland et al. 2006; Li,

Qin et al. 2006) In the present contribution, we extend our studies to investigate the ability of phospholipid adsorbate to suppress acid generation from actual coal mining waste rather than from pristine pyrite samples used in prior studies. To accomplish this objective the pH, [SO_4^{2-}], and [Fe] of effluent evolving as a function of time from test columns individually packed with OWR and phospholipid-treated OWR were compared. Two different phospholipids were studied: 1,2-bis(10,12-tricosadiynoyl)-*sn*-glycerol-3-phosphocholine (23:2 Diyne PC) and a commercially available phosphatidylcholine containing lipid formulation, Phospholipon® 80H. In addition, metagenomic studies were conducted to characterize the microbial communities that were present on the mine tailing (both untreated and lipid pretreated materials) after 3 yrs of reaction. The results from these studies help to more fully evaluate the potential of phospholipids for suppressing AMD under real environmental conditions.

6.2. Experimental Materials and Methods

6.2.1 Materials

Research grade phospholipid, 1,2-bis (10,12-tricosadiynoyl)-*sn*-glycerol-3-phosphocholine (23:2 Diyne PC), was purchased from Avanti lipids (Figure 1). The commercially available Phospholipon® 80H was purchased from Lipoid Corporation. According to the manufacturer specifications, the Phospholipon® 80H (referred to as 80H) formulation contained at a minimum 60% hydrogenated phosphatidylcholine type lipid, a maximum of 10% lysophosphatidylcholine (contains 1 fatty acid group), and fatty acid (~85 % stearic acid and ~15 % palmitic acid). We presume that the suppression of iron sulfide oxidation in the presence of 80H (detailed below) is due to the presence of

the hydrogenated phosphatidylcholine lipid component of 80H.(Elsetinow, Borda et al. 2003) To better characterize the phosphatidylcholine component we analyzed the 80H with high pressure liquid chromatography/mass spectroscopy (HPLC). The major fraction was associated with a m/z value of 790.6 that could be associated with a molecular formula of $C_{44}H_{88}NO_8P$ (e.g., see Figure 6.1 for 1,2-dioctadecanoyl-sn-glycero-3-phosphocholine).

6.2.2 Mining Samples

Two types of mining OWR were used in this study: the difference between the two being the time that they were exposed to weathering conditions at the mining site. The sample used in this study denoted as fresh-AMD waste (FOWR) was collected from the mining site in western Pennsylvania only days after its excavation. The second sample denoted as aged-AMD waste (AGOWR) was collected up to five years of weathering at the mining location. Visually the FOWR and AGOWR differed in that the FOWR was grayish while the AGOWR contained a heterogeneous mixture of gray and yellow particles, suggesting iron and/or manganese oxidation. Pure pyrite was used as a reference material in some of our experiments and the sample used was purchased from Wards Scientific (#49-5884).

6.3 Characterization Techniques

6.3.1 Brunauer-Emmet Teller Surface Area Measurement (BET)

BET was used to determine the specific surface area (SSA) of the different AMD samples, using N_2 as the adsorption gas. The BET instrument model used was ASP 2002

V1.05 from Micromeritics. Approximately ≥ 100 mg of dry fine crushed pyrite, AGOWR, or FOWR was placed in a BET glass container for degassing and analysis. All samples were de-gassed (i.e., desorbing for residual superficial water) at 100 ˚C for 600 minutes prior to any surface area measurements. The SSA for pyrite, AGOWR, and FOWR used in this study was 10.95 ± 0.76, 46.98 ± 0.66, and 2.93 ± 0.04 m^2/g, respectively.

6.3.2 X-ray Fluorescence (XRF) Analysis

The elemental composition of AGOWR and FOWR samples were characterized with XRF using a nondestructive Niton XL3t^{TM} XRF Analyzer Handheld from Thermo Scientific. The portable Niton XL3t^{TM} XRF Series analyzer was equipped with a 50 kV miniaturized X-ray tube and a scintillation detector. The detection limits for the major and trace elements were on the order of a few part per million (ppm or mg/L). Results from the XRF analysis of typical samples used in this study are presented in Table 6.1.

6.3.3 X-ray Powder Diffraction (XRD)

Mine OWR samples were characterized by XRD using an Apex Duo: Bruker Instrument Service equipped with a charge couple detector diffraction system (CCD). Both FOWR and AGOWR samples were air dried at room temperature and crushed to fine powder form, and then placed into 0.7 mm O.D. capillary tubes for data collection. Samples were scanned at the wavelength, λ = 0.71073 Å (molybdenum, MoKα X-ray source), and at nearly constant irradiation volumes in the 2θ range of 5-50^o with a step size of 0.02° at a rate of 180 seconds/step at room temperature. Eva Software was used to process the XRD diffractograms presented in this contribution.

6.4 Columns Experiments

A schematic of a typical packed column used in our study is shown in Figure 1. Before adding any of the lipid-pretreated or lipid-free OWR, the columns were loaded with pre-cut disks prepared with geotextile polyfiber fish filter pads and glass beads (~10 mm diameter) at the bottom of the columns to prevent clogging of the filter and to maintain the water flow-rate. The columns were 50 cm in length and 6 cm in diameter.

6.4.1 Preparation of Phospholipon® 80H treated OWR and column experiments

FOWR and AGOWR (~25 g) samples (i.e., FOWR/80H or AGOWR/80H) were individually dispersed into 250 ml of water containing ~4 g of phospholipid for 30 min. Control experiments were set up in a similar way except that the FOWR and AGOWR were not pre-exposed to phospholipid.

Two types of column experiments were conducted in this study. In the first type, water having a neutral pH was continuously flowed through the sample columns at a flow rate of 1.5 mL/min. Aliquots of ~10 to 30 mL stored in glass vials were periodically collected and later analyzed for pH, $[SO_4^{2-}]$, and $[Fe]_{tot}$.

We also conducted a selected group of stop-flow column experiments. In these experiments the samples of interest were not subjected to a continuous flow of water. Instead packed column containing sample with or without lipid was filled with water (pH 7), but the solution phase was not allowed to flow for a given period of time. We refer to these columns experiments below as STFOWR/80H and STFOWR (with and without 80H lipid, respectively). After a defined period of time the entire liquid fraction was allowed to elute from the column for analysis. The column was then refilled with water and the fill-elute cycles were carried out over an extended period of time as indicated in the data plots below.

6.4.2 Preparation of 23:2 Diyne PC treated OWR and column experiment

The exposure of FOWR to 23:2 Diyne PC was carried out differently than with the 80H. In this case, 25 g of FOWR was placed in a 200 mL suspension containing ~4 g of 23:2 Diyne PC. Unlike the exposure process used for the 80H lipid, the FOWR/23:2 Diyne PC suspension was stirred and simultaneously exposed to the UV light emitted by a 900 watt Xe lamp (Schoeffel Instrument-Corp) for approximately 3 hours. We also prepared samples by using persulfate ($S_2O_8^{2-}$) as an initiator for the cross linking process. Prior literature used persulfate to initiate the cross-linking of di-ethylene functionalized phopholipids.(Lawson, Lee et al. 2003) In this case, we exposed FOWR/23:2 Diyne PC to sodium thiosulfate (2.2 mM) and potassium persulfate (2.2 mM) ($Na_2S_2O_3$ + $K_2S_2O_8$), but this OWR sample containing column was not exposed to the UV radiation. Columns for these experiments were set-up under continuous water conditions (pH 7) for exposure times up to 3 year. The columns temperature was kept at approximately 25 ºC.

6.4.3 Analysis of the column effluents

$[Fe]_{tot}$ was measured in the column effluent using the Stookey Ferrozine method.(Stookey 1970)' (Viollier, Inglett et al. 2000) Samples used for this analysis were first acidified with ascorbic acid to reduce Fe^{3+} to Fe^{2+} prior to the introduction of Ferrozine to the effluent. The absorbance of the Fe^{2+}-ferrozine complex was monitored with UV-vis spectroscopy (Evolution 201, Thermo Scientific) at 560 nm. $[Fe]_{tot}$ (sum of Fe^{3+} and Fe^{2+}) was determined using a standard calibration curve. $[SO_4^{2-}]$ was determined with ion chromatography (IC). Sample aliquots (~1.5 mL) were filtered with 0.22 μm polyethersulfone membrane filter and injected with a 1 mL syringe. If effluent samples were not analyzed immediately after they were collected, the effluents were kept in glass vials air-tight and stored in a refrigerator.

6.4.4 Metagenomic analysis of the microbial communities in the column experiments

At the end of the column tests (2-3 yrs depending on the experiment), samples of the ORW material were manually collected under sterile conditions and centrifuged at 6,000 g for 30 min. Aliquots of the original dry samples were also collected. Total DNA was then extracted from approximately 250 mg of samples using the PowerSoil DNA Extraction kit (MoBio, Carlsbad, CA). Partial 16S rDNA genes were amplified by PCR using barcoded universal prokaryotic primers, 519F (5'-CAGCMGCCGCGGTAATWC-3') and 1086R (5'-CTGACGRCRGCCATGC-3'), combined with Roche 454 adaptors. After visualization by agarose gel electrophoresis, the PCR products flanked with adaptors were purified using the Agencourt Ampure PCR Purification system (Beckman Coulter, Beverly, MA) and quantified using a Nanodrop-2000 spectrophotometer (Nano Drop Technologies, Wilmington, DE). DNA extraction and PCR amplification were

conducted in triplicate for each sample. A metagenomic library was then constructed by pooling equimolar concentrations of all 16S rDNA products. The library was sequenced using a 454 GS Junior pyrosequencing system (Roche Diagnostics, Indianapolis, IN). Pyrosequencing data were filtered and analyzed to determine the bacterial diversity and the distribution of major taxonomic groups using the QIIME package (http://qiime.org/). The impact of various parameters, including pH, [SO_4^{2-}], and [Fe] on the microbial community profile was studied by redundancy analysis (RDA) using CANOCO 4.5 software (Biometris, Wageningen, The Netherlands) with unrestricted Monte Carlo permutation test. For data processing and analysis, the replicate sequences of each sample were pooled polled together. For quality control of the results, the sequences of each replicates were compared by clustering analysis using the QIIME package.

6.5 Results

6.5.1 Microscopy and chemical analysis

Table 6.1 summarizes XRF data from both the FOWR and AGOWR samples. As expected the major constituents of both OWR samples included Fe, S, and Ca. It is of interest to key in on the Fe and S content, since these elements presumably exist in the samples to a significant extent as FeS_2, the oxidation of which is the root cause of AMD. Inspection of the results shows that both sulfur and iron are in significantly higher concentrations in FOWR than in AGOWR. This result is presumably due to the oxidation of pyrite and resulting loss of iron and sulfur during aging in the actual coal mining environment.

Table 6.1. XRF quantitative chemical elements analysis of dry fresh and aged OWR rocks.

Elements	FOWR (ppm)	AGOWR (ppm)
Sr	533.84 ± 10.24	78.28 ± 3.39
Rb	36.98 ± 3.75	< LOD
Th	12.95 ± 4.79	19.99 ± 3.98
Pb	10.07 ± 5.33	18.1 ± 4.68
Se	4.62 ± 2.93	10.76 ± 2.42
Zn	338.24 ± 20.65	< LOD
Cu	126.57 ± 20.21	56.56 ± 11.37
Ni	176.72 ± 40	< LOD
Fe	39306.26± 380.61	10681.81 ± 158.81
Mn	649.3 ± 78.4	< LOD
Cr	82.48 ± 20.57	801.22 ± 35.92
Ti	1206.39 ± 94.34	8566.32 ± 177.99
Sc	157.03 ± 64.16	32.62 ± 12.36
Ca	117586.23 ± 841.95	2605.85 ± 131.62
K	8618.74 ± 369.74	671.44 ± 135.26
S	945061.56 ± 44137.18	866191.19 ± 37821.64
Ba	167.03 ± 29.5	< LOD

XRD analysis of both OWR samples were performed and compared to a pure pyrite standard. Figure 6.2a exhibits a diffractogram for FeS_2, and this mineral exhibits diffraction lines associated with d-spacing values of ~3.13, 2.71, 2.42, 2.21, 1.92, 1.63, and 1.04 Å. XRD results for the as as-received FOWR sample are similar to those of the FeS_2 reference material, suggesting that pyrite is the predominant crystalline phase in the FOWR soil. A notable difference between the two patterns, however, is the presence of weak and broader lines observed in the $2\theta^{o}$ range of 5-12^{o}, indicating that FOWR contains in addition to pyrite, poorly amorphous crystalline mineral phases. Diffraction data associated with the as-received AGOWR soil shows a significant loss of pyrite XRD reflection lines and the appearance of new reflection lines < 15^{o} (Figure 6.2b) relative to the diffractogram associated with FOWR. The presence of these crystalline structures may be associated with SiO_2 and/or other phases mixture of iron oxyhydroxide with metal sulfate associated with AGOWR. Also included in Figure 6.2 are diffractograms associated with lipid-treated FOWR and AGOWR after 3 years of exposure to water in our column experiments. We will return to these XRD results below in the discussion section.

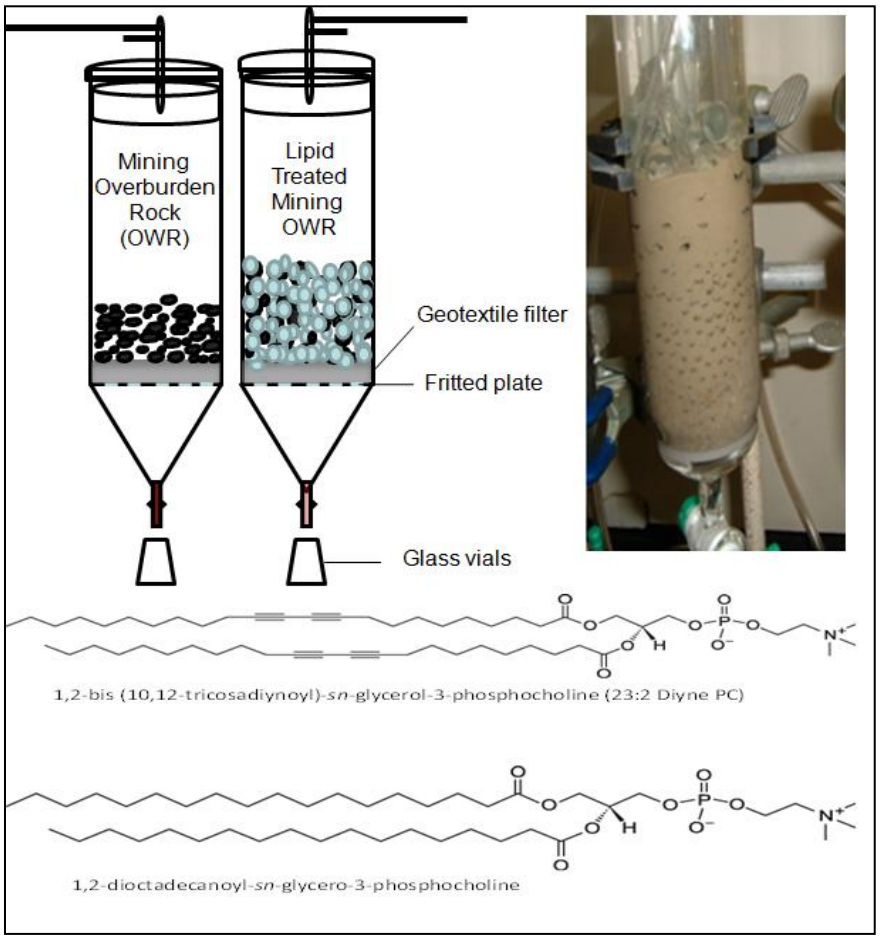

Figure 6.1. Schematic (left) of the packed column. Glass beads were interspersed to aid the flow of solution through the column. The photograph on the right shows column loaded with mining OWR samples. The top structure is of 1,2-bis (10,12-tricosadiynoyl)-*sn*-glycerol-3-phosphocholine (23:2 Diyne PC) lipid. The bottom structure of 1,2-

dioctadecanoyl-sn-glycero-3-phosphocholine is shown as a representative example of a possible phosphatidylcholine lipid that might be present in the commercially available Phospholipon® 80H used in this study (based on HPLC/MS analysis).

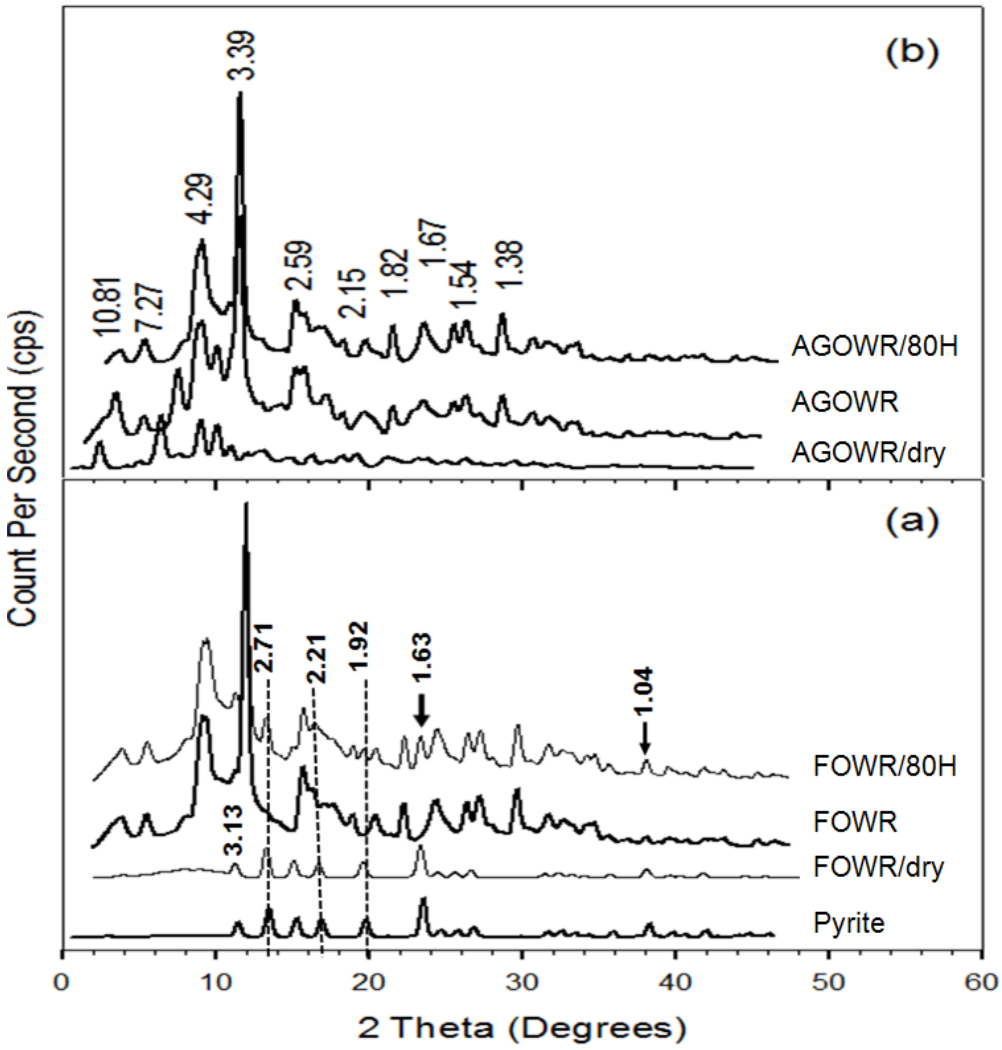

Figure 6.2. XRD diffractograms of reference pyrite mineral compared to FOWR (a), and AGOWR (b). XRD data associated with FOWR is similar to the reference pyrite sample. This similarity suggests that pyrite is the major crystalline sulfide bearing phase in the FOWR. The XRD diffractogram associated with AGOWR shows a much smaller

contribution from pyrite. The most top two overlay diffractograms are associated with the characterization of AMD after exposure to water collected from the columns matrices up to 3 yrs.

6.6 FOWR and AGOWR packed columns with and without lipid pretreatment

6.6.1 Treatment of FOWR and AGOWR with 80H lipid

Data presented in Figure 6.3a shows that the pH of the effluent associated with the FOWR/80 and AGOWR/80H as a function of time. Inspection of the data shows that the pH of the effluent associated with FOWR/80H at the earliest collection times was 6 or above. In contrast to the FOWR/80H sample, the pH of the effluent associated with AGOWR/80H was near 4 at the earliest collection times, but rose rapidly to a pH near 7 after 4 weeks of flow. After one month the pH associated with both FOWR/80H and AGOWR/80H showed a remarkable stability over the course of the 3.5 yr experiment; the average pH of the effluent was 6.85 and 7.07, for FOWR/80H and AGOWR/80H, respectively (Table 6.2). In contrast, the effluent associated with FOWR or AGOWR that had not been pretreated with 80H had an average pH of 3.71 and 3.46, respectively over the same period of time.

Inspection of the sulfate data shown in Figure 6.3b is generally consistent with the pH data. At the earliest measurement times, $[SO_4^{2-}]$ measured for the lipid treated samples are similar to the untreated samples. As the reaction time progresses, however, there is a reduction in $[SO_4^{2-}]$ in the effluent associated with FOWR and AGOWR that was pretreated with lipid. The average $[SO_4^{2-}]$ in the effluent averaged over the entire

experimental run was reduced by about 70% (see Table 6.2) when the mine tailings were pretreated with lipid.

Figure 6.3c and d exhibit effluent pH and [SO_4^{2-}] as a function of time for the stop-flow column experiments (see experimental methods). At the earliest collection times the effluent associated with STFOWR/80H and STFOWR exhibited a pH near 3. After 3 months the effluent from STFOWR/80H had a pH near 6 while the untreated sample effluent remained near pH 3. The pH of the STFOWR/80H effluent remained in the 6-7 range for 2.5 years while the untreated sample-effluent had a relatively constant pH of 3 for the same time frame. There were also significant differences between the [SO_4^{2-}] profiles for STFOWR/80H and STFOWR. In particular [SO_4^{2-}] was initially 200 mg/L from the effluent of STFOWR/80H, but rapidly decreased to <10 mg/L after 1 month and [SO_4^{2-}] remained low for 2.5 year run. In contrast, the untreated STFOWR was associated with a [SO_4^{2-}] of 2000 mg/L, and this value did not decrease dramatically until about 15 months into the experiment. At a run time of 2.5 years the last measured value for [SO_4^{2-}] was 707 mg/L.

Table 6.2. Summary of results

Columns	**Final** $pH_{Avr.}$	**$[SO_4^{2-}]_{Avr.}$** (mgL^{-1})	**$[Fe_{Tot}]_{Avr.}$** (mgL^{-1})	**$[SO_4^{2-}]_{Avr.}$** (%) Reduced	**$[Fe_{Tot}]_{Avr.}$** (%) Reduced	**Time** Months
AGOWR	3.5	269.4	38.3	73.9	76.2	23.3
AGOWR/80H Lipid	7.1	70.4	9.1			
FOWR	3.7	61.9	92.2	74.8	66.7	40.7
FOWR/80H Lipid	6.9	15.6	30.7			
STFOWR	3.0	1713.6	13.8	97.8	88.4	29.8
STFOWR/80H Lipid	6.0	37.5	1.6			
$FOWR_{Ctrl}$	3.8	424.4	13.4	77.4	94.3	39.7
FOWR/23:2 Diyne (UV)	6.2	96.1	0.8			
FOWR/23:2 Diyne	6.0	94.1	1.9	79.6	85.8	30.6

*$FOWR_{Ctrl}$ is a separate lipid-free column that was exposed without persulfate and phospholipid coatings under similar conditions as those of FOWR/23:3 D with UV and without UV columns exposure.

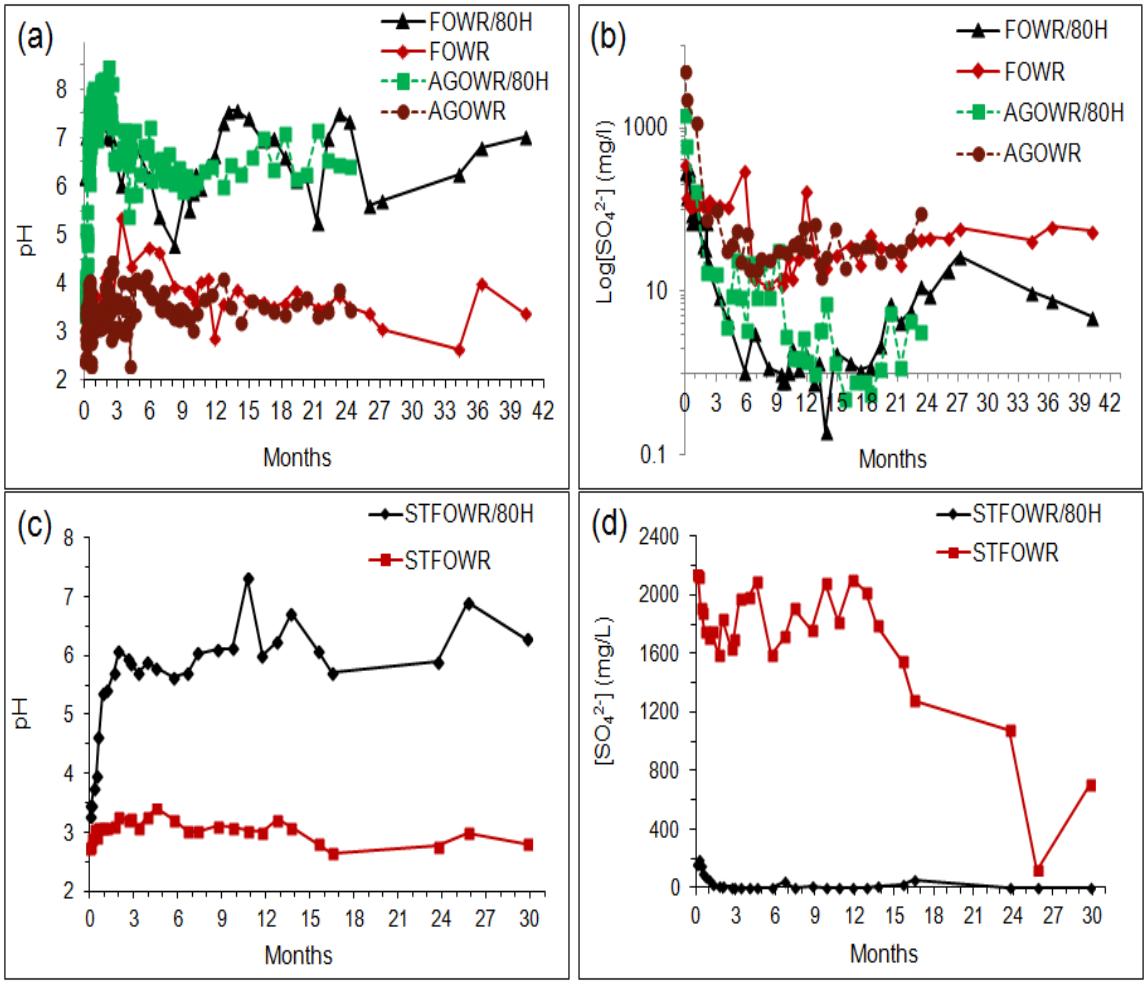

Figure 6.3. (a) pH and (b) SO_4^{2-} versus time data for the uncoated and the coated mining OWR samples with the 80H Phospholipon that were exposed to a continuous flow of water (3 years). (c) pH and (d) $[SO_4^{2-}]$ monitored for FOWR samples that was pretreated with 80H phospholipon from the "stop-flow column" experiments. In these experiments the columns were filled and after a defined period of time emptied of the liquid

component. The column was then re-filled. These empty-fill cycles were done at well-defined times for 30 months. The data are associated with the pH and [SO_4^{2-}] concentration of the effluent that was periodically removed from the column.

6.6.2 Treatment of AGOWR and FOWR with 23:2 Diyne PC

Figure 6.4a and b exhibits data for the pH and [SO_4^{2-}] associated with the effluent for FOWR pretreated with the 23:2 Diyne PC lipid (with persulfate or UV treatment) and FOWR that was not pre-treated with the lipid. The pH of the effluent for the 23:2-PC treated mine FOWR remained in the pH ~6-7 range over the 3 year run. However, the average pH was 6.21 for the UV-treated lipid/FOWR system, lower than the average for the 80H treated mine OWR.

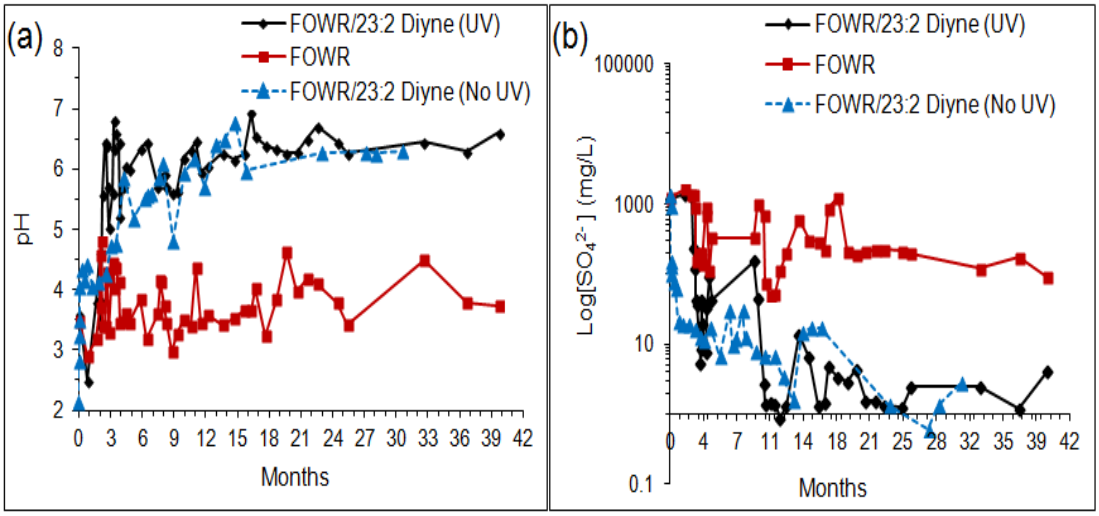

Figure 6.4. (a) pH and (b) [SO_4^{2-}] versus time data for FOWR and FOWR that was pretreated with 23:2 Diyne phospholipid. One of the FOWR/23:2 D PC samples were exposed to UV radiation in an attempt to facilitate the cross-linking of the diacethylene group containing lipids.

6.6.3 Fe concentration in the effluent of column experiments

Figure 6.5(a-d) exhibits data showing the Fe concentration in the effluent of the different column experiments. While the average $[Fe]_{tot}$ in the effluent of AGOWR and FOWR is elevated compared to the respective lipid-pretreated sample, there is no clear trend with time. We point out that at pH values higher than 6, which is typical of the lipid-pretreated sample, the insolubility of Fe(III)-bearing solids would largely preclude their presence in the effluent. We are not sure of the origin of the fluctuations in the Fe concentration data, especially for the untreated FOWR and AGOWR. One might speculate that the fluctuations are at least in part due to dissolution and re-precipitation reactions occurring during the evolution over time of the chemical and structural properties of the FOWR and AGOWR samples.

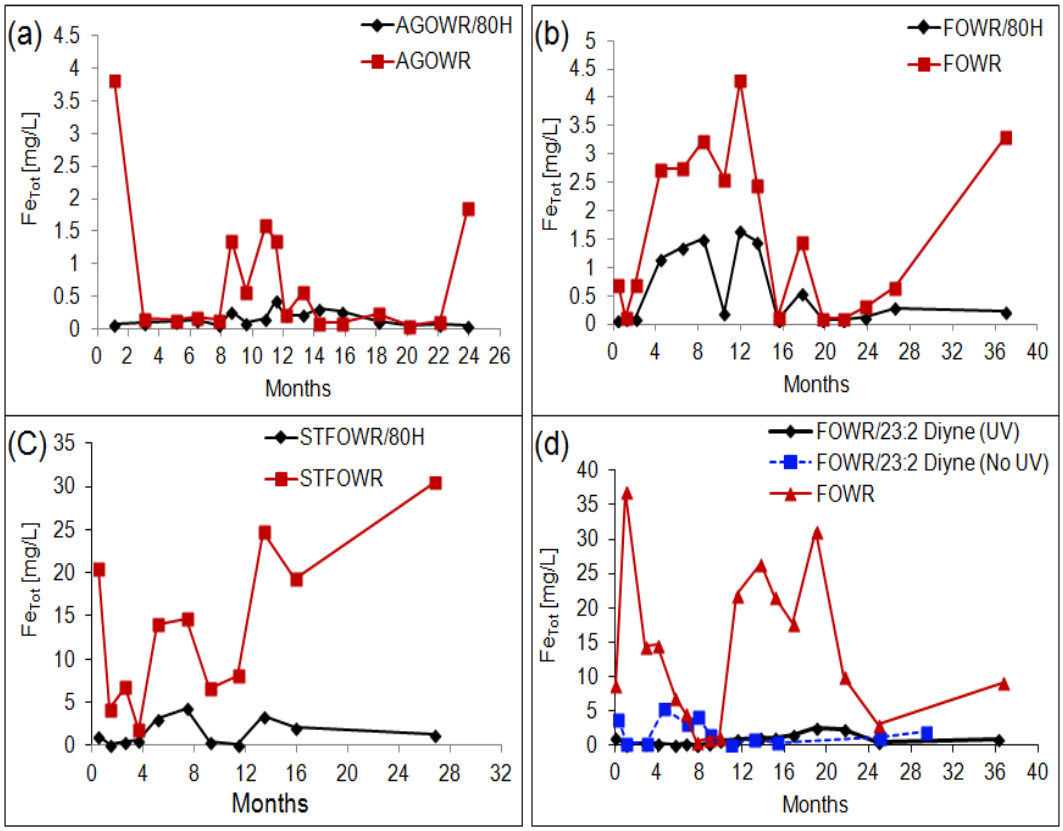

Figure 6.5. Average total iron (Fe_{Tot}) determination reported from the effluent AMD columns coated with AGOWR/80H (a), FOWR/80H (b), STFOWR/80H (c), and FOWR/23:2 Diyne PC (d). From all the control columns without the lipid coatings presence a higher amount of dissolved Fe_{Tot} release is measured relative to the coated lipid/OWR samplings with 80H phospholipon, and 23:2 Diyne PC under various conditions.

6.7 Metagenomic Analysis of FOWR and AGOWR

The microbial community structure developing in the test columns at the end of the exposure period, as well as in the as-received FOWR and AGOWR samples, was determined using 16S rDNA metagenomic analysis. The sequencing process generated over 140,000 reads (3,000 - 5,000 reads per sample) with a median read length of 538 bp. Examination of the microbial community profiles shows in general good agreement between the replicates of each sample, reflecting the consistency of DNA extraction, PCR amplification, and sequencing processes.

6.7.1 Diversity

Based on the Shannon diversity indexes, the microbial diversity in the original OWR samples was rather low, with indexes ranging from 3.3 to 3.4. The diversity increased significantly in all samples after incubation in the test and control columns, reaching indexes from 5.25 to 8.0. The diversity indexes were higher in the control samples than in lipid-treated samples, with the exception of the lipid/UV-treated FOWR sample, which showed a higher diversity than the FOWR control (Table 6.3).

6.7.2 Abundance

The relative abundance of bacterial groups in the as-received OWR samples showed a predominance of Proteobacteria, Firmicutes, Actinobacteria, and Bacteriodetes (Figure 6.6). The relative bacterial abundance in all column samples shows that Proteobacteria was the predominant phylum, representing 43-80% of the classified sequences. Besides Proteobacteria, Acidobacteria, Actinobacteria, Firmicutes, and Nitrospirae were the dominant phyla across all samples. Relatively higher proportions of Proteobacteria, Firmicutes, and Acidobacteria were observed in all lipid-treated samples; while higher proportions of Actinobacteria and Nitrospira were observed in the untreated OWR samples (see Figure 6.6).

Table 6.3. Alpha diversity indexes of OWR column samples and dry samples.

Sample	Shannon Index	Goods Coverage	Chao1	PD Whole Tree	OTUs	Equitability
FOWR/23.2D (UV)	3.64	0.94	3809	92.4	1928	0.48
FOWR.23/2D (no UV)	5.08	0.92	6007	120.9	2666	0.64
FOWR/80H	4.52	0.92	5328	115.7	2418	0.58
FOWR	4.44	0.93	4686	96.1	2054	0.58
AGOWR/80H	5.56	0.89	6805	135.0	3081	0.69
AGOWR	5.20	0.91	6249	128.0	2790	0.66
FOWR/dry	3.28	0.99	1074	27.6	424	0.54
AGOWR/dry	3.42	0.98	859	26.9	459	0.56

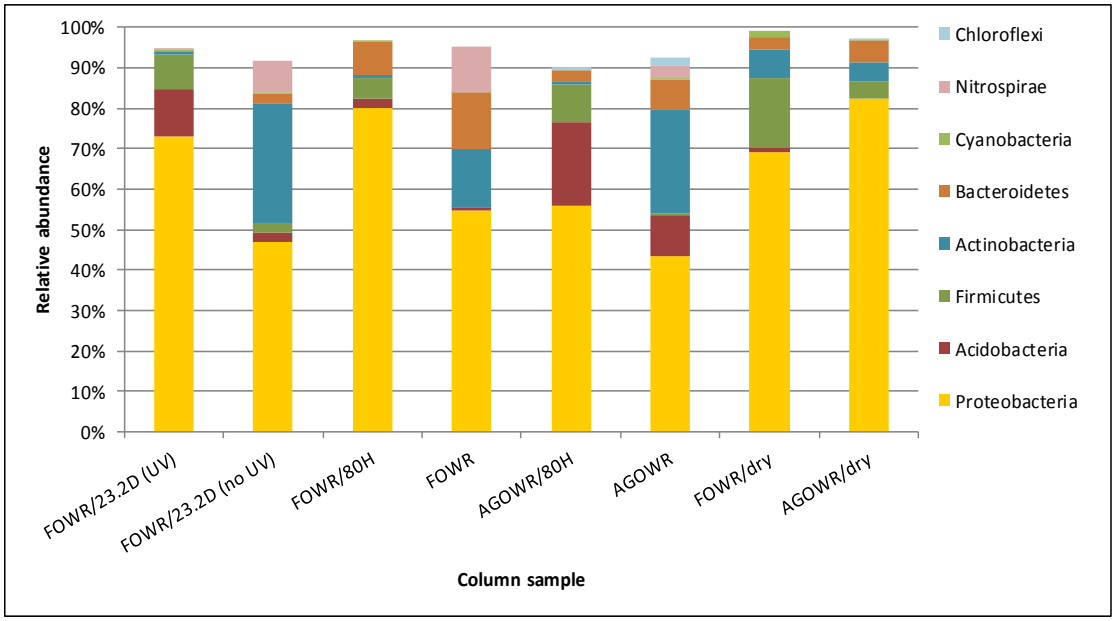

Figure 6.6. Abundance of major bacteria phyla detected in the column samples and dry samples. The phyla containing less than 1% of the total microbial species were not represented.

6.7.3 AMD microorganisms

The examination of the abundance of the specific bacterial families previously detected in AMD samples (Brett et al., 2003) revealed that the non-treated samples contained much higher proportions of AMD-specific species (42 to 45%) than the lipid-treated samples (11 to 23%).(Brubaker and Wildeman 2001) AMD species included mostly members of Acidobacteriaceae, Acidimicrobiaceae, Leptospirillaceae, Acetobacteraceae, Gallionellaceae, and Acidithiobacillaceae (Figure 6.7). Moreover, the non-treated samples contained many autotrophic iron and/or sulfur oxidizing AMD-specific species (21 to 39%), which were almost absent in the lipid-treated samples (~0%) (Figure 6.8). On the other hand, lipid-treated samples showed enrichment in Holophagaceae, Comamonadacae, and Xanthomonadaceae, suggesting that members of these families can use the lipids as a carbon and energy source

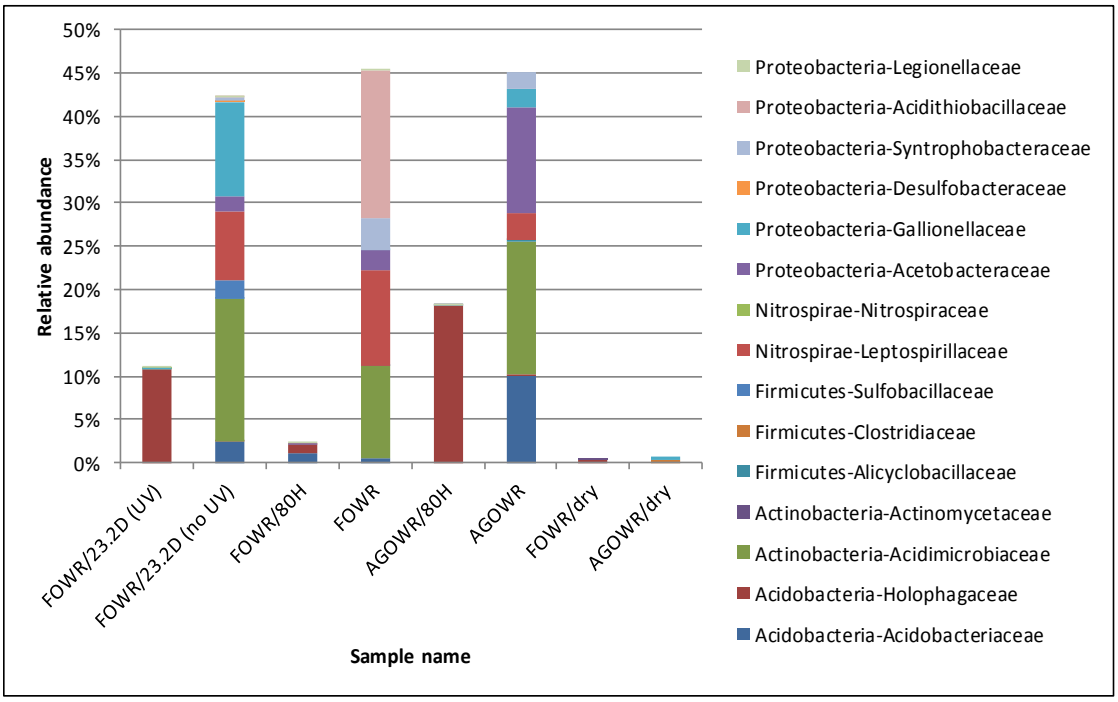

Figure 6.7. Abundance of AMD-specific bacteria families detected in the column samples and dry samples.

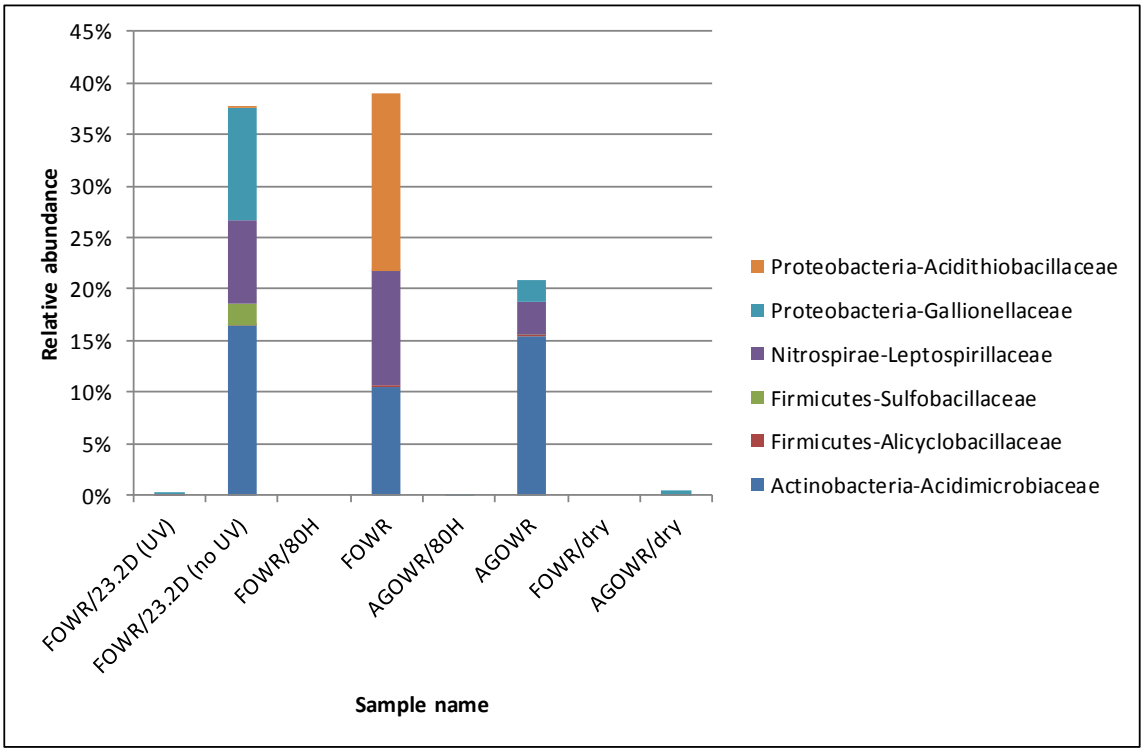

Figure 6.8. Abundance of AMD-specific bacteria families detected in the column samples and dry samples.

6.7.4 Redundancy analysis

Redundancy analyses (RDA) were conducted to estimate the effect of critical AMD parameters including pH, [SO_4^{2-}], and [Fe_{Tot}], on the structure of the microbial communities in the test column samples. As expected, the ordination diagram shows inverse correlation between sulfate and iron concentrations and pH (Figure 6.9). The diagram also shows that bacterial phyla containing most AMD-specific species, including Acidobacteria, Actinobacteria, and Nitrospirae, were present in the non-treated samples, with low pH and high levels of sulfate and iron. On the contrary, Proteobacteria and Firmicutes were found in treated samples, with relatively high pH and low sulfate and iron as summarized in the ordination diagram in Figure 6.9. Analysis of the results show that microbial communities typical of AMD environments develop on the untreated OWR whereas these AMD-associated communities do not develop on the mine OWR that were pretreated with phospholipid.

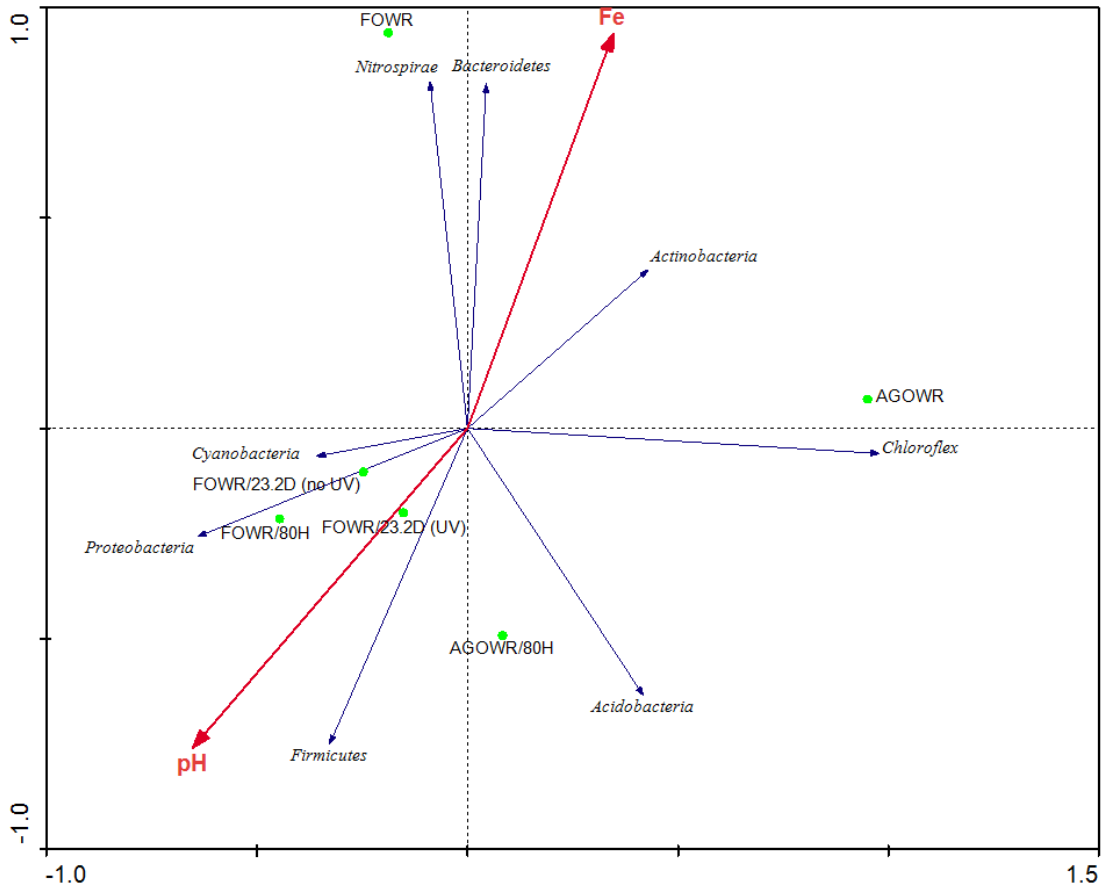

Figure 6.9. Ordination diagram showing the impact of several parameters, including pH, sulfate, and iron, on the abundance of major bacteria lineages detected in the column samples and dry samples.

6.8 Discussion

Perhaps there are two major results from this study that we feel are worthy of discussion. First, the exposure of mining OWR to phospholipid has a remarkable effect in suppressing chemistry that results in the oxidation of metal sulfide and the production of waters with low pH and elevated concentrations of metals (i.e., iron in our case). Prior studies from our laboratory showed that phosphatidylcholine lipids had a similar effect on pure pyrite model samples, but the experiments were short-term (e.g., 1 month) while the tests here were conducted for 3 years. While FOWR and AGOWR are rather complex mixtures of soil and rock, the results do suggest that the mechanism by which the phospholipid decreases AMD chemistry is due to binding to the iron sulfide component. We speculate based on our prior studies that the suppression of metal sulfide oxidation chemistry on FOWR/80H and AGOWR/80H is due to the phosphatidylcholine component of 80H. The large reduction in the rate of sulfate released in the presence of lipid coated AGOWR, as well as the higher pH of the effluent relative to the untreated AGOWR indicates that adsorbed 80H phospholipid significantly suppresses the oxidation of the sulfur component of AGOWR that leads to AMD.

Similar to 80H, pretreatment of FOWR with 23:2 Diyne PC showed a remarkable resistance to AMD chemistry. As mentioned before, the 23:2 Diyne PC contains diacetylene groups in the hydrocarbon tails. Prior studies from our laboratory showed that the exposure of this lipid to UV light when adsorbed on pyrite resulted in the cross-linking of the lipid tails.(Zhang, Jia et al. 2012) The oxidation of pyrite treated in this way was greatly suppressed (compared to untreated pyrite) and the resulting cross-linked

hydrophobic coating showed resistance to both an autotrophic and heterotrophic bacterium (*Acidithiobacillus ferrooxidans* and *Acidiphilium acidophilum*, respectively).(Hao, Murphy et al. 2009) The present study shows that 23:2 Diyne lipid has a similar ability to suppress AMD-like chemistry on pyrite-bearing OWR.

Based on prior studies from our laboratory, phosphatidylcholine lipids (which contain two fatty acid chains) with suitable fatty acid chain lengths suppress the oxidation of pyrite. The ability of the lipid to form a bilayer structure on the surface of the pyrite, which depends on the chain length, appears to be a prerequisite for the suppression.(Elsetinow, Borda et al. 2003) Spectroscopic studies suggest that the phosphate group of the phosphatidylcholine binds strongly to the Fe-component of pyrite.(Zhang, Jia et al. 2012) Lipids containing only a single fatty acid chain, such as stearic acid (or presumably lysophosphatidylcholine lipid) which the 80H formulation contains, would not have the ability to suppress pyrite oxidation based on our prior studies.(Zhang, Jia et al. 2012)

XRD results presented above from Figure 6.2a and b show that FOWR has a larger fraction of pyrite than AGOWR. This result is reasonable considering that FOWR had been collected soon after excavation at the mining site and would not have undergone as much AMD generating chemistry as AGOWR. The possibility that phospholipid is suppressing AMD chemistry by binding to the pyrite component of FOWR (and AGOWR) is probably best shown by returning to further analyze the XRD diffractograms exhibited in Figure 6.2a that are associated with FOWR and FOWR/80H XRD diffractograms after > 3 years of reaction. In particular, reflections due to pyrite are still

observable for the FOWR/80H sample (most noticeable at d-spacing of 2.71, 2.42, 1.92, 1.63 Å) whereas they are absent in the FOWR diffractogram. In short, lipid protected pyrite from decomposition reactions during the 3 year study. Interestingly, there were significant changes between the as-received FOWR and after 3 years of reaction. While the pyrite was protected, there were significant structural changes in the AMD tailing components as evidenced by the appearance of additional reflections in the 3-year sample compared to the as-received FOWR sample. Actually, the FOWR sample after 3 years looks very similar to the as-received AGOWR (see Figure 6.2b) sample. Exposure to water for the 3 years has likely resulted in many dissolution repreciptation reactions that likely formed various crystalline phases. We are currently conducting experiments to allow the identification of some of these new crystalline phases.

What we believe is a second significant result from our study is that the lipid-inspired suppression of AMD chemistry has a dramatic effect on the composition of the microbial communities. This is a profound result in the sense that it implies that the intentional modification of mine tailings, for example in a coal mining site, to inhibit AMD will change the nature of the microbial makeup of the site. This contention is consistent, for example, with prior field-study research that has shown that the composition of microbial communities associated with AMD afflicted environments change after such areas underwent remediation by limestone treatment (Basu, Gupta et al. 2012). We distinguish our study from this prior study in the sense that we have intentionally modified OWR by selectively binding a molecule (i.e., phospholipid) to the active-AMD generating phase in the OWR. Studies to determine how altering the

microbial communities by chemically modifying OWR will affect other chemistry at coal mining sites should be a future area of study.

With regard to our microbial based results, bacterial species detected in all the samples were distributed into 8 distinct phyla (the phyla containing less than 1% of the total microbial species were not considered). Five out of these 7 phyla are known to contain most AMD-specific species: Proteobacteria, Acidobacteria, Actinobacteria, Firmicutes, and Nitrospirae (Brubaker and Wildeman 2001). The original as-received OWR samples were characterized by a rather low microbial diversity. AMD microbial communities typically contain a limited number of distinct species that are capable to thrive under the extreme AMD conditions (low pH, high metal content) and to use specific electron donors available in these environments (reduced iron and sulfur).(Brubaker and Wildeman 2001) A relatively higher proportion of Proteobacteria (mainly beta- and alpha-Proteobacteria) was observed in all lipid-treated samples, suggesting enrichment in heterotrophic species using lipids as carbon and energy source. On the contrary, higher proportion of Actinobacteria and Nitrospira was observed in the control samples (lipid-free), suggesting that bacterial communities in non-treated samples were dominated by autotrophic bacteria using reduced iron and/or sulfur. Although the as-received OWR samples contained a low proportion of strains typically found in AMD (< 1%), the column treatment resulted in a significant increase of AMD-specific bacteria, ranging from 11 to 24% in lipid-treated samples and from 42 to 45% in control, non-treated samples. These results showed that lipid treatment dramatically reduced the development of AMD-specific species, which provides additional evidence about the efficiency of the treatment for the mitigation of AMD generation. On the other hand,

lipid-treated samples show enrichment in heterotrophic bacteria suggesting that lipids can be used as carbon and energy source. Interestingly, the most abundant AMD bacteria detected in all treated samples belong to the *Geothrix* genus, which includes versatile heterotrophic species capable of using ferric iron as an electron acceptor. (Coates, Ellis et al. 1999)

6.9 Summary

We believe that the results presented in this contribution suggest that the use of phospholipid to suppress AMD chemistry is an option that deserves further attention. Unlike the majority of treatments that generally involve the application of base (e.g., calcium oxide) to AMD-afflicted waters, the direct application of phospholipid offers the possibility of inhibiting the root cause of AMD. More remarkable is that the presence of the phospholipid shifts the composition of the microbial community away from microbes common to AMD environments that use electron donors such as ferrous iron. Interestingly, more heterotrophic bacteria are associated with the phospholipid coated samples, but the stability of the phospholipid appears to be excellent for the extent of our trial of > 3 years. Future experiments are underway to better test the effectiveness of the phospholipid under conditions that are even closer to the actual AMD environment.

6.10 Acknowledgments

D. R. S. and A.M.P.L greatly appreciated support from the Nanotechnology Institute of Pennsylvania for grants and Bridges to Doctorate Programs from the LSAMP/Louis Stroke for Minority Participants. Special thanks to the undergraduate students Sopheavy Siek, Eric Grant Gibbs and Birane Fall for their efforts working of the AMD columns. We specially thank graduate students Justin Northrup and Conrad Pfeiffer for their help with the HPLC/MS lipids analysis. We greatly thank David Plasket from the Glass blowing shop at Temple University. Also, the support and help received from Dr. George Myer, Dr. Nicholas C. Davatzes, James Ladd, and Steve Peterson from the Department of Earth and Environmental Science are greatly appreciated.

CHAPTER 7
7.1 SUMMARY AND REMARKS

The research presented is this dissertation highlights important chemistry associated with Al-, Fe-, mixed Al/Fe-oxyhydroxide nanoparticles. This work also addresses remediation strategies of to suppress the oxidation of pyrite iron sulfide (FeS_2) minerals from AMD refuse that are relevant to complex environmental problems.

7.1.2 Reactivity of Al/Fe Oxyhydroxides Toward Adsorbed $CO_{2(gas)}$

Research showed that the ferrihydrite surface is not significantly affected by low Al (0-30 mol%) inclusion into the ferrihydrite mineral, and there is only formation of crystalline AlOOH phases (e.g., bayerite/gibbsite) at an Al concentration ≥ 30 mol% substitution. Similarly, the binding geometry of adsorbed carbonate and bicarbonate species, which are formed in the presence of atmospheric $CO_{2(gas)}$ on the ferrihydrite surface, were not found to be considerably affected as Al substitution (up to 30 mol%) into the pure mineral. However, at Al substitution higher than 30 mol%, the adsorption capacity of the Al/Fe oxyhydroxide particles toward carbonate and bicarbonate decreased because of the formation of discrete phases of gibbsite/bayerite on the ferrihydrite surface. It was possible to calculate and distinguish the different adsorbed vibrational frequencies which are formed as the bridged solvated binuclear carbonate and the mononuclear monodentate bicarbonate complexes ($\delta_{4(HCO3^-)}$) bound to the Fe atom at ~1227 cm^{-1} and the Al atom ~1238 cm^{-1} relative to mixed Al/Fe when compared to pure Fe-oxyhydroxide clusters upon CO_2 interaction with the structural mineral surface using

DFT calculations. These calculated frequencies are found to be well correlated to the IR experimental vibrational modes. We concluded that the adsorbed carbonate and bicarbonate species formed have a higher affinity for amorphous or semi-crystalline iron nanoparticles within the lower range of Al mol% substituted into the ferrihydrite surfaces. As such, the structure and reactivity of the iron oxyhydroxide, ferrihydrite, and mixed Al/Fe oxyhydroxides are of potential significant interest in the context of a substrate for CO_2 capture. Furthermore, the results could help with an understanding of the interaction of dry binary Al/Fe oxyhydroxides (e.g., aerosols atmospheric chemistry) with environmental atmospheric CO_2 in both the aqueous or gas phases.

7.1.3 FerriFh Surface Reactivity Toward and $CO_{2(gas)}$ under Various Pressure Conditions

Chapter 3 presented the reactivity of the ferrimagnetic iron oxyhydroxide product compared to its precursor ferrihydrite toward gaseous CO_2 adsorption in the presence and absence of adsorbed organic citrate under various pressure conditions. XRD results showed a rapid phase transformation to hematite mineral (α-Fe_2O_3) upon aging of the ferrihydrite without adsorbed organic citrate. Adsorbed citrate is found to inhibit the formation of adsorbed carbonate and bicarbonate onto both dry ferrihydrite and its ferrimagnetic phase (FerriFh) upon gaseous CO_2 adsorption as evidenced by the ATR-FTIR investigation. Following the decontamination (citrate-free UV/O_3 process) of the FerriFh particles, ATR-FTIR results indicated the formation of bidentate binuclear carbonate species and monodentate-like bicarbonate complexes with similar binding geometries as on the ferrihydrite mineral surfaces. However, at elevated pressures (>50 psi) and under a closed CO_2 system, a loss of metastable bicarbonate complexes

occurred, but an increase in adsorbed carbonate species formation remained due to high pressure loading of $CO_{2(gas)}$. The results are of significant advantage because the enhancement of the ordered ferrimagnetic ferrihydrite structure with larger particles sizes (6-12 nm) may also serve as surface sinks for mineral carbonation in CO_2 capture. The material is often found in natural aerobic soils under elevated temperature and pressure conditions.

7.1.4 Adsorbed CO_3^{2-} and PO_4^{3-} Onto Al/Fe Oxyhydroxide Surfaces

ATR-FTIR combined with quantum chemical calculations were used to investigate aqueous phosphate co-adsorption with carbonate species as a function of pH, loading, ionic strength, and increasing Al substitution on the iron oxyhydroxide mineral surfaces under in-situ and ex-situ environmental conditions. The adsorption of carbonate and phosphate followed the typical trend for oxyanion adsorption (inner-sphere) on metal oxyhydroxide structures: there was a decrease in CO_3^{2-} and PO_4^{3-} uptake with increasing pH. Both species showed similar affinity for the same adsorption sites on the mineral surface. Most importantly, phosphate uptake increased as Al substitution increased in the iron oxyhydroxide up to 30 mol% (possibly due to a slight increase in particles surface area) compared to pure ferrihydrite, ferrimagnetic ferrihydrite, and goethite minerals under similar pH (with NaCl ~10 mM) conditions. Results from the DFT vibrational calculations suggested the presence of an inner-sphere, mono-protonated phosphate complex and de-protonated phosphate species between pH 5-9. Only the non-protonated species (in either bidentate or monodentate binding configuration) occurred at pH above 9. Our results agree well with prior and similar studies using the phosphate and Al- and

Fe-oxyhydroxide systems. However, the main interesting conclusion from this work is that the presence of Al incorporation showed a direct effect on the adsorbed phosphate species binding geometry on the mixed Al/Fe structures.

7.1.5 Phospholipid Treated OWR and Column Experiments

Phospholipid bilayers were used as an adsorbate to inhibit the oxidative decomposition of pyrite in the presence of microbial communities to form sulfuric acid and iron oxide. The organic phospholipids, which contain a hydrophilic head and hydrophobic hydrocarbon tails, form protective lipid-bilayers (also multilayers) that bind to reactive FeS_2 surface sites. The lipids suppressed the release of Fe_{Tot} and SO_4^{2-} during pyrite oxidation and also resulted in the increase of the pH of effluent water to circumneutral (5.5-7.5), compared to the untreated pyrite samples (with pH ~2-4.5). The use of the phospholipids showed potential for use in suppressing AMD chemistry under simulated environmental conditions.

BIBLIOGRAPHY

Akcil, A. and S. Koldas (2006). "Acid Mine Drainage (AMD): causes, treatment and case studies." Journal of Cleaner Production **14**(1213): 1139-1145.

Anderson, P. R. and M. M. Benjamin (1990). "Surface and Bulk Characteristics of Binary Oxide Suspensions." Environmental Science & Technology **24**(5): 692-698.

Arai, Y. and D. L. Sparks (2001). "ATR-FTIR spectroscopic investigation on phosphate adsorption mechanisms at the ferrihydrite-water interface." Journal of Colloid and Interface Science **241**(2): 317-326.

Arai, Y. and D. L. Sparks (2007). Phosphate reaction dynamics in soils and soil components: A muiltiscale approach. Advances in Agronomy, Vol 94. **94:** 135-179.

Arai, Y., D. L. Sparks, et al. (2004). "Effects of Dissolved Carbonate on Arsenate Adsorption and Surface Speciation at the Hematite-Water Interface." Environmental Science and Technology **38**(3): 817-824.

Aschenbrenner, O., P. McGuire, et al. (2011). "Adsorption of carbon dioxide on hydrotalcite-like compounds of different compositions." Chemical Engineering Research & Design **89**: 1711-1721.

Bachu, S., D. Bonijoly, et al. (2007). "CO2 storage capacity estimation: Methodology and gaps." International Journal of Greenhouse Gas Control **1**(4): 430-443.

Baltrusaitis, J. and V. H. Grassian (2005). "Surface reactions of carbon dioxide at the adsorbed water-iron oxide interface." J. Phys. Chemi. B **109**(25): 12227-12230.

Baltrusaitis, J. and V. H. Grassian (2010). "Carbonic Acid Formation from Reaction of Carbon Dioxide and Water Coordinated to Al(OH)(3): A Quantum Chemical Study." Journal of Physical Chemistry A **114**: 2350-2356.

Baltrusaitis, J., J. Schuttlefield, et al. (2007). "FTIR spectroscopy combined with quantum chemical calculations to investigate adsorbed nitrate on aluminium oxide surfaces in the presence and absence of co-adsorbed water." Physical Chemistry Chemical Physics **9**(36): 4970-4980.

Baltrusaitis, J., J. Schuttlefield, et al. (2011). "Carbon dioxide adsorption on oxide nanoparticle surfaces." Chemical Engineering Journal **170**(2-3): 471-481.

Bargar, J. R., J. D. Kubicki, et al. (2005). "ATR-FTIR spectroscopic characterization of coexisting carbonate surface complexes on hematite." Geochimica Et Cosmochimica Acta **69**(6): 1527-1542.

Barrn, V. and J. Torrent (2002). "Evidence for a simple pathway to maghemite in Earth and Mars soils." Geochimica et Cosmochimica Acta **66**(15): 2801-2806.

Barron, V., J. Torrent, et al. (2003). "Hydromaghemite, an intermediate in the hydrothermal transformation of 2-line ferrihydrite into hematite." American Mineralogist **88**(11-12): 1679-1688.

Barron, V., J. Torrent, et al. (2012). "Critical evaluation of the revised akdalaite model for ferrihydrite-Discussion." American Mineralogist **97**(1): 253-254.

Basu, T., K. Gupta, et al. (2012). "Performances of As(V) adsorption of calcined (250 degrees C) synthetic iron(III)-aluminum(III) mixed oxide in the presence of some groundwater occurring ions." Chemical Engineering Journal **183**: 303-314.

Bazilevskaya, E., D. D. Archibald, et al. (2011). "Aluminum coprecipitates with Fe (hydr)oxides: Does isomorphous substitution of Al(3+) for Fe(3+) in goethite occur?" Geochimica Et Cosmochimica Acta **75**(16): 4667-4683.

Becke, A. D. (1992). "Density-Functional Thermochemistry .1. the Effect of the Exchange-Only Gradient Correction." Journal of Chemical Physics **96**(3): 2155-2160.

Becke, A. D. (1997). "Density-functional thermochemistry .5. Systematic optimization of exchange-correlation functionals." Journal of Chemical Physics **107**(20): 8554-8560.

Benali, O., M. Abdelmoula, et al. (2002). The behaviour of phosphate ions as corrosion inhibitor for Fe(II)-Fe(III) hydroxycarbonate green rust.

Bertelsen, P., W. Goetz, et al. (2004). "Magnetic Properties Experiments on the Mars Exploration Rover Spirit at Gusev Crater." Science **305**(5685): 827-829.

Bhandari, N., D. B. Hausner, et al. (2010). "Photodissolution of Ferrihydrite in the Presence of Oxalic Acid: An In Situ ATR-FTIR/DFT Study." Langmuir **26**(21): 16246-16253.

Bishop, J. L. and E. Murad (2002). "Spectroscopic and geochemical analyses of ferrihydrite from springs in Iceland and applications to Mars." Geological Society, London, Special Publications **202**(1): 357-370.

Bocher, F., A. Gehin, et al. (2004). "Coprecipitation of Fe(II-III) hydroxycarbonate green rust stabilised by phosphate adsorption." Solid State Sciences **6**(1): 117-124.

Borch, T., Y. Masue, et al. (2007). "Phosphate imposed limitations on biological reduction and alteration of ferrihydrite." Environmental Science & Technology **41**(1): 166-172.

Brubaker, L. M. and T. Wildeman (2001). "Use of steel slag in the remediation of acid mine drainage." Abstracts of Papers of the American Chemical Society **221**: U178-U178.

Busca, G. and V. Lorenzelli (1982). "Infrared Spectroscopic Identification of Species Arising from Reactive Adsorption of Carbon Oxides on Metal-Oxide Surfaces." Mater. Chem. **7**(1): 89-126.

Cabello, E., M. P. Morales, et al. (2009). "Magnetic enhancement during the crystallization of of ferrihydrite at 25 and 50 degrees Celsius." Clays and Clay Minerals **57**(1): 46-53.

Campbell, T. (1999). "Dynamics of Oxidation of Aluminum Nanoclusters using Variable Charge Molecular-Dynamics simulations on Parallel Computers." Physical Reviews **82**(4866).

Cao, F. L., Y. F. Wu, et al. (2008). "Preparation and property of discoid aluminum-doped alpha-Fe2O3 particles." Acta Chimica Sinica **66**(12): 1405-1410.

Carta, D., M. F. Casula, et al. (2009). "Structural and magnetic characterization of synthetic ferrihydrite nanoparticles." Materials Chemistry and Physics **113**(1): 349-355.

Chadwick, J., D. H. Jones, et al. (1986). "A Mossbauer Study of Ferrihydrite and Aluminum Substituted Ferrihydrites." J. Magn. Magn. Mater. **61**(1-2): 88-100.

Childs, C. W. (1992). "Ferrihydrite - a Review of Structure, Properties and Occurrence in Relation to Soils." J.Plant Nutr. Soil Sc. **155**(5-6): 441-448.

Choi, S., J. H. Drese, et al. (2009). "Adsorbent Materials for Carbon Dioxide Capture from Large Anthropogenic Point Sources." ChemSusChem **2**(9): 796-854.

Chupas, P. J., X. Y. Qiu, et al. (2003). "Rapid-acquisition pair distribution function (RA-PDF) analysis." Journal of Applied Crystallography **36**: 1342-1347.

Cismasu, A. C., F. M. Michel, et al. (2012). "Properties of impurity-bearing ferrihydrite I. Effects of Al content and precipitation rate on the structure of 2-line ferrihydrite." Geochim. Cosmochim. Acta **92**: 275-291.

Cismasu, A. C., F. M. Michel, et al. (2011). "Composition and structural aspects of naturally occurring ferrihydrite." CR Geoscience **343**(2-3): 210-218.

Coates, J. D., D. J. Ellis, et al. (1999). "Geothrix fermentans gen. nov., sp. nov., a novel Fe(III)-reducing bacterium from a hydrocarbon-contaminated aquifer."

International Journal of Systematic and Evolutionary Microbiology **49**(4): 1615-1622.

Cornell R. M., S. U. (2003). The Iron Oxides:Structure, Properties, Reactions, Occurences and Uses. Weinheim. New York . Chichester, Willey~VCH Verlag GmbH & Co.

Cudennec, Y. and A. Lecerf (2006). "The transformation of ferrihydrite into goethite or hematite, revisited." Journal of Solid State Chemistry **179**(3): 716-722.

D. Briggs, M. P. S. (1992). Practical Surface Analysis –Auger and X-Ray Photoelectron Spectroscopy, Wiley.

Daou, T. J., S. Begin-Colin, et al. (2007). "Phosphate adsorption properties of magnetite-based nanoparticles." Chemistry of Materials **19**(18): 4494-4505.

Del Nero, M., C. Galindo, et al. (2009). "Surface reactivity of α-Al_2O_3 and mechanisms of phosphate sorption: In situ ATR-FTIR spectroscopy and ς potential studies." Journal of Colloid and Interface Science **342**(2): 437-444.

Edwards, K. J., M. O. Schrenk, et al. (1998). "Microbial oxidation of pyrite: experiments using microorganisms from an extreme acidic environment." American Mineralogist **83**: 1444 - 1453.

Elsetinow, A. R., M. J. Borda, et al. (2003). "Suppression of pyrite oxidation in acidic aqueous environments using lipids having two hydrophobic tails." Advances in Environmental Research **7**(4): 969-974.

Elsetinow, A. R., J. M. Guevremont, et al. (2000). "Oxidation of {100} and {111} surfaces of pyrite: Effects of preparation method." American Mineralogist **85**(3-4): 623-626.

Elsetinow, A. R., M. A. A. Schoonen, et al. (2001). "Aqueous geochemical and surface science investigation of the effect of phosphate on pyrite oxidation." Environmental Science & Technology **35**(11): 2252-2257.

Elzinga, E. J. and D. L. Sparks (2007). "Phosphate adsorption onto hematite: An in situ ATR-FTIR investigation of the effects of pH and loading level on the mode of phosphate surface complexation." Journal of Colloid and Interface Science **308**(1): 53-70.

Evangelou, V. P., A. K. Seta, et al. (1998). "Potential Role of Bicarbonate during Pyrite Oxidation." Environmental Science and Technology **32**(14): 2084-2091.

Fassbinder, J. W. E., H. Stanjekt, et al. (1990). "Occurrence of magnetic bacteria in soil." Nature **343**(6254): 161-163.

Filip, J., R. Zboril, et al. (2007). "Environmental applications of chemically pure natural ferrihydrite." Environmental Science & Technology **41**(12): 4367-4374.

Ford, G. C., P. M. Harrison, et al. (1984). "Ferritin - Design and Formation of an Iron-Storage Molecule." Philosophical Transactions of the Royal Society of London Series B-Biological Sciences **304**(1121): 551-&.

Geremias, R., R. Laus, et al. (2008). "Use of coal mining waste for the removal of acidity and metal ions Al (III), Fe (III) and Mn (II) in acid mine drainage." Environmental Technology **29**: 863-869.

Giles, D. E., M. Mohapatra, et al. (2011). "Iron and aluminium based adsorption strategies for removing arsenic from water." Journal of Environmental Management **92**(12): 3011-3022.

Gimsing, A. L. and O. K. Borggaard (2007). "Phosphate and glyphosate adsorption by hematite and ferrihydrite and comparison with other variable-charge minerals." Clays and Clay Minerals **55**(1): 108-114.

Gleisner, M., R. B. Herbert, et al. (2006). "Pyrite oxidation by Acidithiobacillus ferrooxidans at various concentrations of dissolved oxygen." Chemical Geology **225**: 16 - 29.

Gonzalez, E., M. C. Ballesteros, et al. (2002). "Reductive dissolution kinetics of Al-substituted goethites." Clays and Clay Minerals **50**(4): 470-477.

Gorham, N. T., T. G. St Pierre, et al. (2008). "Magnetic energy-barrier distributions for ferrihydrite nanoparticles formed by reconstituting ferritin." Journal of Applied Physics **103**(5).

Hammarstrom, J. M., P. L. Sibrell, et al. (2003). "Characterization of limestone reacted with acid-mine drainage in a pulsed limestone bed treatment system at the Friendship Hill National Historical Site, Pennsylvania, USA." Applied Geochemistry **18**(11): 1705-1721.

Hammersley, A. P., S. O. Svensson, et al. (1996). "Two-dimensional detector software: From real detector to idealised image or two-theta scan." High Pressure Research **14**(4-6): 235-248.

Hao, J., C. Cleveland, et al. (2006). "The effect of adsorbed lipid on pyrite oxidation under biotic conditions." Geochemical Transactions **7**(1): 8.

Hao, J., R. Murphy, et al. (2009). "Effects of phospholipid on pyrite oxidation in the presence of autotrophic and heterotrophic bacteria." Geochimica et Cosmochimica Acta **73**(14): 4111-4123.

Harrington, R., D. B. Hausner, et al. (2009). "Investigation of Surface Structures by Powder Diffraction: A Differential Pair Distribution Function Study on Arsenate Sorption on Ferrihydrite." Inorganic Chemistry **49**(1): 325-330.

Harvey, O. R. and R. D. Rhue (2008). "Kinetics and energetics of phosphate sorption in a multi-component Al(III)-Fe(III) hydr(oxide) sorbent system." Journal of Colloid and Interface Science **322**(2): 384-393.

Hausner, D. B., N. Bhandari, et al. (2009). "Ferrihydrite reactivity toward carbon dioxide." Journal of Colloid and Interface Science **337**(2): 492-500.

Herlihy, A. T., P. R. Kaufmann, et al. (1993). "The effects of acidic deposition on streams in the Appalachian Mountain and Piedmont Region of the Mid-Atlantic United States." Water Resour. Res. **29**(8): 2687-2703.

Hiemstra, T., R. Rahnemaie, et al. (2004). "Surface complexation of carbonate on goethite: IR spectroscopy, structure and charge distribution." Journal of Colloid and Interface Science **278**(2): 282-290.

Hong, H.-J., J.-S. Yang, et al. (2011). "Arsenic Removal Behavior by Fe-Al Binary Oxide: Thermodynamic and Kinetic Study." Separation Science and Technology **46**(16): 2531-2538.

Hong, H. J., W. Farooq, et al. (2010). "Preparation and Evaluation of Fe-Al Binary Oxide for Arsenic Removal: Comparative Study with Single Metal Oxides." Separation Science and Technology **45**(12-13): 1975-1981.

Houghton, J. T., Meria Filho, L.G., Callander, B.A., Harris, N., Kattenberg, A., Maskell, K., (1996). "The Climate change." Cambridge University Press

Ismail, H. M., D. A. Cadenhead, et al. (1997). "Surface reactivity of iron oxide pigmentary powders toward atmospheric components: XPS, FESEM, and gravimetry of CO and CO_2 adsorption." Journal of Colloid and Interface Science **194**: 482-488.

Izgec, O., B. Demiral, et al. (2008). "CO_2 injection into saline carbonate aquifer formations I: laboratory investigation." Transport in Porous Media **72**(1): 1-24.

Jambor, J. L. and J. E. Dutrizac (1998). "Occurrence and Constitution of Natural and Synthetic Ferrihydrite, a Widespread Iron Oxyhydroxide." Chemical Reviews (Washington, D. C.) **98**(7): 2549-2585.

Janney, D. E., J. M. Cowley, et al. (2000). "Transmission electron microscopy of synthetic 2- and 6-line ferrihydrite." Clays Clay Miner. **48**(1): 111-119.

Jensen, M. B., L. G. M. Pettersson, et al. (2005). "CO_2 sorption on MgO and CaO surfaces. A comparative quantum chemical cluster study." Journal of Physical Chemistry B **109**(35): 16774-16781.

Jentzsch, T. L. (2006). "Influence of aluminum doping on ferrihydrite nanoparticle reactivity (vol 110, pg 11746, 2006)." Journal of Physical Chemistry B **110**(37): 18729-18729.

Khare, N., D. Hesterberg, et al. (2004). "XANES determination of adsorbed phosphate distribution between ferrihydrite and boehmite in mixtures." Soil Science Society of America Journal **68**(2): 460-469.

Kloprogge, J. T., L. V. Duong, et al. (2006). "XPS study of the major minerals in bauxite: Gibbsite, bayerite and (pseudo-)boehmite." Journal of Colloid and Interface Science **296**(2): 572-576.

Kubicki, J. D., M. Aryanpour, et al. (2012). "Quantum mechanical calculations on FeOH nanoparticles." Geoderma **189â€“190**(0): 236-242.

Kubicki, J. D., K. W. Paul, et al. (2012). "ATR-FTIR and Density Functional Theory Study of the Structures, Energetics, and Vibrational Spectra of Phosphate Adsorbed onto Goethite." Langmuir **28**(41): 14573-14587.

Kubicki, J. D., K. W. Paul, et al. (2012). "ATR-FTIR and Density Functional Theory Study of the Structures, Energetics, and Vibrational Spectra of Phosphate Adsorbed onto Goethite." Langmuir **28**(41): 14573-14587.

Kwon, K. D. and J. D. Kubicki (2004). "Molecular orbital theory study on surface complex structures of phosphates to iron hydroxides: Calculation of vibrational frequencies and adsorption energies." Langmuir **20**(21): 9249-9254.

Lawson, G. E., Y. Lee, et al. (2003). "Formation of Stable Nanocapsules from Polymerizable Phospholipids." Langmuir **19**(16): 6401-6407.

Lee, C. T., W. T. Yang, et al. (1988). "Development of the Colle-Salvetti Correlation-Energy Formula into a Functional of the Electron-Density." Physical Review B **37**(2): 785-789.

Lefevre, G. (2004). "In situ Fourier-transform infrared spectroscopy studies of inorganic ions adsorption on metal oxides and hydroxides." Advances in Colloid and Interface Science **107**(2-3): 109-123.

Li, W., A.-M. Pierre-Louis, et al. (2013). "Molecular level investigations of phosphate sorption on corundum (Î±-Al_2O_3) by 31P solid state NMR, ATR-FTIR and quantum chemical calculation." Geochimica et Cosmochimica Acta **107**(0): 252-266.

Li, Z., Z. Qin, et al. (2006). "Synthesis of diphenyl carbonate from CO_2, phenoxide, and CCl_4 with $ZnCl_2$ as catalyst." Chemistry Letters **35**(7): 784-785.

Liu, Q. Y. and K. Osseo-Asare (2000). "Synthesis of monodisperse Al-substituted hematite particles from highly condensed metal hydroxide gels." Journal of Colloid and Interface Science **231**(2): 401-403.

Liu, W. Y., C. J. Moran, et al. "Quantitative Risk-Based Approach for Improving Water Quality Management in Mining." Environmental Science & Technology **45**: 7459-7464.

Liu, Y.-T. and D. Hesterberg (2011). "Phosphate Bonding on Noncrystalline Al/Fe-Hydroxide Coprecipitates." Environmental Science & Technology **45**(15): 6283-6289.

Luengo, C., M. Brigante, et al. (2006). "Kinetics of phosphate adsorption on goethite: Comparing batch adsorption and ATR-IR measurements." Journal of Colloid and Interface Science **300**(2): 511-518.

Manceau, A. (2011). "Critical evaluation of the revised akdalaite model for ferrihydrite." American Mineralogist **96**(4): 521-533.

Marchand, E. A. and P. Plumb (2005). "Minerals and mine drainage." Water Environment Research **77**: 1858-1927.

Masue, Y., R. H. Loeppert, et al. (2007). "Arsenate and arsenite adsorption and desorption behavior on coprecipitated aluminum : iron hydroxides." Environmental Science & Technology **41**(3): 837-842.

Meldrum, F. C., B. R. Heywood, et al. (1992). "Magnetoferritin - Invitro Synthesis of a Novel Magnetic Protein." Science **257**(5069): 522-523.

Michel, F. M., S. M. Antao, et al. (2006). "Size and structure of ferrihydrite from PDF analysis." Abstracts of Papers, 232nd ACS National Meeting, San Francisco, CA, United States, Sept. 10-14, 2006: GEOC-133.

Michel, F. M., V. Barron, et al. (2007). "Ordered ferrimagnetic form of ferrihydrite reveals links among structure, composition, and magnetism." Proceedings of the

National Academy of Sciences of the United States of America **107**(7): 2787-2792.

Michel, F. M., V. Barron, et al. (2010). "Ordered ferrimagnetic form of ferrihydrite reveals links among structure, composition, and magnetism." Proc. Natl. Acad. Sci. U.S.A. **107**(7): 2787-2792.

Michel, F. M., L. Ehm, et al. (2007). "The structure of ferrihydrite, a nanocrystalline material." Science **316**(5832): 1726-1729.

Michel, F. M., L. Ehm, et al. (2007). "Similarities in 2- and 6-line ferrihydrite based on pair distribution function analysis of x-ray total scattering." Chemistry of Materials **19**(6): 1489-1496.

Michel, F. M., H.-A. Hosein, et al. (2010). "Reactivity of ferritin and the structure of ferritin-derived ferrihydrite." Biochim. Biophys. Acta, Gen. Subj. **1800**(8): 871-885.

Michel, F. M., H. A. Hosein, et al. (2010). "Reactivity of ferritin and the structure of ferritin-derived ferrihydrite." Biochimica Et Biophysica Acta-General Subjects **1800**(8): 871-885.

Michel, F. M., J. B. Parise, et al. (2007). "The Structure of Ferrihydrite, a Nanocrystalline Material." Science **316**(5832): 1726-1729.

Mohai, M. (2004). "XPS MultiQuant: multimodel XPS quantification software." Surface and Interface Analysis **36**(8): 828-832.

Murphy, R., K. Lammers, et al. (2010). "Ferrihydrite phase transformation in the presence of aqueous sulfide and supercritical CO_2." Chem. Geol. **271**(1-2): 26-30.

Murphy, R., K. Lammers, et al. (2011). "Ferrihydrite phase transformation in the presence of aqueous sulfide and supercritical CO_2." Chemical Geology **271**(1-2): 26-30.

Oelkers, E. H. and J. Schott (2005). "Geochemical aspects of CO_2 sequestration." Chemical Geology **217**(3-4): 183-186.

Oganov, A. R., R. J. Hemley, et al. (2013). "Structure, Bonding, and Mineralogy of Carbon at Extreme Conditions." Reviews in Mineralogy and Geochemistry **75**(1): 47-77.

Ostrofsky, M. and A. Schworm (2011). "A history of acid mine contamination, recovery, and eutrophication in Sandy Lake, Pennsylvania." Journal of Paleolimnology **46**(2): 229-242.

Palandri, J. L. and Y. K. Kharaka (2005). "Ferric iron-bearing sediments as a mineral trap for CO_2 sequestration: Iron reduction using sulfur-bearing waste gas." Chem. Geol. **217**(3-4): 351-364.

Parise, J. B., R. Harrington, et al. (2010). "Understanding the composition and structure of ferrihydrite." Geochimica Et Cosmochimica Acta **74**: A793-A793.

Paufler, P. (2007). "Complete online set of International tables for crystallography, Vols. A-G. Edited by H. Fuess, Th. Hahn, H. Wondratschek, U. Muller, U. Shmueli, E. Prince, A. Authier, V. Kopsky, D. B. Litvin, M. G. Rossmann, E. Arnold, S. Hall and B. McMahon. Springer, jointly published with the IUCr, 2007. http://it.iucr.org." Acta Crystallographica Section A **63**(6): 483.

Persson, P., N. Nilsson, et al. (1996). "Structure and bonding of orthophosphate ions at the iron oxide aqueous interface." Journal of Colloid and Interface Science **177**(1): 263-275.

Peter J. Larkin (2011). IR and Raman Spectroscopy " *Principles anf Spectral Interpretation*". Waltham, MA, Elsevier Inc.

Pierre-Louis, A.-M., D. B. Hausner, et al. (2013). "Adsorption of carbon dioxide on Al/Fe oxyhydroxide." J Colloid Interface Sci.

Piszora, P. and E. Wolska (1998). X-ray powder diffraction study on the solubility limits in the goethite-diaspore solid solutions. (Eds.), Epdic 5, Pts 1 and 2. R. Delhez and E. J. Mittemeijer. **278-2:** 584-588.

Qui, X. (2004). " PDFgetX2: a GUI-driven program to obtain the pair distribution function from x-ray powder diffraction data." Journal of Applied Crystallography **37**: 678.

R. M. Cornell, U. S. (2003). "The Iron Oxides Structure, Properties, Reactions, Occurences and Uses." (Second Ed.).

Rahnemaie, R., T. Hiemstra, et al. (2007). "Carbonate adsorption on goethite in competition with phosphate." Journal of Colloid and Interface Science **315**(2): 415-425.

Rhoton, F. E. and J. M. Bigham (2005). "Phosphate adsorption by ferrihydrite-amended soils." Journal of Environmental Quality **34**(3): 890-896.

Rubasinghege, G., P. K. Kyei, et al. (2012). "Proton-promoted dissolution of alpha-FeOOH nanorods and microrods: Size dependence, anion effects (carbonate and phosphate), aggregation and surface adsorption." Journal of Colloid and Interface Science **385**: 15-23.

Schulze, D. G. and U. Schwertmann (1984). "THE INFLUENCE OF ALUMINUM ON IRON-OXIDES .10. PROPERTIES OF AL-SUBSTITUTED GOETHITES." Clay Minerals **19**(4): 521-539.

Schwertmann, U. (1991). Iron Oxides in the Laboratory: Preparation and Characterization. Weinheim, New York, Chichester, Willey-VCH.

Schwertmann, U. (1991). "Solubility and Dissolution of Iron-Oxides." Plant and Soil **130**(1-2): 1-25.

Schwertmann, U. (2000). Iron Oxides in the Laboratory: preparation and characterization. Weinheim. New York . Chichester, Willey~VCH.

Schwertmann, U., J. Friedl, et al. (1999). "From Fe(III) ions to ferrihydrite and then to hematite." Journal of Colloid and Interface Science **209**(1): 215-223.

Schwertmann, U., J. Friedl, et al. (2000). "The effect of Al on Fe oxides. XIX. Formation of Al-substituted hematite from ferrihydrite at 25 degrees C and pH 4 to 7." Clays and Clay Minerals **48**(2): 159-172.

Schwertmann, U., J. Friedl, et al. (2000). "The effect of clay minerals on the formation of goethite and hematite from ferrihydrite after 16 years' ageing at 25 DegC and pH 4-7." Clay Minerals **35**(4): 613-623.

Scott, A. P. and L. Radom (1996). "Harmonic Vibrational Frequencies: An Evaluation of Hartree-Fock, Møller-Plesset, Quadratic Configuration Interaction, Density Functional Theory, and Semiempirical Scale Factors." The Journal of Physical Chemistry **100**(41): 16502-16513.

Silva, N. J. O., V. S. Amaral, et al. (2005). "Magnetic behavior of iron (III) oxyhydroxy nanoparticles in organic-inorganic hybrid matrices." Journal of Magnetism and Magnetic Materials **290-291**(Pt. 2): 962-965.

Silva, N. J. O., V. S. Amaral, et al. (2006). "Structural and magnetic studies in ferrihydrite nanoparticles formed within organic-inorganic hybrid matrices." Journal of Applied Physics **100**(5).

Singer, P. C. and W. Stumm (1970). "Acid mine drainage: the rate-limiting step." Science **167**: 1121 - 1123.

Stookey, L. L. (1970). "Ferrozine - a New Spectrophotometric Reagent for Iron." Analytical Chemistry **42**(7): 779-&.

Strongin, D. R., C. P. Grey, et al. (2010). "Surface science studies of environmentally relevant iron (oxy)hydroxides ranging from the nano to the macro-regime." Surf. Sci. **604**(13â€“14): 1065-1071.

Strongin, D. R., C. P. Grey, et al. (2010). "Surface science studies of environmentally relevant iron (oxy)hydroxides ranging from the nano to the macro-regime." Surface Science **604**(13-14): 1065-1069.

Sujana, M. G. and S. Anand (2010). "Iron and aluminium based mixed hydroxides: A novel sorbent for fluoride removal from aqueous solutions." Applied Surface Science **256**(23): 6956-6962.

Tamilarasan, P. and S. Ramaprabhu (2012). "Polyaniline-magnetite nanocapsules based nanocomposite for carbon dioxide adsorption." International Journal of Greenhouse Gas Control **10**: 486-493.

Taylor, R. M. and R. M. McKenzie (1980). "The Influence of Aluminum on Iron-Oxides .6. the Formation of Fe(II)-Al(III) Hydroxy-Chlorides, Fe(II)-Al(III)Hydroxy-Sulfates, and Fe(Ii)-Al(Iii)Hydroxy-Carbonates as New Members of the Pyroaurite Group and Their Significance in Soils." Clays and Clay Minerals **28**(3): 179-187.

Tejedor Tejedor, M. I. and M. A. Anderson (1990). "Protonation of Phosphate on the Surface of Goethite as Studied by Cir-Ftir and Electrophoretic Mobility." Langmuir **6**(3): 602-611.

Torrent, J. and V. BarrÃ³n (2000). "Key Role of Phosphorus in the Formation of the Iron Oxides in Mars Soils?" Icarus **145**(2): 645-647.

Torrent, J., Q. S. Liu, et al. (2007). "Magnetic enhancement and iron oxides in the upper luochuan Loess-paleosol sequence, Chinese Loess plateau." Soil Science Society of America Journal **71**: 1570-1578.

Torrent, J., U. Schwertmann, et al. (1992). "Fast and Slow Phosphate Sorption by Goethite-Rich Natural Materials." Clays and Clay Minerals **40**(1): 14-21.

Villalobos, J. O. L. a. M. (2000). "Carbonate adsorption on goethite under closed and open CO_2 conditions " Geochemica et Cosmochimica Acta **64**(22): 3787-3802.

Violante, A., E. Barberis, et al. (2003). "Factors affecting the formation, nature, and properties of iron precipitation products at the soil-root interface." J. Plant Nutrt. **26**(10 & 11): 1889-1908.

Violante, A., G. S. R. Krishnamurti, et al. (1998). "Formation and stability of hydroxy aluminum iron montmorillonite complexes: Influence of ferrous iron." Soil Science Society of America Journal **62**(5): 1448-1454.

Viollier, E., P. W. Inglett, et al. (2000). "The ferrozine method revisited: Fe(II)/Fe(III) determination in natural waters." Applied Geochemistry **15**(6): 785-790.

Vu, H. P., S. Shaw, et al. (2008). "Transformation of ferrihydrite to hematite: an in situ investigation on the kinetics and mechanisms." Mineralogical Magazine **72**(1): 217-220.

Wijnja, H. and C. P. Schulthess (2001). "Carbonate adsorption mechanism on goethite studied with ATR-FTIR, DRIFT, and proton coadsorption measurements." Soil Science Society of America Journal **65**(2): 324-330.

Xu, W., D. B. Hausner, et al. (2011). "Structural water in ferrihydrite and constraints this provides on possible structure models." American Mineralogist **96**(4): 513-520.

Ye, T., D. Wynn, et al. (2001). "Photoreactivity of Alkylsiloxane Self-Assembled Monolayers on Silicon Oxide Surfaces." Langmuir **17**(15): 4497-4500.

Zhang, X. V., S. P. Ellery, et al. (2007). "Photodriven reduction and oxidation reactions on colloidal semiconductor particles: Implications for prebiotic synthesis." Journal of Photochemistry and Photobiology a-Chemistry **185**(2-3): 301-311.

Zhang, X. X., Y. F. Jia, et al. (2012). "Bacterial reduction and release of adsorbed arsenate on Fe(III)-, Al- and coprecipitated Fe(III)/Al-hydroxides." Journal of Environmental Sciences-China **24**(3): 440-448.

Zhao, J. M., F. E. Huggins, et al. (1994). "Ferrihydrite - Surface-Structure and Its Effects on Phase-Transformation." Clays and Clay Minerals **42**(6): 737-746.

APPENDIX A: SUPPLEMENTAL INFORMATION (SI)

Further characterization of 2-line ferrihydrite and samples containing low aluminum substitutions were performed using high-energy X-ray total scattering coupled with pair distribution function (PDF) analysis. The PDF technique was used in this study to estimate the average size of nanoparticulates samples, and the average particles sizes were estimated with ImageJ software. X-ray scattering experiments were carried out at beam line 11-ID-C at the Advanced Photon Source (APS), Argonne National Laboratory using monochromatic radiation of energy 114.46 KeV (λ = 0.10786 Å). Samples were loaded dry into a polyimide (kapton) capillary. The diffracted beam was collected using a Perkin-Elmer amorphous silicon detector. The conversion from 2D to 1D was carried out using the program Fit2D (Hammersley, Svensson et al. 1996). PDFs were generated by Fourier transform of the total structure function, S(Q) (Q_{max} = 30 $Å^{-1}$), corrected as outlined previously using the program PDFgetX2 (Chupas, Qiu et al. 2003)'(Qui 2004).

This plot shows the subtraction results for the PDF of 5 mol% Al and 30 mol% from the pure ferrihydrite in the search of indentifying the precipitated phase at Al content above 10 mol%. The PDF for Al/Fe with 30% Al was obtained using a Qmax of 24 $Å^{-1}$. Previously, we would have taken the three PDFs (0, 5 and 30% Al), and lined them up. At first glance, there is little difference between them.

The Fourier transform of the total structure function, S(Q) (Q_{max} = 30 $Å^{-1}$) for the dry samples yields the PDF or G(r) which is a real space representation of the atomic ordering of the material (Hammersley, Svensson et al. 1996). Figure 1A shows pair distribution function patterns for 0, 5, and 30 mol % Al doped ferrihydrite, respectively. The patterns for the synthesized samples show that the PDF of ferrihydrite, Al 5 %, and 30 % doped Fhyd which are consistent with a single phase base on the comparison of the most intense scattering features in the short-range ordering (i.e., distances of 1-5 Å). Furthermore, the short-rang ordering appears is almost indistinguishable, but the intermediate range atomic ordering (5 to 20 Å) attenuates similarly over the distance range of 15 to 20 Å for all three samples. The PDF is consistent for ferrihydrite scattering domain sizes ranging from 2 to 6 nm (Harrington, Hausner et al.),(Michel, Barron et al. 2007). This result suggests that Al can be homogeneously incorporated in the ferrihydrite up to 30 At % on the basis of the PDF patterns comparison. Like a traditional XRD pattern, the PDF can be taken as a fingerprint of the phase (Michel, Antao et al. 2006). The peaks match in each PDF is strong evidence that the phases are at least morphologically homogenous up to 30 At % Al substitution ferrihydrite

SI Figure 1A. PDF results for the 5 mol% Al and 30 mol% compared to ferrihydrite

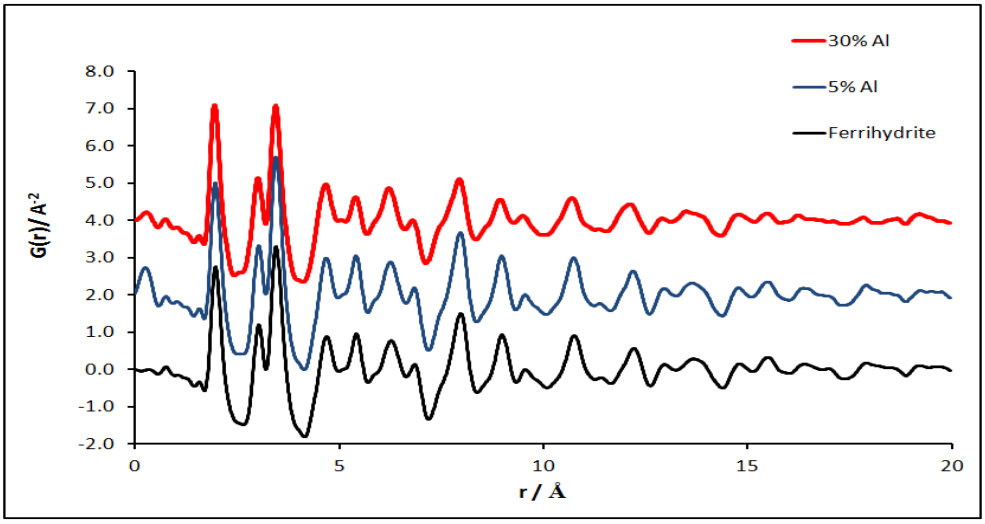

Supplemental Information (SI) Table 1A. Experimental versus calculated vibrational frequencies for Al bound phosphate structural complexes with their fitting correlation parameters (Fit Pars: A is y-intercept, B-slope, R^2-goodness of fit, SD-standard deviation, and N-number of data points) at pH 5

Samples	Al 0%	Al 5%	Al 10%	Al 30%	Persson	Al 0%	Al 5%	Al 10%	Al 30%	Persson	Al 0%	Al 5%	Al 10%	Al 30%	Persson
pH	5	5	5	5	4.2-5.71	5	5	5	5	4.2-5.71	5	5	5	5	4.2-5.71
Fit Pars.	MH_2	MH_2	MH_2	MH_2	MH_2	MH_1	MH_1	MH_1	MH_1	MH_1	MH_0	MH_0	MH_0	MH0	MH0
A	31.16	88.46	45.66	17.28	5.76	13.12	1.72	77.82	38.31	77.75	40.50	115.88	85.38	41.79	21.35
B	0.96	0.91	0.95	0.97	1.00	1.01	1.01	0.92	0.96	0.93	1.08	1.17	0.92	1.05	1.02
R^2	0.99	0.98	0.97	0.99	0.98	0.99	1.00	0.99	0.98	0.99	0.99	0.99	0.98	0.99	0.98
SD	14.16	17.76	21.39	12.06	16.68	15.42	6.91	17.66	18.66	10.21	16.12	7.60	23.76	9.25	21.73
N	5	5	5	4	6	5	4	4	4	4	4	3	4	3	4

Supplemental Information (SI) Table 2A. Experimental versus calculated vibrational frequencies for Al bound phosphate structural complexes with their fitting correlation parameters (Fit Pars: A is y-intercept, B-slope, R^2-goodness of fit, SD-standard deviation, and N-number of data points) at pH 7

Samples	Al 0%	Al 5%	Al 10%	Al 30%	Persson	Al 0%	Al 5%	Al 10%	Al 30%	Persson	Al 0%	Al 5%	Al 10%	Al 30%	Persson
pH	7	7	7	7	7.9	7	7	7	7	7.9	7	7	7	7	7.9
Fit Pars.	MH_2	MH_2	MH_2	MH_2	MH_2	MH_1	MH_1	MH_1	MH_1	MH_1	MH_0	MH_0	MH0	MH0	MH0
A	53.64	65.29	46.66	157.18	1.64	29.92	30.03	59.38	123.41	197.87	67.08	38.92	87.21	3.13	438.96
B	0.94	0.94	0.96	1.15	1.01	0.96	1.02	1.06	0.88	1.21	0.95	0.97	1.09	0.99	1.46
R^2	0.97	0.98	0.98	0.99	1.00	0.99	0.99	0.98	1.00	0.99	0.99	0.99	0.99	0.99	0.98
SD	21.68	18.67	17.64	9.52	4.09	16.83	14.55	16.56	4.21	16.46	14.95	17.68	17.186	16.66	13.95
N	5	5	6	4	4	4	5	5	4	4	3	4	3	3	3

Supplemental Information (SI) Table 3A: Experimental versus calculated vibrational frequencies for Al bound phosphate structural complexes with their fitting correlation parameters (Fit Pars: A is y-intercept, B-slope, R^2-goodness of fit, SD-standard deviation, and N-number of data points) at pH 9

Samples	Al 0%	Al 5%	Al 10%	Al 30%	Arai/Sparks	Persson	Al 0%	Al 5%	Al 10%	Arai/Sparks	Persson	Al 0%	Al 5%	Al 10%	Arai/Sparks	Persson
pH	9	9	9	9	9	9.4	9	9	9	9	9.4	9	9	9	9	9.4
Fit Pars.	MH_2	MH_2	MH_2	MH_2	MH_2	MH_1	MH_1	MH_1	MH_1	MH_1	MH1	MH0	MH0	MH0	MH0	Al_2-MH0
A	3.02	10.29	88.62	36.66	35.03	194.22	22.50	39.74	85.79	98.25	45.28	54.66	23.01	137.2	96.46	35.26
B	0.99	0.99	1.083	0.97	1.02	1.20	0.98	1.03	0.91	0.90	0.95	1.06	1.02	0.86	1.09	0.96
R^2	0.99	0.98	0.98	0.96	0.99	0.98	0.98	0.99	0.99	0.99	0.98	0.99	0.98	0.89	0.99	0.97
SD	13.83	22.31	17.852	27.79	7.76	21.44	18.06	13.53	13.50	6.89	21.20	13.21	22.05	33.94	12.08	17.47
N	4	4	5	4	4	4	4	4	4	3	3	3	4	3	3	3

APPENDIX B: SUPPORTING INFORMATION (SI)

SI Figure 1B. Reflecting the consistency of DNA extraction, PCR amplification, and sequencing processes for the quality control results of fresh overburden waste rock (FOWR) columns coated with the 23:2 Diyne PC and exposed to UV treatment.

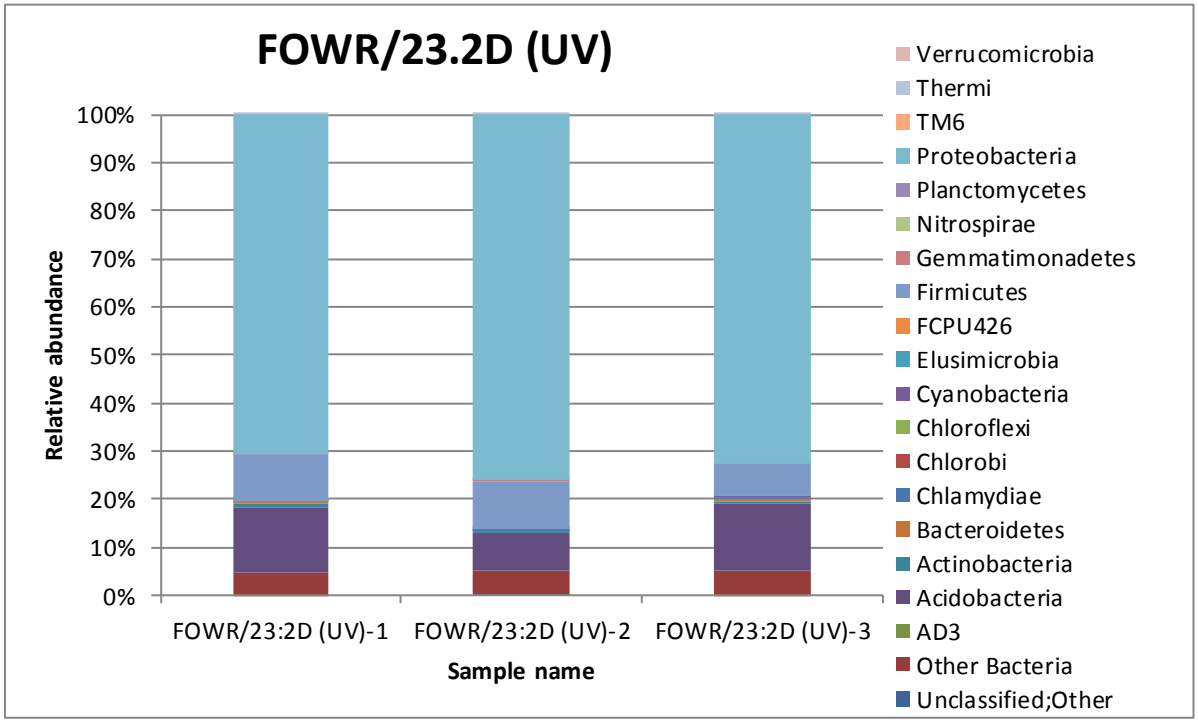

SI Figure 2B. Quality control results from the FOWR/23:2 Diyne column in the absence of UV exposure.

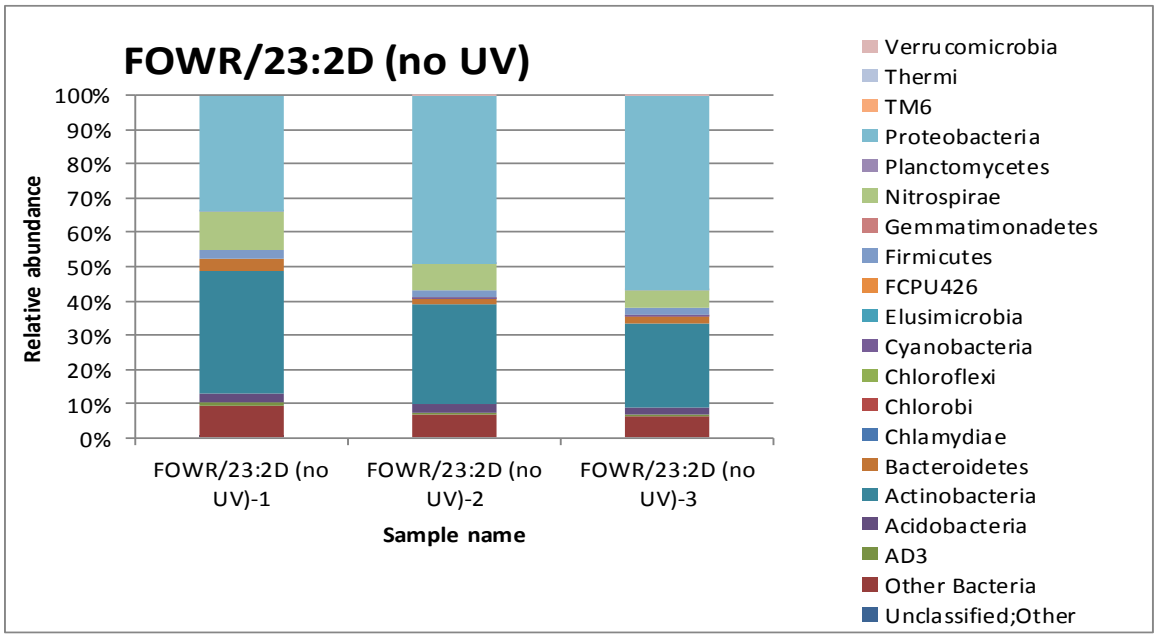

SI Figure 3B Continued. Quality control resulted from the FOWR/80H treated column.

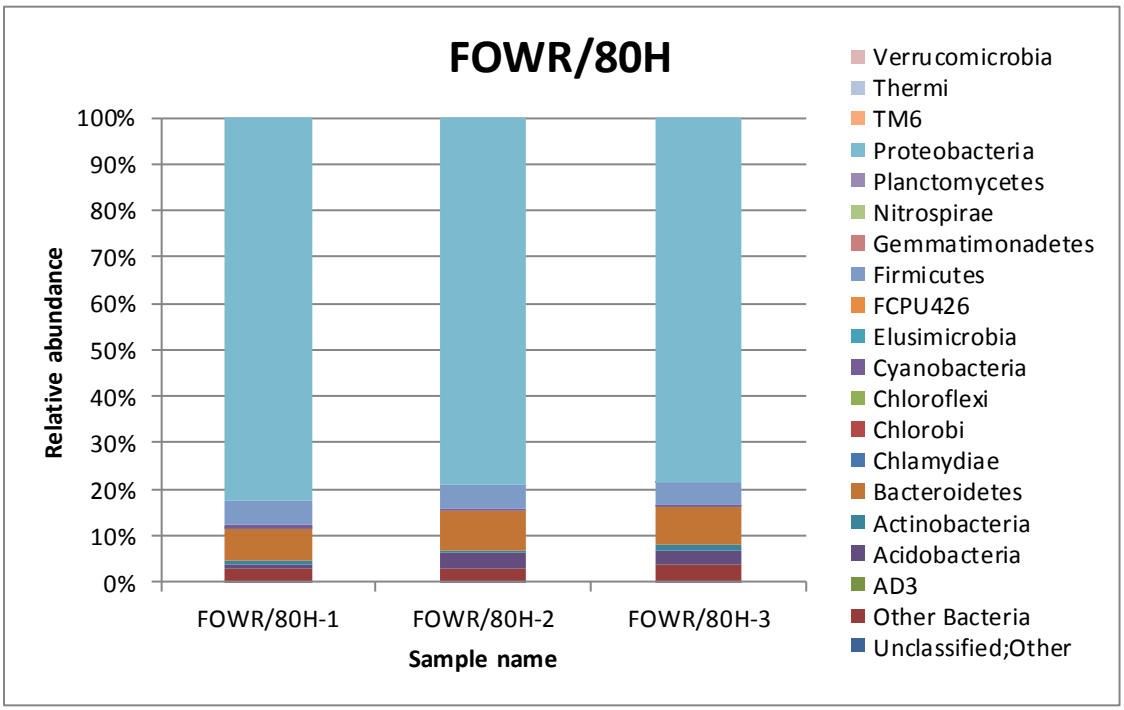

SI Figure 4B Continued. Quality control resulted from the FOWR untreated column.

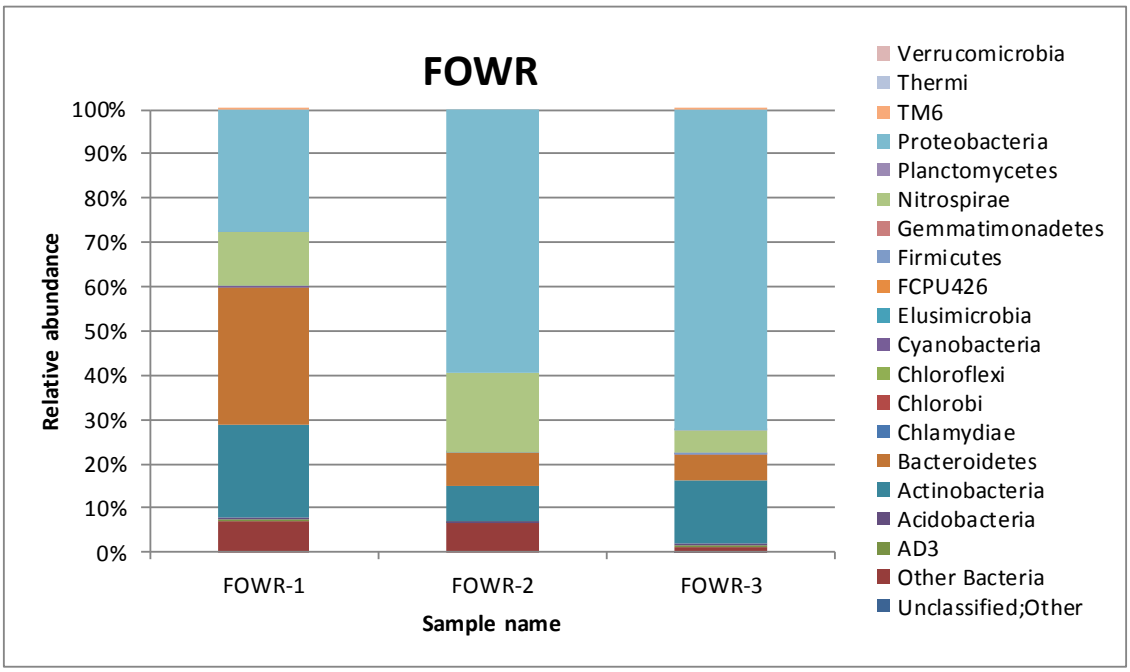

SI Figure 5B Abundance of AMD-specific bacteria families detected in the different column samples compared to the OWR dry samples.